

Light generation, size constraints, and dynamic cavities in silicon photonics

Thesis by
Jeffrey M. Shainline

Submitted in partial fulfillment of the
requirements for the degree of Doctor of Philosophy
in the Program in Physics at Brown University

Brown University
Providence, Rhode Island
Defended June 30, 2010

© Copyright 2010 by Jeffrey M. Shainline

Acknowledgements

I am deeply grateful for the assistance I received throughout graduate school from many people. I was extremely fortunate to work under Dr. Xu because he was patient with my approach to research and allowed me to develop quite independently. I also grew immensely as a scientist by watching his creative process. My lab mates were also consistently helpful. Beginning with the training I received from Dr. Aijun Yin, Dr. Pavel Kossyrev, and the collaboration with Dr. Efraim Rotem and later working alongside Dr. Gustavo Fernandes, Dr. Zhijun Liu, and Dr. Lyuba Kutznetsova, I benefited a great deal from the stream of post-docs that ran through the lab. For brainstorming, sharing ideas, and friendship, the other graduate students in the lab were critical. Senior students—such as Teng-Fang Kuo and Chih-Hsun Hsu—led as examples of how to succeed in our lab. I learned a great deal from conversations with Hongsik Park. Although his projects were quite different from mine, his discipline and his ability to dive extremely deep into a project inspired me to do the best I could with my work. And I regularly benefited from the perspective and friendship of Steven Palefsky. No list of acknowledgements about the Laboratory for Emerging Technologies would be complete without a tip of the hat to the lab manager, Dr. Jin-Ho Kim, who does so much to keep the ship sailing, or to Jeff Brown, our Administrative Assistant, whose contributions to the process of doing research and operating a lab are immeasurable.

Professor Rashid Zia deserves special acknowledgement as a mentor throughout my time at Brown. Not only did I learn a great deal from taking his Computational Electromagnetics and Nano-optics classes and from participating in his Quantum Optics summer reading course and his Optical Experimentation summer laboratory course, but I benefited immensely from working closely with him in a less formal setting to understand topics like

the Green's dyadic and the local density of optical states. Dr. Zia's approach to science is incredibly thorough and meticulous. As a mentor he is patient and generous with his time. The scientist that I am today was deeply impacted by his guidance, and my experience at Brown was shaped by his friendship.

Other members of the scientific community were instrumental in my research. The work on light emission from nanopatterned Si benefited from discussions with Professors Michael Aziz, Federico Capasso, Gordon Davies and George Watkins, and was made possible by support from the Office of Naval Research and Dr. Chagaan Baatar. The work on silicon microdisks was made possible by Dr. Gernot Pomrenke and the grant support of AFOSR (FA9550-07-1-0286) and to the WCU program at SNU, Korea. The work presented in this thesis was performed in part at the Center for Nanoscale Systems (CNS), a member of the National Nanotechnology Infrastructure Network (NNIN), which is supported by the National Science Foundation under NSF award no. ECS-0335765. CNS is part of the Faculty of Arts and Sciences at Harvard University.

Finally, I am deeply grateful for the contributions made by my family to my education. My parents helped me financially all through college giving me the opportunity to focus on physics and learn the fundamentals. They were also quite supportive and encouraging all through graduate school. Karlene Shainline was a very supportive and patient girlfriend and fiancé through times when I needed someone to believe in me unconditionally and through circumstances where it took a lot of courage to believe in our relationship. I am now so lucky to have her as my wife.

Preface

Graduate school has been a fruitful time of learning physics, but also—and perhaps more importantly—it has been a time of learning how to manage projects and of learning how to choose which projects to take on and learning where my interests really lie. I believe there are very few Ph.D. advisors who give their graduate students as much freedom as Dr. Xu, and as is often said with great freedom comes great responsibility.

When I joined Dr. Xu's lab, a previous graduate student, Sylvain Cloutier, had recently demonstrated a silicon laser emanating from an unusual source of light. At this time Dr. Cloutier was leaving the lab and I, along with Dr. Efraim Rotem, were charged with the task of learning as much as we could about the source of light in nanopatterned silicon and making it brighter. At this time I knew nothing about the field of silicon photonics, but this seemed like a great project for a graduate student to dive into. I learned a great deal from working with Dr. Rotem, and we had some success in developing the understanding of the nanopatterned silicon laser and improving the optical properties of nanopatterned silicon. This work constitutes Chapter 2 of this thesis.

But after a year our grant ran out, and Dr. Rotem moved back to Israel. I began writing code to model the nanopatterned silicon structure as a photonic crystal. This work is presented in Chapter 3 of this thesis.

Around the time I finished the plasmonic band structure calculations, Dr. Xu received a grant with the goal of making optical resonant cavities which were smaller than the wavelength of light they stored. I was immediately drawn to this project and asked Dr. Xu if I could take it on. This project had it all: structures that were challenging to fabricate, but not so hard that a single graduate student could not figure it out; theory that was interesting

but did not require a full-time theorist; and an experimental apparatus that I was excited to build. So I began working on this project full force, and within a year and a half we had achieved what the grant was paying us to do. This work is presented in Chapter 8. We then branched out. Postdoc Zhijun Liu led the effort to make subwavelength lasers, and I became interested in tunable interactions enabled by tunable microdisks. My work on tunable resonators is presented in Chapter 9.

During my background research related to tunable resonators I realized just how interesting and important the field of silicon photonics is. As a scientist I am most interested in projects that enable communication and information processing. Silicon photonics is poised to have an enormous impact on communication and information technology in this century. Some of my current ideas related to how the work presented in this thesis may be relevant to future technologies are presented in Chapter 10.

As you can see this thesis is something of a chronological history of my time in Dr. Xu's lab. I now feel prepared to become a professional in the field of photonics and make a career contributing to technologies that advance the state of human communication and information processing capability. I am very grateful to Dr. Xu for providing me the setting, funding, and guidance to get to this point.

Jeffrey M. Shainline

Providence, Rhode Island

“Graceful swans of never topple to the earth.”

—Billy Corgan

Dedicated to my parents who made my education possible and my wife for her patience and support when graduate school was less than pleasant.

Contents

Dedication	viii
1 Introduction: Why silicon photonics?	1
I Light generation and manipulation in nanopatterned silicon	5
2 Light generation from nanopatterned silicon	7
2.1 The challenge of extracting light from silicon	7
2.2 Nanopatterned silicon	9
2.3 The G center	9
2.4 Increasing the intensity of the G line	12
2.4.1 Creation of G centers	13
2.4.2 Increasing carbon concentration with solid-phase epitaxy	13
2.5 Luminescence increase from nanopatterned C-enriched Si	15
2.6 Summary of our work on G centers in nanopatterned Si	17
3 Light propagation in a plasmonic crystal	19
3.1 Metallodielectric metamaterials and photonic crystals	20
3.2 Three-component metallodielectric photonic crystals with dispersion and damping	21
3.3 Theoretical methodology	22
3.4 Results and discussion	25

3.5	Closing remarks	30
II	Subwavelength and dynamic resonant microcavities	33
4	Resonances in optical cavities	35
4.1	Resonances in nature	35
4.2	History of optical microcavities	36
4.3	Size domains in optical microcavities	38
5	Microdisk theory	43
5.1	Microdisk geometry	43
5.2	First principles analytical model	44
5.2.1	Reduction to a scalar problem	44
5.2.2	Brief discussion of polarization	47
5.2.3	Boundary and quantization conditions	48
5.2.4	The effective index of refraction	49
5.2.5	The radial boundary	51
5.2.6	Field components	52
5.2.7	Consideration of the effective potential	53
5.3	The quantum disk	55
5.4	Cavity Q , photon lifetime, photon path length and resonance spectral shape	57
6	Tapered fiber spectroscopy	61
6.1	The craft of pulling tapered fibers	64
6.2	Taking data with tapered fibers	66
7	Fabrication of silicon microdisks	71
8	Subwavelength silicon microdisks	75
8.1	The context for wavelength-scale photonic components	75

8.2	Review of microdisk theoretical considerations	76
8.3	Fabrication of subwavelength silicon microdisks	79
8.4	Experimental details and results of subwavelength silicon microdisks	80
8.5	Analysis from a tunneling perspective	86
8.6	Subwavelength lasers	87
8.7	Conclusions	90
9	Dynamic broad tuning of whispering-gallery modes in silicon microdisks	93
9.1	Context for tunable resonators and existing technologies	95
9.2	Modeling and fabrication of wired microdisks	97
9.3	Broad tuning and general characteristics of wired microdisk modes	101
9.4	Damage to microdisk mode spectrum due to sidewall contacts	108
9.5	Summary of wired microdisk work	111
10	Future Directions	113
10.1	Tunable Interactions	113
10.2	New tunable cavity designs	115
10.3	Ultimate goals	118
A	Erbium doping, porous silicon, silicon nanocrystals, and Raman generation	121
A.1	Er doping	121
A.2	Porous silicon	123
A.3	Quantum confined structures	124
A.4	Raman conversion and other non-linear methods	126
B	Numerical aspects of the plasmonic crystal calculation	127
C	Numerical methods for calculation of microdisk modes and quality factors.	131
C.1	Resonant frequencies and mode volumes obtained with Comsol weak form approach	131

C.2	Finite-difference frequency-domain approach to calculation of microdisk	
	Q factors	132
D	Simple model for thermal switching time in wired microdisks	135

List of Figures

1.1	Two technologies which have been extraordinarily successfully and are converging to Si photonics. (a) A multi-core Si processor. (b) Optical fibers made of glass.	2
2.1	Si photoluminescence taken from the 1989 review of emissive point defects in Si written by Gordon Davies and cited in Ref. [1]. The spectra are taken at 26K and recorded with four different slit widths (1000 μm , 450 μm , 300 μm and 100 μm) to give varying amplification and resolution. The labels refer to the combinations of phonons which are involved in the various luminescence pathways. G is the $k = 0$ optical phonon mode. The peak labeled 0 is the ideally-forbidden zero-phonon component.	8
2.2	PL data taken adapted from Ref. [2]. Spectra were acquired at 10K. In black (lower spectrum) is the PL from an unpatterned SOI sample. The red (upper spectrum) is from the nanopatterned SOI sample. The 1.278nm G line is present.	9

2.3	<p>PL spectrum of Si bombarded with 100keV Si⁺ to a fluency of 10¹⁴Si⁺/cm² and annealed at 250°C for 30min. The ZPL at 1218nm dominates the spectrum. It is the well-known <i>W</i> line to be discussed later in the present article. The ZPL at 1149nm is believed to be the <i>Q</i> line associated with a C-Li complex [3]. There is believed to be a forbidden transition at the same center observable below 2K. The Li and C present in the lattice are residual contaminants introduced during the growth of the crystal. The broader luminescence from 1149nm beyond 1218nm are from a variety of phonon replicas of the <i>Q</i> center and the <i>W</i> center as well as a multitude of other weakly-luminescing centers. The ZPL at 1560nm is the <i>C</i> line, believed to be associated with a C-O complex [4]. The band edge luminescence is observable at 1130nm. However, the presence of so much damage in the lattice and so many optically active defects makes band-edge radiative recombination unlikely.</p>	10
2.4	<p>Schematic of the <i>G</i> center. (a) Tetrahedral structure of Si bonds. (b) <i>G</i> center in the emissive B configuration. Atoms involved in the <i>G</i> center are depicted in full opacity whereas atoms not participating in the point defect are shown as semitransparent.</p>	11
2.5	<p>Schematic of the luminescence mechanism in <i>p</i>-type Si. A donor state of the <i>G</i> center in the B⁰ configuration acquires a hole from the valence band to form the B⁺ state. The acceptor state then captures an electron from the conduction band to form the B* state. The B* state makes an electric dipole transition back to the B⁰ state.</p>	12
2.6	<p>Schematic of the implantation and annealing process for solid-phase epitaxy. A pristine, crystalline Si lattice (a) is amorphized by bombarding with Si ions and is then implanted with C ions (b). The crystal is subsequently re-grown by annealing using the undamaged bottom layer as a seed layer (c). 14</p>	14

2.7	Schematic of the nanopatterned Si fabrication process. (a) SEM image of a free-standing AAO membrane [5]. (b) The AAO membrane is placed atop an SOI wafer and used as an etch mask. (c) An array of nanopores in the SOI wafer results from RIE through the AAO etch mask. In this image the AAO has been removed.	15
2.8	Photoluminescence spectrum of nanopatterned Si and nanopatterned C-enriched Si. The inset shows a semi-log plot of the region containing the <i>G</i> line and phonon replicas. The peak of the <i>G</i> line in C-enriched material was shown to be as much as 33 times that of unenriched SOI.	16
3.1	AAO nanopore array filled with Au. The AAO is anodized to have $10\mu\text{m}$ deep pores of $\sim 50\text{nm}$ diameter. A metallic contact is made to the back of the array, and the entire structure is then coated with an insulator, leaving only the top of the array open to fluidic conduction. The structure is placed in a Au electrodeposition chamber, and the pores are filled with Au via electrodeposition.	19
3.2	Nanopatterned Si with Au evaporated into the pores. The nanopatterned Si array is fabricated as described in Chapter 2, but before removing the AAO mask the sample is mounted in an electron beam evaporation chamber and Au is deposited in the pores.	20
3.3	The Wigner-Seitz cell of the two-dimensional three-component crystal. The lattice constant is a . The radius of the inner core cylinder is R . The thickness of the shell is d . The three dielectric regions are shown. The first Brillouin zone and points of high symmetry are shown in the inset.	22
3.4	The three lowest photonic bands of a two-component photonic crystal composed of metallic cylinders of filling factor 0.01 (a-c) and .1 (d-f) arranged in a square lattice. (a,d) The real part of the band structure. (b,e) The imaginary part of the band structure. (c,f) The lifetime of the states.	25

- 3.5 The six lowest E -polarized photonic bands of a two-component photonic crystal composed of metallic cylinders arranged in a square lattice. (a) Metallic filling factor is 0.1. (b) Metallic filling factor is 0.6. 27
- 3.6 The six lowest E -polarized photonic bands of a three-component photonic crystal composed of metallic cylinders surrounded by a dielectric shell of permittivity $\epsilon = 12$ arranged in a square lattice. The filling factor of the dielectric is 0.1. (a,b) Real part of the band structure. (c,d) Lifetime of the states. (a,c) Metallic filling factor is 0.1. (b,d) Metallic filling factor is 0.6. Discontinuities in the imaginary parts of the band structure result from the fact that eigenvalues are sorted by real part of ω ; when one lists the eigenvalues this way on either side of a band crossing and then plots a truncated number of bands, the imaginary parts of the eigenvalues can appear discontinuous. 27
- 3.7 The six lowest E -polarized photonic bands of a three-component photonic crystal composed of dielectric cylinders of permittivity $\epsilon = 12$ surrounded by a metallic shell arranged in a square lattice. The filling factor of the dielectric is 0.1. (a,b) Real part of the band structure. (c,d) Lifetime of the states. (a,c) Metallic filling factor is 0.1. (b,d) Metallic filling factor is 0.6. 27
- 3.8 The lowest propagating frequency of E -polarized modes for two-component, three-component metallic core and three-component metallic shell photonic crystals plotted as a function of filling factor of the metallic component of the cylinders. The filling factor of the dielectric components is 0.1. 29

4.1	Optical microcavities of different types. Q is plotted versus the characteristic size of the structures. The y axis is logarithmic while the x is linear. On the low- Q , small d end of the figure we have (a) and (b), which we fabricated and studied. These are of diameter just below (a) and just above (b) the resonant wavelength. In (a) the Q is limited by radiation and is ~ 200 . In (b) the radiation limited Q is ~ 5000 . (c) A zipper photonic crystal cavity is $> 20\mu\text{m}$ in one dimension, but much smaller in the transverse dimensions. The Q limited by the material absorption of SiN is $\sim 10^5$ [6]. (d) A ring resonator is shown with $10\mu\text{m}$ diameter and $Q \sim 10,000$ limited by surface scattering [7]. (e) A Si microdisk with $10\mu\text{m}$ diameter made in our lab. The surface-scattering-limited Q is $\sim 10^5 - 10^6$. (f) A 2-D photonic crystal defect cavity with Q near 10^6 [8]. (g) A silica microsphere with radiation-limited Q exceeding 10^8 [9]. (h) A silica toroid with radiation-limited- Q exceeding 10^8 [9].	39
4.2	Field profiles of two microdisk whispering-gallery modes are shown. (a) The H_z component of the $\text{TE}_{1,50}$ mode. (b) The H_z component of the $\text{TE}_{2,46}$ mode	40
4.3	Relationship between disk radius and azimuthal mode order. Data obtained numerically as described in Appendix C. The radius of the cavity was varied to obtain each resonance as close to 1570nm as possible. The height of the disk is 240nm . Five mode families are shown. Of these, only the TE_1 mode family is present in disks with diameters less than the resonant wavelength of 1570nm . The $\text{TE}_{1,2}$ - $\text{TE}_{1,5}$ modes are calculated to exist in subwavelength cavities, and are seen to fall below the black line in the figure separating cavities that are smaller than the free-space resonant wavelength from those that are larger (admittedly a somewhat arbitrary differentiation). The mode solver did not converge to the $\text{TE}_{1,1}$ mode, most likely due to the fact that the resonance is poorly-confined and has a Q of order 1.	40

4.4	Calculated Q factors of the TE modes in Fig. 4.3. The subwavelength modes $TE_{1,4}$ and $TE_{1,5}$ are calculated to have Q factors exceeding 100, indicating potential for laser and device applications.	41
5.1	The microdisk structure under consideration. The height of the disk is h , and its radius is a . The permittivity of the material is ϵ which is taken to be frequency-independent. The region inside the disk is referred to as region I. Above and below the disk is region II. Beyond the radius of the disk is region III.	44
5.2	The relationship between disk height and effective index of refraction. The index of refraction is set at 3.48 and the wavelength is 1550nm. The effective index is similar for the two polarizations in thick disks, but as the disk gets thinner the TM effective index drops off much faster than the TE. . . .	49
5.3	Here we consider a disk of height 250nm with index fixed at 3.48. The wavelength is the variable. We see that the effective index of the TM modes decays faster with increasing wavelength than the TE modes. The difference $\bar{n}(\lambda) - \bar{n}(\lambda = 1550nm)$ is plotted rather than simply $\bar{n}(\lambda)$ because the fractional change in \bar{n} with wavelength is much smaller than the difference between \bar{n} for the two polarizations, so a plot of $\bar{n}^{TE}(\lambda)$ and $\bar{n}^{TM}(\lambda)$ simply looks like two straight lines, and the physical comparison is lost. . .	50
5.4	In this plot the wavelength is 1550nm and the height is 250nm. Physical index is the variable. Here we see that the effective index of the TM modes grows faster with increasing index than the TE modes.	50
5.5	Field profiles of the $TE_{1,51}$ mode in the $\rho - z$ plane. Angular dependence of the form $\exp(im\phi)$ is assumed, and the absolute values of the field components are shown.	52
5.6	Field profiles of the $TE_{2,46}$ mode in the $\rho - z$ plane. Angular dependence of the form $\exp(im\phi)$ is assumed, and the absolute values of the field components are shown.	53

5.7	Field profiles of the $TE_{3,41}$ mode in the $\rho - z$ plane. Angular dependence of the form $\exp(im\phi)$ is assumed, and the absolute values of the field components are shown.	53
5.8	Field profiles of the $TM_{1,33}$ mode in the $\rho - z$ plane. Angular dependence of the form $\exp(im\phi)$ is assumed, and the absolute values of the field components are shown.	53
5.9	Field profiles of the $TM_{2,29}$ mode in the $\rho - z$ plane. Angular dependence of the form $\exp(im\phi)$ is assumed, and the absolute values of the field components are shown.	54
5.10	The effective potential. V_{eff} enters the radial equation for the scalar generating function (Eq. 5.34) and is responsible for optical confinement. The tunneling barrier is apparent at $\rho = a$, and the tunneling distance, d_T , is labeled.	55
6.1	Schematic of the tapered-fiber pulling and spectroscopy apparatus. An optical microscope (not shown) is located above the sample. In pulling mode, the fiber is mounted suspended between the two opposing $x - y - z$ stages. The stages are used to move the fiber into the flame. They are then pulled apart as the fiber is heated. Once the fiber is pulled, the H_2 torch is removed from the vicinity, and the stages are used to move the fiber into the near field of the microcavity under the microscope. The tunable laser is then injected into the fiber. The transmission as a function of wavelength can be monitored on the optical spectrum analyzer (OSA), or the net power through the fiber can be monitored on the power meter.	62
6.2	Taking data with a tapered fiber. (a) Schematic of a tapered fiber near a Si microdisk. (b) Image taken from above through the 100x objective of the optical microscope. The diameter of the disk is $10\mu\text{m}$, and the fiber is $\sim 2\mu\text{m}$. (c) Image of a subwavelength Si microdisk with $1.35\mu\text{m}$ diameter.	62

6.3	Tapered-fiber spectrum of a $10\mu\text{m}$ diameter disk. Many modes with varying Q factors and different depths of coupling to the fiber are present. . . .	68
6.4	Identifying mode families in the tapered-fiber spectrum. The most prominent mode family, TE_3 , is highlighted, and the wavelength spacing is labeled. In addition to the wavelength spacing, the similarity in depth of coupling helps us identify the group of resonances as a mode family. . . .	68
6.5	Identifying mode families in the tapered-fiber spectrum. By analyzing FSRs and depth of coupling we can make educated guesses to identify six mode families. They are color-coded.	69
6.6	The same tapered-fiber spectrum as in Figs. 6.3-6.5. Here we highlight each mode family separately.	69
6.7	A high-resolution tapered-fiber spectrum of a high- Q mode in a Si microdisk. (a) A 1nm wavelength window shows the resonance of interest. An SEM image depicts the Si microdisk. (b) The data from (a) fit to a Lorentzian. The extracted Q factors are 590,000 and 700,000 for the two modes of the doublet.	69
7.1	Schematic of the Si microdisk fabrication process. (1) We begin with pristine SOI. (2) Electron-beam resist is spin coated on the chip and the pattern is written with electron-beam lithography. (3) The written pattern is developed, leaving the disk etch mask. (4) The pattern is transferred to the Si device layer using RIE. (5) The devices are isolated on a plateau for tapered-fiber access. (6) Undercut with HF is performed to optically isolate the disk.	71
7.2	Several wavelength-scale Si microdisks isolated on a ridge. The disks have slightly different diameters, so the undercut results in pedestals of differing widths.	73

7.3	Close-up SEM images of three completed microdisks. (a) A large microdisk of $10\mu\text{m}$ diameter. Because the radius of this cavity is more than $3\mu\text{m}$ (the thickness of the buried oxide layer) the HF undercut can remove the entire buried oxide layer—with the exception of the pedestal—without lifting off the microdisk (b) A wavelength-scale cavity. (c) A cavity in which resist reflow was utilized to smooth the sidewalls. The departure from sidewall verticality is apparent.	73
8.1	Comparison of microdisks in two size domains. (a) A $10\mu\text{m}$ Si microdisk. (b) A tapered-fiber spectrum from a $10\mu\text{m}$ disk with a complicated mode spectrum consisting of several modes with Q factors exceeding 100,000 and many exceeding 10,000. (c) A high-resolution scan of what appears to be a single mode in (b) reveals three distinct contributions, further emphasizing the richness of the mode spectrum of this large disk. (d) SEM image of a disk with diameter smaller than the resonant wavelength. (e) A full 100nm tapered-fiber spectrum with a single resonance. The FSR of TE_1 modes in this disk at these azimuthal mode orders is $\sim 200\text{nm}$. Contrasting (e) with (b), one observes the simplicity of the mode spectrum in the small disk relative to the large disk. (f) A fit of the data in (e) gives a value of 257 for the measured Q factor of the $m = 4$ mode.	81
8.2	Silicon microdisks of decreasing diameters and tapered fiber spectra. (a-d) SEM images of disks of diameter $1.89\mu\text{m}$, $1.75\mu\text{m}$, $1.48\mu\text{m}$, and $1.35\mu\text{m}$ respectively. Resonant transmission dips in tapered fiber spectra acquired from the disks are shown. The y -axes of the plots on the right are transmission in arbitrary units and the x -axis is wavelength detuning.	82

8.3	Fabricated structures and calculated field profiles of microdisks for $m=7$ and $m=4$ modes. (a) Disk of $1.89\mu\text{m}$ diameter. (b) $\text{Re}(H_z)$ field profile of $m=7$ mode in the $y - z$ plane calculated with the FDFD method. $Q = 18, 200$. (c) Far field ($\log_{10}(\text{Re}(H_z))$) for the same disk. (d) $\text{Re}(H_z)$ in the $x - y$ plane calculated analytically. (e) Disk of $1.35\mu\text{m}$ diameter. (f-h) Calculations for the $1.35\mu\text{m}$ disk corresponding to those in (b)-(d).	82
8.4	Microdisk Q versus m . Experimental data, theoretical values obtained with FDFD and a fit to an exponential function are shown. The linear relationship between the disk radius, r_0 , and m is shown in the inset.	82
8.5	The effective potential and tunneling parameters. The tunneling distance, d_T , is proportional to m , so the tunneling probability, T , decays as $\exp(-\kappa'm)$. The Q is inversely proportional to the tunneling probability and behaves as $\exp(\kappa'm)$	86
8.6	The layered structure of the quantum well gain medium. Six InGaAs quantum wells are separated by AlInAs barrier layers. The quantum wells are contained within InGaAs cladding layers on an InP substrate.	88
8.7	Quantum well subwavelength laser. (a) SEM image of the fabricated microdisk on the InP substrate. (b) μ -PL spectra at various pump powers. . . .	89
8.8	Evidence for lasing in the subwavelength microdisk. (a) Linewidth narrowing as a function of pump power. (b) Integrated intensity of the PL versus pump power on a log-log plot shows threshold behavior.	90
9.1	Three coupled Si microdisks each of $5\mu\text{m}$ diameter in a triangular photonic molecule configuration.	93
9.2	Three Si microdisks of $10\mu\text{m}$ diameter to coupled to each other via a waveguide.	94

9.3	Two tapered-fiber spectra from $10\mu\text{m}$ disks, offset on the y -axis for clarity. These two $10\mu\text{m}$ disks were fabricated at the same time on the same chip and are separated by a few hundred microns. The slight discrepancies between the two spectra result from minor fabrication differences between the two disks. This slight mode mismatch is difficult to overcome and becomes more of an issue as the size of the disks is reduced. Such a mode mismatch makes it difficult for the structures in Fig. 9.1 and 9.2 to achieve strong coupling. We seek a method to tune the mismatched spectra into resonance with one another after fabrication.	94
9.4	Microdisk structure with electrical contacts. (a) SEM image of the structure under consideration. (b) Electro-thermal simulation data. The surface temperature of the structure is shown.	97
9.5	SEM image of the full layout of a tunable microdisk sample. All disks are seen to be isolated on a plateau. The wire bonds are made directly to the Si pads which taper to the nanowire contacts which enter the side walls of the Si microdisks. The nanowire contacts as well as the wire bonds sweep away from the region of the disk where the tapered fiber accesses the disk. Three unwired disks are observable at the center of the structure. These disks are included in the fabrication process for the purpose of comparing wired to unwired disks.	99
9.6	Tapered fiber spectra of a tunable microdisk. Spectra are shown at tuning powers from 0W to 1.6mW. Several prominent peaks are labeled and their behavior characterized.	101

9.7	Difference in mode shifts between TE and TM polarized modes. (a) Experimental data of resonant wavelength shifts for fifteen modes of various radial orders as a function of power. TE and TM modes are seen to separate into distinct groups independent of radial mode order. (b) Theoretical prediction of mode shifts for six TE and six TM modes of various radial mode orders plotted as a function of power. The corresponding index of refraction labels the x -axis on the top.	104
9.8	$ \mathbf{E} ^2$ calculated for the (a) TE _{2,42} mode and (b) TM _{2,25} mode. Field profiles are plotted in the $\rho - z$ plane and are assumed to have $\exp(im\phi)$ azimuthal dependence.	105
9.9	Tapered fiber spectrum from a wired microdisk. Several features of this spectrum will be analyzed in the following plots.	105
9.10	Lorentzian fit to a high-resolution scan of the resonance near 1578nm. The contribution to loading of the Q from the fiber is assessed by taking successive measurements while moving the fiber away from the disk. The resulting measured Q exceeds 18,000 and is affected by contributions to loss from material absorption due to doping as well as scattering from the nanowire contacts.	106
9.11	A Lorentzian fit to the resonance near 1597nm. This is the resonance with the best coupling to the tapered fiber. The measured Q factor exceeds 15,000.	106
9.12	Switching data from the same resonance as shown in Fig. 9.11. With the application of 5V (100 μ W) the well-coupled resonance can be shifted by far more than a full width at half maximum. While the thermal switching may not be fast, it can be highly energy efficient.	107

9.13	Tapered-fiber spectra of broad tuning in the same sample studied in Figs. 9.9-9.12. Here we show spectra taken at applied voltages from 0V-30V in 5V steps. The powers are 0W, 120 μ W, 550 μ W, 120 μ W, 1.1mW, 1.7mW, 2.4mW, and 3.2mW respectively. This disk is slightly less energy efficient than the sample studied in Fig. 9.6, most likely due to a slightly broader pedestal.	108
9.14	Color-coded mode family identification of the same tapered-fiber spectrum as shown in Fig. 9.9. The TE ₁ and TE ₂ mode families are not identified with the same techniques as described in Section 6.2.	109
9.15	The same spectrum as shown in Figs. 9.9 and 9.14, but with individual modes families highlighted. The techniques described in Section 6.2 to identify mode families lead us to identify the TE ₃ (a), TE ₄ (b), TM ₁ (c), and TM ₂ (d) mode families, but the TE ₁ and TE ₂ mode families elude our identification. In (e) we have highlighted in blue six small peaks which are likely the scattered remnants of TE ₁ and TE ₂ modes which have suffered due to the perturbation of the nanowire contacts. In red we have highlighted the peak characterized in Fig. 9.10	109
10.1	Dimer photonic molecule with one wired microdisk capable of being tuned into resonance with the adjacent disk. Here, one of the disks has been made smaller than the other so the pedestal is smaller and more flexible for possible optomechanical experiments.	114
10.2	In cavity-QED it is critical that the emission wavelength be on resonance with a cavity mode. In small cavities (with desirable small mode volumes) the large FSR and sensitivity to fabrication imperfections makes it quite difficult to achieve coupling of narrow-line emitters to high- <i>Q</i> modes. Our device may offer a solution to this problem by enabling the cavity mode to be tuned to the emission wavelength.	115

- 10.3 An alternative thermal tuning design. A metal ring is deposited at the center of the Si microdisk. Contacts made to this ring are isolated from the Si disk by a cladding layer. This structure requires several additional mask alignment steps (best performed with deep-UV lithography) and does not allow the disk to be used as a sensor, but the heating element is kept away from the whispering-gallery mode volume. Several features of this design were independently proposed in Ref. [10]. 116
- 10.4 Another alternative thermal tuning design. Here, metallic vias are placed at the center of a microring. Current is passed through the ring. This design will be especially energy efficient due to the small thermal mass and the fact that the current is passing only directly through the optical mode volume. This structure will also require several mask alignments and is best fabricated with deep-UV photolithography. This device will likely be covered in a cladding layer, and so will also not be able to be used as a sensor. This design has been largely championed by Dr. Michael Watts [11, 12]. . . 117
- 10.5 An optical device with integrate-and-fire behavior and variable output routing. The design utilizes two tunable resonators. (a) The device with no optical input. The first resonator is tuned to a given wavelength. For this design, all light in the circuit is at this wavelength. The tuning of the second resonator will be discussed shortly. (b) The optical input (possibly arriving from many independent channels) begins to build up in the first resonator. (c) The integrated optical field has built up to the point where it has heated the first resonator and detuned its resonant frequency. The incident optical signal now passes the first resonator. (d) The optical signal which passed the first resonator arrives at the second resonator and is split into two paths. The second resonator is tuned to determine the fraction of the light that travels down each path. 120

- B.1 The eigenvalue spectrum for E -polarization plotted in the complex plane for a metallic core surrounded by a dielectric shell with $\epsilon_i = 12$. The filling factor of each component is 0.1. The first N eigenvalues are plotted in red and have $\text{Re}(\omega) < 0$. The second N are in black and have $\text{Re}(\omega) \approx 0$. The third N are in blue with $\text{Re}(\omega) > 0$ 129
- B.2 The eigenvalue spectrum for E -polarization plotted in the complex plane for a metallic core surrounded by a dielectric shell with $\epsilon_i = 12 - .1i$. The filling factor of each component is 0.1. The first N eigenvalues are plotted in red and have $\text{Re}(\omega) < 0$. The second N are in black and have $\text{Re}(\omega) \approx 0$. The third N are in blue with $\text{Re}(\omega) > 0$ 129
- B.3 The eigenvalue spectrum for E -polarization plotted in the complex plane for a metallic core surrounded by a dielectric shell with $\epsilon_i = 12 + 0.1i$. The filling factor of each component is 0.1. The first N eigenvalues are plotted in red and have $\text{Re}(\omega) < 0$. The second N are in black and have $\text{Re}(\omega) \approx 0$. The third N are in blue with $\text{Re}(\omega) > 0$ 129

List of Tables

2.1	Parameters for implantations utilized for C-enriched Si fabrication. The RTA was performed in an N ₂ ambient in the temperature range between 650–900°C for 10s. The best results were obtained for RTA performed at 800°C.	14
8.1	Theoretical and measured microdisk modal parameters	84

Chapter 1

Introduction: Why silicon photonics?

In the course of human technological innovation, few materials have been as impactful as silicon (Si). Si is an abundant resource constituting fully one quarter of the Earth's crust by mass, second only to oxygen. It is the eighth most common element in the universe, but is often bound to other elements to form dust, glass, and rock [13]. After the invention of the transistor revolutionized the electronics industry, Si emerged as a suitable substance for large-scale fabrication of crystalline material. The ability to isolate Si and form it into high-purity crystalline material was surely one of the great technological feats of the 20th century, and one of the most game-changing technological adaptations in the history of humanity. The technology of Si crystal growth, doping, and complimentary metal-oxide-semiconductor (CMOS) device design and integration was perhaps the defining technology of the latter half of the 20th century.

The success and ubiquity of Si electronic devices—epitomized by the Si processor, an example of which is shown in Fig. 1.1(a)—is motivation in and of itself to develop Si photonic devices; the promise of technologies with integrated optical and electrical components working in harmony on a single chip is a powerful call to action. Fortuitously, many optical properties of Si are highly-conducive to information processing and communication. One of the most significant physical properties of Si is its ability to grow a robust insulating oxide layer. In making a field-effect transistor, this has been a critical advantage of Si over other semiconductors, and the ability to grow an oxide layer as an optical in-

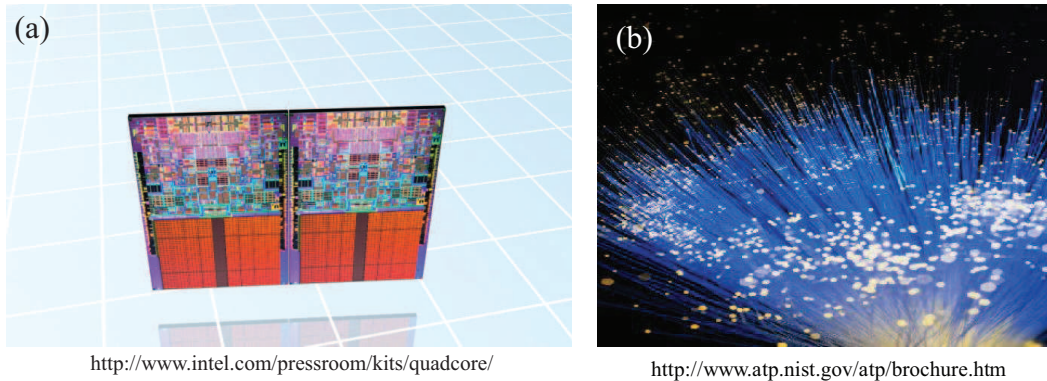


Figure 1.1: Two technologies which have been extraordinarily successful and are converging to Si photonics. (a) A multi-core Si processor. (b) Optical fibers made of glass.

insulator is critical to the utilization of Si as a platform for optical devices. Another critical feature of Si which makes it attractive for optical purposes is the high index of refraction and high transmissivity at wavelengths near 1550nm, what is known as the *C*-band of near-infrared electromagnetic wavelengths most frequently used in long-distance optical signal transmission through optical fibers.

The technology of optical fibers (shown in Fig. 1.1(b)), for which the 2009 Nobel Prize in physics was awarded, relies on the fact that thin threads of glass can guide light-waves for extraordinary distances with minimal loss or dispersion. The fact that light at the same wavelength can be transmitted through Si is critical for the utility of Si as an optical processing medium. In fact, an important application of Si photonics is to serve as a technological platform to bridge Si electronics to fiber optics.

The birth of the field of Si photonics occurred in the late 1980s with the demonstration of Si waveguides [14] and developed rapidly with layered structures of high-index on low-index materials [15] and more recently with the development of silicon-on-insulator (SOI) wafers. SOI wafers are semiconductor wafer substrates with three layers: a thin Si layer atop an insulating SiO₂ layer atop a thick Si handle layer wafer. The idea is to fabricate all working optical or electrical devices on the top thin Si layer. These devices are then insulated—optically, electrically, and thermally—by the oxide. Optical insulation is achieved

because the index of refraction of SiO_2 is 1.46 whereas that of Si is 3.48 near 1550nm. Electrical insulation is achieved because the electrical conductivity of SiO_2 is $\sim 10^{14}\Omega\cdot\text{cm}$ while for doped silicon it can be less than $1\Omega\cdot\text{cm}$. Thermal insulation is achieved because the thermal conductivity of SiO_2 is $\sim 1.38\text{W/m K}$ and for Si it is $\sim 149\text{W/m K}$ at room temperature. The thick Si below provides structural integrity for the devices. SOI wafers with many different layer thicknesses may be purchased for many different applications. We will further discuss the specific parameters chosen for this study in the subsequent chapters.

In this thesis we consider several problems in the rapidly-developing field of Si photonics. In the Part I of the thesis we look at the problem of generation of light from Si (Chapter 2), and we consider possibilities of novel light propagation environments enabled by combining metallic and dielectric components (Chapter 3). In Part II we transition to what has been the bulk of my graduate work—the study of Si microdisks. In Chapter 4 we introduce the history and context of contemporary microcavity research. Chapter 5 gives the necessary theoretical background for our microdisk work. Chapter 6 describes the experimental technique of tapered fiber spectroscopy used to characterize Si microcavities. The fabrication of Si microdisks is discussed in Chapter 7. In Chapter 8 we consider size constraints which place lower limits on the size of individual resonant elements which may be utilized in a photonic circuit. In Chapter 9 we discuss techniques for dynamic, broad tuning of resonant photonic elements. The thesis concludes in Chapter 10 with a discussion of possible routes forward which could build on the work presented here.

Part I

Light generation and manipulation in nanopatterned silicon

Chapter 2

Light generation from nanopatterned silicon

2.1 The challenge of extracting light from silicon

In this chapter we introduce the challenge of extracting light from silicon. We briefly outline several techniques which have been utilized to address this challenge. We then focus on our work to utilize the G center in silicon for its emissive properties.

The effort to devise structures of Si which efficiently and controllably emit light is driven by the desire to integrate novel optical circuitry into well-established electronic designs to make possible new information processing and storage architectures. Since the overwhelming majority of existing electronics is manifest in Si, it seems intuitive that one elegant approach would be to integrate Si-based photonic devices into the Si-based electronic devices. Nature presents a quandary: the extremum of the conduction band at the Brillouin zone center is a maximum in Si; six symmetric Δ valleys lie in the X directions 1.1eV above the top of the valence band at room temperature, and thus the Si bandgap is indirect. Electron-hole recombination therefore requires a phonon. In bulk Si, the cross section for this three-body process is small and luminescence is inefficient. Recombination is almost entirely via non-radiative pathways at room temperature. However, at low temperature non-radiative processes are suppressed along with phonon population and a

large variety of radiative recombination pathways become observable; low-temperature photoluminescence is one way to gain insight into the physics of electron-hole radiative recombination in Si. A low-temperature photoluminescence spectrum of bulk Si is shown in Fig. 2.1.

A central challenge in extracting light from Si is that modifications intended to augment radiative capability necessarily change the structure and in so doing introduce new non-radiative mechanisms and additional optical losses. The performance of electronic devices depends crucially on the quality of the Si lattice, and predictions regarding how devices will respond to perturbations such as dopants, strain, dislocations, surfaces etc., requires knowledge not just of a pristine Si lattice, but also of how the material behaves when it departs in any way from the form we know well—that of an ideal, infinite crystal.

In Appendix A we briefly discuss the luminescence which results from a variety of types of modifications to pristine Si. In particular, we discuss the luminescence from Erbium-doped Si, porous Si, quantum confined structures including superlattices, quantum wires and nanocrystals, the luminescence by extended defects such as $\{311\}$ defects which are large enough to introduce a sizeable strain perturbation to the lattice. In addition to the discussion of these techniques which generate light from Si by modifying the Si in various ways, we also discuss stimulated Raman scattering which makes use of the intrinsic non-linear optical properties of the material. This discussion of other techniques which have been utilized to generate light from silicon has been relegated to an appendix to allow us to quickly move to a discussion of our work on nanopatterned silicon.

2.2 Nanopatterned silicon

As discussed in Appendix A, many methods have been utilized to overcome the indirect bandgap of Si to create a medium with efficient optical emission. The work here on nanopatterned Si was motivated by the desire to affect the Si lattice locally and controllably to utilize some combination of quantum confinement, strain, and surface properties.

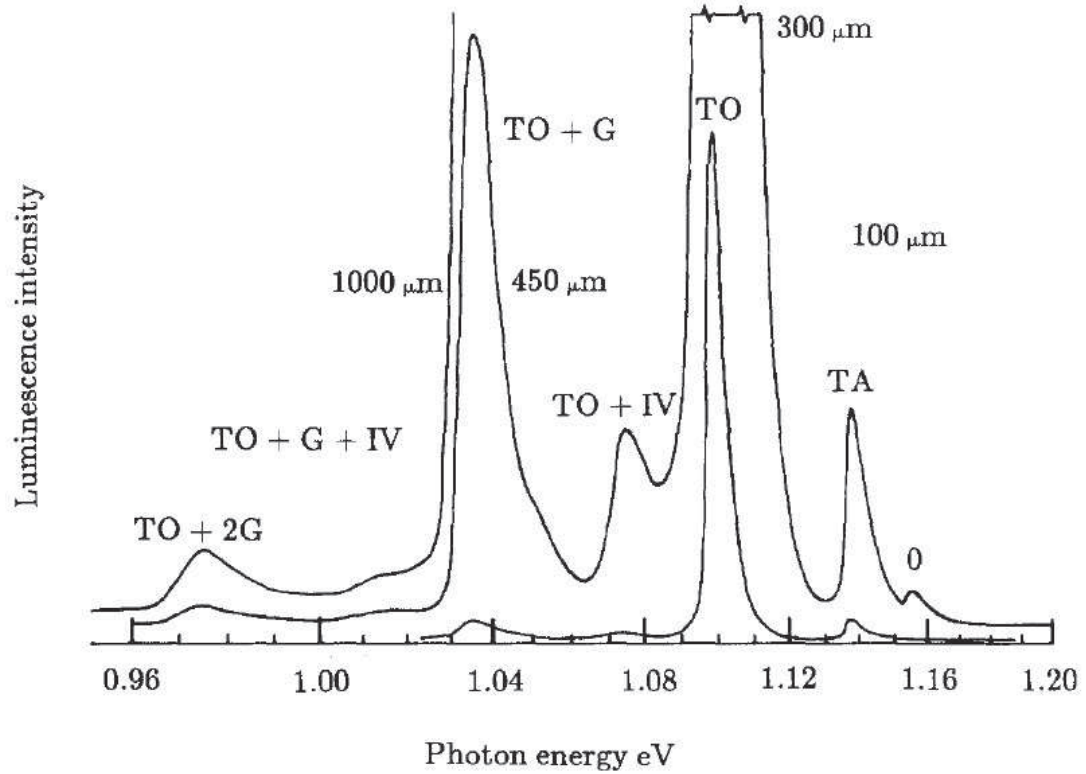


Figure 2.1: Si photoluminescence taken from the 1989 review of emissive point defects in Si written by Gordon Davies and cited in Ref. [1]. The spectra are taken at 26K and recorded with four different slit widths ($1000\mu\text{m}$, $450\mu\text{m}$, $300\mu\text{m}$ and $100\mu\text{m}$) to give varying amplification and resolution. The labels refer to the combinations of phonons which are involved in the various luminescence pathways. G is the $k = 0$ optical phonon mode. The peak labeled 0 is the ideally-forbidden zero-phonon component.

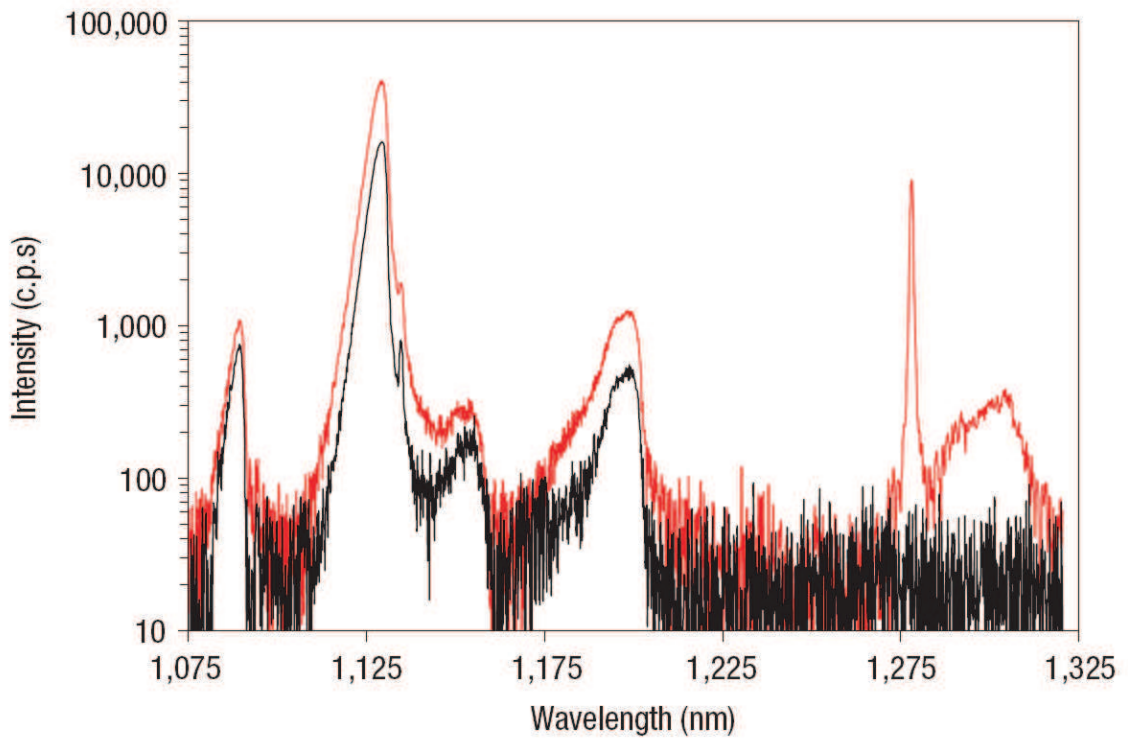


Figure 2.2: PL data taken adapted from Ref. [2]. Spectra were acquired at 10K. In black (lower spectrum) is the PL from an unpatterned SOI sample. The red (upper spectrum) is from the nanopatterned SOI sample. The 1.278nm *G* line is present.

As is often the case in scientific research, what resulted was entirely different.

Our contributions to nanopatterned Si research followed the work presented in Ref. [2]. In Ref. [2], a membrane of anodized aluminum oxide (AAO) containing a hexagonal array of throughpores was placed on a silicon-on-insulator (SOI) wafer and subsequently used as an etch mask for reactive ion etching (RIE). The result was a hexagonal mesh of nanopores with 50nm diameter and 100nm pitch. While quantum confinement or strain would likely result in broad optical features in a photoluminescence (PL) spectrum, what was observed in the PL measured from the nanopatterned Si was a narrow, zero-phonon line called the *G* line, as is shown in Fig. 2.2.

2.3 The G center

The G line is known to result from the G center, a type of point defect in the Si lattice. Even the highest-quality crystalline structures realizable to date contain many lattice vacancies and substitutional or interstitial impurities. Any such localized departure from the crystalline order is referred to as a point defect [16, 17]; point defects are usually comprised of one or a few vacancies or impurities interacting with the lattice. Such defects are always present after the growth of a crystal, and more are introduced in the steps necessary to process semiconductor devices. Solid state scientists beginning in the 1950s and continuing through the present day have explored the nature of a multitude of species of point defects in Si [1, 18–23]. They have been most commonly produced via ion, gamma ray, neutron or electron irradiation. An especially comprehensive review of optically-active point defects in Si is contained in Ref. [1]. Point defects give rise to electron states with energies in the band gap. The vast majority of point defects are not optically active and simply serve as non-radiative recombination pathways. Some point defects, however, give rise to pairs of states in the band gap with a non-vanishing electric dipole matrix element. PL spectra of samples with these optically-active point defects are characterized by narrow lines, called zero-phonon lines (ZPLs). An example of such a PL spectrum is shown in Fig. 2.3. A point defect with two electric-dipole-connected states (E_1 and E_2) in the band gap gives rise to a four level system. The conduction band edge is the highest energy level, and transition from E_c to E_2 is in general a fast, phonon-assisted process. The transition from E_2 to E_1 is the optical transition. Non-radiative transition from E_1 to E_v is also fast. Therefore, obtaining population inversion with E_2 over E_1 seems like a sensible goal [24]. However, it is often the case that effects such as exciton thermalization before and after trapping, transitions from E_2 to E_c and non-radiative recombination from E_c to E_v quench the luminescence above a defect-dependent temperature which is always quite low and is usually below liquid N_2 temperature. Further consideration of point defects for lasing is given in Ref. [24].

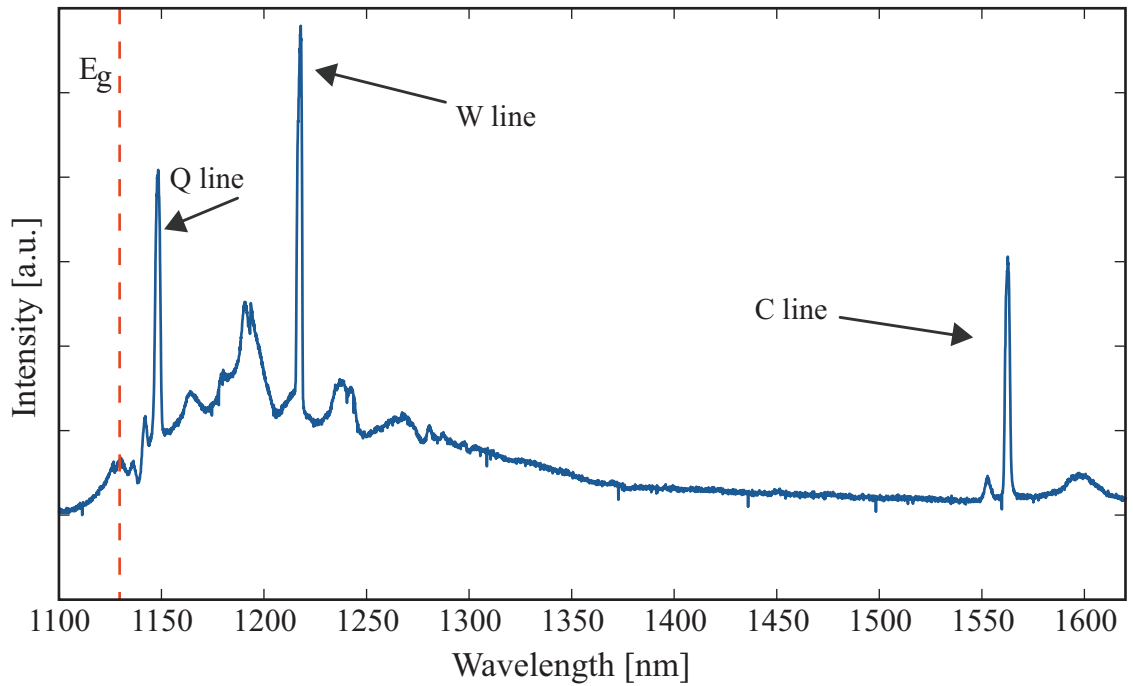


Figure 2.3: PL spectrum of Si bombarded with 100keV Si^+ to a fluency of $10^{14}\text{Si}^+/\text{cm}^2$ and annealed at 250°C for 30min. The ZPL at 1218nm dominates the spectrum. It is the well-known *W* line to be discussed later in the present article. The ZPL at 1149nm is believed to be the *Q* line associated with a C-Li complex [3]. There is believed to be a forbidden transition at the same center observable below 2K. The Li and C present in the lattice are residual contaminants introduced during the growth of the crystal. The broader luminescence from 1149nm beyond 1218nm are from a variety of phonon replicas of the *Q* center and the *W* center as well as a multitude of other weakly-luminescing centers. The ZPL at 1560nm is the *C* line, believed to be associated with a C-O complex [4]. The band edge luminescence is observable at 1130nm. However, the presence of so much damage in the lattice and so many optically active defects makes band-edge radiative recombination unlikely.

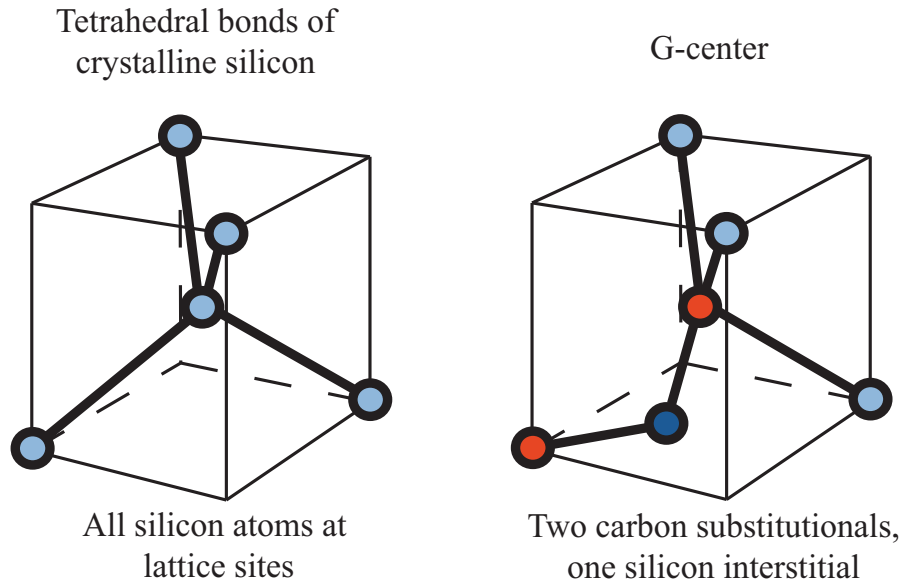


Figure 2.4: Schematic of the *G* center. (a) Tetrahedral structure of Si bonds. (b) *G* center in the emissive B configuration. Atoms involved in the *G* center are depicted in full opacity whereas atoms not participating in the point defect are shown as semitransparent.

The *G* line is known to originate from the *G* center [25–27], which is a point defect comprised of two carbon atoms and one Si interstitial atom [26], as illustrated in Fig. 2.4. The physics of the *G* center is complicated by the fact that it is a bistable defect with configurations labeled A and B. Only B is optically active, so we limit our discussion to the B configuration.

The mechanism of luminescence in Si containing *G* centers depends on the position of the Fermi level. The mechanism of luminescence in *p*-type material is shown schematically in Figure 2.5. The *G* center can trap an electron from the conduction band in an “acceptor state” or trap a hole from the valence band in a “donor state”. Note here the terms acceptor and donor are taken from the point of view of the defect. Excitation is the result of a sequential capture of an electron and a hole by the *G* center. The *G* line at 1278nm is the result of an electric-dipole-mediated transition between two states of the *G* center, namely the B^* and the B^0 states.

In Ref. [2], the 1278nm emission was incorrectly attributed to an unrelated point defect

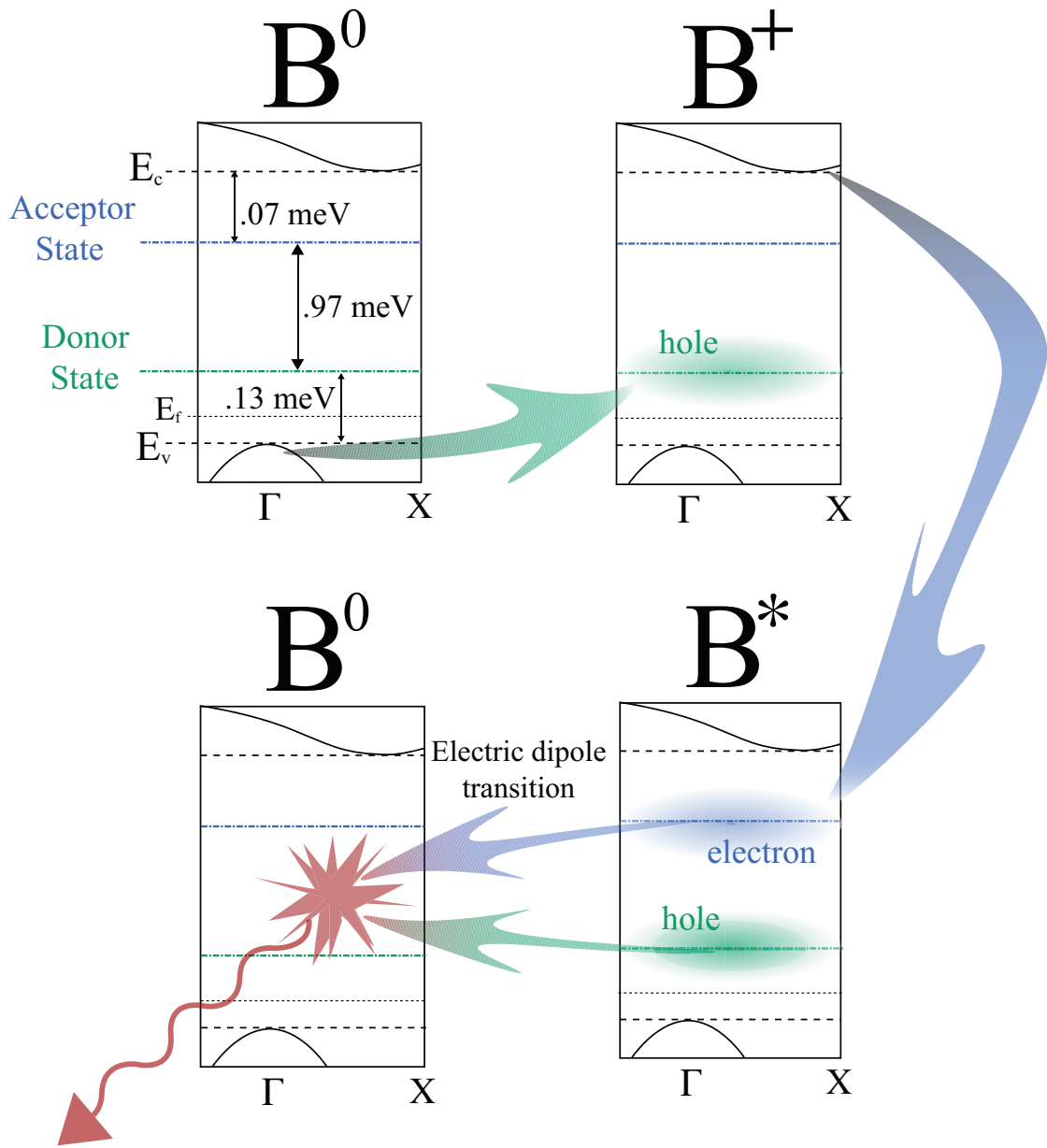


Figure 2.5: Schematic of the luminescence mechanism in *p*-type Si. A donor state of the *G* center in the B^0 configuration acquires a hole from the valence band to form the B^+ state. The acceptor state then captures an electron from the conduction band to form the B^* state. The B^* state makes an electric dipole transition back to the B^0 state.

known as the A center, and it was unclear whether the carbon from which the G centers were created came from the native carbon in the silicon or from an external source introduced during the RIE process. Understanding and controlling the mechanisms involved in the creation of G centers by nanopatterning is critical to further investigation into properties and possibilities of G -center luminescence in this system. In Ref. [2], stimulated emission and optical gain, characteristics of lasing, from G centers emitting at a wavelength of $1.28\mu\text{m}$ have been observed in periodic nanopatterned crystalline silicon under optical excitation at cryogenic temperatures. The emissive G centers were found as early as the 1960s in irradiated silicon [28]. Early studies were interested in investigating the effects of radiation damage via electron, ion or gamma ray bombardment, mostly for the purposes of assessing, containing, and suppressing the undesirable consequences in electronic applications [1, 25, 26, 29]. These bombardment techniques necessarily inflict damage on the entire lattice and thereby increase both the electronic and optical losses. Previously, electroluminescence from G centers was demonstrated in an electron-irradiated p - n junction [30]. The advantage of G -center introduction via nanopatterning for the purpose of fabricating light-emitting devices is that the damage to the lattice is contained in thin shells at the walls of etched pores [2, 31–33] while leaving the majority of the lattice in its pristine form.

2.4 Increasing the intensity of the G line

Following the work in Ref. [2], our objective was to increase the production of light in nanopatterned Si by increasing the number of G centers formed in the nanopatterning process. We studied G center photoluminescence from nanopatterned carbon-rich SOI obtained by solid-phase epitaxy. A 33-fold increase in G line intensity compared to unprocessed SOI was observed. These results indicate that the G centers can be formed from carbon in the silicon crystal prior to the RIE process and also suggest a way to increase the emission efficiency of this system.

2.4.1 Creation of G centers

Substitutional carbon atoms are necessary for G center formation and occur naturally in silicon wafers at concentrations between 10^{15} and 10^{17} atoms/cm³ depending on the crystal growth technique [1]. A G center is created when a mobile interstitial carbon atom (C_i) binds with a substitutional carbon atom (C_s). The process is understood to proceed as follows: silicon interstitials (Si_i) are created as the result of a damage event. A mobile Si_i can then migrate to a C_s . The C_s then gives its lattice site to the Si_i in a process known as the Watkins exchange mechanism [34]. The resulting mobile C_i can then migrate until it binds to a C_s forming a C_sC_i pair, known as the G center. Thus, G -center creation depends both on the density of C_s present in the lattice [35] and on the density of introduced Si_i s.

2.4.2 Increasing carbon concentration with solid-phase epitaxy

Carbon doping of silicon using conventional ion implantation is limited by the low solid solubility of carbon in silicon (on the order of 10^{17} atoms/cm³). Carbon ion implantation at levels exceeding the solid solubility results in precipitation of SiC. Instead, solid-phase epitaxial (SPE) regrowth is employed. This method takes advantage of the increased carbon solubility at the interface between crystalline and amorphous Si [36]. A schematic of the process is shown in Fig. 2.6. The Si crystal is pre-amorphized by Si^+ ion implantation prior to the C^+ ion implantation. The crystal is then annealed to induce SPE re-growth. Substitutional carbon concentrations of up to 7×10^{20} /cm³ were achieved using this method [37]. At such high concentrations, approximately one in every 1000 atoms in the lattice is a C atom. In this work, p -type SOI (250nm Si on a $3\mu\text{m}$ BOX, $20\Omega\cdot\text{cm}$, commercially available from Soitech) was used. The details of the C-enriched Si fabrication are given in Table 2.1.

The concentration of the implanted carbon atoms in our work was approximately 10^{19} /cm³, 400 times more than the manufacturer-specified carbon content of 2.5×10^{16} /cm³. Substitutional carbon in silicon is usually detected by its local vibrational mode IR absorp-

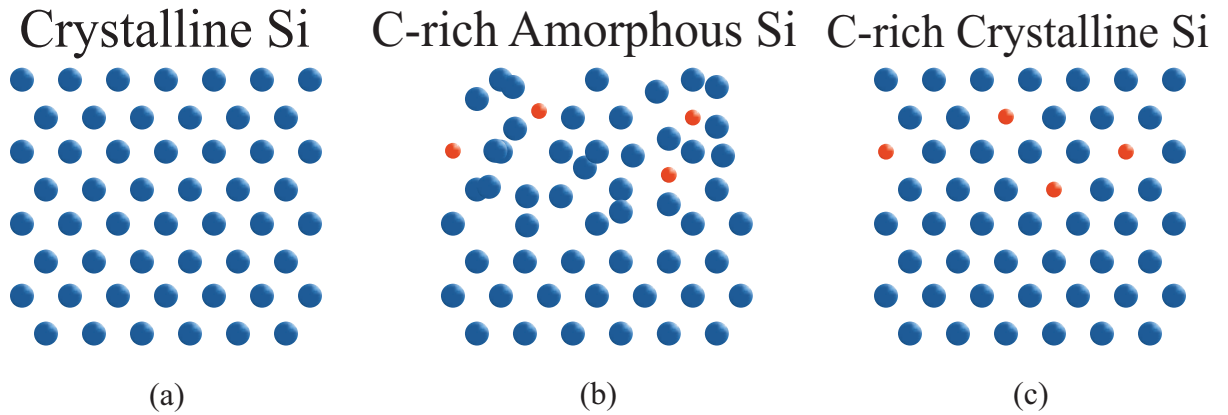


Figure 2.6: Schematic of the implantation and annealing process for solid-phase epitaxy. A pristine, crystalline Si lattice (a) is amorphized by bombarding with Si ions and is then implanted with C ions (b). The crystal is subsequently re-grown by annealing using the undamaged bottom layer as a seed layer (c).

Table 2.1: Parameters for implantations utilized for C-enriched Si fabrication. The RTA was performed in an N₂ ambient in the temperature range between 650–900°C for 10s. The best results were obtained for RTA performed at 800°C.

Step	Species	Dose	Energy	Temp.	Mean Depth	End of range
Amorphization	Si	10 ¹⁵	65keV	-120°C	95nm	200nm
Implantation	C	10 ¹⁴	18keV	24°C	60nm	120nm

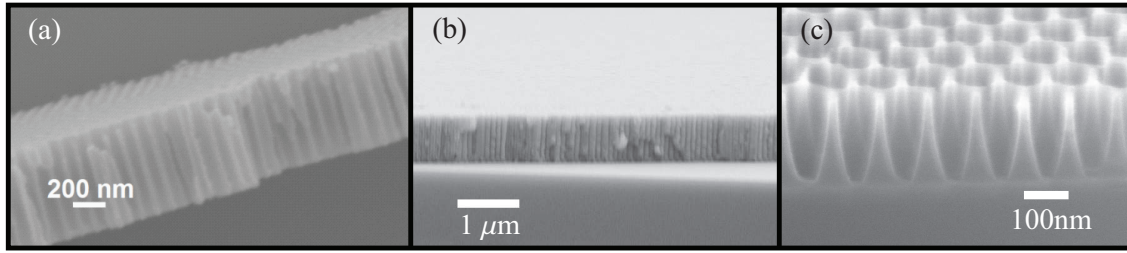


Figure 2.7: Schematic of the nanopatterned Si fabrication process. (a) SEM image of a free-standing AAO membrane [5]. (b) The AAO membrane is placed atop an SOI wafer and used as an etch mask. (c) An array of nanopores in the SOI wafer results from RIE through the AAO etch mask. In this image the AAO has been removed.

tion at 607cm^{-1} [1]. In this study, the maximal absorbance at 607cm^{-1} —expected if all implanted carbon atoms were incorporated into substitutional sites—was less than 0.1%. This low absorbance was due to the fact that only a thin layer ($\sim 100\text{nm}$) of carbon-rich silicon was present in the samples, making the detection of this absorbance line below the sensitivity limit of available FTIR instrumentation. Therefore, we could not meaningfully and quantitatively evaluate the fraction of C that was actually incorporated as C_s .

2.5 Luminescence increase from nanopatterned C-enriched Si

The periodically nanopatterned C-enriched Si structure was fabricated using the highly-uniform self-organized AAO nanopore membrane as an etch mask [2, 5]. The free-standing AAO membrane was lifted from an aqueous solution by a C-enriched Si wafer and subsequently etched in an RIE machine. The RIE conditions were as follows: Cl_2 , 20sccm; BCl_3 , 5sccm; 50mTorr; 100W; 24°C ; 6min. A schematic of the fabrication process and an SEM image of the patterned C-enriched Si are shown in Fig. 2.7.

Fig. 2.8 shows the photoluminescence spectra at 25K of the nanopatterned C-enriched Si on SOI and of similarly nanopatterned SOI without carbon enrichment. The 514nm line

of an argon ion laser was used for excitation. The excitation power was 200mW and the beam spot size was 3mm in diameter. The emitted photoluminescence was collected using a 3", F/4 concave mirror and focused onto a spectrometer. The resolution of the spectrometer was calibrated using a narrow-line (200kHz) external cavity diode laser and was determined to be $0.13 \pm 0.02\text{nm}$. A cooled InGaAs photodiode array was used to measure the intensity of the PL. The phonon-assisted band-edge PL at 1130nm is similar for both samples and serves as a good reference for comparing the two sets of data. The similarity in the band-edge emission linewidth and peak height is indicative of crystallinity being recovered after the SPE. In the reference nanopatterned SOI sample the *G* line intensity is 1300 counts per second while in the C-enriched sample the *G* line intensity is 43,000 counts per second, an increase by a factor of 33. While the results in Fig. 2.8 display the most intense *G* line observed, *G* line intensities exceeding 20,000CPS were consistently obtained from the C-enriched material. The wide band extending from the *G* line to longer wavelengths consists of several phonon replica modes of the *G* line [25, 38]. These results confirm that the carbon in the silicon crystal is responsible for the creation of *G* centers and also provides a path for increasing the efficiency and gain of this material.

The measured linewidths of $1.5 \pm 0.1\text{nm}$ (C-enriched) and $1.1 \pm 0.1\text{nm}$ (unenriched) are considerably broader than the reported linewidth of 0.1–0.2nm at 25K [1, 39]. This linewidth broadening is likely due to the variety of strain environments [1] experienced by *G* centers located in the pore walls. TEM images showing evidence of compressive strain in the pore walls are presented in Ref. [40]. The linewidth broadening in the C-enriched nanopatterned SOI versus the reference nanopatterned SOI is likely due to the presence of a variety of strain environments caused by $C_{i,s}$, $C_{s,s}$ and other residual damage present after amorphization, C implantation, and SPE regrowth. In addition to leading to linewidth broadening, the presence of compressive strain in the pore walls decreases the band gap locally, which may lead to funneling of excitons from the pristine bulk crystal to the regions dense with *G* centers near pore walls [41], facilitating efficient filling of *G* centers.

The temperature dependence of the *G* line emission at temperatures above 40K can be

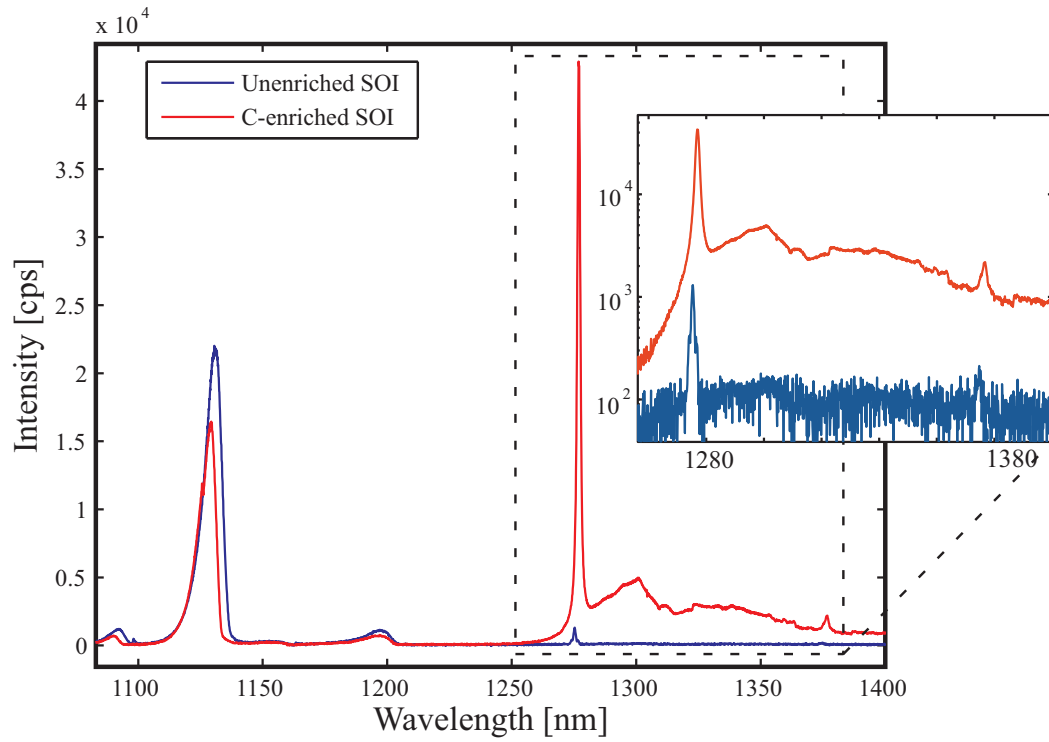


Figure 2.8: Photoluminescence spectrum of nanopatterned Si and nanopatterned C-enriched Si. The inset shows a semi-log plot of the region containing the *G* line and phonon replicas. The peak of the *G* line in C-enriched material was shown to be as much as 33 times that of unenriched SOI.

modeled according to [20, 25, 39]

$$I_G(T) = I_0 [1 + Ce^{-E_a/kT}]^{-1}, \quad (2.1)$$

where I_0 is the intensity at 40K. Equation 9.2 models a two level system where the excited state of the G center is thermally depopulated into a higher level separated by E_a , and C is the ratio of degeneracy between these two levels. Previously obtained values for E_a and C are $55 \pm 3\text{meV}$ and $2 - 8 \times 10^4$, respectively [20], $35 \pm 5\text{meV}$ (C not given) [39], $68 \pm 6\text{meV}$ and 8.9×10^6 [25]. The G line intensity of the two samples presented in Fig. 2.8 was measured at temperatures between 40K and 80K and fitted according to Eq. 9.2. The obtained values were $E_a = 39\text{meV}$, $C = 8300$ for carbon enriched Si and $E_a = 40.1\text{meV}$, $C = 3500$ for non-enriched Si. The two values of E_a we obtained are very close and in within the range of previously obtained values. The relatively small values of C are not yet understood. However, the large variations of this constant in previous reports imply that it is very much affected by the measurement setup employed.

2.6 Summary of our work on G centers in nanopatterned Si

In this work we demonstrated that nanopatterning of carbon-rich silicon created via solid-phase epitaxial regrowth after amorphization and carbon implantation can lead to a significant increase in the intensity of the G line emission. An increase by a factor of 33 was achieved in our studies, and samples with intense G line were consistently manufactured. We hypothesize that the nanopatterned system is intrinsically beneficial for efficient optical activity. Utilizing the nanopatterning technique to create G centers allows for a large surface area with which the energetic ion etchants can interact with the crystal to create silicon self-interstitials which lead to G centers while maintaining the crystallinity, band structure, and carrier lifetime of the crystal away from the etched surfaces of the pores. In this way, the unetched regions of the crystal act, under pumping, as a carrier reservoir to the G

centers embedded in the pore walls.

Having studied several fundamental aspects of the light emission and fabrication of G centers, a next exciting area of research would be to utilize G centers for cavity-QED and quantum optics experiments. Coupling G centers to high- Q , small-mode-volume cavities offers a route to further enhance G -center emission from Si. Also, it should be mentioned that while the G center was studied in detail here, there are many point defects in Si that could be used for similar future experiments.

While the utilization of G centers, and more generally point defects, as light emitters in Si is interesting in an academic sense, the quenching of luminescence with temperature is a limitation which will be quite difficult to overcome and may prove to be an insurmountable barrier to utilization of this luminescence in devices. Because Si is passive at telecom wavelengths near 1550nm and has a high index of refraction in this range, it is excellent for fabrication of waveguiding structures. However, III-V materials such as InP are excellent for emission at these wavelengths, and therefore make for poor waveguides. Perhaps the best way to work within the confines of nature is to utilize the strengths of each material. Such hybrid solutions are currently being well-explored. Still, the fabrication difficulties which lead to high costs for such structures are motivating many to look elsewhere for solutions. At present, the strongest contender is SiGe. Ge is much easier to work into a Si fab line than III-V materials, and SiGe has some promise for light emission in the telecom band. In the long term, on-chip photonic devices will probably utilize either III-V or SiGe emitters, but point-defect luminescence remains interesting for other reasons. In Chapter 8 we discuss many aspects of silicon microcavities which are relevant to quantum optics, and in Chapter 9 we discuss methods for controlling the coupling between a quantum emitter and an optical microcavity. First, in Chapter 3 we discuss a structure which incorporates Si and a metal to control the propagation of light.

Chapter 3

Light propagation in a plasmonic crystal

Our work on nanopatterned Si led us to ask what else we could do with the AAO as a fabrication template for optical structures. Several ideas occurred to us. In regards to light propagation and emission in Si, we wondered if controlling the density of optical states would enhance emission from point defects sufficiently to allow them to operate at higher temperatures. We were also interested in combining the plasmonic properties of metals with dielectrics to create new light propagation environments. Following the work of Dr. Aijun Yin [42], a former lab member, we proceeded to fabricate metallic nanowire arrays in AAO, as shown in Fig. 3.1. We also considered combining plasmonic components with the nanopatterned Si array, as shown in Fig. 3.2. In this structure there are three indices of refraction, that of Au, air, and Si. The fabrication of these structures led to the task of modeling the optical properties of light propagation in periodic structures comprised of metal, Si, and air. Due to the dispersive properties of the metal component, this task is somewhat non-trivial. The remainder of this chapter describes the calculation and some of the interesting conclusions drawn from the modeling.

3.1 Metallodielectric metamaterials and photonic crystals

Metamaterial environments have the potential to enhance or suppress the emission of light as well as to slow light propagation and even achieve a negative index of refraction. Studies

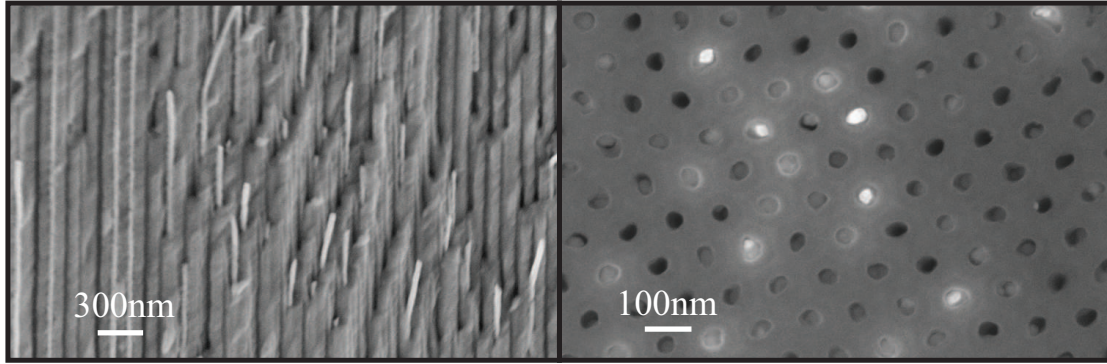


Figure 3.1: AAO nanopore array filled with Au. The AAO is anodized to have $10\mu\text{m}$ deep pores of $\sim 50\text{nm}$ diameter. A metallic contact is made to the back of the array, and the entire structure is then coated with an insulator, leaving only the top of the array open to fluidic conduction. The structure is placed in a Au electrodeposition chamber, and the pores are filled with Au via electrodeposition.

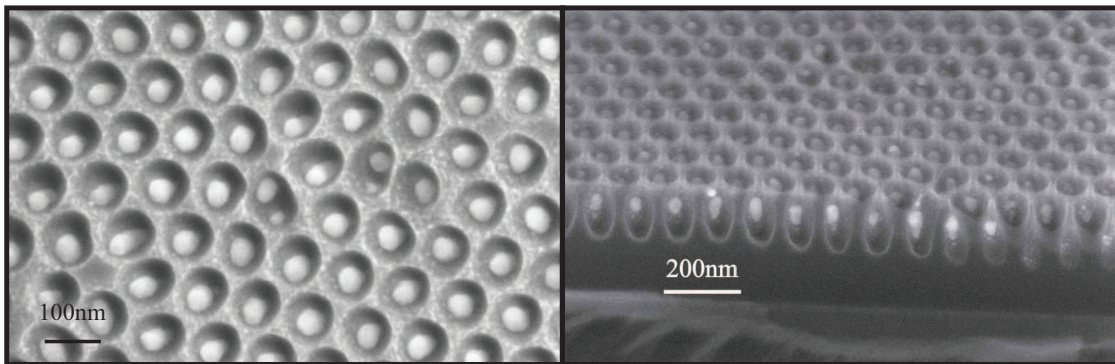


Figure 3.2: Nanopatterned Si with Au evaporated into the pores. The nanopatterned Si array is fabricated as described in Chapter 2, but before removing the AAO mask the sample is mounted in an electron beam evaporation chamber and Au is deposited in the pores.

of periodic as well as aperiodic dielectric and metallic environments have been undertaken with the goal of devising systems which offer maximal control of the generation, storage and propagation of light. In particular, metamaterials composed of coupled metal and dielectric components with feature sizes comparable to or less than the wavelength of light display rich optical behavior such as negative index of refraction and slow pulse propagation. Systems with material periodicity on the scale of the wavelength of light have attracted much attention lately; the potential to engineer a modified vacuum in which the photonic density of states is modified to either enhance or suppress spontaneous emission has been of interest to many researchers [43–46]. Additionally, creation of photonic environments wherein light traveling in all directions propagates significantly slower than in vacuum or with a negative index of refraction are important pursuits. Recent progress toward the fabrication of three-component photonic crystals [47] demands theoretical consideration of the optical properties of such structures [46].

Methods of calculating photonic band structures have been developed over the last two decades. Among these are finite element methods [48], finite-difference time-domain (FDTD) [49, 50], scattering matrix [51], transfer matrix[52] and plane wave expansion methods [53, 54]. FDTD [49, 50], variations of the plane wave expansion technique [55–59], and other techniques [60, 61] have proven useful for calculating the photonic band structures of systems with metallic components arranged in a periodic array. However, most studies to date treat the metallic components with the free electron model, and damping is often neglected.

3.2 Three-component metallodielectric photonic crystals with dispersion and damping

The present work is focused on two-dimensional periodic structures with one dielectric and one metallic component contained in a background dielectric, as depicted in Fig. 3.3. In particular, we extend the theoretical framework of the plane wave technique [53–56]

for the calculation of photonic band structures to three-component photonic crystals containing one metallic component. Dispersion and dissipation in the metallic regions of the photonic crystals are taken into consideration with a complex, frequency-dependent permittivity which we model as

$$\epsilon(\omega) = 1 - \frac{\omega_p^2}{\omega(\omega + i\gamma)}. \quad (3.1)$$

We consider two-dimensional arrays of infinite right circular cylinders arranged in a square lattice (see Fig. 3.3). While our work with the AAO would have led us to consider a hexagonal array, for numerical simplicity and to gain intuition we consider a square array in this study. The cylinders consist of either a metallic core surrounded by a dielectric shell or a dielectric core surrounded by a metallic shell. The cylinders are embedded in a homogeneous lossless medium which is set to be vacuum in this work. The permittivity of the dielectric is treated as a constant. The main point of this study is to contrast the dispersion relation of the metallic core case with the metallic shell case. It is found that the metallic shell structures have far greater potential to reduce the group velocity of propagating modes, in some cases reducing it to 0.05 that in vacuum, nearly an order of magnitude less than the metallic core structures can achieve. The metallic shell structures also have far greater potential to give rise to structural band gaps.

For two-dimensional light propagation one can consider two orthogonal polarizations: the electric field perpendicular to the direction of propagation (parallel to the axis of the cylinders in our case, referred to as E -polarization), or the magnetic field perpendicular to the direction of propagation (H -polarization). The theoretical framework utilized in this report is based on a plane wave expansion. This approach converges nicely for E -polarization but encounters numerical convergence problems for H -polarization. For this reason, and because many of the unique physical features arise for E -polarized light in this geometry, we focus the rest of this study on E -polarized electromagnetic fields.

The structure of this Chapter is as follows. In Section 3.3 we discuss the theoretical methodology. In Section 3.4 we analyze the photonic band structures of two-dimensional three component plasmonic crystals. The study is summarized in Section 3.5. Aspects of

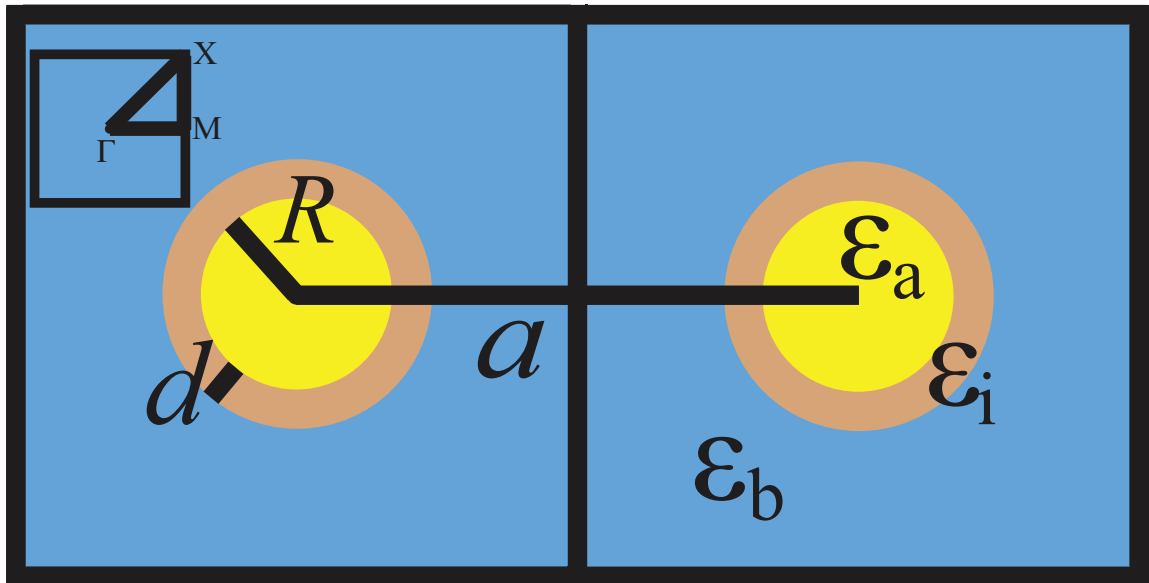


Figure 3.3: The Wigner-Seitz cell of the two-dimensional three-component crystal. The lattice constant is a . The radius of the inner core cylinder is R . The thickness of the shell is d . The three dielectric regions are shown. The first Brillouin zone and points of high symmetry are shown in the inset.

the numerical treatment are discussed in Appendix B.

3.3 Theoretical methodology

We consider electromagnetic waves propagating in the $x - y$ plane. We utilize the plane wave methodology [53, 55] wherein the dominant field component and the permittivity are expanded in the basis of plane waves. The following derivation results in a linear eigenvalue problem which takes into consideration the Drude dispersion (including damping) of the metal. The derivation is similar to that presented in Ref. [55], but is generalized in the present treatment to treat three-component photonic crystals with one metallic component. The z -component of the electric field and the material permittivity are expanded as

$$E_z(\mathbf{x}) = \sum_{\mathbf{G}} B(\mathbf{k}, \mathbf{G}) \exp(i(\mathbf{k} + \mathbf{G}) \cdot \mathbf{x}). \quad (3.2)$$

$$\epsilon(\mathbf{x}, \omega) = \sum_{\mathbf{G}} \tilde{\epsilon}(\mathbf{G}, \omega) \exp(i\mathbf{G} \cdot \mathbf{x}). \quad (3.3)$$

\mathbf{x} is a vector in the $x - y$ plane and \mathbf{G} is a vector of the reciprocal lattice. For the case of the square lattice $\mathbf{G} = (2\pi/a)(m\hat{x} + n\hat{y})$ where m and n are integers, \hat{x} and \hat{y} are unit vectors and a is the lattice constant, as shown in Fig. 3.3. The summations range over all m and n from negative to positive infinity; numerical investigations necessarily truncate the summation. The coefficients $\tilde{\epsilon}$ are given by [54]

$$\tilde{\epsilon}(\mathbf{G}, \omega) = \begin{cases} \epsilon_b f_2 + \epsilon_a f_1 + \epsilon_i f_i, \\ 2f_1(\epsilon_a - \epsilon_b) \frac{J_1(GR)}{GR} \\ + 2f_i(\epsilon_i - \epsilon_b) \frac{J_1[G(R+d)]}{G(R+d)} \end{cases} \quad (3.4)$$

$\tilde{\epsilon}$ depends on ω through the frequency dependence of either ϵ_a or ϵ_b . In Eqn. 3.4 the top element of the list is for $\mathbf{G} = 0$ and the bottom element for $\mathbf{G} \neq 0$. For a square lattice, $f_1 = \pi R^2/a^2$, $f_i = \pi(R+d)^2/a^2 - f_1$, $f_3 = \pi(R+d)^2/a^2$, and $f_2 = 1 - f_3$ [54]. From Maxwell's equations, one can derive the following partial differential equation obeyed by

the dominant field component.

$$\left(\frac{\partial^2}{\partial x^2} + \frac{\partial}{\partial y^2} + \epsilon(\mathbf{x}, \omega) \frac{\omega^2}{c^2} \right) E_z = 0. \quad (3.5)$$

Inserting the expansions of Eq. 3.2 and 3.3 into Eq. 3.5 we obtain

$$(\mathbf{k} + \mathbf{G})^2 B(\mathbf{k}, \mathbf{G}) = \frac{\omega^2}{c^2} \tilde{\epsilon}(0, \omega) B(\mathbf{k}, \mathbf{G}) + \frac{\omega^2}{c^2} \sum_{\mathbf{G} \neq \mathbf{G}'} \tilde{\epsilon}(\mathbf{G} - \mathbf{G}', \omega) B(\mathbf{k}, \mathbf{G}'). \quad (3.6)$$

We are now in a position to insert the expansion coefficients $\tilde{\epsilon}$ given by Eq. 3.4. We consider two geometries. The metallic core case is the configuration where the cores of the cylinders are metallic, i.e., permittivity given by Eq. 3.1, and are covered by shells of constant permittivity. The metallic shell case is the configuration in which the cores of the cylinders are modeled by a constant permittivity and the shells are metallic. Introducing $\xi = \omega/c$, we arrive at the following non-linear equation for the metallic core case.

$$(\xi^3 \mathbf{C} - \frac{i\gamma}{c} \xi^2 \mathbf{C} - \xi \mathbf{D} - \mathbf{E}) \mathbf{B}(\mathbf{k}) = \mathbf{0}, \quad (3.7)$$

where

$$\begin{aligned} (\mathbf{C})_{\mathbf{G}\mathbf{G}'} &= (\epsilon_b f_2 + \epsilon_i f_i + f_1) \delta_{\mathbf{G}\mathbf{G}'} + 2f_1(1 - \epsilon_b) \frac{J_1(|\mathbf{G} - \mathbf{G}'|R)}{|\mathbf{G} - \mathbf{G}'|R} \\ &+ 2f_i(\epsilon_i - \epsilon_b) \frac{J_1[|\mathbf{G} - \mathbf{G}'|(R + d)]}{|\mathbf{G} - \mathbf{G}'|(R + d)}, \end{aligned} \quad (3.8)$$

$$(\mathbf{D})_{\mathbf{G}\mathbf{G}'} = \left[(\mathbf{k} + \mathbf{G})^2 + f_1 \frac{\omega_p^2}{c^2} \right] \delta_{\mathbf{G}\mathbf{G}'} + 2f_1 \frac{\omega_p^2}{c^2} \frac{J_1(|\mathbf{G} - \mathbf{G}'|R)}{|\mathbf{G} - \mathbf{G}'|R}; \quad (3.9)$$

$$(\mathbf{E})_{\mathbf{G}\mathbf{G}'} = \frac{i\gamma}{c} (\mathbf{k} + \mathbf{G})^2 \delta_{\mathbf{G}\mathbf{G}'}. \quad (3.10)$$

For the metallic shell case we obtain the same non-linear equations, but the matrix elements are given by

$$\begin{aligned} (\mathbf{C})_{\mathbf{G}\mathbf{G}'} &= (\epsilon_a f_1 + \epsilon_b f_2 + f_i) \delta_{\mathbf{G}\mathbf{G}'} + 2f_1(\epsilon_a - \epsilon_b) \frac{J_1(|\mathbf{G} - \mathbf{G}'|R)}{|\mathbf{G} - \mathbf{G}'|R} \\ &+ 2f_i(1 - \epsilon_b) \frac{J_1[|\mathbf{G} - \mathbf{G}'|(R + d)]}{|\mathbf{G} - \mathbf{G}'|(R + d)}, \end{aligned} \quad (3.11)$$

$$(\mathbf{D})_{\mathbf{G}\mathbf{G}'} = \left[(\mathbf{k} + \mathbf{G})^2 + f_i \frac{\omega_p^2}{c^2} \right] \delta_{\mathbf{G}\mathbf{G}'} + 2f_i \frac{\omega_p^2}{c^2} \frac{J_1(|\mathbf{G} - \mathbf{G}'|R)}{|\mathbf{G} - \mathbf{G}'|R}; \quad (3.12)$$

The matrix \mathbf{E} is the same in both cases.

The non-linear equation is equivalent to the following set of linear equations.

$$\begin{pmatrix} 0 & \mathbb{I} & 0 \\ 0 & 0 & \mathbb{I} \\ \mathbf{C}^{-1}\mathbf{E} & \mathbf{C}^{-1}\mathbf{D} & \frac{-i\gamma}{c}\mathbb{I} \end{pmatrix} \begin{pmatrix} \mathbf{B} \\ \mathbf{a} \\ \mathbf{b} \end{pmatrix} = \xi \begin{pmatrix} \mathbf{B} \\ \mathbf{a} \\ \mathbf{b} \end{pmatrix}. \quad (3.13)$$

The first two equations resulting from the matrix-vector multiplication in Eq. 3.13 define $\mathbf{a} = \xi\mathbf{B}$ and $\mathbf{b} = \xi^2\mathbf{B}$. The third equation is equivalent to Eq. 3.7. Eq. 3.13 has been diagonalized for k -vectors in the fundamental eighth of the first Brillouin zone. The resulting band structures are presented and discussed in Section 3.4.

3.4 Results and discussion

Band structures were obtained by diagonalization of Eq. 3.13 for 599 k -values from across the Brillouin zone. Convergence studies showed that results obtained using 441 plane waves and 1681 waves agreed to four significant figures. Thus, the band structures presented here were acquired with 441 plane waves. In all spectra presented here we plot $\omega a/2\pi c$ with the normalization convention $\omega_p a/2\pi c = 1$. In other words, we define the plasma frequency as $\omega_p = 2\pi c/a$ to make the problem scale-invariant. With this definition we can let a take any value as long as R and d are shifted accordingly to achieve the same filling factors. In our simulations we set $a = 1$. However, it should be noted that one can use more physical parameters, such as the bulk plasma frequency of a given metal. If one then chooses the lattice constant $a = 2\pi c/\omega_p$ and the filling factors are kept constant the results will be the same. In all studies the damping parameter $\gamma = 0.01\omega_p$. The lifetime is defined as $1/\tau = -2\text{Im}(\omega)$.

Band structures and lifetimes for two-component photonic crystals composed of metallic cylinders in vacuum with filling factors of 0.01 and 0.1 are presented in Fig. 3.4 to illustrate the trends observed as metallic fraction is increased. The near-degeneracy of the first and second bands along the M – X direction and between the second and third bands

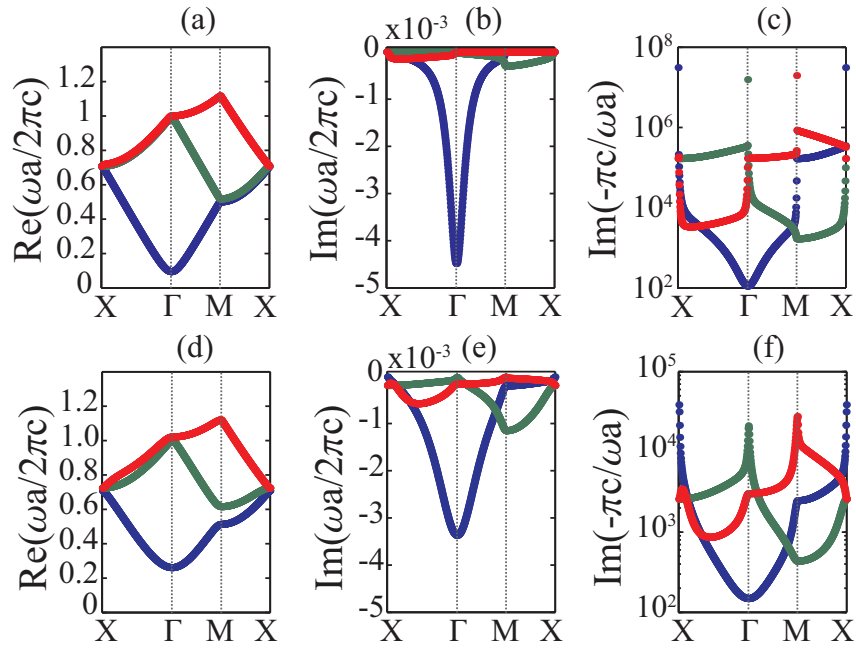


Figure 3.4: The three lowest photonic bands of a two-component photonic crystal composed of metallic cylinders of filling factor 0.01 (a-c) and .1 (d-f) arranged in a square lattice. (a,d) The real part of the band structure. (b,e) The imaginary part of the band structure. (c,f) The lifetime of the states.

along the $X - \Gamma$ direction in the case of the 0.01 filling fraction is broken as the filling fraction is increased (compare Fig. 3.4(a) and 3.4(d)). For small filling factors, the imaginary parts of the eigenvalue band structure at the symmetry points display discontinuous behavior (see Fig. 3.4(c)). This is because the cross-section of the wires is small; only exactly along the lines of symmetry of the Brillouin zone do multiple reflections occur resulting in the formation of standing waves, which significantly enhance the lifetime of the states. A general trend for all structures considered here is the decrease of lifetime with increase of metallic filling factor. For all values of the filling factor, the band with the shortest lifetime is the lowest band, but as the filling factor is increased, the lifetimes of higher bands become comparable to that of the lowest band. For the two-component photonic crystal with lossy metallic cylinders in vacuum, all states—including the vacuum-like states above the plasma frequency—are damped, meaning that the imaginary part of all eigenvalues is less than zero, corresponding to decay in time.

In Figs. 3.5-3.7 the real and imaginary parts of the band structures for two-component crystals, three-component metallic core and three-component metallic shell are juxtaposed for the cases where the filling factor of the metallic component is 0.1 and 0.6. It should be noted that in Figs. 3.5-3.7 six bands are plotted; however in Fig. 3.5 the y -axis extends to 1.6 whereas it is only necessary to extend it to 1.2 for the three-component cases. For sufficiently large filling factor, the real part of the band structures of two-component photonic crystals composed of metallic cylinders are characterized by two bandgaps, as seen in Fig. 3.5(b). From zero frequency to a cutoff there is a bandgap due to the inability of the E -polarized electromagnetic waves to propagate in the negatively permittive material. This bandgap is seen in Figs. 3.5-3.7. The size of this bandgap increases with the filling factor of the metallic component. The second bandgap occurs between the first and second bands. The bandgap between the first and second bands is clearly seen in Fig. 3.5(b). This bandgap is structural in that it is due to the production of standing waves caused by multiple reflections in the crystal; this bandgap can be observed in photonic crystals composed of dielectric cylinders, and the presence and size of this bandgap also depends on

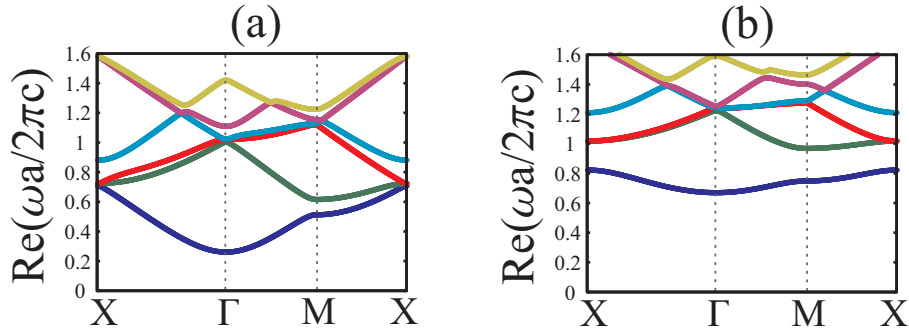


Figure 3.5: The six lowest E -polarized photonic bands of a two-component photonic crystal composed of metallic cylinders arranged in a square lattice. (a) Metallic filling factor is 0.1. (b) Metallic filling factor is 0.6.

the filling factor. For photonic crystals composed of dielectric cylinders, this bandgap will have a maximal value at a given filling factor that is generally different from the maximal filling factor. For the two-component plasmonic crystal the bandgap continues to increase as the fill factor is increased to its maximum value of 0.78. For fill factors above approximately 0.6 there is only one band below the plasma frequency, as is shown in Fig. 3.5(b). Above the plasma frequency, where the permittivity approaches unity, the dispersion relation shows the linear behavior one expects from electromagnetic waves propagating in vacuum.

In Fig. 3.6(b) one sees the structural bandgap has been filled, although the filling factor of the metal is still 0.6, as it was in Fig. 3.5(b). This closing of the structural bandgap between the second and third bands is characteristic of dielectric cylinders with increased filling factor and contrasts the behavior of purely metallic cylinders. In Fig. 3.7, where the metallic component is the outer shell of the cylinder, one sees an increase of the structural band gap, indicating the cylinder array maintains the character of metallic cylinders. However, in contrast to Fig. 3.5(b) there are four bands below the plasma frequency.

In Figs. 3.5-3.7 one can also see how the different structural configurations affect the group velocity of the propagating waves. For the lowest band in each case, the maximum of the group velocity occurs along the $X - \Gamma$ direction. For the two-component case with

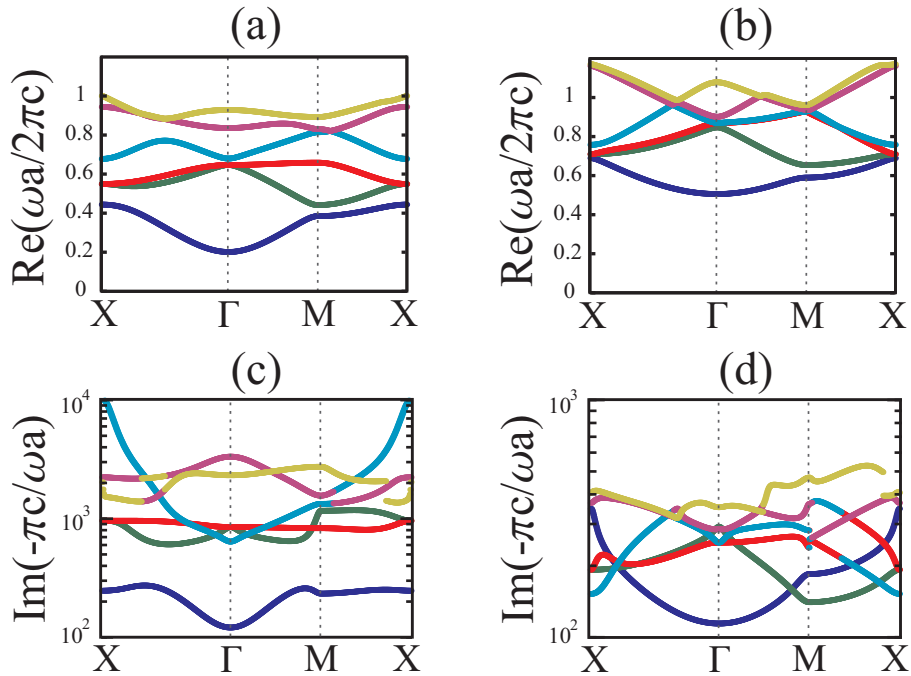


Figure 3.6: The six lowest E -polarized photonic bands of a three-component photonic crystal composed of metallic cylinders surrounded by a dielectric shell of permittivity $\epsilon = 12$ arranged in a square lattice. The filling factor of the dielectric is 0.1. (a,b) Real part of the band structure. (c,d) Lifetime of the states. (a,c) Metallic filling factor is 0.1. (b,d) Metallic filling factor is 0.6. Discontinuities in the imaginary parts of the band structure result from the fact that eigenvalues are sorted by real part of ω ; when one lists the eigenvalues this way on either side of a band crossing and then plots a truncated number of bands, the imaginary parts of the eigenvalues can appear discontinuous.

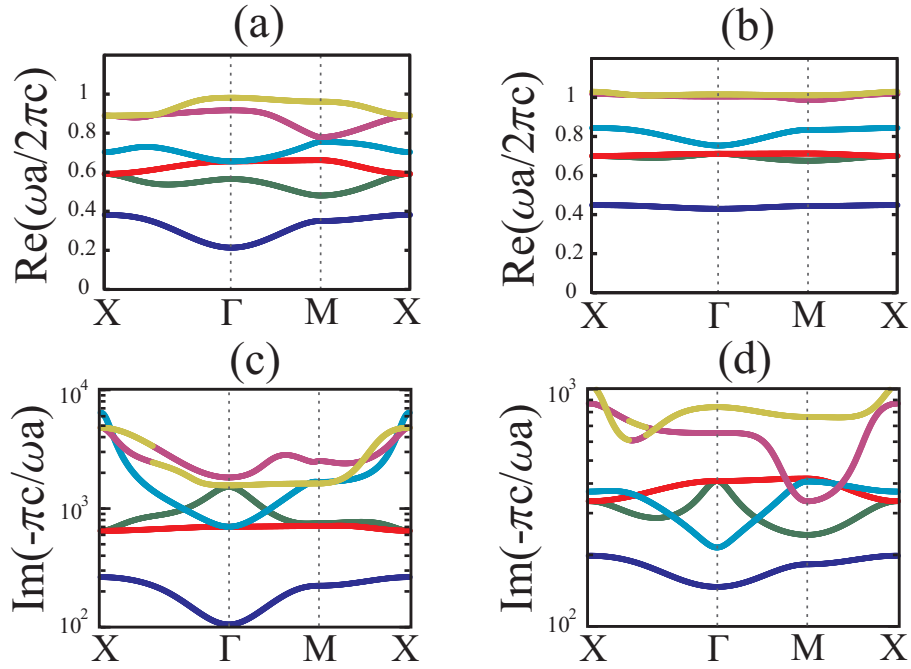


Figure 3.7: The six lowest E -polarized photonic bands of a three-component photonic crystal composed of dielectric cylinders of permittivity $\epsilon = 12$ surrounded by a metallic shell arranged in a square lattice. The filling factor of the dielectric is 0.1. (a,b) Real part of the band structure. (c,d) Lifetime of the states. (a,c) Metallic filling factor is 0.1. (b,d) Metallic filling factor is 0.6.

filling factor 0.6 (Fig. 3.5(b)) the maximum group velocity is $0.3343c$, which is slightly less than $0.4078c$, the value for the three-component metallic core case of the same metallic filling factor (Fig. 3.6(b)). However, the maximum group velocity of the lowest band for the three-component shell case (Fig. 3.7(b)) is $0.0449c$, nearly an order of magnitude smaller. Such a trend continues up to and above the plasma frequency. The sixth band in both cases of three-component configurations is near the plasma frequency. In these two cases the maximum of the group velocity is along the $M - X$ direction. For the three-component metallic core case the maximum is $0.5630c$ and for the metallic shell case the maximum is $0.0672c$. These considerations indicate that of the three structural configurations considered in this study, the three-component metallic shell configuration is most effective in creating a medium where electromagnetic waves below the plasma frequency propagate with a significantly reduced group velocity. Above the plasma frequency, all three cases demonstrate free-wave-like propagation as one would expect.

Inspection of the lifetimes of the propagating waves in the metallic core case versus the metallic shell case reveals the increase of metallic filling factor decreases the lifetimes for both geometries. Moving from Fig. 3.6(c) to 3.6(d) one observes that the lowest propagating band maintains a similar lifetime near the Γ point of the Brillouin zone and experiences an increase in lifetime with increased metallic filling factor near the X point due to the increase in group velocity with the closing of the structural band gap. However, all higher bands suffer a decrease in lifetime, some by more than an order of magnitude. Moving from 3.7(c) to 3.7(d) one finds a similar lifetime near the Γ point and a reduced lifetime near the X point for the metallic shell case. Still, the lifetime of the lowest band across the Brillouin zone is not affected dramatically by increasing the metallic filling factor from 0.1 to 0.6, but the lifetimes of higher bands are more significantly affected.

For all cases considered here the lowest allowed frequency for a propagating mode increases with increasing filling factor of the metallic component. It is interesting to compare the values of this cutoff frequency as a function of filling factor for the three cases considered here. As a basis for comparison, we note that $\omega_p = \sqrt{Ne^2/m\epsilon_0}$ where N is the

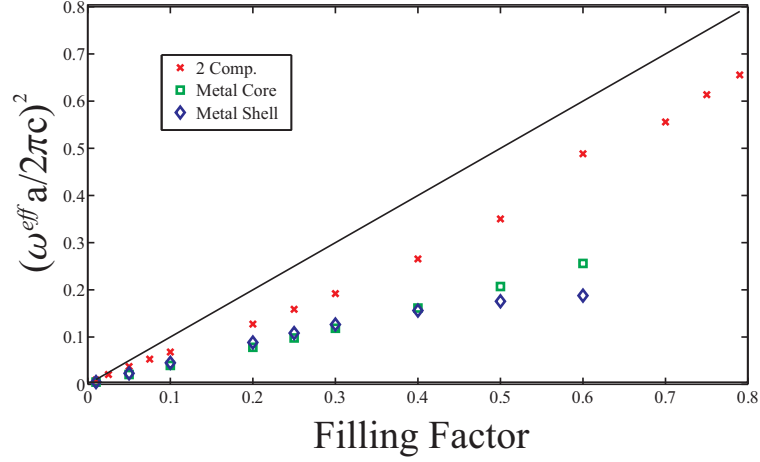


Figure 3.8: The lowest propagating frequency of E -polarized modes for two-component, three-component metallic core and three-component metallic shell photonic crystals plotted as a function of filling factor of the metallic component of the cylinders. The filling factor of the dielectric components is 0.1.

electron density, e is the electron charge and m is the electron mass. We can define an effective plasma frequency for the crystal given by $\omega_p^{eff} = \sqrt{N_{eff}e^2/m\epsilon_0}$ where $N_{eff} = fN$. Here f is the filling factor of the metallic component of the crystal. Thus, $(\omega_p^{eff})^2 = f\omega_p^2$, or, invoking the normalization we have been using $(\omega_p^{eff}a/2\pi c)^2 = f$. Therefore, if the effective plasma frequency determined the lowest allowed frequency of a propagating mode, we should see a linear relationship between the square of the normalized cutoff frequency and the filling factor. In Fig. 3.8 we show the lowest allowed propagating frequency plotted against the filling factor for the two and three-component photonic crystals. In all cases, the lowest allowed frequency falls below the line $(\omega_p^{eff}a/2\pi c)^2 = f$ and in both the cases of the metallic core and the metallic shell the lowest allowed frequency for a given filling factor falls below that for the two-component case.

It is interesting to consider which aspects of the data presented in Figs. 3.4-3.8 can be explained by consideration of light propagating in an effective index environment, which can be explained by consideration of the resonant properties of individual cylinders and which must take into account the complete structural configuration including the core/shell

structure of the cylinders and the geometric arrangement of the cylinders into a lattice. For wavelengths much longer than the lattice constant, the electromagnetic waves experience an average material medium; inability of light to propagate below the lowest band—a phenomenon which occurs in the metallic shell and core structures as well as in the two-component cylinders—can be understood in the effective index picture. In the metallic core case, the structural band gap closes with increased filling factor. This is a feature of dielectric photonic crystals. Thus, one may be inclined to assume the features of the structural band gap are governed by the exterior layer of the cylinders. Another feature, the significant flattening of the bands with increased filling factor, only occurs in the metallic shell case. While it seems apparent that the crystalline arrangement gives rise to the structural band gap, which arises in two-component photonic crystals as well, the slow group velocity seems to be unique to the shell structures. In order to gain more insight into the relation between the slow group velocity and the resonances of individual cylinders, one would need to have an understanding of the resonances of the individual metallic shell cylinders. Individual metallic cylinders coated with dielectric have scattering cross sections with many features [62]. Because metallic shell cylinders have two exposed surfaces, surface plasmons may be excited on both surfaces and may hybridize to give rise to even more complicated scattering cross sections [63]. Understanding how the resonances of the constituent cylinders contribute to the slow group velocity of the array is a worthwhile pursuit but is beyond the scope of this work.

3.5 Closing remarks

We have considered light propagation in two-dimensional arrays of metallodielectric cylinders. Unique features of band structures were analyzed. In particular, covering the metallic cylinders in a dielectric shell was shown to close the structural bandgap as the filling factor of the metal core was increased. However, the presence of a dielectric core in a metal cylinder did not have the same effect on the band structure. Photonic crystals composed of

metallic shells surrounding dielectric cores were shown to significantly flatten the photonic bands below the plasma frequency indicating the creation of a medium in which light propagates with an anomalously slow group velocity. Bands with a maximum group velocity of $0.05c$ were discovered. In the same structure, the maximum group velocity of any band below the plasma frequency was approximately $0.06c$, with the exception of one band which had a group velocity of $0.3c$ near the Γ point of the Brillouin zone.

In closing it is important to note that analysis of this system requires consideration of a large parameter space. This study is by no means meant to be an exhaustive account of the possibilities of the system, rather as an illustration of the significance of the arrangement of the components as well as the filling factors of a three component plasmonic crystal.

We now move to Part II of the thesis where we consider several aspects of light storage in Si microdisks.

Part II

Subwavelength and dynamic resonant microcavities

Chapter 4

Resonances in optical cavities

Our work on plasmonic crystals, as discussed in Chapter 3, allowed us to explore ways in which metals can be coupled to dielectrics to modify light propagation. This led to consideration of geometries in which plasmonic elements could be coupled to dielectric structures to confine light in small volumes [64–66]. This line of thinking led us to explore the smallest Si microcavities to date. This Part of the thesis explores our work on Si microdisks which began by trying to make the smallest possible optical resonators for a given wavelength of operation. We then began exploration of microcavities with dynamically-tunable resonance spectra.

4.1 Resonances in nature

Resonant phenomena are ubiquitous in nature and occur in systems as diverse as mechanical pendulums and biological systems. Many problems in the physical sciences can be reduced to the determination of resonant frequencies and the properties of the resonances of the system. At these resonant frequencies energy injected into the system will be stored for a characteristic time that is orders of magnitude larger than at non-resonant frequencies.

Optical resonances constitute a particularly exciting class of resonant phenomena. Improvements during the last half century in the material quality of optical cavities as well as available light sources has allowed the field of cavity optics to make substantial advances.

There are many fascinating things to investigate in the context of light stored in a small volume of space. The interaction of light with atoms and materials leads to many rich natural phenomena. Important new technologies made possible when light can be stored in a small volume for a long time are based on these physical principles.

In this part of the thesis we focus on optical resonant cavities of wavelength-scale dimensions. In particular, the medium of crystalline Si is the central platform for our microcavity experiments. We fabricate thin, cylindrical microdisk cavities for the modes that propagate around their perimeter. These so-called whispering-gallery modes are named for their physical analogy to acoustical propagating waves at the interior perimeter of domed architectures. Before further discussing whispering-gallery modes in Si microdisks it is useful to explain the choice of Si as the central platform for our experiments.

4.2 History of optical microcavities

Electromagnetic resonators were first proposed in 1939 in a prophetic paper by Richtmyer [67]. However, due to the unavailability of suitable materials, Richtmyer's proposals lay dormant for a quarter century. Once high-permittivity, low-loss materials advanced to the point where fabrication was economical, microwave and other electromagnetic cavities began to be explored.

A major step forward for optical resonators was taken when glass microspheres were created by melting the end of an optical fiber. Due to the surface tension of the liquid glass, the glass beads are highly spherical and maintain this shape once cooled. This is yet another instance of the significant evolution enabled by the development of optical fibers (see Chapter 1). These optical cavities support electromagnetic resonances from the optical to the near-IR regions of the electromagnetic spectrum. These cavities have been well studied, most notably by Dr. Kerry Vahala's lab at Caltech. They can have cavity quality (Q) factors near 10^9 [9], and phenomena from stimulated Raman scattering to single molecule detection has been observed.

While these glass spheres are an excellent platform for laboratory experiments, resonant cavities on a planar substrate are more suitable for integrated device applications. Many significant studies of planar micro-scale disk-shaped cavities were conducted in a very short time during the early 1990s at Bell Labs. These microdisks were utilized as laser cavities, and at that time were the smallest laser cavities in the world. They were manufactured from compound semiconductor substrates with a quantum well gain medium grown by MBE and MOCVD atop InP handle wafers. In a series of papers, researchers associated with the Bell Labs group demonstrated room temperature laser action and electrically-injected lasers in wavelength-scale cavities [68–70]. Almost 20 years later it remains difficult to make significant strides beyond what they were able to accomplish with wavelength-scale lasers.

All the microdisk work out of Bell Labs was oriented toward laser generation, and this is not a coincidence. In order to study their cavities, the cavities themselves needed to generate light. Once the cavities were generating light, the task was to make the light coherent. Once the device layer of the substrate was designed to generate light, it was no longer a suitable passive medium for waveguide routing and on-chip processing of optical signals. The point is this: modern photonic structures can broadly be lumped into two categories—those that generate light and those that transport, store, or process optical signals. The Bell Labs group made great contributions to on-chip light generation technology, especially from microdisk cavities. Their platform of quantum-confined structures made from compound semiconductors remains the preferred approach for on-chip light generation. For the other arm of photonics, that of on-chip transportation and processing, different media are required.

Many photonic circuits in contemporary applications are made from high-index polymers. However, a seminal technological advance was made in the late 1990s with the development of SOI wafers, as discussed in Chapter 1. These wafers allow for the creation of high-index-contrast photonic circuits on a CMOS-compatible platform. Because silicon is transmissive in the near-IR, high- Q resonant cavities operating at those wavelengths can

be achieved. SOI wafers have been used to fabricate many resonant elements such as microrings and microdisks, and the introduction of SOI changed the way scientists conceived of photonic waveguides. Silicon microdisks have been explored quite extensively, most notably by Dr. Oskar Painter's lab at Caltech. In this thesis we advance the state of the art both by exploring the fundamental limit of silicon microdisk size and by creating silicon microdisks which have tunable resonance spectra. Both of these contributions are important for photonic circuit applications aiming to fit many devices in a small region of space and to create photonic circuits with functionality that can vary in time with locally-applied voltage. Before discussing in more detail the specific technologies we have developed, we first explore the fundamental physics of microdisk cavities.

4.3 Size domains in optical microcavities

As was discussed in Section 4.2, silicon microdisk and microring resonators are emerging as critical elements in many integrated photonics applications. The purpose of our research was to investigate the smallest resonators to determine how small a silicon microdisk could be made and retain well-defined resonances with fairly large Q . Optical microcavities of a variety of geometries and sizes have been investigated for a number of purposes from information processing to chemical sensing. In Fig. 4.1 we show a number of the different technologies that have been utilized to store light. The images are plotted qualitatively with an x -axis of characteristic size and a y -axis of Q factor. On the extreme high- Q end of the plot are glass microcavities—microspheres and microtoroids—fabricated in a manner that makes use of the surface tension of melted glass to form remarkably smooth sidewalls. These cavities are generally 20-100 μm in diameter. Quality factors exceeding 10^8 have been demonstrated in such structures. These quality factors are usually limited by radiation and material absorption, although such glass structures are susceptible to corrosion from moisture in the atmosphere and tend to degrade fairly quickly after fabrication.

Mid-range (10-20 μm diameter) silicon microdisks and ring resonators have been shown

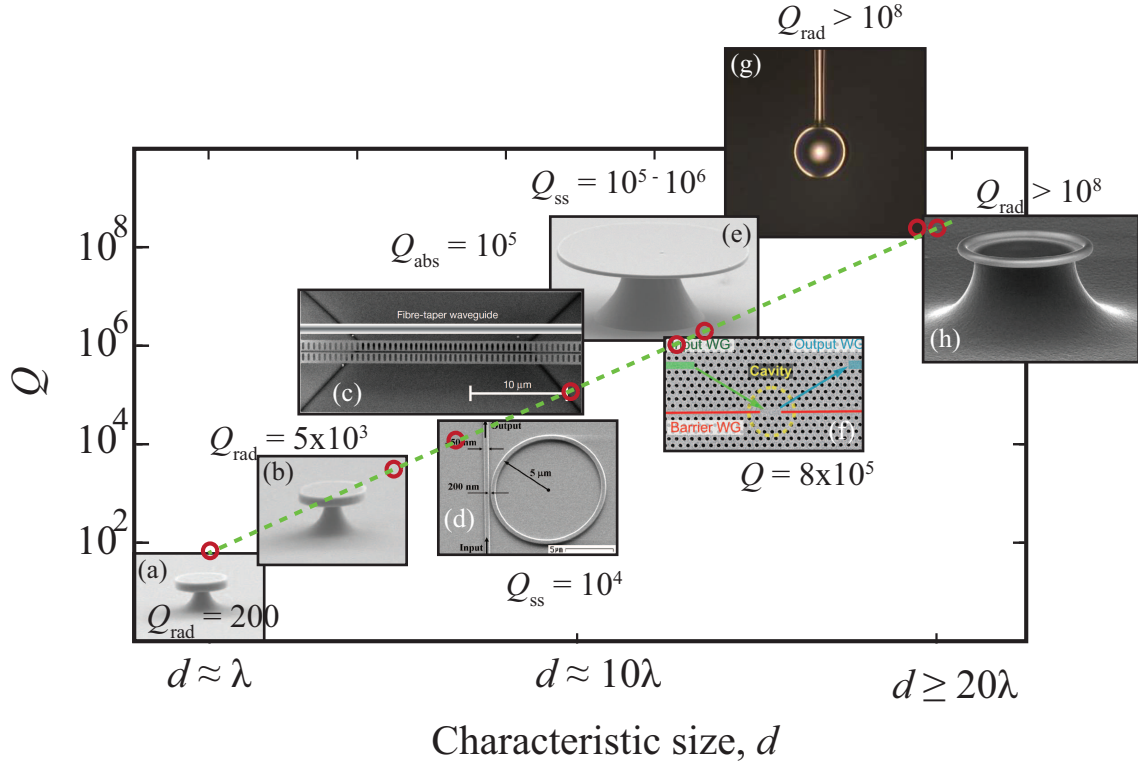


Figure 4.1: Optical microcavities of different types. Q is plotted versus the characteristic size of the structures. The y axis is logarithmic while the x is linear. On the low- Q , small d end of the figure we have (a) and (b), which we fabricated and studied. These are of diameter just below (a) and just above (b) the resonant wavelength. In (a) the Q is limited by radiation and is ~ 200 . In (b) the radiation limited Q is ~ 5000 . (c) A zipper photonic crystal cavity is $> 20\mu\text{m}$ in one dimension, but much smaller in the transverse dimensions. The Q limited by the material absorption of SiN is $\sim 10^5$ [6]. (d) A ring resonator is shown with $10\mu\text{m}$ diameter and $Q \sim 10,000$ limited by surface scattering [7]. (e) A Si microdisk with $10\mu\text{m}$ diameter made in our lab. The surface-scattering-limited Q is $\sim 10^5 - 10^6$. (f) A 2-D photonic crystal defect cavity with Q near 10^6 [8]. (g) A silica microsphere with radiation-limited Q exceeding 10^8 [9]. (h) A silica toroid with radiation-limited- Q exceeding 10^8 [9].

to be capable of having Q factors exceeding 10^6 [71]. Fabrication of such high- Q microdisks often makes use of surface tension as well, but in this case in a resist reflow step. This allows for microdisks with Q factors not limited by surface scattering, but rather surface chemical effects [71]. Fabrication of mid-range silicon microdisks without resist reflow often produces disks with Q factors around 10^5 limited by surface scattering [72] (see Chapter 7).

In our work we sought to explore the bottom left of Fig. 4.1. For practical and scientific purposes we wanted to know how small we could make silicon microdisks before they no longer gave rise to resonant states. In particular, we wanted to know if it is possible to make a microdisk smaller in every spatial dimension than the free-space resonant wavelength of light being stored within the cavity, a so-called subwavelength cavity.

We began our study by conducting accurate simulations of microdisk modes based on the numerical techniques described in Appendix C. The field profiles of two microdisk modes are shown in Fig. 4.2. TE modes are shown (with electric field predominantly in the plane of the disk), and H_z is plotted. The modes propagate around the perimeter of the disk; the curvilinear Laplacian creates a centrifugal barrier, and the high index material holds confines the material within a potential well (see discussion in Chapter 5). The modes are classified by their radial and azimuthal mode orders. The radial mode order (one in Fig. 4.2(a) and two in Fig. 4.2(b)) corresponds to the number of maxima of the absolute value of the dominant field component in the radial direction. The azimuthal mode order (50 in Fig. 4.2(a) and 46 in Fig. 4.2(b)) corresponds to the number of maxima of the dominant field component in the angular direction.

In Fig. 4.3 we plot the azimuthal mode indices of five mode families (see section 5.2.3), three TE and two TM, versus microdisk radius. The resonant wavelength for this calculation was kept as close to 1570nm as possible. In Fig. 4.3 one sees that there are in fact several resonances for which the diameter of the disk is smaller than the resonant wavelength. These occur only in first radial order TE modes for which the effective index of refraction is larger than for the TM modes and for which the component of the wave vector

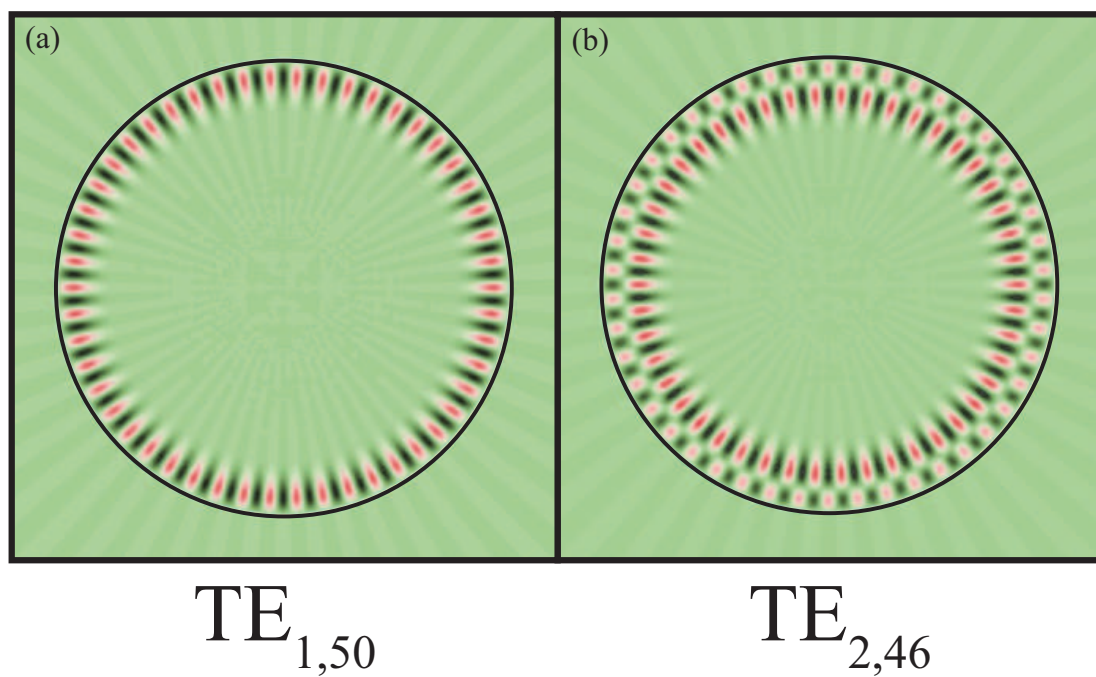


Figure 4.2: Field profiles of two microdisk whispering-gallery modes are shown. (a) The H_z component of the $TE_{1,50}$ mode. (b) The H_z component of the $TE_{2,46}$ mode

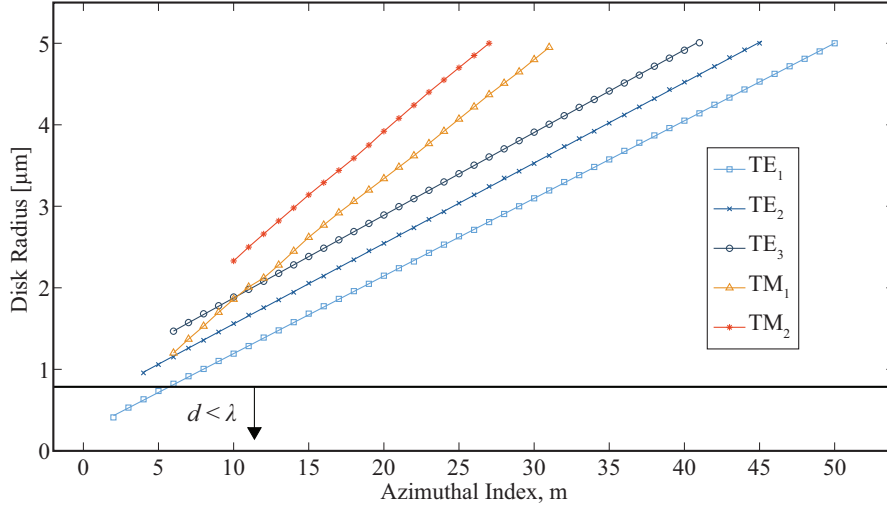


Figure 4.3: Relationship between disk radius and azimuthal mode order. Data obtained numerically as described in Appendix C. The radius of the cavity was varied to obtain each resonance as close to 1570nm as possible. The height of the disk is 240nm. Five mode families are shown. Of these, only the TE_1 mode family is present in disks with diameters less than the resonant wavelength of 1570nm. The $TE_{1,2}$ - $TE_{1,5}$ modes are calculated to exist in subwavelength cavities, and are seen to fall below the black line in the figure separating cavities that are smaller than the free-space resonant wavelength from those that are larger (admittedly a somewhat arbitrary differentiation). The mode solver did not converge to the $TE_{1,1}$ mode, most likely due to the fact that the resonance is poorly-confined and has a Q of order 1.

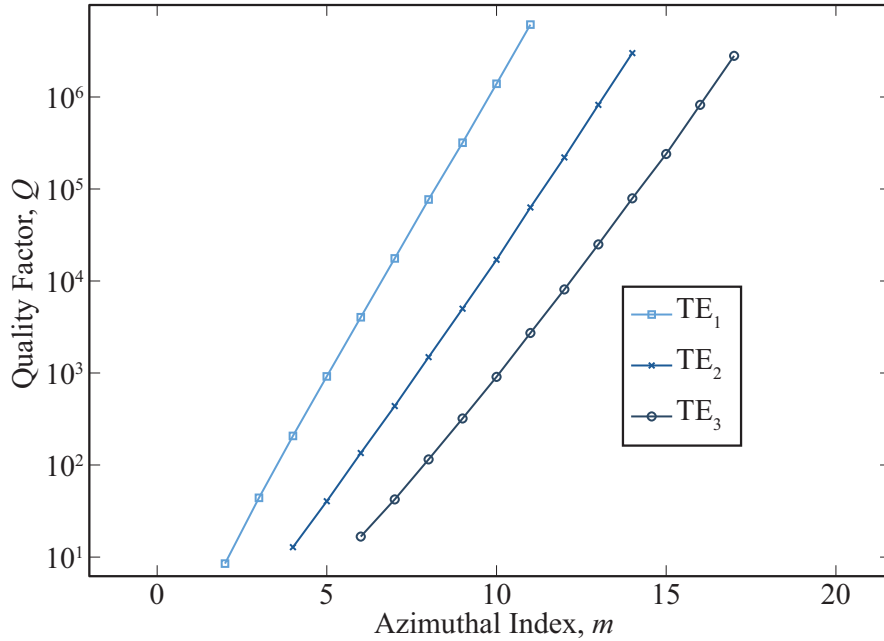


Figure 4.4: Calculated Q factors of the TE modes in Fig. 4.3. The subwavelength modes TE_{1,4} and TE_{1,5} are calculated to have Q factors exceeding 100, indicating potential for laser and device applications.

in the azimuthal direction is maximized thus minimizing momentum in the radial direction which leads to tunneling through the effective potential. The next question is whether the Q factors of these modes are large enough to make the cavities worth investigating. If one wishes to make a laser, Q factors will need to be at least 100 – 1000. For sensing and cavity QED, $Q \sim 20,000$ is necessary. In Fig. 4.4 we show the calculated Q factors of the modes shown in Fig. 4.3. Figure 4.4 reveals that the theoretical radiation-limited Q factors for the wavelength-scale disks are reasonably high, between 100 and 10,000. This is encouraging and indicates that the effort to create subwavelength Si microdisks is potentially worthwhile.

Our investigations into frontiers in Si microdisks is presented in the remainder of the thesis as follows. In Chapter 5 we present a theoretical discussion of the physics of microdisks. In Chapter 6 we discuss the method of tapered-fiber spectroscopy for characterizing the resonance spectra of microdisks. Chapter 7 contains a discussion of the techniques

used to fabricate Si microdisks. We present our work on microdisks which are smaller than the free-space resonant wavelength of the light they store in Chapter 8. We move to a discussion of dynamically-tunable silicon microdisks in Chapter 9. We conclude the thesis with a discussion of future work which could build on our research in Chapter 10.

Chapter 5

Microdisk theory

In this section we write Maxwell's equations for the dielectric disk and reduce them to a single ordinary differential equation for the radial dependence of the field from which much insight about the system can be gained. We obtain the complete spatial dependence of the fields and apply boundary conditions to arrive at a pair of coupled quantization conditions for the complex-valued wave vectors and effective indices of the eigenmodes. While these coupled transcendental equations are somewhat cumbersome to deal with directly, the first-principles analytical treatment of the problem gives us a great deal of physical insight. We compare the equations governing the electromagnetic system to those governing a quantum disk [73]. Then, to obtain accurate eigenvalues for the system we conduct numerical simulations. These analytical and numerical models guide our thinking about the microdisk system and inform our fabrication for the next section where we study Si microdisks which are smaller than the free space resonant wavelength of light being stored.

5.1 Microdisk geometry

The structure under consideration is shown in Fig. 5.1. A right circular cylinder of radius a and height h has the center of its volume at the origin. The disk is made of a material with frequency-independent relative permittivity, ϵ , and is surrounded by vacuum.

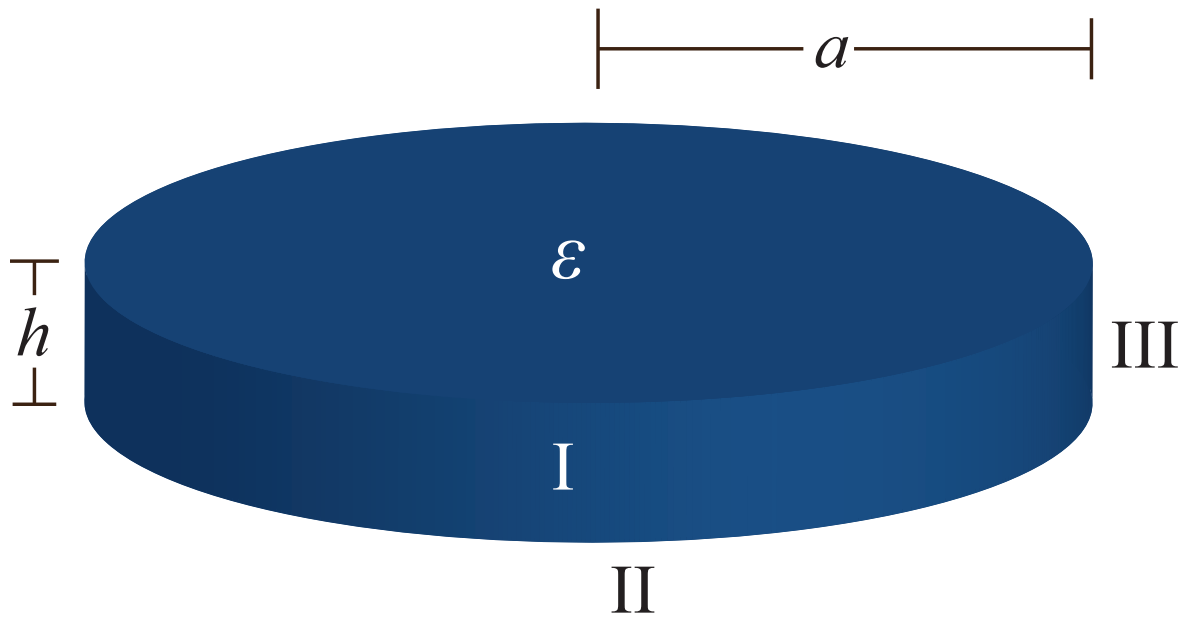


Figure 5.1: The microdisk structure under consideration. The height of the disk is h , and its radius is a . The permittivity of the material is ϵ which is taken to be frequency-independent. The region inside the disk is referred to as region I. Above and below the disk is region II. Beyond the radius of the disk is region III.

5.2 First principles analytical model

Our treatment here builds upon the calculations presented in Refs. [74] and [75].

5.2.1 Reduction to a scalar problem

Maxwell's equations for the source-free system with piecewise-constant permittivity and vacuum permeability read

$$\nabla \times \mathbf{E} = -\mu_0 \frac{\partial \mathbf{H}}{\partial t}; \quad (5.1)$$

$$\nabla \times \mathbf{H} = \epsilon \epsilon_0 \frac{\partial \mathbf{E}}{\partial t}; \quad (5.2)$$

$$\nabla \cdot \mathbf{E} = 0; \quad (5.3)$$

$$\nabla \cdot \mathbf{H} = 0. \quad (5.4)$$

Because the magnetic field has a divergence equal to zero (Eq. 5.4), we can make use of the fact that the divergence of a curl is identically zero and introduce a vector potential [76] related to the magnetic field by

$$\mathbf{H} = \nabla \times \mathbf{A}. \quad (5.5)$$

Substituting the relation from Eq. 5.5 into Eq. 5.1 we have

$$\nabla \times \left(\mathbf{E} + \mu_0 \frac{\partial \mathbf{A}}{\partial t} \right) = 0. \quad (5.6)$$

Making use of the fact that the curl of a gradient is identically zero, we can introduce the scalar potential as

$$\mathbf{E} + \mu_0 \frac{\partial \mathbf{A}}{\partial t} = -\nabla \phi. \quad (5.7)$$

Taking the time derivative of Eq. 5.7 and using Eq. 5.2, Eq. 5.5, and the definition of the vector Laplacian ($\nabla^2 \mathbf{A} = \nabla \times \nabla \times \mathbf{A} - \nabla(\nabla \cdot \mathbf{A})$), we can write

$$\nabla(\nabla \cdot \mathbf{A} + \epsilon \epsilon_0 \frac{\partial \phi}{\partial t}) - \nabla^2 \mathbf{A} + \frac{\epsilon}{c^2} \frac{\partial^2 \mathbf{A}}{\partial t^2} = 0. \quad (5.8)$$

Here we have used $c = (\epsilon_0 \mu_0)^{-1/2}$. We now eliminate the first term in Eq. 5.8 by working in the Lorenz gauge [76]:

$$\nabla \cdot \mathbf{A} + \epsilon \epsilon_0 \frac{\partial \phi}{\partial t} = 0. \quad (5.9)$$

Equation 5.8 is thus reduced to a vector wave equation which reads

$$\nabla^2 \mathbf{A} - \frac{\epsilon}{c^2} \frac{\partial^2 \mathbf{A}}{\partial t^2} = 0. \quad (5.10)$$

Assuming $\mathbf{A}(\mathbf{r}, t) = \mathbf{A}(\mathbf{r})e^{-i\omega t}$, Eq. 5.10 reduces to the vector Helmholtz equation,

$$(\nabla^2 + k^2)\mathbf{A} = 0, \quad (5.11)$$

where $k^2 = \epsilon \frac{\omega^2}{c^2}$ is the spatial frequency of the system. Using Eq. 5.7 and the definition of the Lorenz gauge from Eq. 5.9, we can write the electric field completely in terms of the magnetic vector potential,

$$\mathbf{E} = \frac{1}{\epsilon\epsilon_0} \int \nabla(\nabla \cdot \mathbf{A})dt - \mu_0 \frac{\partial \mathbf{A}}{\partial t}. \quad (5.12)$$

Maxwell's equations for the system (Eqs. 5.1-5.4) are invariant under the exchange $\mathbf{E} \leftrightarrow \mathbf{H}$, $\epsilon\epsilon_0 \leftrightarrow -\mu_0$. In this source-free problem we can then define an electric vector potential related to the electric field by

$$\mathbf{E} = \nabla \times \mathbf{F}. \quad (5.13)$$

The magnetic field can then be constructed from \mathbf{F} in a manner analogous to Eq. 5.12. To form a complete basis for the two independent polarizations of electromagnetic waves, we choose \mathbf{A} and \mathbf{F} in terms of scalar functions as

$$\mathbf{A}(\rho, \phi, z; t) = k_0 g(\rho, \phi, z) \exp(-i\omega t) \hat{z}, \quad (5.14)$$

and

$$\mathbf{F}(\rho, \phi, z, t) = ik_0 c \mu_0 f(\rho, \phi, z) \exp(-i\omega t) \hat{z}. \quad (5.15)$$

In general, the vector Laplacian can be written in component form as

$$\nabla^2 \mathbf{A} = \begin{pmatrix} \frac{\partial^2 A_\rho}{\partial \rho^2} + \frac{1}{\rho} \frac{\partial^2 A_\rho}{\partial \phi^2} + \frac{\partial^2 A_\rho}{\partial z^2} + \frac{1}{\rho} \frac{\partial A_\rho}{\partial \rho} - \frac{2}{\rho^2} \frac{\partial A_\phi}{\partial \phi} - \frac{A_\rho}{\rho^2} \\ \frac{\partial^2 A_\phi}{\partial \rho^2} + \frac{1}{\rho} \frac{\partial^2 A_\phi}{\partial \phi^2} + \frac{\partial^2 A_\phi}{\partial z^2} + \frac{1}{\rho} \frac{\partial A_\phi}{\partial \rho} - \frac{2}{\rho^2} \frac{\partial A_\rho}{\partial \phi} - \frac{A_\phi}{\rho^2} \\ \frac{\partial^2 A_z}{\partial \rho^2} + \frac{1}{\rho} \frac{\partial^2 A_z}{\partial \rho^2} + \frac{\partial^2 A_z}{\partial z^2} + \frac{\partial A_z}{\rho} \frac{\partial A_z}{\partial \rho} \end{pmatrix} \quad (5.16)$$

Choosing vector potentials each with only a \hat{z} component each greatly simplifies this expression so that only the \hat{z} component remains. The full electric and magnetic fields are obtained from the combination of \mathbf{A} and \mathbf{F} :

$$\mathbf{E} = \frac{1}{\epsilon\epsilon_0} \int \nabla(\nabla \cdot \mathbf{A}) dt - \mu_0 \frac{\partial \mathbf{A}}{\partial t} + \nabla \times \mathbf{F}, \quad (5.17)$$

and similarly for \mathbf{H} . Explicitly, the components of the electric and magnetic fields in terms of the scalar generating functions f and g are given by

$$E_\rho(\rho, \phi, z) = i\omega\mu_0 \left(\frac{k_0}{\rho k^2} \frac{\partial^2 g(\rho, \phi, z)}{\partial \rho \partial z} + \frac{1}{\rho} \frac{\partial f(\rho, \phi, z)}{\partial \phi} \right); \quad (5.18)$$

$$E_\phi(\rho, \phi, z) = i\omega\mu_0 \left(\frac{k_0}{\rho k^2} \frac{\partial^2 g(\rho, \phi, z)}{\partial \phi \partial z} - \frac{\partial f(\rho, \phi, z)}{\partial \rho} \right); \quad (5.19)$$

$$E_z(\rho, \phi, z) = i\omega\mu_0 k_0 \left(g(\rho, \phi, z) + \frac{1}{k^2} \frac{\partial^2 g(\rho, \phi, z)}{\partial z^2} \right); \quad (5.20)$$

$$H_\rho(\rho, \phi, z) = \frac{\partial^2 f(\rho, \phi, z)}{\partial \rho \partial z} + \frac{k_0}{\rho} \frac{\partial g(\rho, \phi, z)}{\partial \phi}; \quad (5.21)$$

$$H_\phi(\rho, \phi, z) = \frac{1}{\rho} \frac{\partial^2 f(\rho, \phi, z)}{\partial \phi \partial z} - k_0 \frac{\partial g(\rho, \phi, z)}{\partial \rho}; \quad (5.22)$$

$$H_z(\rho, \phi, z) = k^2 f(\rho, \phi, z) + \frac{\partial^2 f(\rho, \phi, z)}{\partial z^2}. \quad (5.23)$$

Substituting Eq. 5.14 into Eq. 5.11 we find that the scalar generating functions obey a scalar Helmholtz equation.

$$(\nabla^2 + k^2)g(\rho, \phi, z) = 0. \quad (5.24)$$

In cylindrical coordinates this reads

$$\frac{\partial^2 g}{\partial \rho^2} + \frac{1}{\rho} \frac{\partial g}{\partial \rho} + \frac{1}{\rho^2} \frac{\partial^2 g}{\partial \phi^2} + \frac{\partial^2 g}{\partial z^2} + k^2 g = 0. \quad (5.25)$$

This partial differential equation is separable, so we insert the ansatz

$$g(\rho, \phi, z) = R(\rho)\Phi(\phi)Z(z). \quad (5.26)$$

If we assume $\Phi(\phi) = e^{im\phi}$ and $\frac{d^2 Z(z)}{dz^2} = -\beta^2 Z(z)$, Eq. 5.25 can be reduced to the ordinary differential equation

$$\left(\frac{\partial^2 R}{\partial \rho^2} + \frac{1}{\rho} \frac{\partial R}{\partial \rho} \right) + \left(T^2 - \frac{m^2}{\rho^2} \right) R = 0, \quad (5.27)$$

where

$$T^2 = k^2 - \beta^2 \equiv k_0^2 \bar{n}^2. \quad (5.28)$$

Equation 5.27 is Bessel's equation. The fully-vectorial Maxwell's equations have now been reduced to a single, scalar ordinary differential equation. The spatial dependence of the scalar generating functions in the three regions of space, as defined in Fig. 5.1, is given by

$$g(\rho, \phi, z) = \begin{cases} C_I J_m(T_I \rho) \cos(\beta_I z) e^{im\phi}, & \text{region I} \\ C_{II} J_m(T_{II} \rho) e^{\beta_{II}(|z|-h/2)} e^{im\phi}, & \text{region II} \\ C_{III} H_m^{(1)}(T_{III} \rho) \cos(\beta_{III} z) e^{im\phi}, & \text{region III} \end{cases} \quad (5.29)$$

where J_m is a Bessel function of order m , and $H_m^{(1)}$ is a Hankel function of the first kind of order m . We can then obtain the full electric and magnetic fields with Eqs. 5.18-5.23. The scalar generating function $f(\rho, \phi, z)$ is defined similarly with different coefficients which must be determined from boundary conditions.

5.2.2 Brief discussion of polarization

As mentioned above, the scalar generating function f will have the same form as g given by Eq. 5.29 with different constants to be determined by boundary conditions. However, in the disks considered here it is sensible to consider TE and TM polarizations separately. We define TE modes as those modes for which the scalar generating function $g = 0$ and TM modes as those for which $f = 0$. For TE modes $E_z = 0$ and for TM modes $H_z = 0$. In reality, both g and f are always non-vanishing, but naturally modes with polarizations approximately obeying these conditions occur with the amplitude of f being much larger than g for TE modes and vice versa for TM modes. Such an approximation for the two polarizations turns out to be quite accurate when one compares to numerical calculations with all six field components. For the remainder of this work we simplify consideration to the two polarizations independently, and Eqs. 5.18-5.23 are reduced accordingly.

5.2.3 Boundary and quantization conditions

We proceed now to apply boundary conditions to the functions in Eqs. 5.18-5.23 with g and f given by Eq. 5.29 to obtain quantization conditions on the various T s and β s, and therefore on k_0 .

Inside the disk we have $k_1^2 = \epsilon k_0^2$. We define the effective index of refraction (\bar{n}) through the relationship

$$T_1 = \bar{n}k_0. \quad (5.30)$$

At the top and bottom of the disk we demand that H_ρ and E_ρ be continuous across the interface. These constraints lead to the transcendental equation

$$\sqrt{n^2 - \bar{n}^2} \tan\left(\frac{hk_0\sqrt{n^2 - \bar{n}^2}}{2}\right) = \xi\sqrt{\bar{n}^2 - 1}, \quad (5.31)$$

where $\xi = 1$ for TE modes and ϵ for TM modes. This is the first of our quantization conditions, and one sees that it depends on both \bar{n} and k_0 . If the wavelength of operation is already known, Eq. 5.31 can be solved to obtain \bar{n} . As such, \bar{n} is obtained purely from the z -dependence of the problem, and is identical to the effective index in the slab waveguide problem. It is referred to as the effective index of refraction because after application of boundary conditions at the top and bottom of the high index material, the solutions inside the high index region behave as if they were propagating in a region of space with index of refraction \bar{n} . Because our intention is for all of our devices to operate in a narrow range of wavelengths within the telecom band, it is worthwhile to spend some time assuming values of λ (and therefore k_0) and discussing the behavior of \bar{n} obtained through solution of Eq. 5.31 in isolation.

5.2.4 The effective index of refraction

In a microdisk, the effective index of refraction multiplies the wave vector to give the propagation constant in the radial direction (Eq. 5.30). It is a highly-physical number in that it determines the confinement of an optical mode. The effective index of refraction is different for TE and TM modes due to the presence of the factor ξ on the right-hand side of

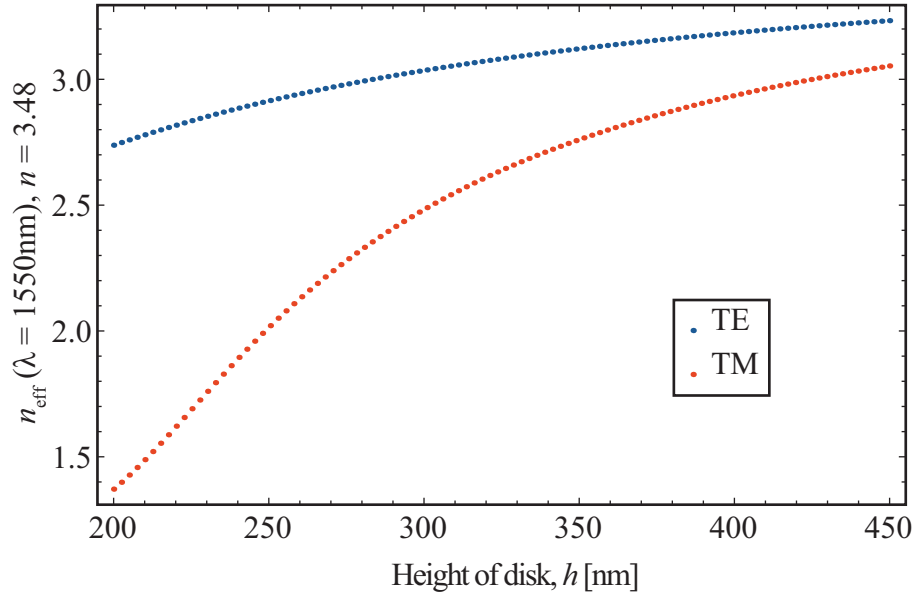


Figure 5.2: The relationship between disk height and effective index of refraction. The index of refraction is set at 3.48 and the wavelength is 1550nm. The effective index is similar for the two polarizations in thick disks, but as the disk gets thinner the TM effective index drops off much faster than the TE.

Eq. 5.31. As we shall see in the remainder of this thesis, this difference in \bar{n} between TE and TM modes has important implications for minimum cavity size (Chapter 8) as well as mode shift with heating (Chapter 9).

There are three important parameters in Eq. 5.31. These parameters are the height of the disk, h , the physical index of refraction of the material, n , and the wavelength of operation, $\lambda = \frac{2\pi}{k_0}$. If we assume we are operating in the wavelength range between 1520 – 1620nm, as will be discussed in Chapter 6, and that our material has a physical index of refraction within a small range around $n = 3.48$, as will be discussed in Chapter 9, then the factor which has the largest impact on the effective index of refraction is the height of the disk. In Fig. 5.2 we have plotted the effective index of refraction, \bar{n} , against the height of the disk, h , over a range of microdisk thicknesses from 200 to 450nm. The wavelength is fixed at $\lambda = 1550\text{nm}$ and the physical index has the value $n = 3.48$. One can see that the effective index of refraction for TE modes is always larger than that for TM modes and that the

discrepancy between the two polarizations increases as the thickness of the disk is reduced. Equation 5.31 was derived from the boundary condition at the upper surface of the disk, so it must be true that the physical origin of the larger effective index of TE modes results from the way the modes of the two polarizations behave at the top and bottom boundaries of the disk. As was discussed in section 5.2.2, TM modes have a strong E_z component. The E_z component of the field vanishes for TE modes. For the TM modes the boundary conditions demand that $E_z^{\text{II}} = \epsilon E_z^{\text{I}}$, and since $\epsilon \sim 12$ this forces the TM modes to have a great deal of intensity just above and below the disk, as will be shown in Fig. 5.8. Since we are dealing with non-magnetic media, all five of the TE mode field components pass continuously through the upper and lower disk boundaries. Therefore, the TE modes are much more confined within the disk than the TM modes, as can be seen in Figs. 5.5-5.9.

It is also useful to study Eq. 5.31 as a function of the wavelength and physical index of refraction. In Fig. 5.3 we fix h at 250nm and n at 3.48. We then plot \bar{n} versus wavelength and find that the effective index of refraction decreases more for TM modes than for TE modes as the wavelength is increased above 1550nm, and the change is highly linear. Next we plot \bar{n} versus the physical index of refraction, n , with $\lambda = 1550\text{nm}$ and $h = 250\text{nm}$. In this case, \bar{n} of the TM modes grows faster than that of the TE modes, but the difference is not as great as it was in the previous plot. These trends have important consequences for tuning of modes, as will be discussed in more detail in Chapter 9. Briefly, if one wishes to tune the mode spectrum by changing the index of refraction (i.e., through the thermo-optic effect) one will simultaneously change the physical index of refraction, and therefore the resonant wavelength, and therefore the effective index of refraction. Ultimately, the result will be that TE modes shift more than TM modes under the same change of physical index of refraction due to the fact that the discrepancy between the effective index of refraction shift in Fig. 5.3 is larger than in Fig. 5.4. As was mentioned above, the boundary conditions considered here are intimately connected to mode confinement. While we can make arguments here based on Eq. 5.31 as to why TE modes will shift more than TM modes, we leave a more complete and physically intuitive discussion of this phenomenon to Chapter 9.

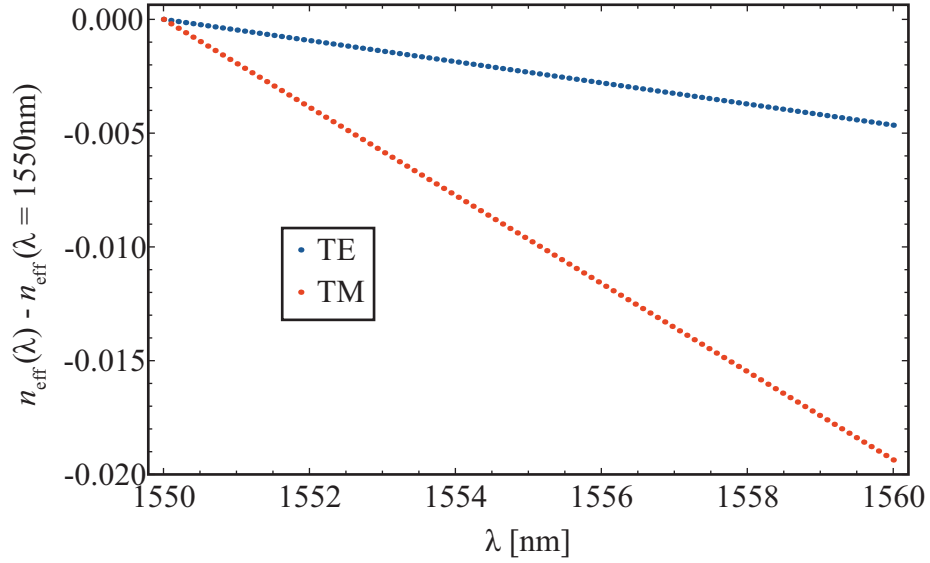


Figure 5.3: Here we consider a disk of height 250nm with index fixed at 3.48. The wavelength is the variable. We see that the effective index of the TM modes decays faster with increasing wavelength than the TE modes. The difference $\bar{n}(\lambda) - \bar{n}(\lambda = 1550\text{nm})$ is plotted rather than simply $\bar{n}(\lambda)$ because the fractional change in \bar{n} with wavelength is much smaller than the difference between \bar{n} for the two polarizations, so a plot of $\bar{n}^{\text{TE}}(\lambda)$ and $\bar{n}^{\text{TM}}(\lambda)$ simply looks like two straight lines, and the physical comparison is lost.

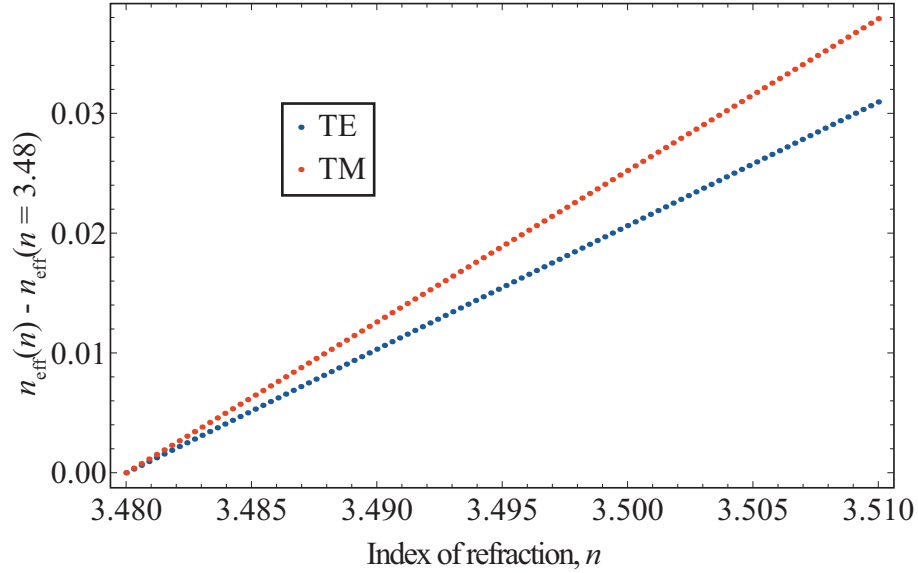


Figure 5.4: In this plot the wavelength is 1550nm and the height is 250nm. Physical index is the variable. Here we see that the effective index of the TM modes grows faster with increasing index than the TE modes.

Note that the entire discussion held here depends only on polarization and not on azimuthal or radial mode order. We now proceed to discuss the other quantization condition derived from the radial boundary conditions.

5.2.5 The radial boundary

At $\rho = a$ we demand continuity of H_z and E_ϕ . These constraints lead to the second transcendental quantization condition:

$$\frac{J_m(T_I a)}{\frac{d}{d\rho} J_m(T_I \rho)|_{\rho=a}} = \zeta \frac{H_m(T_{II} a)}{\frac{d}{d\rho} H_m(T_{II} \rho)|_{\rho=a}}, \quad (5.32)$$

where

$$\zeta = \begin{cases} \frac{T_{II}}{T_I}, & \text{for TE modes} \\ \frac{T_I}{T_{II}}, & \text{for TM modes} \end{cases} \quad (5.33)$$

T_I and T_{II} depend on both k_0 and \bar{n} , so Eqs. 5.31 and 5.32 must be solved self-consistently for k_0 and \bar{n} . As will be discussed in sec. 5.2.7, all microdisk modes are actually quasinormal modes. The frequencies are complex and the modes have a finite lifetime. Complex

frequencies lead to complex wave vectors, so Eqs. 5.31 and 5.33 must be solved in the complex plane. Converging to the desired roots of these transcendental equations is difficult, and it is far easier in practice to simply use a numerical scheme to calculate the complex eigenvalues and field profiles. The details of our numerical methods are given in Appendix C.

The critical information which can be gained from analysis of these quantization conditions is the way the modes of the microdisk mode spectrum are classified. First, as discussed in section 5.2.2 one must specify the polarization of a given mode. Then, one must specify three quantum numbers corresponding to the degree of excitation in the axial, azimuthal, and radial directions. For thin disks with $h < \lambda/2$, only the fundamental quantum number in the axial direction need be considered, and the scalar generating function always takes the form of a cosine with one field maximum in the axial direction within the disk. The azimuthal mode order, m , governs the angular dependence of the field; the scalar generating function has the ϕ dependence $e^{im\phi}$. The radial order specifies the number of maxima of the absolute value of the scalar generating function in the radial direction within the disk. For a given polarization and m , there will be multiple roots to Eq. 5.32. These correspond to the various radial orders for which different values of T solve Eq. 5.32. An example of the complete specification of a mode would be $\text{TE}_{2,42}$. This is a TE-polarized mode of the second radial order with $m = 42$. Modes of a given polarization and radial order with various azimuthal orders are referred to as a mode family. In the next section we illustrate the fields of various modes to develop the readers intuition and grasp of nomenclature.

5.2.6 Field components

Numerical solution of the field components (as discussed in Appendix C) agrees well with the analytical functional forms given by Eq. 5.18-5.23. The field profiles are presented in Figs. 5.5-5.9.

TE_{1,51}

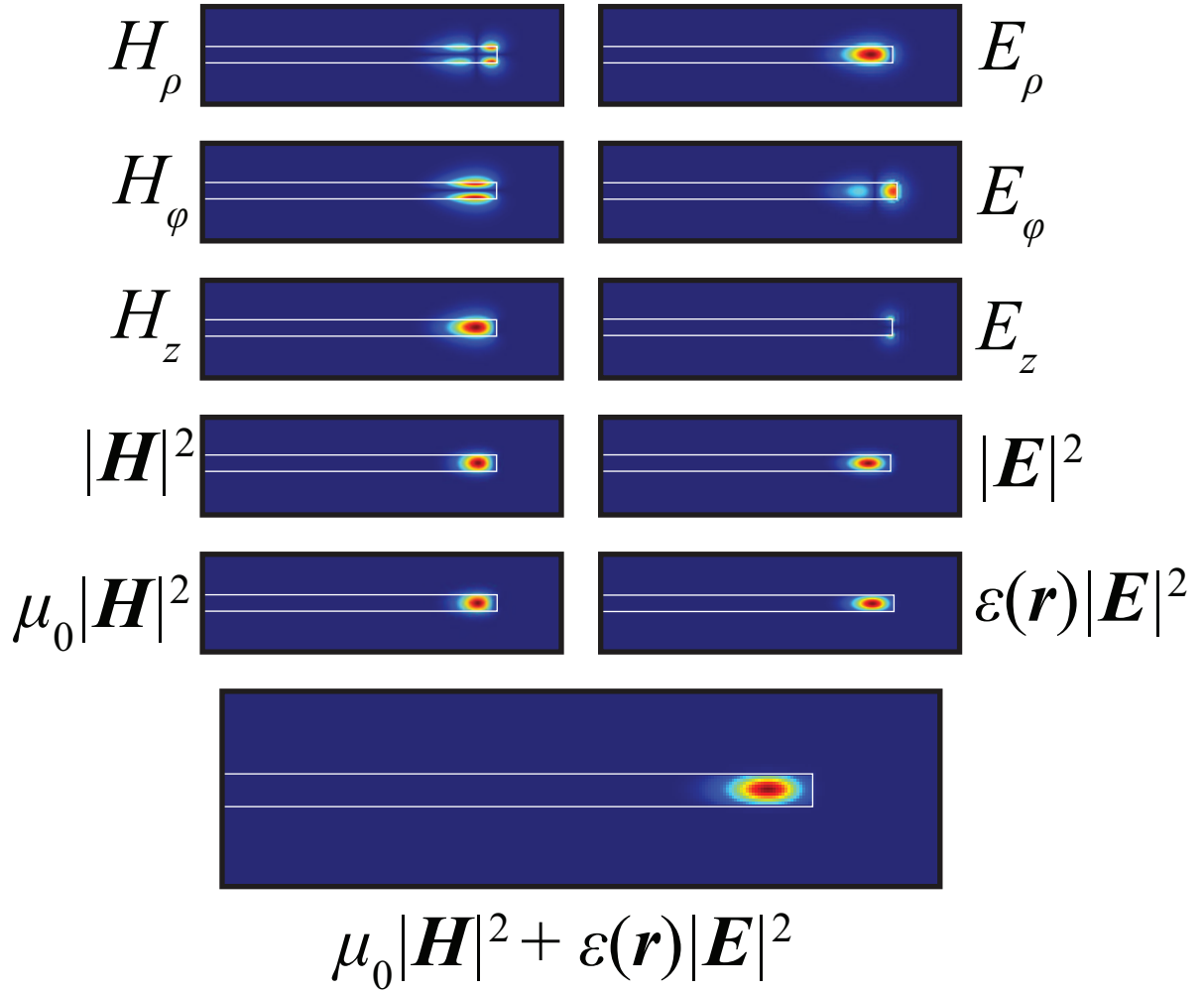


Figure 5.5: Field profiles of the TE_{1,51} mode in the $\rho - z$ plane. Angular dependence of the form $\exp(im\phi)$ is assumed, and the absolute values of the field components are shown.

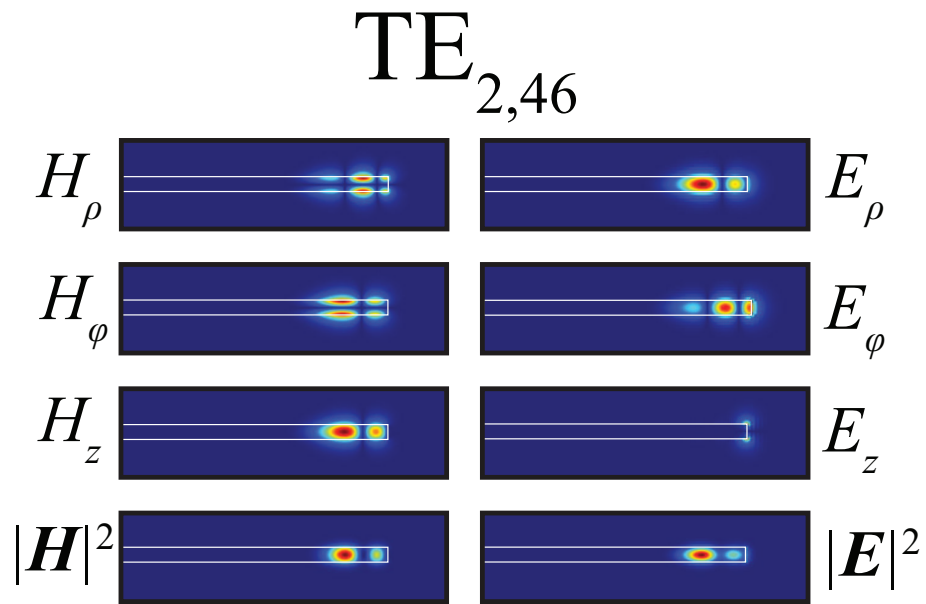


Figure 5.6: Field profiles of the TE_{2,46} mode in the $\rho - z$ plane. Angular dependence of the form $\exp(im\phi)$ is assumed, and the absolute values of the field components are shown.

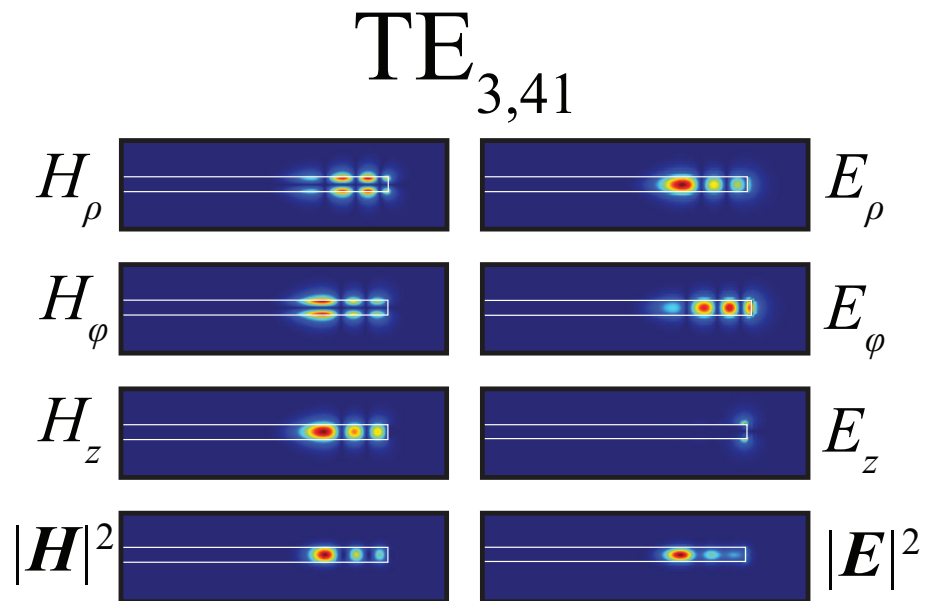


Figure 5.7: Field profiles of the TE_{3,41} mode in the $\rho - z$ plane. Angular dependence of the form $\exp(im\phi)$ is assumed, and the absolute values of the field components are shown.

TM_{1,33}

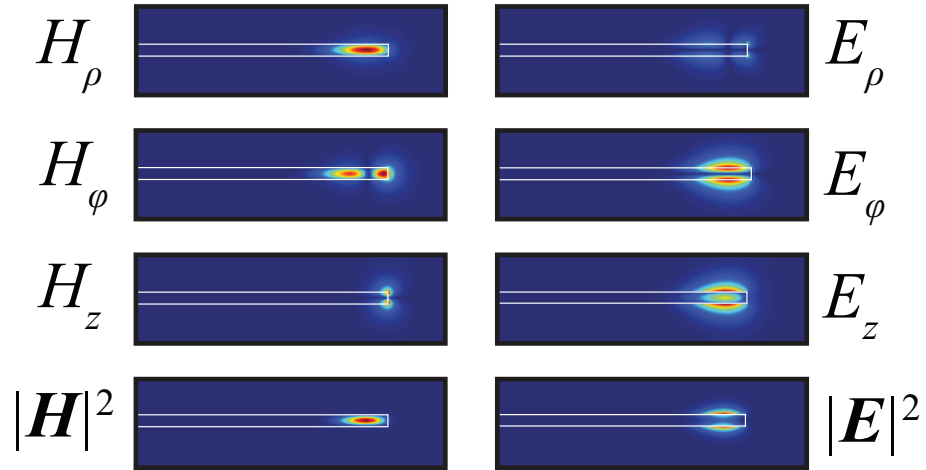


Figure 5.8: Field profiles of the TM_{1,33} mode in the $\rho - z$ plane. Angular dependence of the form $\exp(im\phi)$ is assumed, and the absolute values of the field components are shown.

TM_{2,29}

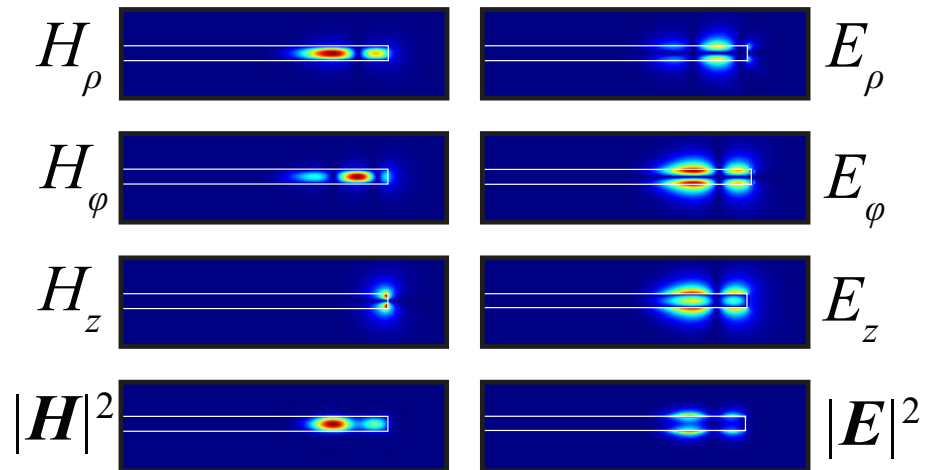


Figure 5.9: Field profiles of the TM_{2,29} mode in the $\rho - z$ plane. Angular dependence of the form $\exp(im\phi)$ is assumed, and the absolute values of the field components are shown.

5.2.7 Consideration of the effective potential

We now proceed to analyze the microdisk problem from the point of view of the effective potential. This analysis builds on that in Ref. [77]. We will then compare the electromagnetic microdisk problem to that of a quantum disk potential. To my knowledge, this comparison has not been made in the literature, but it represents an interesting contrast between the physics of classical electrodynamic and quantum mechanical systems.

For the electromagnetic disk we can rewrite Eq. 5.27 in a manner analogous to a one-dimensional Schrödinger equation.

$$-\left(\frac{d^2}{d\rho^2}R(\rho) + \frac{1}{\rho}\frac{d}{d\rho}R(\rho)\right) + V_{\text{eff}}(\rho)R(\rho) = k_0^2R(\rho). \quad (5.34)$$

The effective potential is defined as

$$V_{\text{eff}}(\rho) \equiv \beta^2 + k_0^2 - k^2 + \frac{m^2}{\rho^2} = k_0^2(1 - \bar{n}(\rho)^2) + \frac{m^2}{\rho^2}. \quad (5.35)$$

A critical difference between Eq. 5.34 and a quantum mechanical Schrödinger equation is that the eigenvalue, k_0^2 , appears both on the right side of the equation as well as in the effective potential term. To justify calling this quantity an effective potential we must show that it produces a well which separates the propagating solutions from bound or quasibound solutions [77]. To do this we make a coordinate transformation by introducing

$$\xi = \ln(k_0\rho). \quad (5.36)$$

Using ξ in Eq. 5.34 we obtain the simple harmonic oscillator equation,

$$\frac{d^2R(\xi)}{d\xi^2} + q(\xi)^2R(\xi) = 0; \quad (5.37)$$

here $q(\xi)$ is given by

$$q(\xi) = \sqrt{\bar{n}^2 e^{2\xi} - m^2} = \rho\sqrt{k_0^2 - V_{\text{eff}}(\rho)}. \quad (5.38)$$

We see that classically allowed, propagating solutions will occur when $k_0^2 > V_{\text{eff}}$. Quasi-bound states occur when $k_0^2 < V_{\text{eff}}$. This shows that the effective potential produces a well which separates propagating solutions from bound states.

Another interesting question we can answer with this analysis is whether the bound states are truly bound or if they are able to tunnel through the barrier to couple to propagating solutions. We are interested in the resonant states for which $k_0^2 < V_{\text{eff}}$. The minimum wave vector is found from

$$k_{\text{min}}^2 = k_{\text{min}}^2(1 - \bar{n}^2) + \frac{m^2}{a^2} \longrightarrow k_{\text{min}} = \frac{m}{na}, \quad (5.39)$$

and can only be zero if m is zero. We can see from Eq. 5.38 that it is impossible to have $q^2 < 0$ for this case. Therefore, all long-lived resonant states must have $m > 0$ and therefore $k_{\text{min}} > 0$. But since $\lim_{\rho \rightarrow \infty} V_{\text{eff}}(\rho) = 0$, this tells us that all allowed values of k_0^2 exceed the value of the effective potential at infinity and, therefore, tunneling through the effective potential barrier is always possible. This tunneling barrier is illustrated in Fig. 5.10. The conclusion from this analysis is that there are no truly bound states in the system, and all resonant states are quasibound with complex eigenfrequencies and finite lifetimes. We now proceed to compare this to the quantum mechanical case where truly bound states may exist.

5.3 The quantum disk

We now contrast the case of the electromagnetic disk with the case of a quantum disk [73]. For the quantum disk the potential is given by

$$V(\mathbf{r}) = \begin{cases} -V_0, & 0 \leq \rho \leq a \text{ and } |z| \leq \frac{b}{2} \\ 0, & \rho > a \text{ or } |z| > \frac{b}{2}. \end{cases} \quad (5.40)$$

Schrödinger's equation reads

$$\frac{-\hbar^2}{2m_e} \nabla^2 \psi(\mathbf{r}) + V(\mathbf{r})\psi(\mathbf{r}) = E\psi(\mathbf{r}), \quad (5.41)$$

where m_e is the mass of the quantum particle. The main difference between Eq. 5.41 and Eq. 5.34 is that k_0^2 is present on both sides of Eq. 5.34, but E only enters the right hand side of Eq. 5.41. We separate variables and assume $\Phi(\phi) = e^{im\phi}$, and $\frac{d^2 Z}{dz^2} = -\beta^2 Z$. This

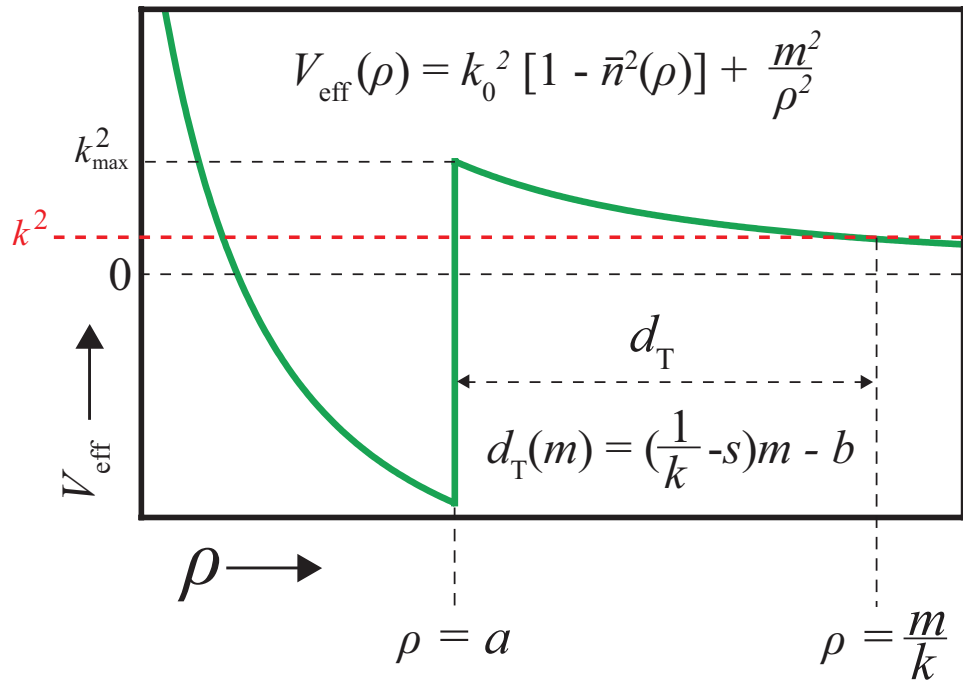


Figure 5.10: The effective potential. V_{eff} enters the radial equation for the scalar generating function (Eq. 5.34) and is responsible for optical confinement. The tunneling barrier is apparent at $\rho = a$, and the tunneling distance, d_T , is labeled.

leads to Bessel's equation for the radial field.

$$-\left(\frac{d^2}{d\rho^2}R(\rho) + \frac{1}{\rho}\frac{d}{d\rho}R(\rho)\right) + \frac{2m_e}{\hbar}V_{\text{eff}}(\rho)R(\rho) = \frac{2m_e}{\hbar}ER(\rho). \quad (5.42)$$

We make the substitution of variables $\rho \rightarrow tr$ where $t = \sqrt{\frac{\hbar^2}{2m_e}}$. We also define $\tilde{\beta} = t\beta$. As we did in the electromagnetic case, we now make the coordinate transformation $\xi = \ln(\sqrt{E}r)$ to further analyze the behavior of the effective potential. This leads to the simple harmonic oscillator equation,

$$\frac{d^2R(\xi)}{d\xi^2} + \left[\frac{(E - V + \tilde{\beta}^2)e^{2\xi}}{E} + m^2\right]R(\xi) = 0. \quad (5.43)$$

We can then identify

$$q^2 = \frac{2m_e}{\hbar^2}(E - V_{\text{eff}})\rho, \quad (5.44)$$

where the effective potential in the quantum case is given by

$$V_{\text{eff}}(\mathbf{r}) = V(\mathbf{r}) + \frac{\hbar^2}{2m_e}\left(\beta^2 + \frac{m^2}{\rho^2}\right). \quad (5.45)$$

From Eq. 5.44 one can see that resonant solutions exist when $E < V_{\text{eff}}$. In terms of the original variables,

$$q^2 = \frac{2m_e}{\hbar^2}[E - V(\mathbf{r})] - \left(\beta^2 + \frac{m^2}{\rho^2}\right), \quad (5.46)$$

and resonant states will occur when

$$E < \frac{\hbar^2}{2m_e}\left(\beta^2 + \frac{m^2}{\rho^2}\right) + V(\mathbf{r}). \quad (5.47)$$

At the lowest point the effective potential has the value $V_{\text{eff}}(a^<) = -V_0 + \frac{\hbar^2}{2m_e}\left(\beta^2 + \frac{m^2}{\rho^2}\right)$, and the height is $V_{\text{eff}}(a^>) = \frac{\hbar^2}{2m_e}\left(\beta^2 + \frac{m^2}{\rho^2}\right)$. The value of the effective potential at infinity is $\lim_{\rho \rightarrow \infty} V_{\text{eff}}(\rho) = \frac{\hbar^2 m^2}{2m_e a^2}$. States which have energies smaller than this threshold and larger than the minimum of the effective potential are truly bound states. This condition reads

$$-V_0 + \frac{\hbar^2}{2m_e}\left(\beta^2 + \frac{m^2}{\rho^2}\right) < E < \frac{\hbar^2 m^2}{2m_e a^2}. \quad (5.48)$$

The energy range thus available to bound states is $\Delta E = V_0 - \frac{\hbar^2 \beta^2}{2m_e}$. This available energy range for bound states is a critical difference of the quantum mechanical problem versus

the electromagnetic problem. Truly bound states with infinite lifetimes can exist in the quantum disk, whereas only quasibound states can exist in the electromagnetic disk. In Section 5.4 we will discuss the lifetime of electromagnetic microdisk states. First, we close the discussion of the quantum disk.

We can complete the analysis of the quantum disk by writing the solutions in the three regions of space and applying boundary conditions. Boundary conditions at the top and bottom of the disk lead to the quantization condition

$$\tan\left(\frac{\beta_I h}{2} + \nu\right) = -i \frac{\sqrt{\frac{2m_e V_0}{h} + \beta_I^2}}{\beta_I}. \quad (5.49)$$

Boundary conditions at $\rho = a$ lead to the quantization condition

$$\frac{\frac{d}{d\rho} J_m(\sqrt{\frac{2m_e}{\hbar^2}(E - \tilde{V}_I)\rho})|_{\rho=a}}{J_m(\sqrt{\frac{2m_e}{\hbar^2}(E - \tilde{V}_I)a})} = \frac{\frac{d}{d\rho} h_m^{(1)}(\sqrt{\frac{2m_e}{\hbar^2}(E - \tilde{V}_{III})\rho})|_{\rho=a}}{h_m^{(1)}(\sqrt{\frac{2m_e}{\hbar^2}(E - \tilde{V}_{III})a})} \quad (5.50)$$

The problem is essentially solved. We find the roots of Eq. 5.49 to obtain β_I . Both β_{II} and β_{III} are known in terms of β_I as are \tilde{V}_{II} and \tilde{V}_{III} . We can then use the value of \tilde{V}_I in Eq. 5.50. Those values of E for which Eq. 5.50 holds are the eigenenergies of the potential.

The important point here is that Eq. 5.49 and Eq. 5.50 are decoupled. This is in contrast the electromagnetic disk case where Eqs. 5.32 and 5.33 are coupled, making a more difficult self-consistent solution necessary.

It would be interesting to analyze the spectrum of Eqs. 5.49 and 5.50 and compare it to Eqs. 5.32 and 5.33, but such a discussion would lead us too far from the relevant discussion at hand. We now proceed to discuss the lifetime of electromagnetic microdisk states as quantified by the quality factor, Q .

5.4 Cavity Q , photon lifetime, photon path length and resonance spectral shape

As discussed in section 5.2.7, all resonant modes of an optical microdisk have complex eigenfrequencies and finite lifetimes. We can therefore write the time dependence as

$$\mathbf{E}(t) \propto e^{i\omega t} = e^{i\omega_r t} e^{-\omega_i t} \equiv e^{i\omega_0 t} e^{-\omega_0 t/2Q} \equiv e^{i\omega_0 t} e^{-t/\tau}. \quad (5.51)$$

The lifetime of a photon in the cavity related to the cavity quality factor, Q , and the imaginary part of the complex frequency by

$$\tau = \frac{2Q}{\omega_0} = \frac{1}{\omega_i}. \quad (5.52)$$

From the definition of Q (Eq. 5.51) we can extract the relationship between Q and ω .

$$Q = \frac{\omega_r}{2\omega_i}. \quad (5.53)$$

The photon path length is simply the speed of light in the medium multiplied by the photon lifetime.

$$\zeta = \frac{c\tau}{n} = \frac{2Qc}{n\omega_0}. \quad (5.54)$$

Equation 5.54 reveals that increasing the cavity Q is analogous to increasing the path length through which the electromagnetic field interacts with the medium. This has important consequences for interactions between quantum emitters and cavity modes [78] as well as for nonlinear optical phenomena [79].

In general, the Q factor of a cavity will have several contributions:

$$Q_{\text{Tot}}^{-1} = \sum_k Q_k^{-1}, \quad (5.55)$$

where Q_k may be the contribution to photon decay from intrinsic radiation loss, as discussed in section 5.2.7, or from surface scattering, material absorption, parasitic coupling to a waveguide, etc.

As will be discussed in Chapter 6, we will measure the resonances of silicon microdisks by studying the transmission through a waveguide coupled to the microdisk cavity. Resonances will be identified as dips in the transmission spectrum corresponding to wavelengths at which tunneling from the waveguide into the microdisk is most probable. We therefore seek an expression relating features of the transmission dips to the cavity Q . The effect of the finite lifetime on the resonance lineshape can be determined by taking the fourier transform of Eq. 5.51.

$$\tilde{E}(\omega) = \frac{E_0}{\pi} \int_0^\infty e^{i\omega_0 t - \frac{\omega_0 t}{2Q}} e^{-i\omega t} dt. \quad (5.56)$$

The integral in Eq. 5.56 gives a Lorentzian lineshape:

$$\text{Re}[\tilde{E}(\omega)] = \frac{E_0}{\pi} \frac{\frac{\omega_0}{2Q}}{(\omega - \omega_0)^2 + (\frac{\omega_0}{2Q})^2}. \quad (5.57)$$

Where we have substituted the half width at half maximum, $\gamma = \frac{\omega_0}{2Q}$. Defining the quantity $\Delta\omega = 2\gamma$ as the full width at half maximum, and using Eq. 5.53 with the defition of γ we obtain

$$Q = \frac{\omega_0}{\Delta\omega}. \quad (5.58)$$

This result informs us that the Q factor of a resonance can be obtained by dividing the center frequency of a resonance by the full width at half maximum. Our measurements will more readily give us data in terms of wavelength. We know that $\omega_0 = \frac{2\pi c}{\lambda_0}$, so $\Delta\omega = -\frac{2\pi c}{\lambda_0^2} \Delta\lambda$. Therefore,

$$Q = \frac{\lambda_0}{\Delta\lambda}. \quad (5.59)$$

When taking data with tapered fiber spectroscopy, as discussed in Chapter 6, we will identify cavity resonant modes by Lorentzian dips in the fiber transmission spectra. A quick estimate for the Q of a resonance can be obtained using Eq. 5.59. A more precise value for the measured Q factor of a resonance can be obtained by fitting data to Eq. 5.57 using nonlinear regression. The method for measuring resonances in microdisks and obtaining the cavity Q from the data is discussed further in Chapter 6.

Chapter 6

Tapered fiber spectroscopy

To experimentally characterize a microdisk one would like to obtain resonant wavelengths and the Q factors of the corresponding resonances. It would also be ideal to obtain field profiles. Because we are interested in materials with purely real indices of refraction (namely Si, $n=3.48$), we are limited to materials that do not generate light. Therefore, our experimental technique must also inject light into the cavity. An experimental technique which is highly accommodating of these requirements is tapered fiber spectroscopy (TFS) [80–82]. TFS has gained popularity in recent years most notably due to the work of Vahala and Painter at Caltech, but the technique traces its roots back to the 1950s [83]. Several papers in the early 1990s developed the technique and addressed basic questions about the shape and optical properties of the tapered fiber waveguides [84–86]. The fundamental limits of tapered fibers have been explored in recent years by Sumetsky and others [87–90]. Also, tapered fibers have begun to be used in more fundamental atomic and optical physics experiments [91–94]. While TFS does not provide us with field profiles, it does provide a means to couple light into the cavity and to identify wavelengths of all cavity modes and the corresponding Q factors. Once the mode spectrum has been obtained with this technique, the quantum numbers of each identified mode are found by comparison with theoretical calculations. From these, the field profiles can be obtained and the system is considered solved. It should be noted that a similar, alternative method is to utilize on-chip waveguides. The strength of TFS over on-chip waveguides is that the tapered fiber waveguide can be moved

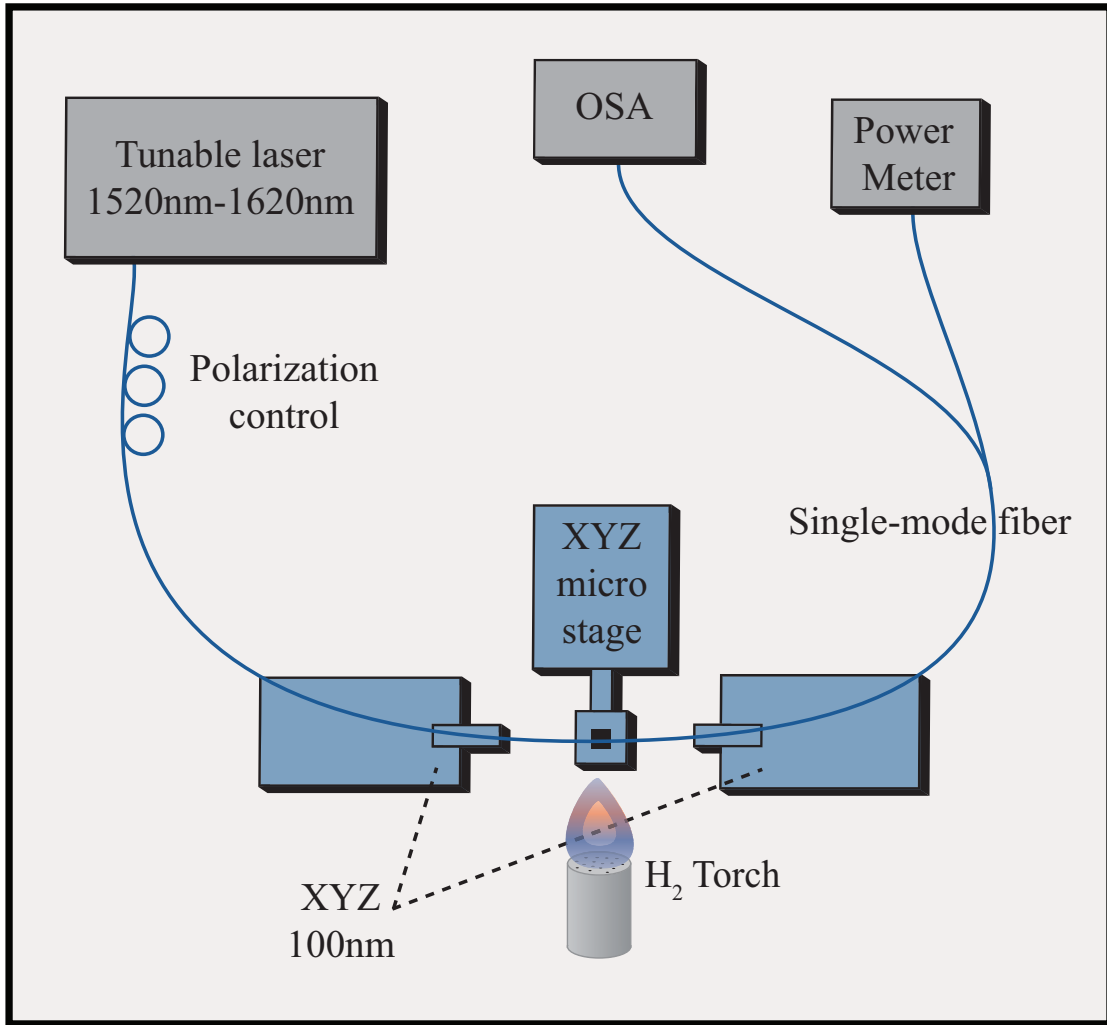


Figure 6.1: Schematic of the tapered-fiber pulling and spectroscopy apparatus. An optical microscope (not shown) is located above the sample. In pulling mode, the fiber is mounted suspended between the two opposing $x-y-z$ stages. The stages are used to move the fiber into the flame. They are then pulled apart as the fiber is heated. Once the fiber is pulled, the H₂ torch is removed from the vicinity, and the stages are used to move the fiber into the near field of the microcavity under the microscope. The tunable laser is then injected into the fiber. The transmission as a function of wavelength can be monitored on the optical spectrum analyzer (OSA), or the net power through the fiber can be monitored on the power meter.

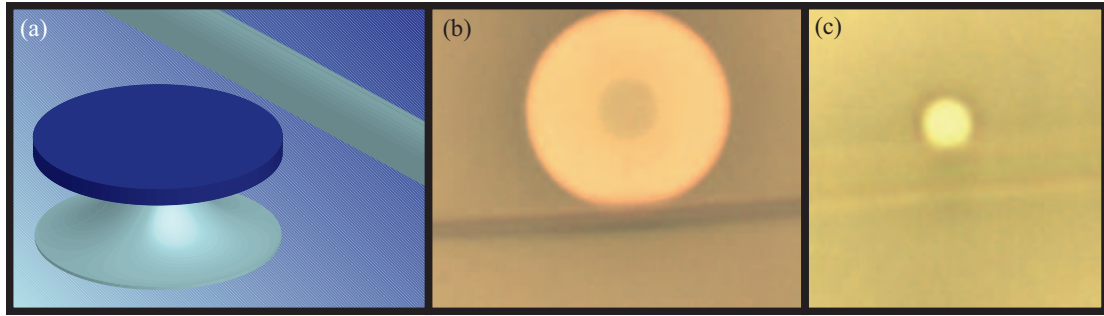


Figure 6.2: Taking data with a tapered fiber. (a) Schematic of a tapered fiber near a Si microdisk. (b) Image taken from above through the 100x objective of the optical microscope. The diameter of the disk is $10\mu\text{m}$, and the fiber is $\sim 2\mu\text{m}$. (c) Image of a subwavelength Si microdisk with $1.35\mu\text{m}$ diameter.

to vary the coupling to the optical modes. Also, a single cavity can be probed with several tapered fibers or different sections of a single fiber to vary the coupling to modes of different polarizations.

At the outset of our research on Si microdisks no one in our lab had previously explored this system. To determine the best experimental technique for the job, we consulted the literature. The groups setting the bar for microdisk research were using TFS. In particular, the labs of Vahala and Painter are leaders in the field of microcavity research, and they use tapered fiber spectroscopy exclusively for their experiments. Several of Dr. Painter's graduate students have described their experimental method and apparatus in detail [72, 95–98], and based on their accounts we were able to bring that technology to our lab.

The essence of the experimental technique is that an optical fiber waveguide is adiabatically drawn to a thin ($\sim 2\mu\text{m}$) waist with an evanescent tail extending beyond the thin fiber into the surrounding space. This tapered optical fiber then functions as a portable waveguide, and transmission spectra through the fiber reveal features of the near field environment of the fiber. When the evanescent field of the tapered fiber is placed in the near field of a microdisk, the optical fiber mode couples to the resonant cavity modes of the disk. The transmission through the fiber is monitored as a function of wavelength as a tun-

able laser injected into the fiber is swept across a portion of the electromagnetic spectrum, in our case the 1520-1620nm region of the telecom band. Lorentzian dips observed in the transmission spectra correspond to cavity resonances. A resonant wavelength is ascertained from the center wavelength of a dip, and the Q factor of that resonance is obtained as the center wavelength divided by the full width at half maximum (as discussed in Section 5.4), and is found by numerically fitting the data points to a Lorentzian function. A schematic of the experimental setup is shown in Fig. 6.1.

6.1 The craft of pulling tapered fibers

Like many experimental techniques, TFS is as much an art as a science. One begins with a length of standard SM-128 optical fiber. The protective polymer coating is stripped away to expose ~ 2 cm of the $125\mu\text{m}$ glass fiber. This section is cleaned with methanol and is mounted, suspended on two opposing mechanical stages. A hydrogen torch equipped with a hush tip is utilized to create a hot, clean, gentle flame capable of bringing the optical fiber to its melting point. Because the tapered fiber is ultimately an optical device, it is very sensitive to contamination. It is for this reason that we use the clean-burning hydrogen torch with only water as a byproduct rather than another type of hot flame such as butane that may coat the taper with undesired combustion products. The objective is to create a $1\text{-}2\mu\text{m}$ filament—a very fragile thread of glass—so action of the hush tip to slow the flow of hydrogen before combustion is critical. Also, no oxygen is injected into the gas line, and the oxygen necessary for combustion is obtained from the ambient environment immediately surrounding the hush tip. This adaptation to a standard hydrogen torch design commonly utilized for welding further decreases the force of the flame to enable fabrication of fragile tapers. The fiber is placed directly in the outer shell of the flame. Because the combustion reaction draws oxygen from the environment, this outer shell is the hottest region of the flame [97]. The mechanical stages holding the fiber are pulled apart at a constant velocity, and the optical power transmitted through the fiber is monitored on an optical power meter.

Our experiments have found that moving the stages directly apart at $250\mu\text{m/s}$ ($-500\mu\text{m/s}$ relative velocity) gives optimal results. Monitoring the power is critical as it reveals the progress of the taper as it is drawn. As is described in Ref. [97], the transmitted power in the fiber oscillates as a function of time, presumably as the the core is thinned and coupling to lossy, cladding modes becomes possible. Ultimately the fiber becomes thin enough that there is no cladding, and only the fundamental guided mode is present. At this point the the transmitted power becomes constant as a function of time, and the fiber pulling is complete. In our experiments a timer is set for 45s. It is unlikely that a fiber will reach a thin enough waist before this. After this, pulling is terminated based on the information received from the power meter. When the transmitted power settles to a constant, the flame is extinguished and the stages are halted. In an industrial or more specialized setting it could be possible to achieve much more reproduceable results, but in our case the size of the flame and the length of fiber placed within the flame experience minor variations from run to run. For these reasons it can be quite difficult to obtain identical fibers from one run to the next. An ideal tapered fiber should have a transmission spectrum almost identical to the spectrum of the fiber before pulling except with a net loss in the overall transmission. It is often the case that fiber pulling is executed and the transmission through the fiber is plagued by spurious oscillations. When this occurs the fiber is abandoned and the process is repeated. For these reasons pulling a tapered fiber can be a tedious undertaking, but it is worth the effort because once equipped with a good fiber the acquisition of data from a number of samples can be achieved rapidly. A schematic of tapered-fiber coupling to a microdisk and microscope images of tapered fibers near large and small microdisks are shown in Fig. 6.2.

In the tapered-fiber-pulling apparatuses in most labs, once the tapered fiber has been pulled, it is removed from the mounts and repositioned on a different stage. Our lab does not employ this approach. The stages used to pull the fiber each have full $x - y - z$ motion control with 100nm resolution. Once the fiber taper has been pulled it is then moved to the focal point of the microscope where the sample is positioned without being removed from the mounts in which it was pulled. Our technique of using the same $x - y - z$ stages to

do the pulling and positioning has strengths and weaknesses. The strengths are that once the fiber is pulled, it requires minimal handling. Handling of a thin fiber taper can lead to damage or breaking of the fiber. Also, with the fiber suspended between two stages, the angle of the fiber relative to the sample can be controlled, and the tension in the fiber can be easily adjusted. The weakness of our approach is that more stages are required for the pulling. We employ this technique not because we are convinced of its superiority, but because our lab already had two opposing $x - y - z$ stages under a microscope for coupling light from lensed fibers into on-chip waveguides. In an effort to utilize as much of the existing equipment as possible without dissociating the existing functionality, we learned to pull and position tapered fibers with the two opposing $x - y - z$ stages.

In our experimental apparatus, the microscope is fixed. The sample and fiber must be moved to its focal point. The sample is mounted on a manual $x - y - z$ motion stage with $\sim 1\text{cm}$ range of motion. The fiber is suspended between two computer-controlled $x - y - z$ stages with 100nm resolution, 10cm range of motion in the plane of the table, and 3cm range of motion perpendicular to the table. These two stages can be moved in unison or separately. The microscope objective and sample stage are contained within a plexiglass box; when the fiber is positioned near the focal point of the objective, the front of the box can be put in place, and the box can be sealed. A tapered fiber exposed to ambient room conditions will degrade over the course of several days. The transmission loss will increase and the fiber will become fragile. When sealed in the plexiglass box with a dessicant and purged with nitrogen, the fiber decays much more slowly, sometimes lasting several weeks to a month.

Once the sample and fiber are both positioned within the field of view of the microscope objective (100X, N.A.=0.8, W.D.=3.5cm), one is prepared to take data.

6.2 Taking data with tapered fibers

The information contained in a tapered fiber transmission spectrum depends on the coupling between the fiber waveguide and the adjacent optical microcavity [80–82]. In general, the coupling to a given cavity mode, $\kappa_{m,n}$, depends on the overlap of the fiber mode with the mode of the cavity in both configuration and momentum space:

$$\kappa_{m,n} \propto \int \psi_f(\mathbf{r}, \mathbf{k}) \psi_c(\mathbf{r}, \mathbf{k}) d^3r d^3k. \quad (6.1)$$

Equation 6.1 has important consequences for TFS and for characterizing microcavities. First, it tells us that the information contained in a spectrum will depend on the position of the fiber relative to the cavity. While intuitive, this is critical to keep in mind when acquiring data. To obtain as much information as possible about a given cavity, it is necessary to take several spectra with the fiber at different positions. While some report the maximum in the coupling between fiber and cavity as a function of position occurring several hundred nanometers away from the cavity perimeter, my experience has been that the coupling (measured as the depth of a dip in the transmission spectrum) continues to improve as the fiber approaches the cavity until the fiber touches the cavity. In general, one wishes to avoid touching the cavity with the fiber as doing so perturbs the modes and can physically damage the cavity. Additionally, the closer one brings the fiber to the cavity the better the coupling will be, but the more perturbed the intrinsic modes of the cavity will be by the presence of the fiber. This can result in shifting of the resonant wavelengths of the modes and loading of the cavity Q factors. Therefore, to obtain values as close as possible to the intrinsic values of the resonant wavelengths and cavity Q s it is often fruitful to begin with the fiber close to the cavity and take a spectrum with strong coupling. The fiber can then be moved away in small steps (in our setup the smallest possible step is 100nm), and additional spectra can be taken at each step. This is a method of obtaining convergence toward the intrinsic values.

The second important consequence of Eq. 6.1 is that in addition to spatial overlap of the fiber field with the cavity field, momentum space overlap is also critical. The propagation

constant of the tapered fiber depends on the thickness of the fiber, and the propagation constant of the modes of the disk depend significantly on the mode order. Also, the effective index for the two polarizations is quite different. This dramatically affects the propagation constants of the two polarizations and therefore coupling to the fiber.

An intuitive way of understanding this overlap integral is that the wave fronts in the fiber must be equally-spaced with the wave fronts of propagation around the perimeter of the disk. In the disk this is determined by the azimuthal mode order. With the 100nm wavelength range of our tunable laser, the TE_1 mode family will have $m \sim 50$, TE_2 will have $m \sim 45$, and TE_3 will have $m \sim 40$ in a $10\mu\text{m}$ -diameter disk. The TM_1 —due to the smaller effective index of refraction—will have $m \sim 32$, and TM_2 modes will have $m \sim 28$. Therefore, the coupling of the fiber to various modes will not be constant. Since the propagation constant of the fiber depends significantly on the fiber diameter, each new fiber will have different coupling to different modes, and since the fiber tapers adiabatically along its length, different sections of the same fiber can have different coupling efficiencies to different modes. All of these factors must be considered when interpreting TFS data.

An example tapered-fiber spectrum from a $10\mu\text{m}$ -diameter Si microdisk is shown in Fig. 6.3. In this spectrum we see a rich array of resonances with varying quality factors and differing depths of coupling to the tapered fiber probe. Upon first inspection of such a spectrum with so many overlapping modes it can be quite difficult to determine the polarization and quantum numbers of each mode. In our experience the best way to determine which modes belong to which mode families is to produce a plot of the spectrum and then import that plot into a drawing program. If the x axis of the plot is scaled so that the 100 nm range of the tunable laser equals 100 of the chosen units in the drawing program, one can draw lines connecting resonances with similar coupling and begin to identify families of modes with well-defined FSRs. This analysis was conducted on the spectrum in Fig. 6.3, and the identified mode families are color-coded in Figs. 6.4 and 6.5. The FSRs of the two polarizations are quite different, and within a polarization the FSR of a given mode family is different from the other mode families of that polarization. Additionally, higher-radial-

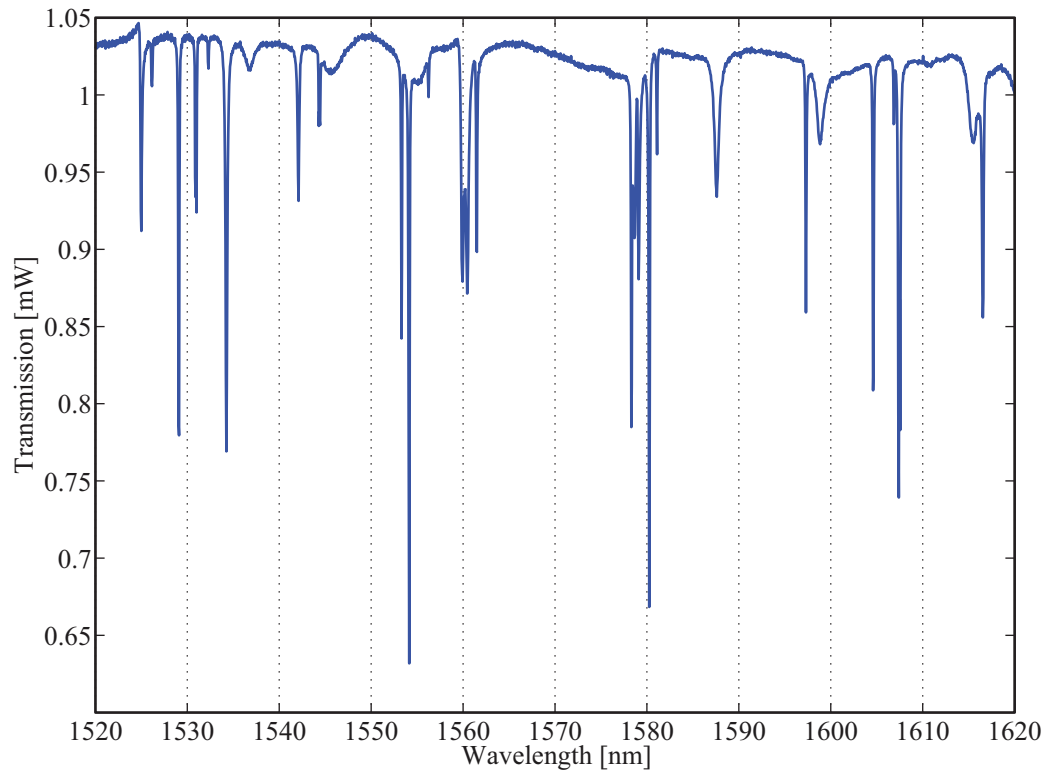


Figure 6.3: Tapered-fiber spectrum of a $10\mu\text{m}$ diameter disk. Many modes with varying Q factors and different depths of coupling to the fiber are present.

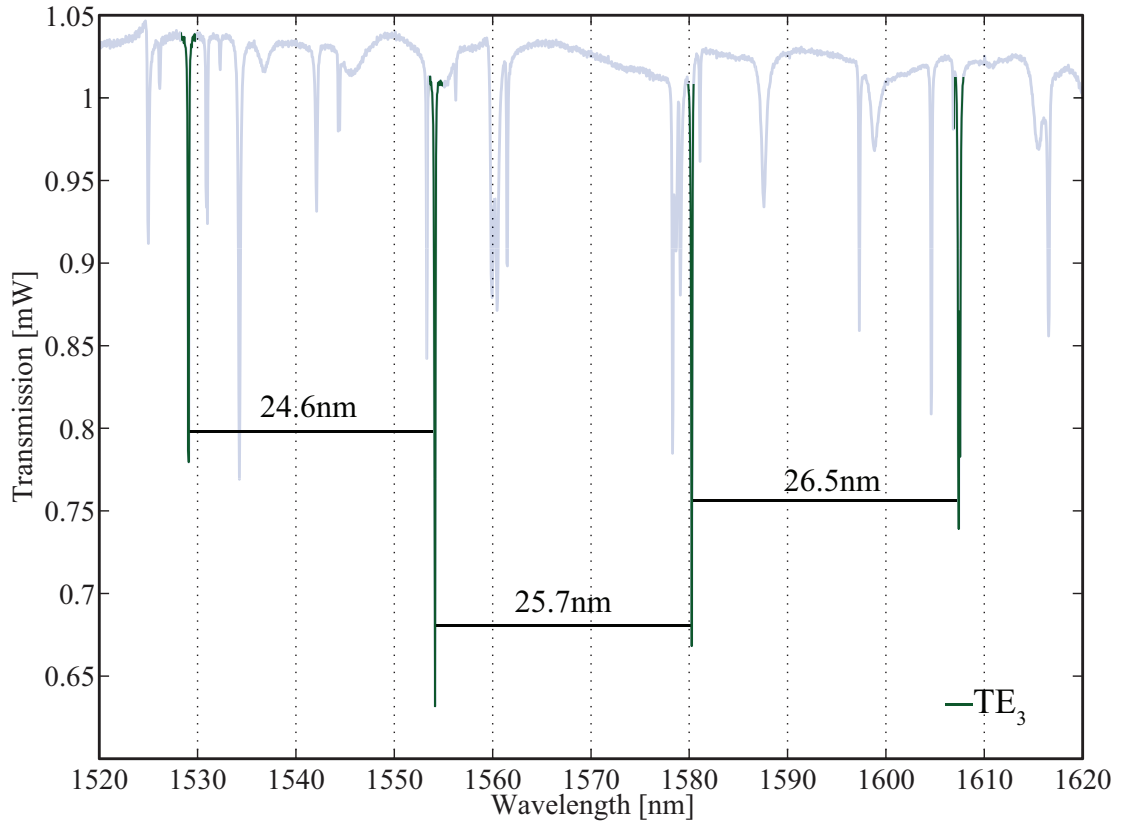


Figure 6.4: Identifying mode families in the tapered-fiber spectrum. The most prominent mode family, TE_3 , is highlighted, and the wavelength spacing is labeled. In addition to the wavelength spacing, the similarity in depth of coupling helps us identify the group of resonances as a mode family.

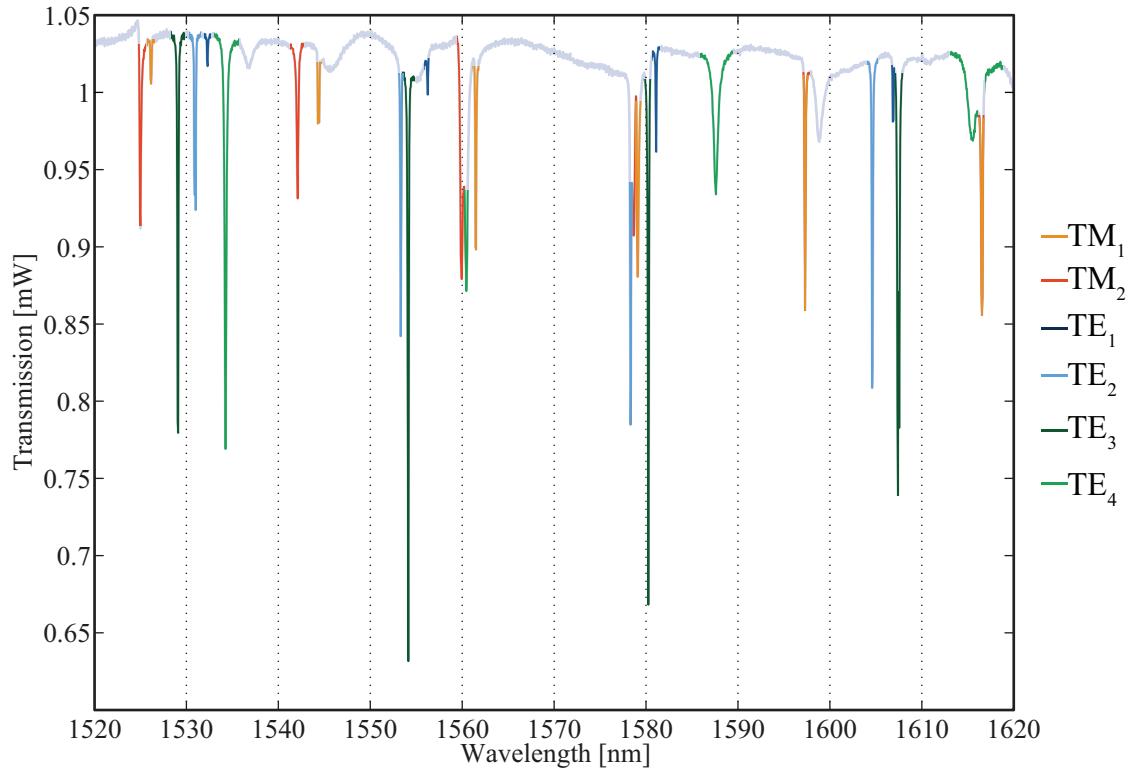


Figure 6.5: Identifying mode families in the tapered-fiber spectrum. By analyzing FSRs and depth of coupling we can make educated guesses to identify six mode families. They are color-coded.

order modes have better coupling to tapered fibers and therefore appear as deeper dips in the transmission spectrum. All of these trends taken together enable us to make educated guesses which allow us to get from Fig. 6.3 to Fig. 6.5. For a more clear presentation of the isolated mode families, in Fig. 6.6 we have highlighted each mode family on a separate plot. By comparing Figs. 6.3-6.6 one can see how all of the modes add together to form the complicated spectrum of a $10\mu\text{m}$ Si microdisk.

While this discussion helps us understand how to interpret a full 100 nm tunable laser scan, it is also often useful to inspect single resonances with higher resolution. In Fig. 6.7 we show a high-resolution scan of a single microdisk resonance. This resonance has an extremely high quality factor, and is actually split into what is referred to as a doublet. This doublet character has its origin in the scattering of the mode from sidewall imperfections, and has long been argued to be the result of degeneracy breaking between clockwise and counterclockwise propagating modes [99]. However, a recent paper argues that this is the incorrect interpretation of the physics [100]. In Fig. 6.7 we show a 1 nm TFS scan with an SEM image of a disk similar to that from which the spectrum was obtained. In the bottom panel we show a narrower region of the spectrum and the curve which results from fitting the spectrum to the sum of two Lorentzians. The extracted quality factors are over 500,000 and 700,000. To obtain quality factors this high, resist reflow was utilized. This and other fabrication techniques will be discussed next in Chapter 7. After Chapter 7 we will proceed to discuss how we have used TFS to measure the smallest silicon microdisks to date as well as silicon microdisks with broadly-tunable resonance spectra.

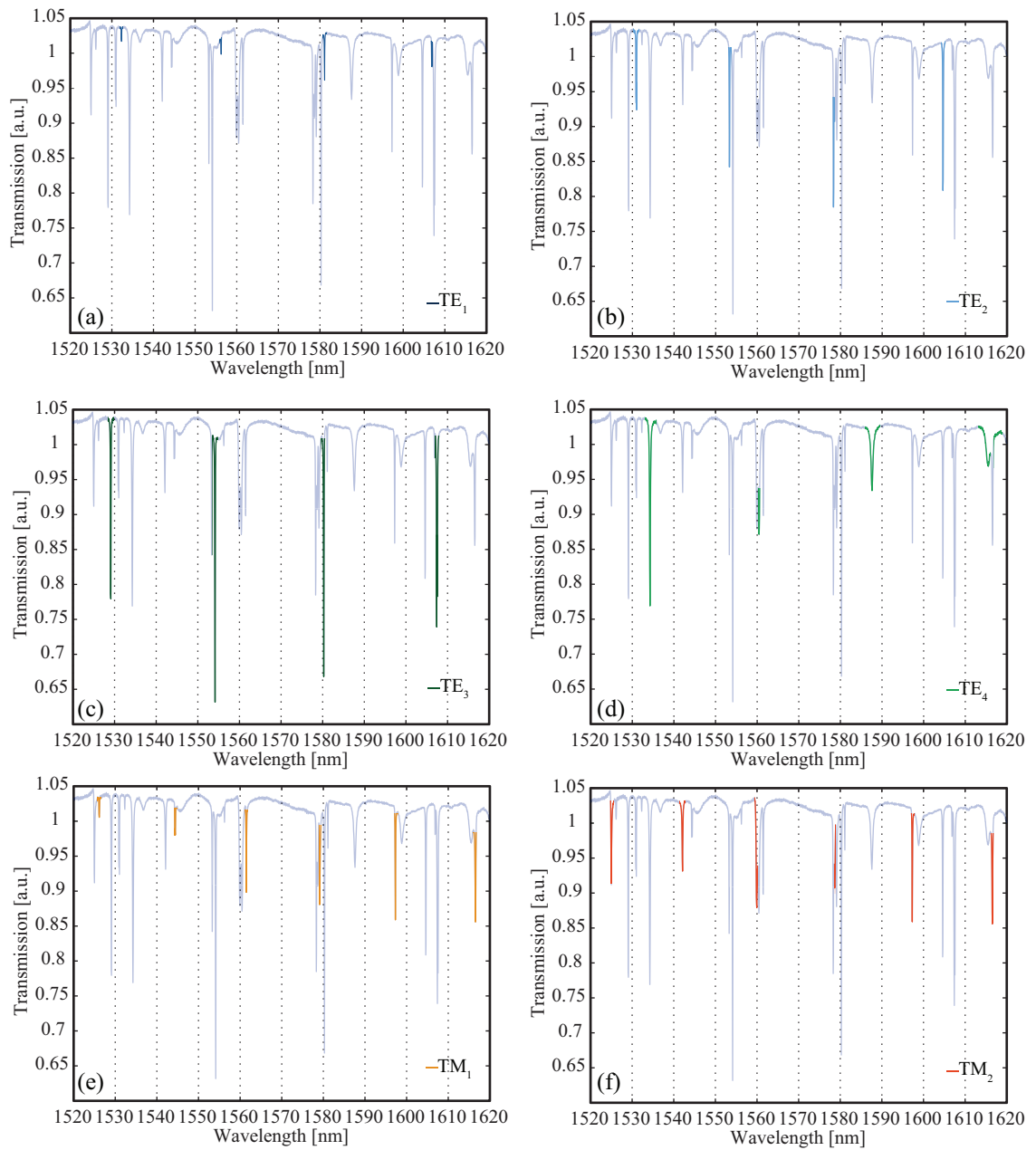


Figure 6.6: The same tapered-fiber spectrum as in Figs. 6.3-6.5. Here we highlight each mode family separately.

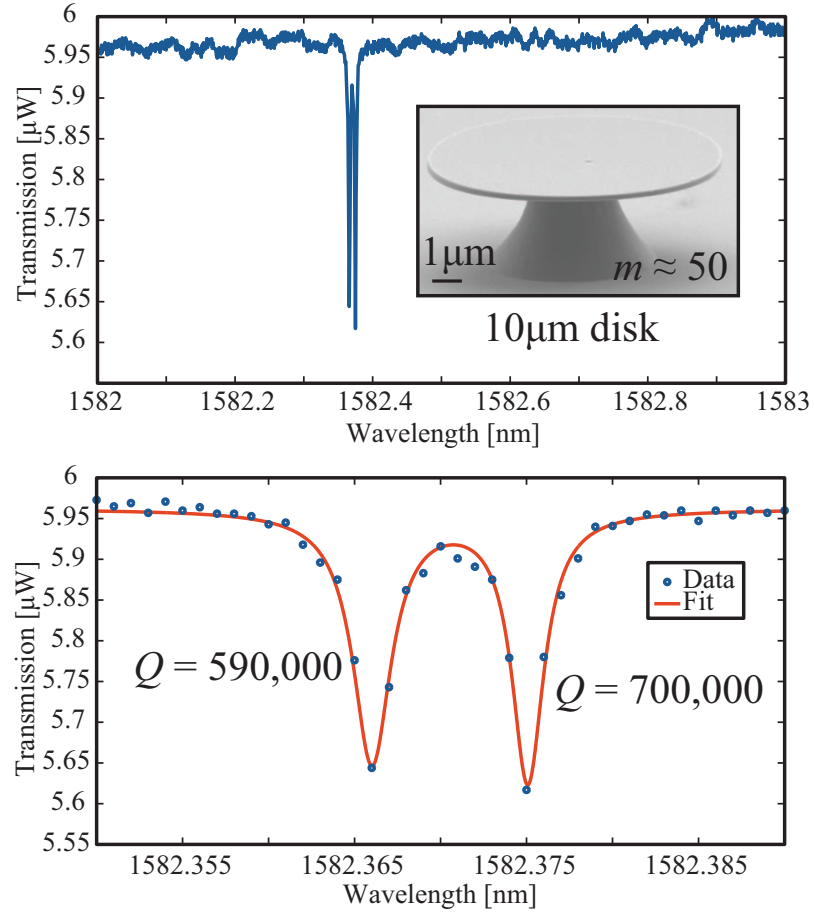


Figure 6.7: A high-resolution tapered-fiber spectrum of a high- Q mode in a Si microdisk. (a) A 1nm wavelength window shows the resonance of interest. An SEM image depicts the Si microdisk. (b) The data from (a) fit to a Lorentzian. The extracted Q factors are 590,000 and 700,000 for the two modes of the doublet.

Chapter 7

Fabrication of silicon microdisks

The technique of fabricating high- Q Si microdisks was developed quite extensively in Oskar Painter's lab at Caltech. Just as in the case of TFS, the accounts of his graduate students [72, 95–98] were sufficient to enable our lab to successfully complete the process.

A schematic of the process of fabricating Si microdisks is shown in Fig. 7.1. The process begins with an SOI wafer with a 250nm device layer atop a $3\mu\text{m}$ buried oxide layer. In step two of the microdisk fabrication process an electron beam resist is spin coated on top of the wafer. The choice of electron beam resist depends on the pattern being produced and whether the electron beam resist will be used as an etch mask or as a mask for metal deposition and lift off. In our case we always used the electron beam resist as an etch mask. In our work we have used two electron beam resists. For single isolated microdisks PMMA (MicroChem) in the positive tone is a good choice. In electron beam lithography positive tone means that the regions where the electron gun exposes the resist will be removed in the chemical developer. Utilizing PMMA in the positive tone to fabricate microdisks necessitates exposing a large region surrounding the disk and not exposing the small circle in the middle that will serve as the etch mask. PMMA can also be used as a negative electron beam resist when exposed at extremely high dosages [101]. In negative electron beam lithography the region where the electron gun exposes the resist remains after chemical development. For certain patterns it is more convenient to utilize a negative electron beam resist. As an alternative to PMMA for negative electron beam

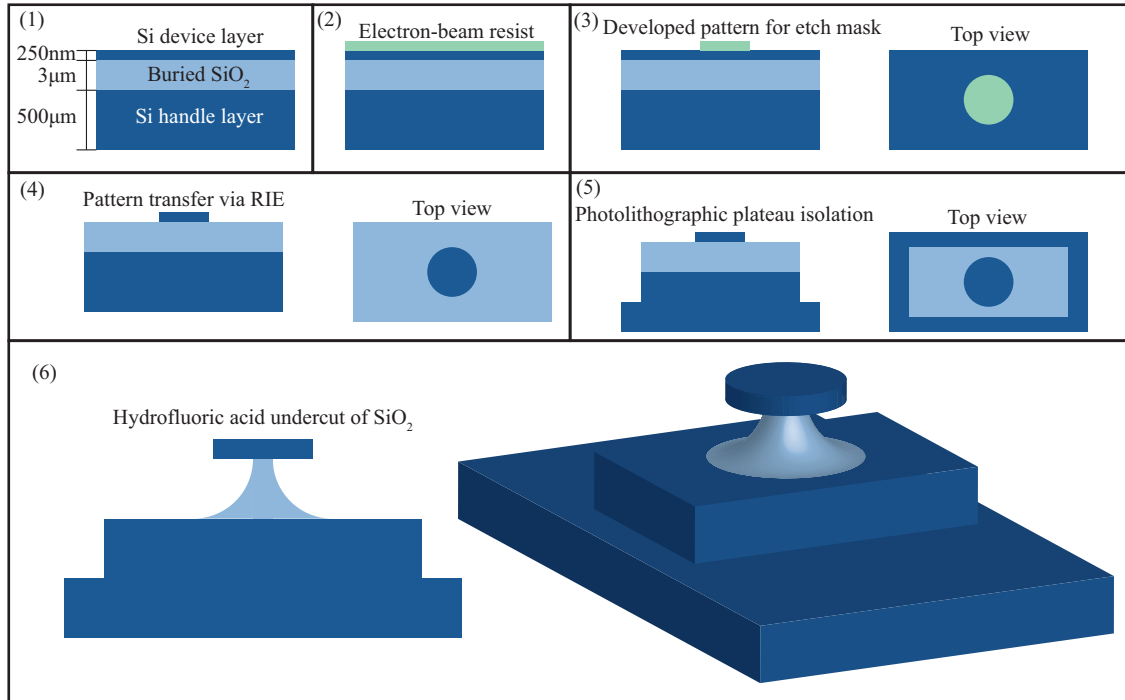


Figure 7.1: Schematic of the Si microdisk fabrication process. (1) We begin with pristine SOI. (2) Electron-beam resist is spin coated on the chip and the pattern is written with electron-beam lithography. (3) The written pattern is developed, leaving the disk etch mask. (4) The pattern is transferred to the Si device layer using RIE. (5) The devices are isolated on a plateau for tapered-fiber access. (6) Undercut with HF is performed to optically isolate the disk.

lithography, the resist XR-1541 (Dow Corning), which is a spin-on glass, works quite well at much lower dosages. In our work we have utilized PMMA as a negative and a positive resist as well as XR-1541 as a negative resist depending upon what is most suitable for the device being fabricated.

In step three of the microdisk fabrication process the electron beam resist is developed leaving only the patterned area to be used as an etch mask. In step four the pattern is transferred to the Si device layer using reactive ion etching (RIE). This RIE etch step can be performed with a number of gases and etching conditions. In our work we used a combination of C_4F_8 and SF_6 gases in what has become quite a standard inductively-coupled plasma RIE process (130sccm SF_6 , 80sccm C_4F_8 , 1200W RF power, 20mTorr).

After having transferred the pattern to the Si device layer we then perform a photolithographic step followed by a deep RIE to isolate the microdisk devices on a plateau. The purpose of this step is to lift the microdisks above the rest of the Si wafer so that when the tapered fiber is brought close to the substrate for measurement of the spectrum of a microdisk, imperfect alignment of the tapered fiber relative to the plane of the wafer will not result in crashing the fiber into the edge of the Si chip. This deep RIE step will etch $\sim 40\mu\text{m}$ first into the SiO_2 layer and then into the Si handle wafer. To etch this deep one needs a thick photo resist layer, and for this purpose we use two layers of S1822 resist. This results in $\sim 4.5\mu\text{m}$ of photoresist. We then use one RIE recipe to etch through the oxide layer and then a Bosch process to etch deep into the Si handle wafer. An SEM image of several microdisks isolated on a plateau is shown in Fig. 7.2.

After the two lithography and etching steps the samples are thoroughly cleaned by sonicating in acetone, rinsing with isopropyl alcohol, rinsing with deionized water and, finally, 15 minutes in a piranha etch solution (1:3 $H_2SO_4:H_2O_2$). After the cleaning, the samples are placed in a buffered hydrofluoric acid solution to undercut the microdisks. This step has two purposes. First, it further lifts the disks above the plane of the wafer to facilitate access with a tapered fiber. Second, it produces a structure of high-index Si where the optical mode volume is surrounded on all sides by air with index of refraction equal

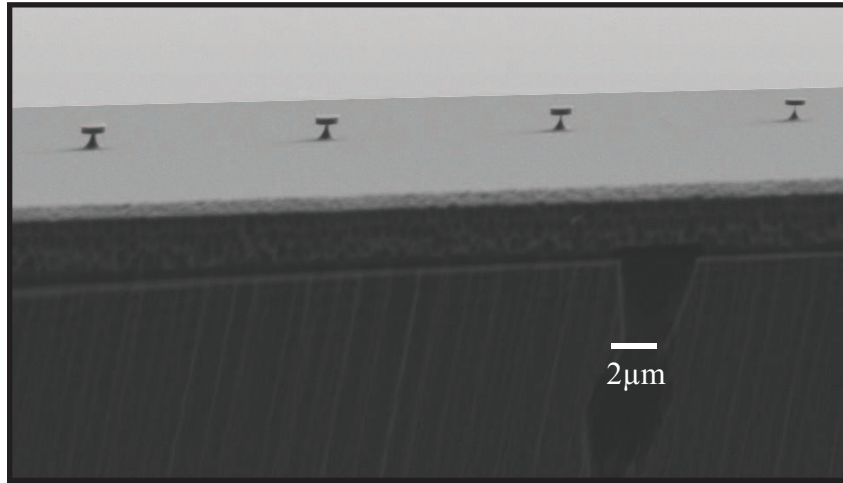


Figure 7.2: Several wavelength-scale Si microdisks isolated on a ridge. The disks have slightly different diameters, so the undercut results in pedestals of differing widths.

to unity. This leads to greater optical confinement within the microdisk, and is especially critical in ultrasmall microdisks such as those discussed in Chapter 8.

In Fig. 7.3 we show SEM images of several Si microdisks. In Fig. 7.3(a) we show a typical Si microdisk of $10\mu\text{m}$ diameter after complete fabrication and undercut has been performed. In Fig. 7.3(b) we show a much smaller microdisk. In this case the diameter of the microdisk is $\sim 2\mu\text{m}$, which is comparable to the wavelength of resonances we are considering.

In the fabrication process the most common flaw which occurs is that the sidewalls of the Si microdisks are not perfectly smooth. This is because the electron beam patterning of the electron beam resist does not lead to a perfectly smooth mask for RIE. The roughness in the etch mask will then be transferred to the Si device layer. The resulting roughness in the sidewalls of the Si microdisks degrades the Q factors of the cavities. If one wishes to have the smoothest sidewalls possible a resist reflow step can be employed prior to etching the silicon device layer (between steps 3 and 4 in Fig. 7.1). To achieve a resist reflow one heats the resist near its melting point after developing. This causes the resist mask to become nearly liquid and begin to flow. At this point surface tension determines the

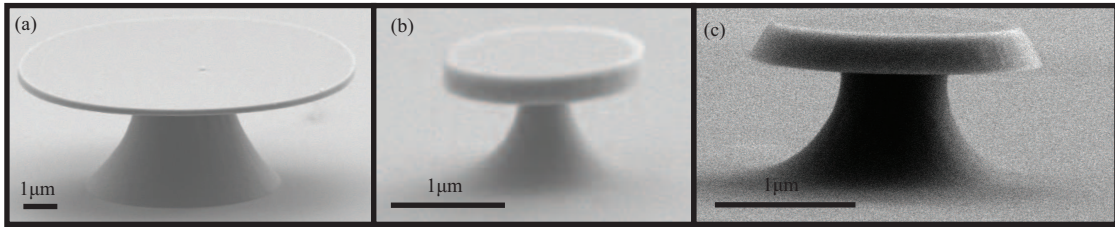


Figure 7.3: Close-up SEM images of three completed microdisks. (a) A large microdisk of $10\mu\text{m}$ diameter. Because the radius of this cavity is more than $3\mu\text{m}$ (the thickness of the buried oxide layer) the HF undercut can remove the entire buried oxide layer—with the exception of the pedestal—without lifting off the microdisk (b) A wavelength-scale cavity. (c) A cavity in which resist reflow was utilized to smooth the sidewalls. The departure from sidewall verticality is apparent.

shape of the perimeter and as such the etch mask can become much more smooth than it would be simply after chemical development. When this resist reflow is employed the sidewall of the microdisk loses its verticality. An example of this is shown in Fig. 7.3(c). If one seeks microdisks with extremely high Q factors, it may be necessary to utilize discs with larger diameters (such as that in Fig. 7.3(a)) and to employ a resist reflow step to achieve maximally smooth sidewalls. This limits the Rayleigh scattering which can degrade cavity Q factors [72, 95]. However, if one seeks to make disks as small as possible while maintaining Q factors as large as possible it is more advantageous to maintain sidewall verticality as the angled sidewalls can contribute to radiation loss.

Having described the process by which Si microdisks are fabricated, we are now in a position to discuss several of the frontiers we have explored in our research on Si microdisks. Next, in Chapter 8, we discuss our explorations of the smallest Si of microcavities studied to date and present our evidence for why these are the smallest Si microcavities with useful optical properties. Then, in Chapter 9, we discuss a device we have created to enable dynamic tuning of the spectra of Si microdisks.

Chapter 8

Subwavelength silicon microdisks

8.1 The context for wavelength-scale photonic components

Planar lightwave circuits face the challenge of entering a market dominated by electronics whose progress has been driven by Moore's law and the ability to fabricate consistently smaller transistors. For photonic circuits, a physical size constraint emerges; the characteristic limiting size is the wavelength of light traversing the circuit. To overcome this physical limitation a great deal of research has recently been conducted to explore the potential of structures at and below this size limit to store and generate light. Beginning with the original demonstration of wavelength-scale microdisk lasers [68–70], more recent demonstrations have shown that structures smaller than the wavelength of light in all three spatial dimensions can give rise to laser action at cryogenic temperatures [64, 65, 102]. Previous experimental studies of passive resonant cavities have explored ring resonators with diameters of approximately twice the free-space wavelength [103], but thorough comparison between theory and experiment has not yet been conducted for cavities smaller than the wavelength. Here we present a study of such subwavelength cavities using tapered optical fibers as the experimental probe. While photonic crystal cavities with mode volumes smaller than the wavelength have been probed with tapered fiber spectroscopy [6, 104], these structures are by definition many wavelengths in size in at least one spatial dimension. Several tapered fiber studies of microdisks have been performed on passive

silicon microcavities [72] as well as on active compound semiconductor cavities [96]. The subwavelength silicon microdisks studied in the present work are smaller than the free-space wavelength of light being stored in the cavity in all spatial dimensions and are much smaller in the axial dimension. To our knowledge, these resonators are, to date, the smallest resonant structures to be probed with tapered fiber spectroscopy or directly coupled to a waveguide. However, the spatial localization necessarily comes with a broadening in momentum space and reduced photon lifetime.

In this work we studied silicon microdisks of diameters ranging from smaller to larger than the wavelength corresponding to resonances of azimuthal mode number (m) from 2 to 7 with resonant wavelengths from $1.52\mu\text{m}$ to $1.62\mu\text{m}$. We have quantified the relationship between the radiation-limited Q factor and m using tapered fiber spectroscopy (as discussed in section 6) and compared our results to finite-difference frequency-domain (FDFD) simulations discussed in Appendix C. The $m = 5$ mode was the mode of highest m in a subwavelength disk and was measured to have radiation-limited $Q = 1250$, indicative of strong potential for room-temperature laser operation if fabricated from or coupled to a gain medium. In Section 8.6 we will present evidence that this $m = 5$ mode in a quantum well microdisk has indeed given rise to laser action.

8.2 Review of microdisk theoretical considerations

In Chapter 5 of this thesis we went into some detail regarding the theoretical framework in which we understand the modes of optical microdisks. For accessibility, we summarize several of the key elements of that discussion here.

Resonances in microdisks can be classified according to three mode numbers corresponding to quantization in the vertical, radial and azimuthal directions [74]. To completely specify the mode one must also specify the polarization as TE-like (H_z is the dominant field component) or TM-like (E_z is the dominant field component). The highest- Q resonances occur when the wave vector is predominantly in the azimuthal direction [105]. Therefore,

we consider only modes of fundamental order in the vertical and radial direction and classify modes by m . Additionally, since we are interested in cavities with the smallest possible ratio of d/λ where d is the diameter of the disk and λ is the free-space resonant wavelength, we see in Fig. 4.3 that this is achieved for first-radial-order TE modes. TM modes and TE modes of higher radial order do not exist in subwavelength cavities.

The partial differential equation describing the system is separable and simplifies to a scalar Helmholtz equation if one assumes $\exp(im\phi)$ angular dependence. It is accurate to make the approximation that modes have purely TE or TM character. The equation governing the z -dependence is identical to that of a slab waveguide [106]. If one chooses β^2 as the separation constant for the equation governing z -dependence (so the functional dependence on z inside the disk is $\cos(\beta z)$ for even modes), then $\beta = k_0(n^2 - \bar{n}^2)^{1/2}$, where k_0 is the free space spatial frequency, n is the index of refraction of the disk (taken to be 3.48 throughout this Chapter), and \bar{n} is the effective index of refraction which enters the radial equation. Satisfying the boundary conditions at the top or bottom of the disk leads to the transcendental equation

$$\sqrt{n^2 - \bar{n}^2} \tan\left(\frac{k_0 h}{2} \sqrt{n^2 - \bar{n}^2}\right) = \xi \sqrt{\bar{n}^2 - 1}, \quad (8.1)$$

where h is the thickness of the silicon disk and $\xi = n^2$ for TM modes and unity for TE modes. For a silicon disk of thickness $h = 250\text{nm}$ operating at $\lambda = 1550\text{nm}$, $\bar{n} = 2.015(2.914)$ for TM (TE) modes. The objective of this study was to explore the regime where the size of the disk is smaller than the free space wavelength. To this end, the substantially larger effective index for TE modes is an indispensable attribute and, as mentioned above, allows only TE modes to exist in subwavelength silicon microdisks. For sufficiently thin disks ($h \leq 300\text{nm}$) at $\lambda \approx 1550\text{nm}$, TE modes have significantly larger radiation-limited quality factors, have larger m for a given disk radius, and for these reasons all modes populating thin subwavelength disks are TE-polarized.

Having obtained the effective index of refraction through consideration of the z equa-

tion alone, the radial equation reads

$$-\frac{1}{\rho} \frac{d}{d\rho} \rho \frac{d}{d\rho} R(\rho) + V_{\text{eff}}(\rho) R(\rho) = k_0^2 R(\rho), \quad (8.2)$$

where

$$V_{\text{eff}}(\rho) = k_0^2 [1 - \bar{n}^2(\rho)] + \frac{m^2}{\rho^2}. \quad (8.3)$$

The solution to Eq. 8.2 inside the disk is a Bessel function, $J_m(T\rho)$ where $T = \bar{n}k_0$, $k^2 = T^2 + \beta^2$, and $k = nk_0$. The effective index of refraction, which enters Eq. 8.2 through Eq. 8.3, is a function of ρ in that it changes abruptly from its value inside the disk (determined by solution of Eq. 8.1) to unity beyond the disk. It is this abrupt change which produces a potential well in which the electromagnetic field predominantly resides.

In Eq. 8.2 we have written Bessel's equation in a non-standard form to make an analogy to a one-dimensional Schrödinger equation, as discussed in more detail in Section 5.3. In this analogy, k_0^2 plays the role of the energy eigenvalue of the quantum eigenstate. One of the limits of this analogy is that k_0 also enters into the effective potential. Special consideration of the curvilinear kinetic energy term must be given if one is to justify the definition of the effective potential as in Eq. 8.3. Discussion of this point is held in Ref. [77] and section 5.2.7. Further consideration of the effective potential picture as applied to subwavelength microdisks is given in section 8.5.

In order to make quantitative predictions about the microdisk modal characteristics, we have used both analytical and numerical methods. Specifically, we investigated the analytical dispersion relations for microdisk whispering gallery modes by solving the appropriate boundary value problem [74, 77, 105–108], as discussed in Chapter 5, and we calculated the quasinormal modes of microdisk resonators using an FDFD mode solver, as described in Appendix C. Adapting the approach described in Refs. [109] and [110], these FDFD calculations leveraged the azimuthal symmetry of the modes (i.e., the $\exp(im\phi)$ dependence) to semi-analytically reduce the 3D resonator geometry to a transverse 2D eigenvalue problem. This full-vectorial method allowed for calculations of all electromagnetic field components as well as the effective mode volume [96], Purcell enhancement [78] and bending-limited

finesse [105]. Although this technique allows for adaptive meshing, a simple Cartesian mesh proved suitable for our calculations. A 10nm grid was utilized for all simulations. Convergence was observed as a function of simulation area. An index of refraction of 3.48 was used to model the silicon disks. See Appendix C for more details.

8.3 Fabrication of subwavelength silicon microdisks

Fabrication of silicon microdisks is discussed in detail in Chapter 7 of this thesis. In that chapter several possible fabrication approaches are described. Here we explain the choices made for the purpose of creating subwavelength disks with maximal radiation-limited Q factors.

As discussed in Chapter 7, several techniques for fabricating microdisks result in angled sidewalls [66, 95, 104]. In some cases the angled sidewalls arise from fabrication steps which produce smoother sidewalls. Smooth sidewalls are of critical importance for microdisks which are not operating in the radiation-limited- Q regime, as Rayleigh scattering from sidewall imperfections is usually the dominant loss mechanism in such disks [95]. However, our theoretical and experimental experience informs us that in the subwavelength regime sidewall verticality is a greater concern than minor sidewall roughness. Silicon microdisks were fabricated on SOI (250nm silicon layer, 3 μ m buried oxide, Soitech). To make disks with sidewalls which are vertical and yet as smooth as possible we perform negative electron beam lithography with PMMA [101] at a dosage of $2 \times 10^4 \mu\text{C}/\text{cm}^2$. At dosages of this magnitude, the polymer units of PMMA crosslink to form a material which is resistant to etchants. In our experiments, this technique has given smoother sidewalls than simply performing positive lithography without resist reflow. The electron exposure is followed by development in acetone and ICP RIE with SF_6 and C_4F_8 . Photolithography and deep ICP RIE are then performed to etch through the 3 μ m SiO_2 insulator layer and through $\sim 30\mu\text{m}$ of the underlying silicon substrate. This isolates the disks on a strip which is lifted above the rest of the substrate and thus makes it easier access the disks with

the tapered fiber. An undercut is performed with buffered hydrofluoric acid. SEM images of fabricated disks are shown in Figs. 8.1-8.3.

8.4 Experimental details and results of subwavelength silicon microdisks

To experimentally characterize the disks we utilize the technique of tapered fiber spectroscopy [6, 72, 95, 96, 104] as discussed in Chapter 6. A tunable laser sweeps the wavelength range from $1.52\mu\text{m}$ to $1.62\mu\text{m}$. The transmission through a tapered fiber coupled to a disk is monitored with an optical spectrum analyzer. The transmission dips are fit to a Lorentzian function, as described in Section 5.4, and the Q factor is extracted from the width and center wavelength.

In Fig. 8.1 we compare a large Si microdisk, with a diameter several times the free space resonant wavelength, to a subwavelength disk. In Fig. 8.1(a) we show an SEM image of the large Si microdisk with $10\mu\text{m}$ diameter. Figure 8.1(d) shows the subwavelength disk with $1.35\mu\text{m}$ diameter. Figures 8.1(b) and (e) contrast the full 100nm tapered fiber scan of the two disks. Figure 8.1(b) shows a scan of the entire tunable laser range for the $10\mu\text{m}$ disk. Radiation-limited Q factors of the modes in this disk can exceed 10^9 , but measured Q factors are $\sim 10^5$ and are limited by scattering from sidewall imperfections. The free spectral range for TE modes is $\sim 27\text{nm}$. Several families of modes of both polarizations are present, and in addition to the highest- Q , fundamental-radial-order modes, lower- Q , higher-radial-order modes are present. Figure 8.1(c) shows a high-resolution scan of a 2nm wavelength window of a tapered fiber spectrum from the $10\mu\text{m}$ -diameter silicon disk. The doublet character of the high- Q mode is apparent, as discussed in Refs. [72, 95, 96, 100] and in Chapter 6. It is interesting to see that what appeared to be a single resonance in the low-resolution scan of Fig. 8.1(b) actually consists of three separate peaks. This is an example of the rich mode spectra which occur in larger microdisks. In Fig. 8.1(e) a tapered fiber spectrum covering the full 100nm range of the tunable laser is shown for the $1.35\mu\text{m}$

disk. The free spectral range is $\sim 200\text{nm}$, and only one resonance is present. If one wishes to use whispering-gallery-mode microcavities for devices such as filters and switches, the large free spectral range of wavelength-scale microdisks is an attractive feature. Another attribute is that higher-radial-order modes do not exist in this wavelength range for a disk of this size. The other features of the spectrum in Fig. 8.1(e) are due to coupling to the substrate. Because these small disks are only a few hundred nanometers from the substrate, coupling of the fiber to the substrate is more prominent than in larger disks. Figure 8.1(f) shows a Lorentzian fit to the spectrum of Fig. 8.1(e), and the extracted Q factor is 257.

As is shown in Fig. 8.1, a size reduction in a microdisk of an order of magnitude has a dramatic effect on the Q factor. The goal of this work was to explore the physical cause of this performance degradation and to analyze the lower limit of disks that could be made before Q factor dropped off completely. For the TE_1 family of modes, the critical regime where Q factor becomes completely radiation limited is for disks with diameters very close to the free-space resonant wavelength which in our study is always within the tunable laser range of 1520-1620nm.

Figure 8.2 shows SEM images of microdisks with diameters varying from $1.89\mu\text{m}$ —with radiation-limited Q on the order of 10^4 —down to a subwavelength disk of approximately $1\mu\text{m}$ diameter with radiation-limited $Q = 257$. Next to each disk is a tapered fiber spectrum of the characteristic resonance of the disk. The SEM images depict the decrease in size of less than a factor of two while broadening of the resonances demonstrates the exponential decrease in Q factor of nearly two orders of magnitude.

SEM images of two completed disks, those from Fig. 8.2(a) and 8.2(d), are shown in Fig. 8.3 along with the calculated near- and far-field profiles of their resonant modes. Contrasting Fig. 8.3(b) and Fig. 8.3(f) one sees the near-field amplitude extending further radially and axially in the subwavelength disk. Contrasting Fig. 8.3(c) and Fig. 8.3(g) one observes the increased far-field radiation emanating from the subwavelength cavity. The in-plane field profiles are shown in Fig. 8.3(d) and (h).

In Fig. 8.4 we present a comparison of the experimentally-obtained Q factors with the

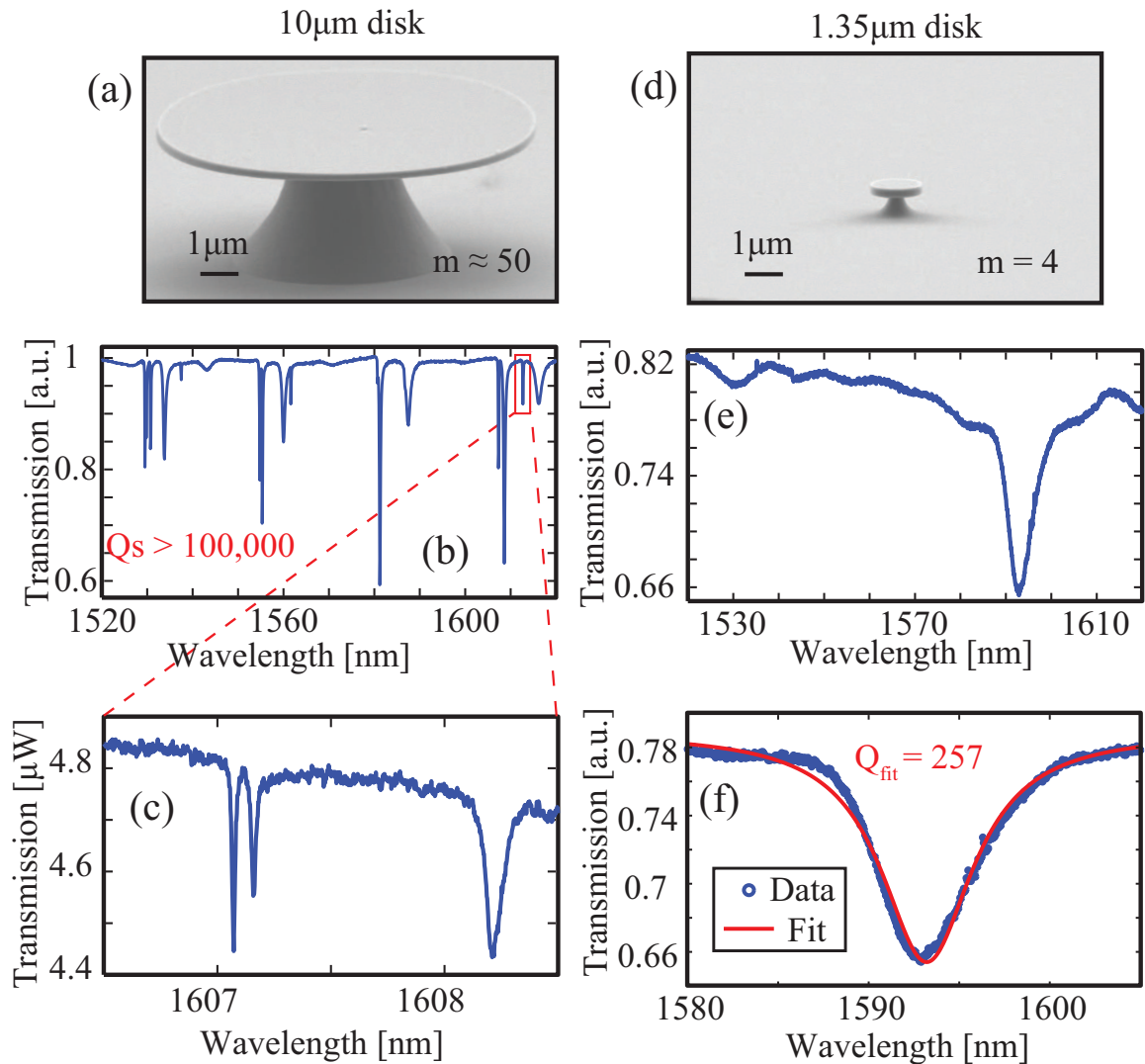


Figure 8.1: Comparison of microdisks in two size domains. (a) A $10\mu\text{m}$ Si microdisk. (b) A tapered-fiber spectrum from a $10\mu\text{m}$ disk with a complicated mode spectrum consisting of several modes with Q factors exceeding 100,000 and many exceeding 10,000. (c) A high-resolution scan of what appears to be a single mode in (b) reveals three distinct contributions, further emphasizing the richness of the mode spectrum of this large disk. (d) SEM image of a disk with diameter smaller than the resonant wavelength. (e) A full 100nm tapered-fiber spectrum with a single resonance. The FSR of TE_1 modes in this disk at these azimuthal mode orders is $\sim 200\text{nm}$. Contrasting (e) with (b), one observes the simplicity of the mode spectrum in the small disk relative to the large disk. (f) A fit of the data in (e) gives a value of 257 for the measured Q factor of the $m = 4$ mode.

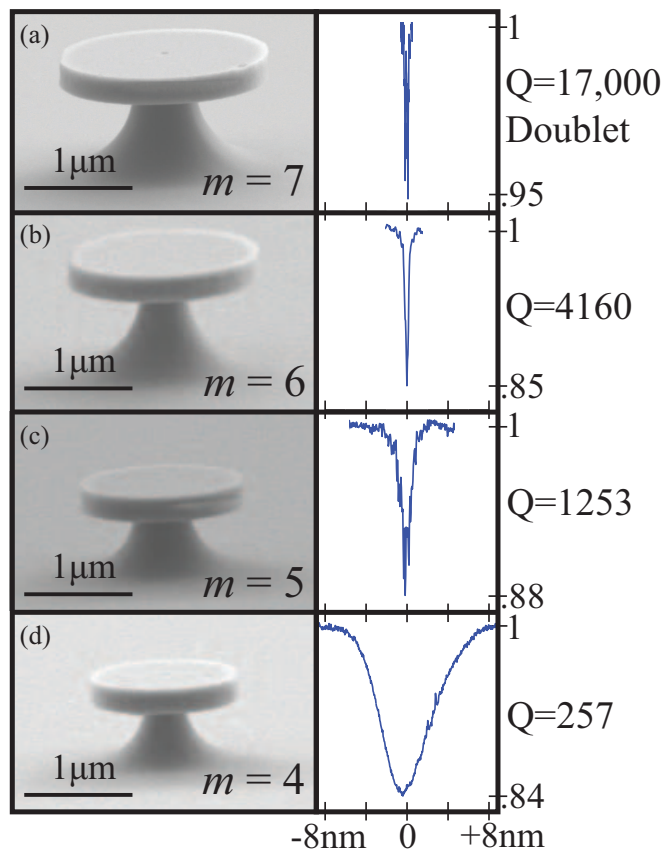


Figure 8.2: Silicon microdisks of decreasing diameters and tapered fiber spectra. (a-d) SEM images of disks of diameter $1.89\mu\text{m}$, $1.75\mu\text{m}$, $1.48\mu\text{m}$, and $1.35\mu\text{m}$ respectively. Resonant transmission dips in tapered fiber spectra acquired from the disks are shown. The y -axes of the plots on the right are transmission in arbitrary units and the x -axis is wavelength detuning.

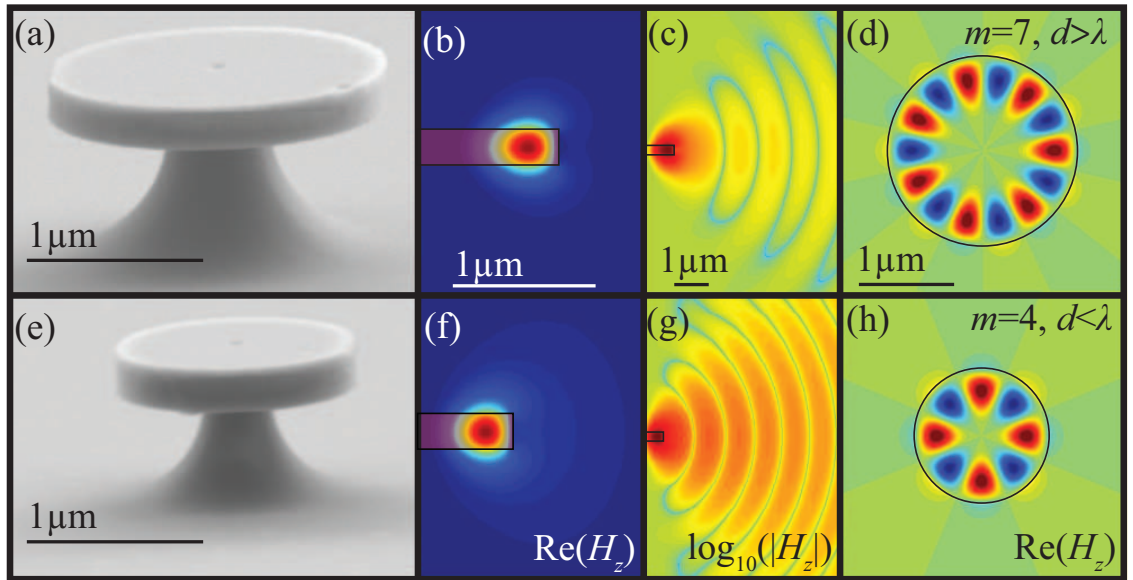


Figure 8.3: Fabricated structures and calculated field profiles of microdisks for $m=7$ and $m=4$ modes. (a) Disk of $1.89\mu\text{m}$ diameter. (b) $\text{Re}(H_z)$ field profile of $m=7$ mode in the $y-z$ plane calculated with the FDFD method. $Q = 18,200$. (c) Far field ($\log_{10}(|\text{Re}(H_z)|)$) for the same disk. (d) $\text{Re}(H_z)$ in the $x-y$ plane calculated analytically. (e) Disk of $1.35\mu\text{m}$ diameter. (f-h) Calculations for the $1.35\mu\text{m}$ disk corresponding to those in (b)-(d).

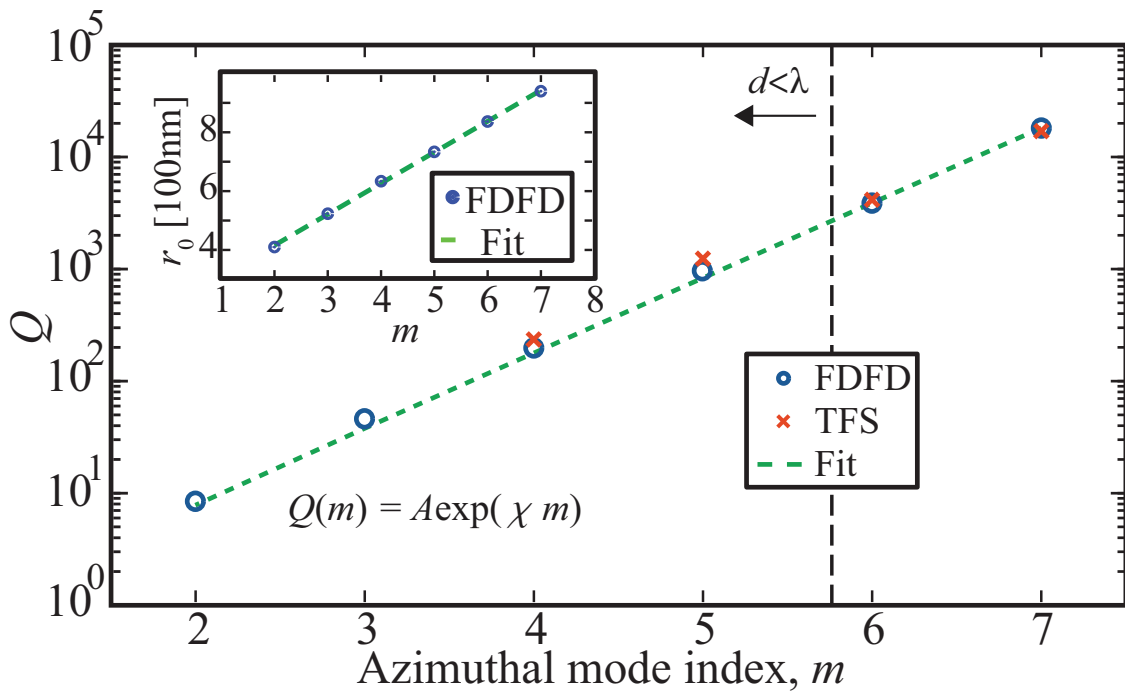


Figure 8.4: Microdisk Q versus m . Experimental data, theoretical values obtained with FDFD and a fit to an exponential function are shown. The linear relationship between the disk radius, r_0 , and m is shown in the inset.

theoretical radiation-limited Q factors obtained with FDFD calculations. The experimental points are acquired using tapered fiber spectroscopy, as described in Chapter 6, and the theoretical points are determined by using the values of disk diameter as measured with SEM in the FDFD mode solver. The thickness of each disk was 250nm. The data for each azimuthal mode order is from a disk of a different radius so the resonant wavelengths are nearly equal. The agreement between experiment and theory indicates that our silicon microdisks have radiation-limited Q factors that are not significantly degraded by minor sidewall perturbations. It should be noted that the measured resonance at $m = 7$ was a doublet mode. The splitting was only observed for the $m = 7$ mode where the Lorentzian is narrow enough to differentiate the two peaks. We find that the $m = 5$ mode is the subwavelength mode of highest m with measured $Q = 1250$. The diameter of the disk was $1.49\mu\text{m}$ and resonant wavelength was $1.543\mu\text{m}$ giving a ratio of $d/\lambda = 0.967$. The $m = 4$ mode was observed in a cavity of diameter $1.35\mu\text{m}$ at wavelength of $\lambda = 1.591\mu\text{m}$ giving $d/\lambda = 0.849$. Due to the limited wavelength window accessible by our tunable laser, and the broad nature of the low- Q $m = 3$ mode, it was not observed in our studies. The theoretical value of $d/\lambda = 0.683$ for the $m = 3$ mode. Below $m = 3$ the resonances have $Q < 10$. To create microdisks with well defined resonances for $m < 3$ and $d/\lambda < 0.7$, metallodielectric architectures, which trade ohmic loss for suppressed radiation, may offer advantages [64–66].

For more direct comparison between experiment and theory, we also present the data in Table 8.1. The radii of the disks, as measured with SEM, the measured resonant wavelengths, and the measured quality factors obtained by fitting the transmission spectra to a Lorentzian function are listed alongside the theoretical values obtained from the FDFD simulations. In addition, the calculated effective mode volumes are given in Table 8.1. The effective mode volume is calculated from the formula

$$\nu_{\text{eff}} = \frac{\int \epsilon(\mathbf{r})|\mathbf{E}(\mathbf{r})|^2}{\max[\epsilon(\mathbf{r})|\mathbf{E}(\mathbf{r})|^2]}. \quad (8.4)$$

To calculate the volume integral in the numerator of Eq. 8.4, $\exp(im\phi)$ angular dependence is assumed, as it was to arrive at Eq. 8.2. This is an important distinction when contrasted

Table 8.1: Theoretical and measured microdisk modal parameters

m	r_{meas}	r_{sim}	λ_{meas}	λ_{sim}	Q_{meas}	Q_{sim}	ν_{eff}
7	$0.945\mu\text{m}$	$0.946\mu\text{m}$	$1.530\mu\text{m}$	$1.555\mu\text{m}$	17,000	18,200	3.07
6	$0.877\mu\text{m}$	$0.876\mu\text{m}$	$1.589\mu\text{m}$	$1.621\mu\text{m}$	4160	3834	2.61
5	$0.743\mu\text{m}$	$0.746\mu\text{m}$	$1.543\mu\text{m}$	$1.581\mu\text{m}$	1253	1010	2.21
4	$0.675\mu\text{m}$	$0.676\mu\text{m}$	$1.591\mu\text{m}$	$1.617\mu\text{m}$	235	198	1.80
3	*	$0.536\mu\text{m}$	*	$1.569\mu\text{m}$	*	47.6	1.52
2	*	$0.416\mu\text{m}$	*	$1.558\mu\text{m}$	*	8.72	1.18

with the work of Ref. [96] wherein standing waves with $\sin(m\phi)$ angular dependence are assumed. The mode volume calculated assuming standing waves is half that of the circulating waves. To calculate the values of the effective mode volume presented in Table 8.1, the integral in Eq. 8.4 was performed over the entire simulation space which extended $2\mu\text{m}$ above and below the disk and $6\mu\text{m}$ in the radial direction.

In using evanescent coupling in transmission measurements to determine the radiation-limited Q of a resonator it is important to consider other loss mechanisms contributing to the measured Q . The relation between the various contributions to cavity loss for this measurement can be expressed as (see section 5.4)

$$Q_{\text{meas}}^{-1} = Q_{\text{rad}}^{-1} + Q_{\text{c}}^{-1} + Q_{\text{p}}^{-1}, \quad (8.5)$$

where the three contributions to the measured Q factor are radiation (Q_{rad}), coupling to the tapered fiber waveguide (Q_{c}), and parasitic losses (Q_{p}) such as sidewall scattering. In the structures considered here, $Q_{\text{rad}} < 20,000$, and Q_{p} in larger disks fabricated with similar methods has been measured to be greater than 100,000. For this reason it is justified to neglect the contribution from Q_{p} in Eq. 8.5. Q_{c} is a function of the gap between the resonator and the waveguide, and this fact can be exploited to determine the relative contributions to Eq. 8.5 from Q_{rad} and Q_{c} . In the experiments performed in this study, the tapered fiber position relative to the disk was controlled with 100nm resolution. As can be seen in Fig. 8.3,

the near field of the modes decays over $1 - 2\mu\text{m}$. To accurately determine Q_{rad} , transmission spectra were taken with the fiber very near the disk to determine resonance positions. The fiber was then incrementally moved away from the disk, and additional spectra were acquired as the gap between the fiber and disk was increased. As in Ref. [72], increasing the gap resulted in a decrease in the depth of the transmission dip and increase in the measured Q . Convergence behavior was observed until the depth of the dip was at the level of the measurement noise; the reported values for Q_{meas} in Fig. 8.4 and Table 8.1 are those from the maximal fiber-disk gap which resulted in a value consistent with the convergence trend and with a deep enough dip to be fit to a Lorentzian. We did not directly measure the fiber-resonator gap, because in measurements of such small disks so close to the substrate it is advantageous to hold the fiber above the plane of the disk, and the devices were only viewed directly from above.

It is important to note that contributions to error in the tapered fiber measurements are numerous. They include coupling between the fiber and disk, noise due to vibrations of the fiber, substrate and disk coupling and perturbation due to the pedestal. Additionally, uncertainty in the measurement of disk diameters with SEM affects comparison between experiment and theory. Because the contributions to error are so varied and each is so difficult to quantify, we do not venture to guess at the uncertainty in the data in Table 8.1. We note that measured resonant wavelengths are within 1-3% of predicted values, measured Q factors are near 10-20% of predicted values, and this is true with or without consideration of the substrate and pedestal in the model. For the lower azimuthal mode numbers, the measured values are consistently higher than the theoretical values, indicating a tendency of the FDFD mode solver to underestimate the radiation-limited Q .

The effect of the substrate is more pronounced if one considers non-undercut resonators in this low- m regime. The theoretical values of the $m = 4$ device listed in Table 8.1 if the entire half space below the disk is filled with dielectric characterized by $n = 1.46$ are $Q_{\text{sim}} = 104$ and $\lambda_{\text{sim}} = 1.630\mu\text{m}$. For the $m = 7$ disk with no undercut $Q_{\text{sim}} = 5265$ and $\lambda_{\text{sim}} = 1.555\mu\text{m}$.

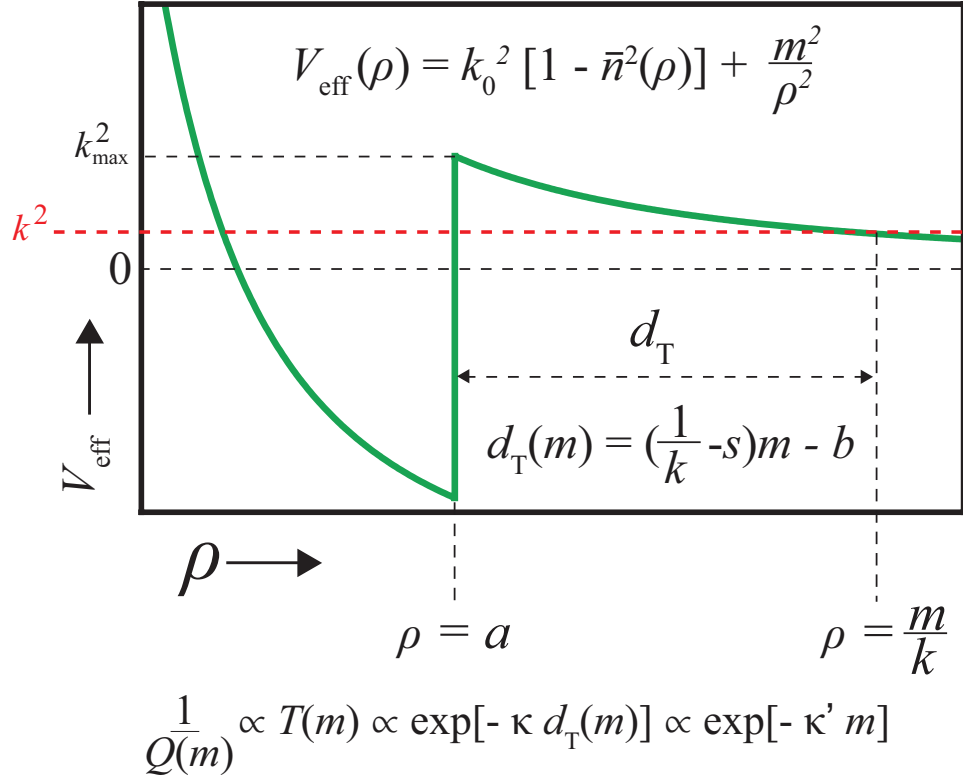


Figure 8.5: The effective potential and tunneling parameters. The tunneling distance, d_T , is proportional to m , so the tunneling probability, T , decays as $\exp(-\kappa' m)$. The Q is inversely proportional to the tunneling probability and behaves as $\exp(\kappa' m)$.

8.5 Analysis from a tunneling perspective

Analysis of our data reveals that m has a linear relationship with r_0 over the range $m = 2-7$ at a (nearly) constant wavelength. Q has an exponential dependence on m of the form $Q(m) = A \exp(\chi m)$, where $A = 0.374$ and $\chi = 1.54$ are parameters which have been determined with non-linear regression. As seen in Fig. 8.4, this expression fits our data quite well over the range of m values considered here. The linear dependence of m on r_0 can be understood because the mode propagates around the circumference of the disk. The effective mode volume also has a linear dependence on m . Thus, the Purcell enhancement decays exponentially with decreased m , as does the finesse [105].

The exponential dependence of Q on m can be understood in the framework of the ef-

fective potential [77, 108] (see Section 5.2.7), which is given by Eq. 8.3 and is plotted in Fig. 8.5. This quantity enters the scalar radial equation for the dominant field component if TE or TM polarization is assumed. As discussed in Section 8.2, V_{eff} changes discontinuously at the edge of the disk, creating a potential well in which the electromagnetic field predominantly resides. There are two features of a potential which affect the tunneling probability: the barrier height and barrier width. For a given wavelength, the height of the tunneling barrier scales as m^2/r_0^2 . In a general one-dimensional tunneling scenario, the tunneling probability will have a power law dependence on barrier height. Therefore, the quadratic dependence of the barrier height on m cannot explain the exponential dependence of Q on m . However, the tunneling probability through a one-dimensional barrier is exponentially dependent on the barrier width. As shown in Fig. 8.5, the radial distance at which the confined mode can emerge to free space is $r = m/k$, and is determined by the condition $V_{\text{eff}} = k_0^2$. Thus, the tunneling barrier thickness is given by $d_{\text{T}} = m/k_0 - r_0$. Using the linear relationship between m and r_0 ($r_0 = sm + b$) the tunneling thickness is $d_{\text{T}} = (1/k - s)m - b$. Thus,

$$\frac{1}{Q(m)} \propto T(m) \propto \exp(-\kappa d_{\text{T}}(m)) \propto \exp(-\kappa' m), \quad (8.6)$$

where T is the tunneling probability and κ and κ' are unknown constants which could be determined from a rigorous treatment. Thus, the exponential dependence of Q on m (and r_0) is consistent with the linear dependence of tunneling barrier width on m .

8.6 Subwavelength lasers

With a radiation-limited Q factor of 1250, the $m = 5$ whispering-gallery mode is a strong candidate for a subwavelength laser. In recent years, subwavelength lasers have attracted a great deal of interest as they are promising components for applications in integrated photonic circuits, local chemical or biological sensing, and imaging. Efforts have been carried on several fronts to reduce laser sizes. Photonic crystal cavities provide subwavelength modal volumes, but their physical size must be several times larger than the wavelength

in at least one spatial dimension [111]. Metallic structures present another approach of confining light on subwavelength scales by utilizing surface plasmon resonances [64–66]. In previous research, metallic waveguides have been employed to realize subwavelength terahertz quantum cascade lasers [112], near-infrared metal coated nanocavity lasers [64], nanosphere plasmonic lasers [113] and nanopatch lasers [114] at cryogenic temperatures. By proper incorporation of low-loss dielectric into metallic structures, subwavelength metalodielectric cavity lasers were also demonstrated at room temperature under pulsed optical pumping [115]. Semiconductor disk cavities represent another candidate for subwavelength lasers by taking advantage of the high Q factors of whispering-gallery modes. Microdisk lasers were first realized in the early 1990s in cavities with diameters larger than the emission wavelength [68–70], and recently disk lasers with diameters equal to and less than the lasing wavelength were demonstrated [102, 116, 117]. For small size subwavelength disk lasers the underlying pedestals have restricted heat conduction due to the limited dimensions and/or low thermal conductivities, which renders the laser operation in continuous-wave (CW) mode challenging. As such, previous small size disk lasers were reported to operate in pulsed mode only [102, 116, 117].

In our work we were able to build upon the knowledge gained from the passive Si microdisk studies to achieve CW operation of subwavelength disk lasers at telecomm wavelengths. A $1.49\mu\text{m}$ diameter, 209nm thick InGaAs/AlInAs disk is shown to lase in single-mode at a wavelength of $1.53\mu\text{m}$ under CW optical pumping at 45K . Indeed, it is the $m = 5$ mode of the microdisk that gives rise to laser action, as discussed in Section 8.4.

The microdisks used in our experiments were fabricated on lattice-matched InGaAs/AlInAs heterostructures grown on an InP substrate using solid-source molecular beam epitaxy (MBE) [118]. The designed layer structure is shown in Fig. 8.6. The quantum well structure is composed of six 9nm -thick InGaAs quantum wells separated by 3nm AlInAs barriers with two 60nm -thick InGaAs cladding layers. The total thickness of the InGaAs/AlInAs layers is 209nm . Electron beam lithography was used to define $\sim 3\mu\text{m}$ -diameter PMMA circles on top of the sample. The PMMA then acted as an etching mask



Figure 8.6: The layered structure of the quantum well gain medium. Six InGaAs quantum wells are separated by AlInAs barrier layers. The quantum wells are contained within InGaAs cladding layers on an InP substrate.

for wet etching. The sample was etched in an acid solution composed of $\text{HNO}_3/\text{HBr}/\text{H}_2\text{O}$ (1:1:20). After wet-etching for ~ 40 seconds, which gives an etching depth of $\sim 1.5\mu\text{m}$, disk cavities with diameters between $1.4 - 1.8\mu\text{m}$ were formed. In order to avoid coupling of the optical mode into the InP substrate, selective wet-etching in a solution of $\text{HCl}/\text{H}_2\text{O}$ (1:2) was conducted at room temperature for ~ 1.5 hours to remove the InP around and below the InGaAs/AlInAs disks. A scanning electron microscope (SEM) image, shown in Fig. 8.7(a) shows a side-view of a representative disk. The disk diameter is $1.49\mu\text{m}$. Its sidewall is vertical and the surfaces are smooth; as discussed in Section 8.3, these features are advantageous for improving the cavity Q factor and minimizing scattering losses. The underlying InP pedestal forms a mountain-like shape with a rough surface. Such a shape is different from multi-faceted shapes reported for quantum cascade disk lasers using the same material system [119, 120] due to different etching conditions and sample geometries. The size of the pedestal is chosen as a compromise between effective heat conduction and prevention of optical mode coupling into the substrate. The high thermal conductivity of

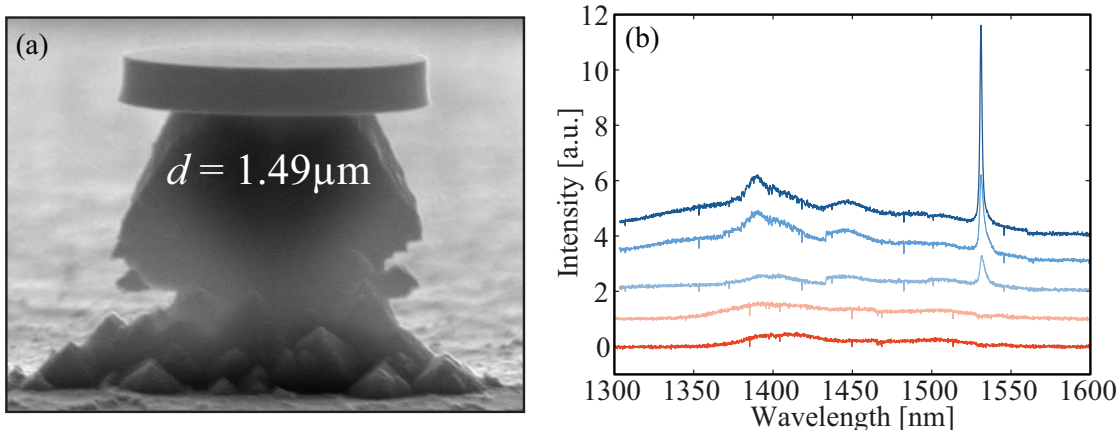


Figure 8.7: Quantum well subwavelength laser. (a) SEM image of the fabricated microdisk on the InP substrate. (b) μ -PL spectra at various pump powers.

the InP pedestal ($\sim 69\text{W}/(\text{m}\cdot\text{K})$ [121]) is more than twice the thermal conductivity of the AlGaAs pedestal in the GaAs-based disk lasers reported in Refs. [116] and [102], and thus enables more efficient heat dissipation.

The microdisks were measured in a micro-photoluminescence (μ -PL) apparatus. The samples were mounted in a low-temperature cryostat cooled with liquid helium. A diode-pumped Nd:Yttrium-Aluminum-Garnet (YAG) laser with relatively long emission wavelength of 1064nm was chosen as the pump laser for minimizing heat generation. The pump light was focused by a $50\times$ microscope objective with a 0.42 numerical aperture and a working distance of 1.7cm to a spot size of $\sim 5\mu\text{m}$ on top of a single disk. The scattered light emission from the disk was collected by the same objective and then directed to a Horiba TRIAX spectrometer with a Peltier-cooled InGaAs photodiode array for recording the spectrum. The measurements were performed under CW optical pumping.

Figure 8.7(b) shows the emission spectra of the $1.49\mu\text{m}$ diameter, 209nm thick disk under different pump intensities at a heat-sink temperature of 45K. At low pump intensities, spontaneous emission from electron-hole radiative recombination in both the quantum well region and the InGaAs cladding layers are measured in the wavelength range from 1350 to 1550nm. When the pump intensity increases beyond $276\text{W}/\text{mm}^2$, a narrow peak appears at

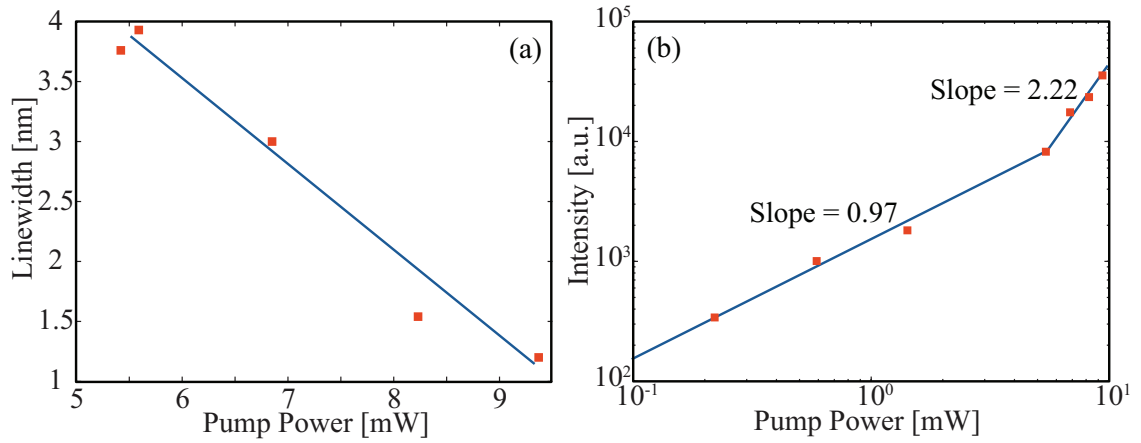


Figure 8.8: Evidence for lasing in the subwavelength microdisk. (a) Linewidth narrowing as a function of pump power. (b) Integrated intensity of the PL versus pump power on a log-log plot shows threshold behavior.

1530nm.

By fitting the emission peaks given in Fig. 8.7(b) to a Lorentzian function, the linewidths—defined as the full width at half maximum (FWHM) (see discussion in section 5.4)—are obtained and plotted in Fig. 8.8(a) as a function of pump intensity. The linewidth decreases from 3.8 to 1.2nm as the pump intensity increases from 276 to 477.2W/mm². Figure 8.8(b) shows the spectrally integrated emission intensity at different pump intensities on a logarithmic scale. The curvature slope changes from 0.97 to 2.58 at pump intensity of ~ 276 W/mm², which indicates threshold behavior. The observed linewidth narrowing and threshold behavior suggest that the emission corresponds to laser action. These characteristics of laser emission were observed at temperatures up to ~ 55 K.

8.7 Conclusions

In conclusion, we have investigated the resonant modes of silicon microdisks that are smaller in every dimension than the free-space wavelength of light being stored in the cavities. We have presented a systematic characterization of the $m = 2 - 7$ modes and

have quantified the linear relationship between m and r_0 as well as the exponential dependence of Q on m . Our experimental data is in agreement with theoretical values for the radiation-limited Q . We have demonstrated the $m = 5$ mode is the highest- Q mode in a subwavelength disk and was measured in our structures to have a $Q = 1250$ at a wavelength of $1.543\mu\text{m}$ in a microdisk of diameter $1.490\mu\text{m}$. Microdisks were then fabricated from an InGaAs/AlInAs quantum well structure, and the $m = 5$ mode investigated in the passive Si subwavelength cavities was shown to lase in the gain medium under optical excitation up to 55K in CW operation.

After our exploration of the smallest length scale of whispering-gallery mode cavities, we turned our attention to slightly larger microdisks and developed a method to dynamically tune the resonance spectra over a broad range of wavelengths. Our efforts on this front are described in Chapter 9.

Chapter 9

Dynamic broad tuning of whispering-gallery modes in silicon microdisks

After spending some time learning the physics of microdisks and having explored different size regimes in isolated microdisks, we became interested in the more sophisticated photonic structures consisting of several coupled microdisks. For example, systems of a few coupled microdisks are often referred to as photonic molecules [122–129] due to the analogy with electronic states of coupled atoms. In Fig. 9.1 we shown an SEM image of a photonic molecule consisting of three coupled Si microdisks in a triangular arrangement. Optical states in similar photonic molecules have been shown to give rise to bonding and antibonding states due to degeneracy splitting [128, 129], just as in atomic systems. Also, such photonic molecules have been theoretically shown to produce optical states with Q factors higher than those of the isolated constituent microdisks and with larger FSR [128].

Another system of coupled microdisks with interesting physics not seen in isolated microdisk systems is shown in Fig. 9.2. In this system several disks of a similar size are evanescently coupled to a waveguide. Such systems have been dubbed Side Coupled Integrated Spaced Sequence of Resonators (SCISSOR) [130] by Robert Boyd's [79] group. While the acronym is awkward, the physics of the system is fascinating. Interesting prop-

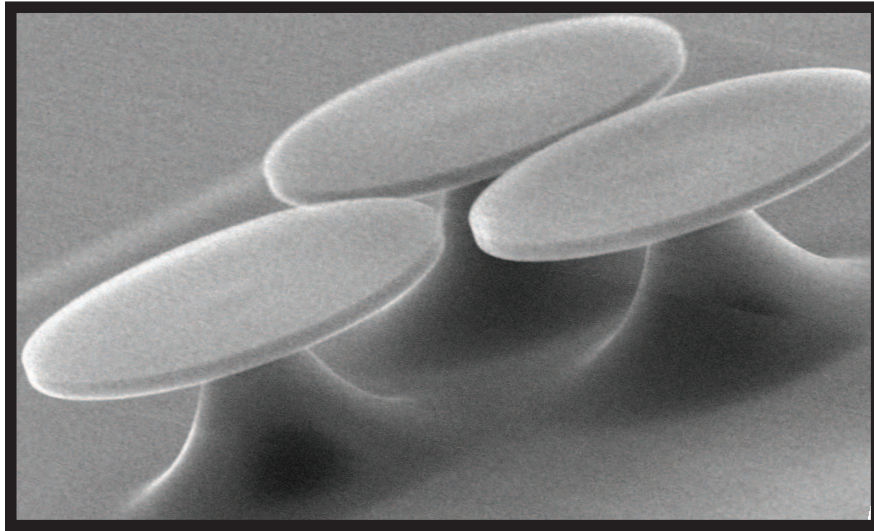


Figure 9.1: Three coupled Si microdisks each of $5\mu\text{m}$ diameter in a triangular photonic molecule configuration.

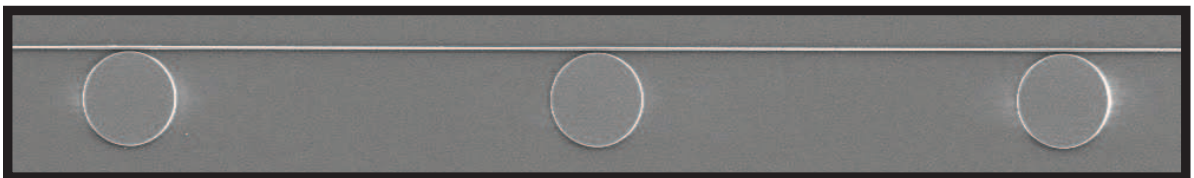


Figure 9.2: Three Si microdisks of $10\mu\text{m}$ diameter to coupled to each other via a waveguide.

agation effects occur such as the existence of solitons wherein the inherent dispersion in the waveguide is compensated by nonlinear phase shifts introduced by the sequence of resonators.

We are interested in studying such systems of coupled resonators, but one major problem arises in the context of optical resonators that does not arise for systems of coupled atoms. This difference is due to the fact that atoms are truly identical particles whereas microcavity resonators can be made to be nearly identical particles, but inevitably have minute structural differences due to fabrication imperfections. Figure 9.3 shows tapered-fiber spectra from two Si microdisks of $10\mu\text{m}$ diameter prepared in the same manner $\sim 100\mu\text{m}$ apart on a chip. One can see that while the spectra are qualitatively similar, the two spectra are shifted a small amount relative to one another. While for some purposes this may be insignificant, if one wishes to achieve strong coupling between two adjacent disks, the fact that the narrow resonances of one disk do not overlap with the resonances of the adjacent disk will eliminate coupling between the two cavities. Our work on tunable resonators began by seeking a method to tune the modes of one cavity into resonance with the modes of an adjacent cavity after fabrication in order to produce photonic molecular structures. The device we invented now promises to have much broader applicability in a variety of photonics applications.

Before describing our method and structure for tuning the resonances of Si microdisks we begin with a discussion of the larger context of tunable optical resonant cavities.

9.1 Context for tunable resonators and existing technologies

Microdisk and microring resonators can operate as functional components in myriad optical devices. Applications include particle sensors, cavity QED, and photonic circuit elements including switches, modulators, filters, and lasers. The ability to tune the mode spectra of these central optical components enables a multitude of dynamic devices. The character-

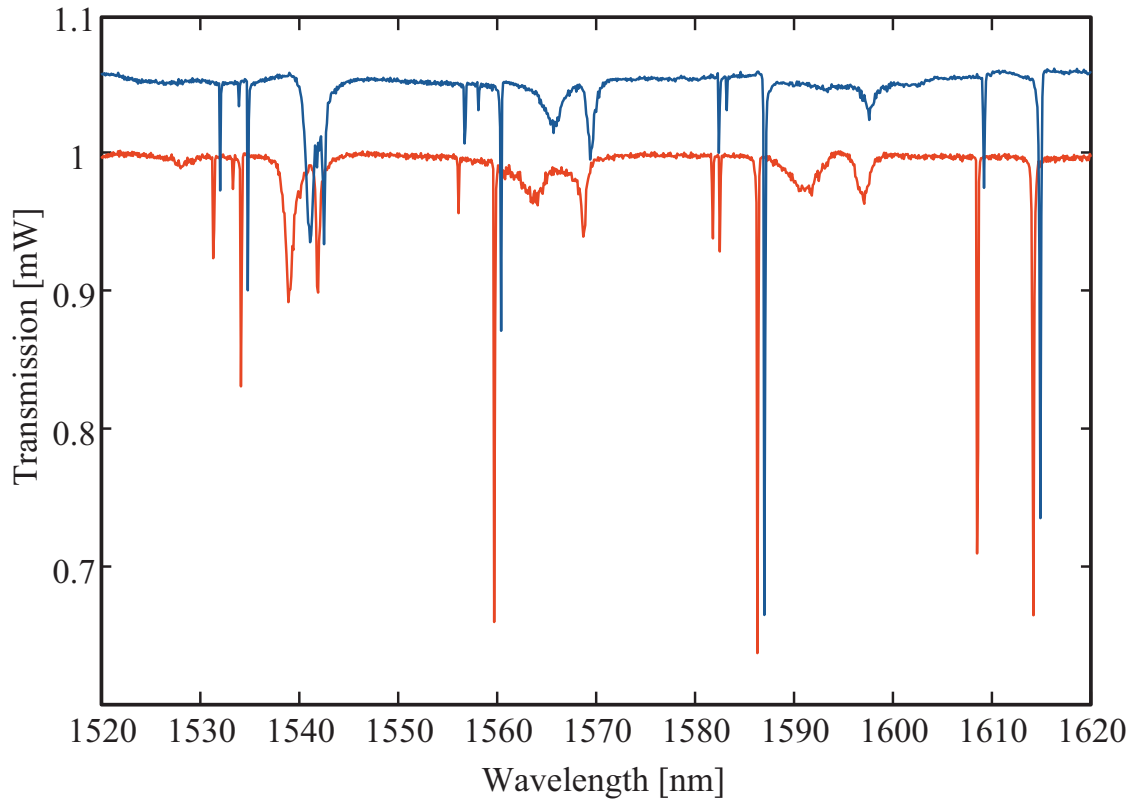


Figure 9.3: Two tapered-fiber spectra from $10\mu\text{m}$ disks, offset on the y -axis for clarity. These two $10\mu\text{m}$ disks were fabricated at the same time on the same chip and are separated by a few hundred microns. The slight discrepancies between the two spectra result from minor fabrication differences between the two disks. This slight mode mismatch is difficult to overcome and becomes more of an issue as the size of the disks is reduced. Such a mode mismatch makes it difficult for the structures in Fig. 9.1 and 9.2 to achieve strong coupling. We seek a method to tune the mismatched spectra into resonance with one another after fabrication.

istics of circular cavity resonators that make them attractive for photonic applications are their small size, large free spectral range (FSR), high cavity quality factor (Q), and ease of fabrication. For large-scale integration, CMOS-compatible, planar silicon structures are advantageous. Any effort to enable tuning in optical microcavities for photonic device applications should retain these attributes.

A number of technologies have been demonstrated to tune optical microcavities. Each of these technologies has strengths and limitations and may find applicability in certain contexts. Carrier injection via a p-i-n junction in a silicon microring [131–133], microdisk [134] and photonic crystal cavity [135] has been achieved with fairly high Q ($\sim 20,000$ [131]), is compatible with the silicon material platform [131–134], allows for fast modulation (18 Gb/s [132]), and can be energy efficient [134]. Laser heating [129, 135] allows for high Q and fairly broad tuning. N_2 adsorption has been utilized for high Q and high resolution tuning [136]. Tuning liquid crystal droplet resonators in a polymer matrix via an external electric field allows for broad tuning (20nm) and fairly high Q ($\sim 12,000$) [137]. Electromechanically-tuned photonic crystal nanobeams have recently been demonstrated with measured Q factors of 13,000, tuning range of 10nm, and low power consumption [138]. Mechanical insertion of a dielectric into the near field of a microring has been shown to achieve broad tuning [139]. Ultrahigh- Q toroid cavities have been tuned thermo-optically with joule heating, but with tuning range of less than 1nm [140]. Many integrated photonic devices have utilized thermal tuning in resonators or waveguides separated from resistive heaters by cladding layers (see Ref. [141] and references therein), but such a design requires heating of the resistive element, the cladding layer, and the optical layer. There remains a demand for an energy-efficient planar silicon device with simple fabrication and no moving parts which can be easily coupled to a waveguide, has broad tuning range, high Q , stable operation, and large packing density allowing for many adjacent devices to be tuned independently on a single chip.

In this work we present a new tunable microdisk design which achieves the aforementioned objectives. The device consists of a silicon microdisk with nanoscale ($\sim 200\text{nm}$)

contacts on either side, as shown in Fig. 9.4(a). The large thermo-optic coefficient of silicon ($1.86 \times 10^{-4} \text{K}^{-1}$), due to the temperature dependence of the silicon bandgap [142, 143], is leveraged to enable modal tuning via joule heating. The principle behind the design is to improve energy efficiency by passing current directly through the optically-active region rather than utilizing an external resistive heater. The device has broad tuning range ($>14 \text{nm}$ demonstrated) with mW tuning power, a simple, CMOS-compatible fabrication, and a well-defined mode spectrum with Q factors exceeding 20,000. The objective of the design is to achieve a versatile structure with low-power broad tuning and simple fabrication. More elaborate fabrication techniques [134, 139] may allow thermal, electrical, or mechanical tuning without placing contacts in the optical mode volume, but such a multi-mask fabrication is time consuming, expensive and, as we show here, not necessary for many applications. If an application only requires a mode shift by a single full-width-at-half-maximum (FWHM), operation of this device can be achieved at powers of approximately $10 \mu\text{W}$ with less than 3V. For broader tuning on the order of a FSR, one only needs $\sim 1 \text{mW}$ of power. In contrast to other tuning designs where a microheater is separated from the resonant element by a cladding layer, our design can leave the resonator exposed to the environment enabling it to be used as a sensor. Limitations of the design include that the point contacts scatter light from the optical mode reducing the photon lifetime, and applications that require fast switching will be constrained by the time required to heat and cool the disk. While thermal tuning is not generally competitive in ultrafast applications such as high-speed modulation [131–134], many devices such as sensors for particles with discrete absorption lines and tunable on-chip lasers may benefit from this structure. The device also enables coupling of narrow-line emitters with cavity modes in cavities with small mode volumes, high Q s, and large FSRs. Further, the fabrication of this device is an important result in that it introduces an entirely new technique to tune individual microcavities, it marks a new standard in energy efficiency of thermally-tuned microcavities, and it opens many possibilities for coupling electronic and optical degrees of freedom. Additionally, many photonic devices with coupled resonant elements suffer from sensitivity to

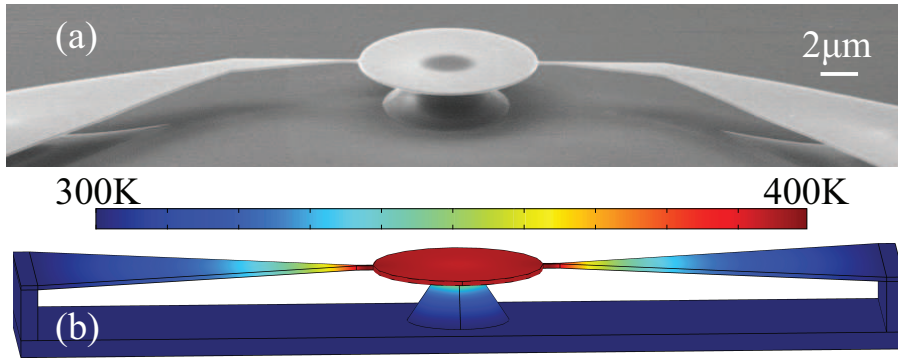


Figure 9.4: Microdisk structure with electrical contacts. (a) SEM image of the structure under consideration. (b) Electro-thermal simulation data. The surface temperature of the structure is shown.

fabrication imperfections. The tunable microdisks presented here offer a purely electrical, low-power means to tune coupled cavities into resonance with one another [129].

9.2 Modeling and fabrication of wired microdisks

Calculations of whispering-gallery mode resonant wavelengths [144, 145] as a function of index of refraction inform us that $\sim 1\text{nm}$ of wavelength tuning can be achieved with a shift of 0.002 in the index of refraction. Shifting the resonances by 10nm requires changing the index of refraction from 3.48 to approximately 3.50. Silicon's relatively large thermo-optic effect allows 10nm shifts to occur with a change of temperature of just over 100K. To anticipate the power required to achieve the desired tuning, the electro-thermal behavior of the device was modeled using Comsol Multiphysics. Figure 9.4(b) shows data from a simulation of a silicon microdisk based on an SOI structure. The modeled disk has $10\mu\text{m}$ diameter contacted on either side by 200nm wide, $1\mu\text{m}$ long contacts. The contacts taper out to aluminum pads, one of which is held at a positive bias of 25V in the simulation and the other at ground. The aluminum pads and the silicon disk are isolated from the silicon wafer below by $3\mu\text{m}$ thick SiO_2 structures. All surfaces are allowed to radiate into air except the tops of the aluminum pads and the bottom of the underlying silicon wafer

which are modeled as heat sinks held at 300K. This model suggests that 1.8mW of power dissipated in the device will raise the temperature by 100K. The simulations reveal that with this design the temperature of the disk can be raised very uniformly over the volume of the disk.

Devices are fabricated from SOI substrates (250nm device layer, 3 μ m buried oxide, Soitec). The first fabrication step is to implant the device layer with Boron to achieve the desired resistivity. The Comsol simulations inform us that the power dissipated in the device needed for broad tuning is \sim 2mW. To achieve this power at 25V, the resistance of the device must be less than 625k Ω . Because we are aiming for Q factors of 10,000-20,000, and because the dominant contribution to photon decay will be scattering by the contacts, we can afford some photon lifetime degradation by free-carrier absorption and plasma losses due to doping. We achieve the desired trade-off between low resistivity and high Q by doping to a concentration of 10^{18} B⁺/cm³ which gives a resistivity of 0.04 Ω ·cm. At this carrier concentration we estimate the quality factor limited by free-carrier absorption and plasma losses to be on the order of 10^5 . In practice, microdisks without contacts fabricated from substrates with such doping concentrations have modes with Q factors from 15,000-50,000, and final wired microdisk devices have resistance of approximately 250k Ω , thus satisfying our criteria that the resistance be less than 625k Ω and Q greater than 20,000 but indicating that less doping could lead to cavities with higher Q factors and still low enough resistances. Boron was implanted to a fluency of 2.5×10^{13} B⁺/cm². Substrates were annealed in a N₂-purged furnace at 1000°C for 20min. The native oxide was removed, and samples were coated with XR-1541 electron beam resist (Dow Corning). Etch masks for disks of 10 μ m diameter with 200nm wide Si electrodes leading to Si pads for wire bonding were patterned. Etching was performed with ICP RIE using SF₆ and C₄F₈. An additional photolithography and deep etching step was performed to isolate the devices on a plateau for tapered-fiber access, as described in Chapter 7. The samples were cleaned with piranha etch and undercut with buffered hydrofluoric acid. The silicon samples were mounted on quartz chips patterned with gold regions for electrical contact. Wire bonds were made

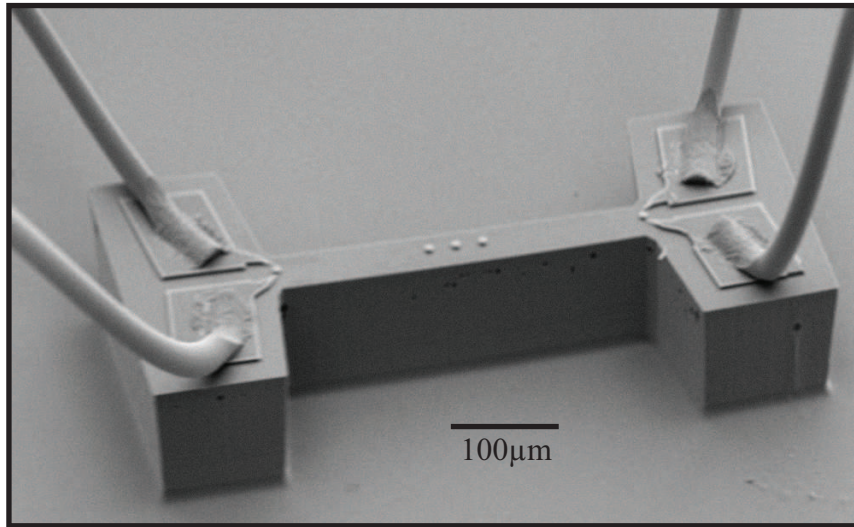


Figure 9.5: SEM image of the full layout of a tunable microdisk sample. All disks are seen to be isolated on a plateau. The wire bonds are made directly to the Si pads which taper to the nanowire contacts which enter the side walls of the Si microdisks. The nanowire contacts as well as the wire bonds sweep away from the region of the disk where the tapered fiber accesses the disk. Three unwired disks are observable at the center of the structure. These disks are included in the fabrication process for the purpose of comparing wired to unwired disks.

from the gold regions directly onto the silicon contact pads. An SEM image of the final completed structure is shown in Fig. 9.5.

As can be seen in Fig. 9.5, the final tunable microdisk sample design consists of two opposing tunable wired microdisks with three non-wired microdisks also isolated on the plateau for comparison during tapered-fiber spectroscopy. The samples were laid out in this manner to facilitate rapid experimental characterization. It was important to have both wired and non-wired microdisks on the same chip to compare spectra. The wired microdisks were oriented in this opposing manner because, as can be seen in Fig. 9.5, the aluminum wires are wire bonded to the substrate and arc up off the plane of the chip. If care is not taken, it is quite possible to crash the tapered fiber into these wires during experimental characterization. Therefore we oriented the wire bonding pads back away from

the disks so that the tapered fiber to access the disk without interfering with the aluminum wires, and we place all five disks (two wired and three non-wired) such that once the fiber is placed near the first wired microdisk it can easily be moved to study the other four disks without having to be lifted above the wire bonds of the other wired microdisk. While it is certainly possible to cram more microdisks onto a chip we found that it was better to fabricate a few high-quality devices and study them thoroughly rather than to fabricate many devices and become confused by which data corresponded to which device. In a general fabrication run two to eight samples similar to that shown in Fig. 9.5 would be fabricated simultaneously. This resulted in 10 to 40 disks requiring experimental characterization. Obtaining thorough tapered-fiber spectra from this many disks is a very time-consuming task. In our experience it was always the case that after studying just a few of these devices we would learn something that would educate us on a better device design to be fabricated next. For this reason it was better to fabricate in small batches more often to save material, time, and to more rapidly evolve our device design.

Several aspects of the device geometry can be modified depending on functionality needs and fabrication capacity. Our choice to undercut the disks to isolate the structures on pedestals was made for two reasons. First, it reduces the thermal contact to the substrate and therefore improves the energy efficiency. Second, the raised disk enables easier access for tapered fiber characterization. If one wishes to use on-chip waveguides, an undercut may still be performed, but care has to be taken to only undercut a small region around the disk so as to not lift off the entire waveguide. For non-undercut devices, the main drawback will be increased energy consumption, but the cooling time will be reduced. Our choice to have 200nm contacts was a compromise between high- Q , structural integrity, and low operating voltage. If one wishes to further improve the Q this can be achieved with a combination of increasing the resistivity of the substrate (by reducing ion implantation dosage) and reducing the width of the contacts. Both modifications will increase the overall resistance of the device and therefore lead to a higher operating voltage. If one can afford these costs, the Q factors can be improved substantially above those presented here. Additionally, the

choice to fabricate tunable microdisks with wires directly in the microdisk sidewalls was motivated by the ease of fabrication. If one wishes only to utilize first-radial-order modes, a superior design would be either to pattern a metal ring at the center of the disk to be used as a heater or to pattern silicon wires which make contact to the inner wall of a microring resonator so that current is passed only through the ring where the optical mode resides. This is likely to be a highly energy efficient design and can be optimized to minimize interaction of the wire contacts with the optical mode. With a suitable design, either of these approaches could lead to broad tuning without contacting the region of the optical mode. The drawback is that in either of these cases contacts have to be made near the center of the structure, and these must be accessed by metal vias that rise up and over the region of the optical mode. This is likely to be at least a three-mask process which is best performed with deep-UV lithography.

9.3 Broad tuning and general characteristics of wired microdisk modes

The optical properties of the microdisks were characterized using tapered-fiber spectroscopy, as discussed in Chapter 6 and in Refs. [72, 95, 136, 144]. With this technique, the evanescent field of the fiber optical mode couples to the microdisk, and resonances are identified as dips in the fiber transmission spectra. Q factors are obtained by fitting the experimental data to a Lorentzian.

Figure 9.6 shows tapered-fiber spectra obtained from a $10\mu\text{m}$ tunable silicon microdisk. The first spectrum had zero applied voltage. The following scans had 10V, 15V, 20V, and 25V respectively. The resonances are seen to shift by 10nm-14nm. Several prominent features have been labeled and their characteristics analyzed in more detail. The $\text{TM}_{2,25}$ mode initially at 1541.77nm shifts to 1552.35nm with 1.6mW of joule heating, a shift of 10.58nm. The Q factor of this mode is measured to be 11,424 in the first spectrum and 12,118 in the final spectrum. These measured Q factors depend significantly on loading

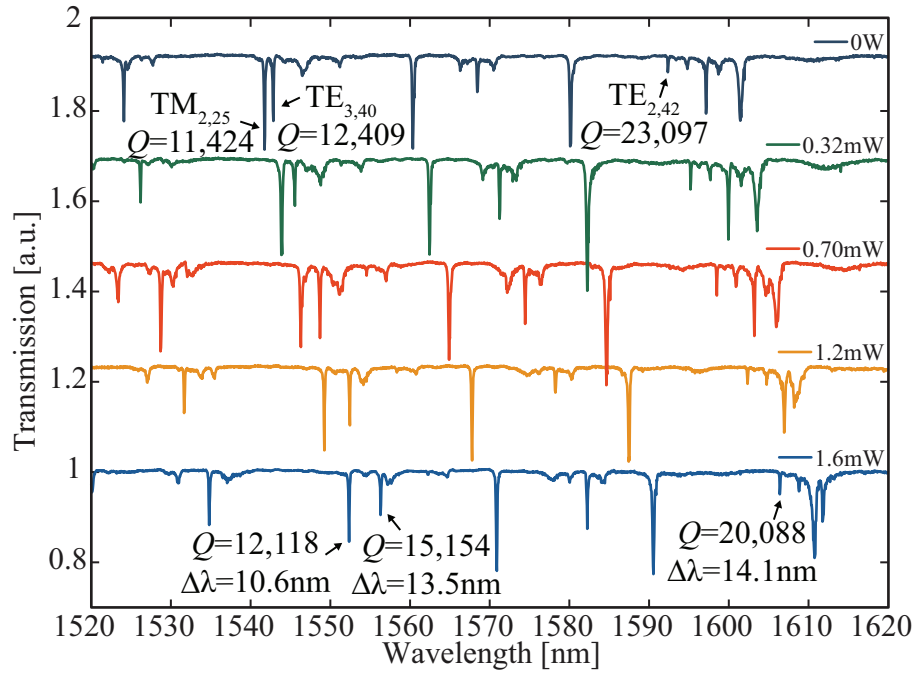


Figure 9.6: Tapered fiber spectra of a tunable microdisk. Spectra are shown at tuning powers from 0W to 1.6mW. Several prominent peaks are labeled and their behavior characterized.

from the fiber [72, 144], and the discrepancy between these two numbers is likely due to minor shifts in the fiber position between the two measurements. The actual unloaded Q is surely higher than in these measurements. In contrast to this TM mode, the $TE_{3,40}$ mode initially at 1542.82nm shifts 13.51nm to 1556.33nm and has a Q factor of $\sim 15,000$ throughout the measurements. The mode observed to have the largest shift and highest Q was the $TE_{2,42}$ mode initially at 1592.38nm and moving to 1606.45nm, a shift of 14.07nm. The Q of this mode was around 20,000 in all measurements, and was measured to have the highest Q in the first spectrum at 23,097. In the final spectrum the measured Q was 20,088. The presence of a multitude of modes with Q factors exceeding 10,000 and some exceeding 20,000 is a strength of this structure and shows that the perturbation due to the electrodes does not degrade the cavity below a functional level.

It is important to understand the various contributions to the measured Q factors. The measured Q will have several contributions, as described by Eq. 9.1.

$$Q_M^{-1} = Q_D^{-1} + Q_C^{-1} + Q_P^{-1}. \quad (9.1)$$

Here Q_M is the measured Q factor obtained by fitting a Lorentzian function to the tapered fiber data. Q_D is the contribution to the Q factor resulting from mechanisms associated with the extra electrons in the material due to doping of the substrate. Q_C is the contribution due to scattering by the contacts. Q_P contains all other parasitic contributions such as scattering due to sidewall roughness not associated with the contacts as well as loading due to the tapered fiber waveguide. The contribution to Q due to radiation loss is negligible in a disk of this size. We have obtained estimates for each of these experimentally by studying different systems with isolated variables. To estimate Q_P we have studied microdisks made with the same fabrication techniques but on substrates without doping and with no contacts in the sidewalls for tuning. In our experiments the measured Q factors of these structures were 40,000-230,000 depending on the specific sample and mode. While it is quite possible to obtain substantially higher Q factors in silicon microdisks [95], doing so necessitates a different choice of electron beam resist and an additional resist reflow step. This reflow is incompatible with our fabrication of nanowire contacts. To estimate Q_C we again utilized

the undoped SOI, but fabricated wired microdisks on the substrates. In these structures Q factors ranging from 15,000-47,000 were measured. Assuming $Q_P = 230,000$ and $Q_D = \infty$, this gives $Q_C = 59,000$ for the mode of highest- Q measured in a wired microdisk without doping. To estimate Q_D we have measured the Q factors of disks created from the doped SOI substrates but without contacts for tuning. In these structures the measured Q factors were in the range of 17,000-50,000, but few exceeded 30,000. We can use these data to make educated guesses about the different contributions to the Q factors in the spectra shown in Fig. 9.6. For example, assuming $Q_P = 200,000$ and $Q_D = 45,000$, using the value of $Q_C = 22,000$ in Eq. 9.1 gives $Q_M = 13,800$, roughly in agreement with the measured Q factor of the $TE_{3,40}$ mode shown in Fig. 9.6. Using the same values for Q_P and Q_D , a value of $Q_C = 47,000$ gives $Q_M = 20,600$, which agrees well with the lowest measured value of the Q factor of the $TE_{2,42}$ mode. It is important to note that while these numbers give estimates for the various contributions to the measured Q factors in these experiments, there is a great deal of room for improvement in future devices both in optimization of the dopant dosage, the contact geometry, and the fabrication, as discussed in Section 9.2.

We further analyze the data in Fig. 9.6 to gain insight into the relationship between mode shift and polarization. Figure 9.7(a) is experimental data of wavelength shift versus power for fifteen modes including modes of both polarizations and various radial orders. Figure 9.7(b) is a theoretical plot of wavelength shift versus power and index of refraction calculated numerically [144]. The temperature of the disk was determined as a function of power dissipated to joule heating using the Comsol simulation shown in Fig. 9.4(b). This temperature was then related to the index of refraction through the thermo-optic coefficient. The Comsol simulations give values for the power which are nearly a factor of two greater than the measured values. This is likely due to minor discrepancies in the geometry and material parameters used in the simulations. In both the theoretical and experimental cases, the modes are seen to separate into two distinct groups depending on the polarization with TE modes shifting $\sim 25\%$ more than TM modes. This dependence on polarization was not

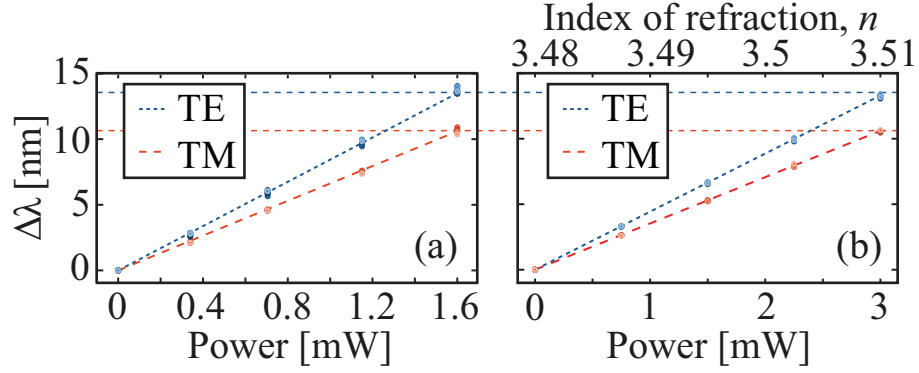


Figure 9.7: Difference in mode shifts between TE and TM polarized modes. (a) Experimental data of resonant wavelength shifts for fifteen modes of various radial orders as a function of power. TE and TM modes are seen to separate into distinct groups independent of radial mode order. (b) Theoretical prediction of mode shifts for six TE and six TM modes of various radial mode orders plotted as a function of power. The corresponding index of refraction labels the x -axis on the top.

observed to depend on radial mode order and can be understood by consideration of the fraction of electrical energy stored in the cavity. This quantity is given by

$$\xi = \frac{\int_{\text{disk}} \epsilon(\mathbf{r}) |\mathbf{E}(\mathbf{r})|^2 d\mathbf{r}}{\int_{\text{all space}} \epsilon(\mathbf{r}) |\mathbf{E}(\mathbf{r})|^2 d\mathbf{r}}. \quad (9.2)$$

We have calculated the quantity ξ given by Eq. 9.2 and the wavelength shift as n goes from 3.48 to 3.51 for six TE and six TM modes of various radial orders with wavelengths near 1550nm. For the TE modes the average value of ξ was 0.9796 with a standard deviation of 8.121×10^{-4} , and the average value of wavelength shift was 13.22nm with a standard deviation of 0.2798nm. For the TM modes the average value of ξ was 0.7836 with a standard deviation of 1.204×10^{-2} , and the average value of wavelength shift was 10.56nm with a standard deviation of 0.1701nm. The ratio of the average value of ξ to average value of wavelength shift is $7.409 \times 10^{-2} \text{nm}^{-1}$ for TE modes and $7.420 \times 10^{-2} \text{nm}^{-1}$ for TM modes. The similarity in these two values indicates that the predominant factor in dictating wavelength shift is the fraction of electrical energy stored within the cavity.

The difference in electric field confinement between modes of the two polarizations

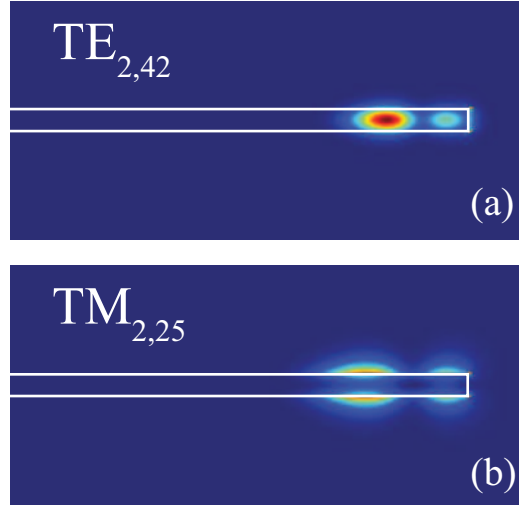


Figure 9.8: $|\mathbf{E}|^2$ calculated for the (a) $\text{TE}_{2,42}$ mode and (b) $\text{TM}_{2,25}$ mode. Field profiles are plotted in the $\rho - z$ plane and are assumed to have $\exp(im\phi)$ azimuthal dependence.

can be seen in Fig. 9.8 where we have plotted the magnitude of the electric field squared for characteristic second-radial order modes. Figure 9.8(a) shows the well-confined $\text{TE}_{2,42}$ mode, and Fig. 9.8(b) shows the $\text{TM}_{2,25}$ mode with prominent near field lobes forced outside the disk by the boundary conditions. The increased localization of TE modes within the disk relative to TM modes can be thought of as leading to an effective thermooptic coefficient which is the product of ξ with the bulk thermooptic coefficient of Si. For TE modes this is $1.82 \times 10^{-4}\text{K}^{-1}$ and for TM modes this is $1.46 \times 10^{-4}\text{K}^{-1}$. This difference in mode shift between the two polarizations has important consequences for applications which seek to utilize two nearby modes. By making use of this feature one can tune the spacing between two modes as well as the absolute position of each mode. It is also possible to tune two modes into or out of degeneracy.

We proceed now to discuss data from another tunable wired microdisk. The full tapered fiber spectrum of this sample is shown in Fig. 9.9. This spectrum has much in common with the spectrum shown in Fig. 9.6. There are several modes with Q factors near 20,000. For example, consider the mode near 1578nm. We have investigated the Q factor of this mode systematically by taking successive tapered-fiber spectra as the fiber was moved away

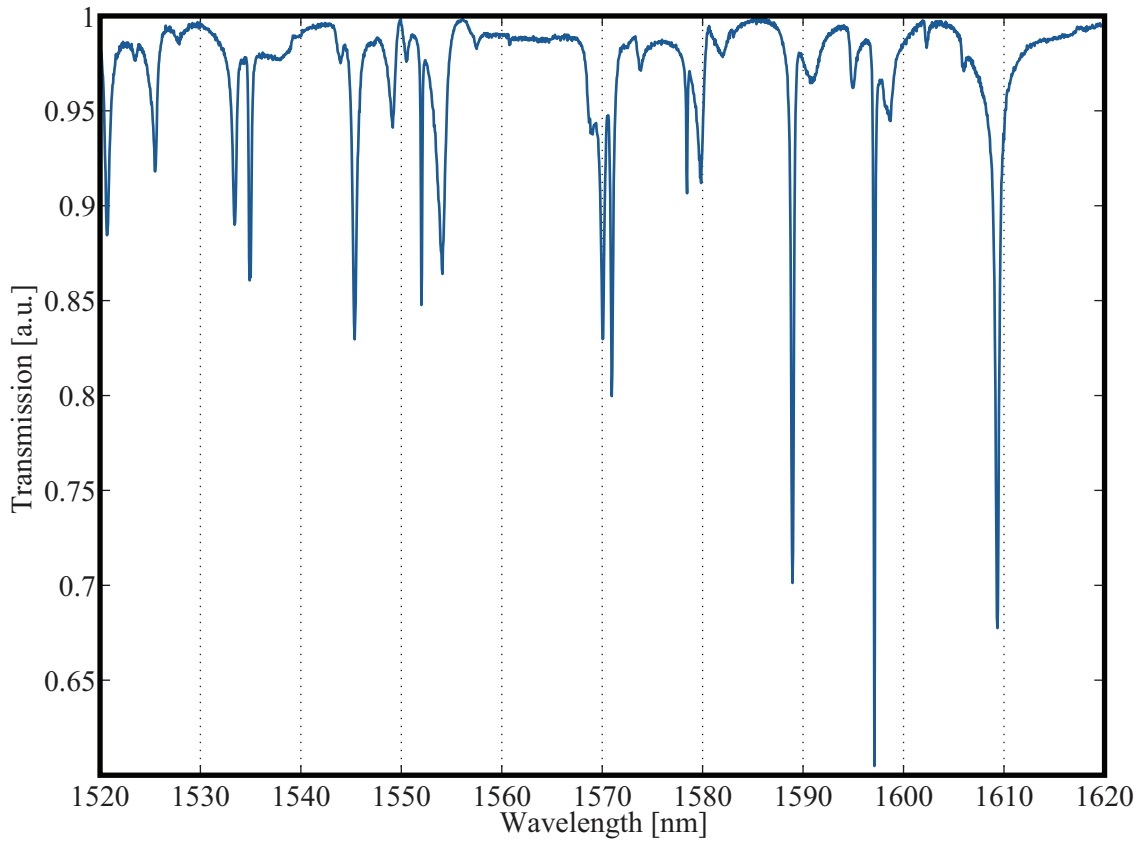


Figure 9.9: Tapered fiber spectrum from a wired microdisk. Several features of this spectrum will be analyzed in the following plots.

from the disk. This data is shown in Fig. 9.10. The highest measured Q of this resonance exceed 18,000. As discussed above, there are several factors that impact this Q factor, the most important of which being the material absorption due to doping and the scattering due to the contacts. We show Fig. 9.10 in addition to the TFS data in Fig. 9.6 to emphasize that our results are repeatable, and that all of our successful samples fabricated with this technique give rise to structures with reasonably high Q factors.

While high Q is often a priority, depending on the application depth of coupling can also be as significant a consideration. The resonance near 1597nm provides some of the best depth of coupling to the tapered-fiber waveguide. We investigated this resonance to determine it's Q factor as well as its potential for switching operation. In Fig. 9.11 we show the fit of a high-resolution tapered-fiber spectrum of this resonance to a Lorentzian function. The extracted Q factor is $\sim 15,000$. For any application that seeks to use a resonator in essentially two states—on or off—critical considerations are the voltage and power required to shift the resonance by a linewidth. A resonance with a Q factor of 15,000 is a good candidate for telecommunications applications due to the compromise between required mode shift—which one would like to minimize—and usable bandwidth—which one would like to maximize [103]. It is often advantageous to be able to achieve operation of a device under 5V, so we wanted to see if we could shift a resonance with $Q = 15,000$ (FWHM $\sim 0.1\text{nm}$) with less than 5V. Of course, the resonance shift depends on the power dissipated to joule heating, not on the voltage alone. Still, with the doping and conductivity chosen by the above considerations we wanted to know the potential for switching operation. As is shown in Fig. 9.12, 5V is more than enough to shift this resonance a full linewidth. The power dissipated to shift the resonance by the 0.7nm shown in Fig. 9.12 was $\sim 100\mu\text{W}$. Depending on the on/off transmission ratio required for a certain application, it may only be necessary to shift the mode by 0.1 – 0.2nm which can be achieved with $\sim 20\mu\text{W}$ of power dissipated to joule heating. This is extremely energy efficient compared to the carrier injection or extraction techniques utilized in modulators [131–134] or compared to thermal tuning structures with metallic heaters separated from the optical layer by

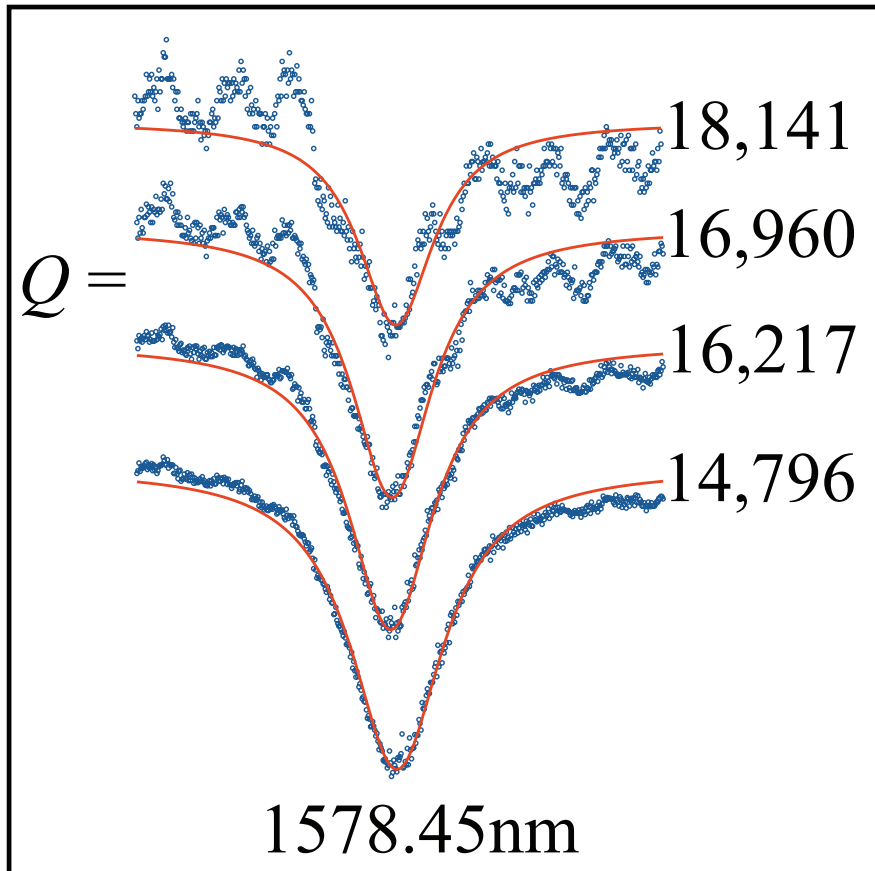


Figure 9.10: Lorentzian fit to a high-resolution scan of the resonance near 1578nm. The contribution to loading of the Q from the fiber is assessed by taking successive measurements while moving the fiber away from the disk. The resulting measured Q exceeds 18,000 and is affected by contributions to loss from material absorption due to doping as well as scattering from the nanowire contacts.

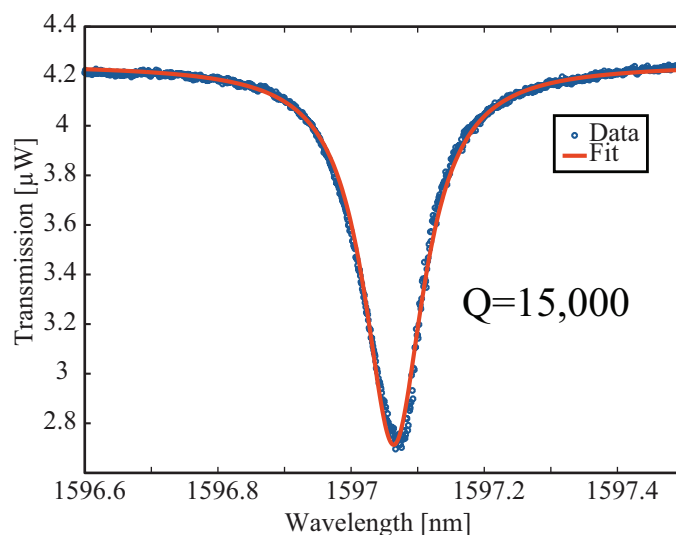


Figure 9.11: A Lorentzian fit to the resonance near 1597nm. This is the resonance with the best coupling to the tapered fiber. The measured Q factor exceeds 15,000.

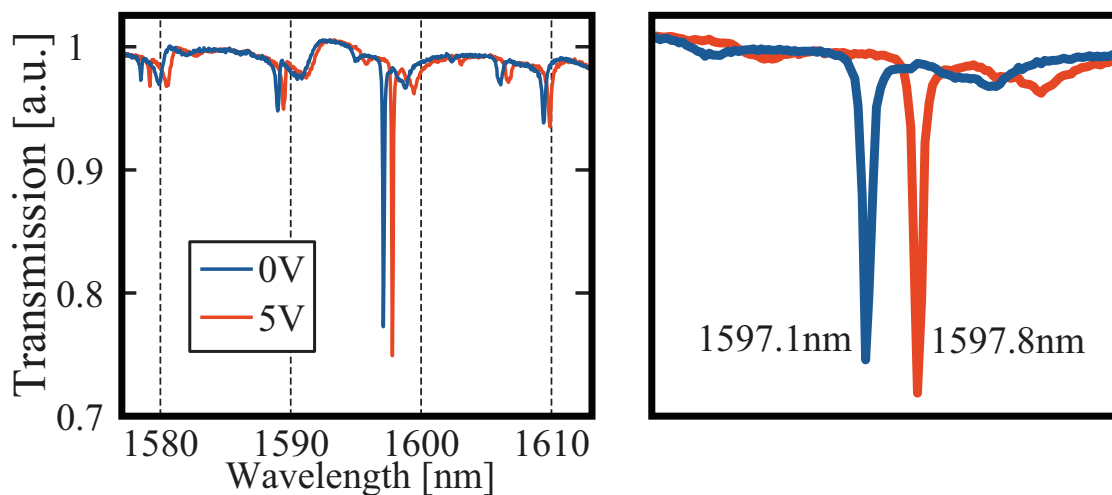


Figure 9.12: Switching data from the same resonance as shown in Fig. 9.11. With the application of 5V ($100\mu\text{W}$) the well-coupled resonance can be shifted by far more than a full width at half maximum. While the thermal switching may not be fast, it can be highly energy efficient.

a cladding layer [141]. However, thermal tuning will always be slower than free-carrier techniques. For ultrafast switching, free-carrier techniques will likely be worth the energy cost. In that context one usually cites the energy required per bit. Although we would like to measure this quantity in our structure, the infrastructure was not available at the time of this work. Still, we can estimate this quantity. If we assume $20\mu\text{W}$ is required to switch from a 0 to a 1 state, and assume the switching time is $1\mu\text{s}$, as claimed by some to be the limit of speed on thermal tuning [12], then 20pJ are required to shift from 0 to 1. As argued in Ref. [134], to find the true power consumption of the device one must multiply this number by $1/4$ to account for the equal probability that the next bit is as likely to be a 0 as a 1. Thus, if we assume $20\mu\text{W}$ is required to shift a linewidth and we assume a $1\mu\text{s}$ switching time the power required should be 5pJ/bit , far greater than the 85fJ/bit reported with a reverse-biased vertical $p-n$ junction operating at 10Gb/s in a Si microdisk reported in Ref. [134]. If, on the other hand, we assume a switching time of 1ns , as some have argued is possible in similar thermally-tuned structures (see Appendix D), the energy use drops to 5fJ/bit , well below the reported record of 85fJ/bit , and below the 10fJ/bit goal of the industry. We are eager to pursue this work further to find out exactly what the switching speed limits are and how low we can drive the energy usage [10].

To close this section we demonstrate that the very same wired microdisk which can be used for low-energy, single-linewidth tuning can also be used for broad tuning with no modification except the voltage applied. Figure 9.13 shows tapered-fiber data of broad tuning observed in the same sample studied in Figs. 9.9-9.12. In Fig. 9.13 we show tuning in steps of 5V from 0V to 30V . Broad tuning of up to 18nm is observed at an applied voltage of 30V (3.2mW). In this sample such broad tuning was demonstrated with complete reversibility and no degradation in the Q factors of the modes.

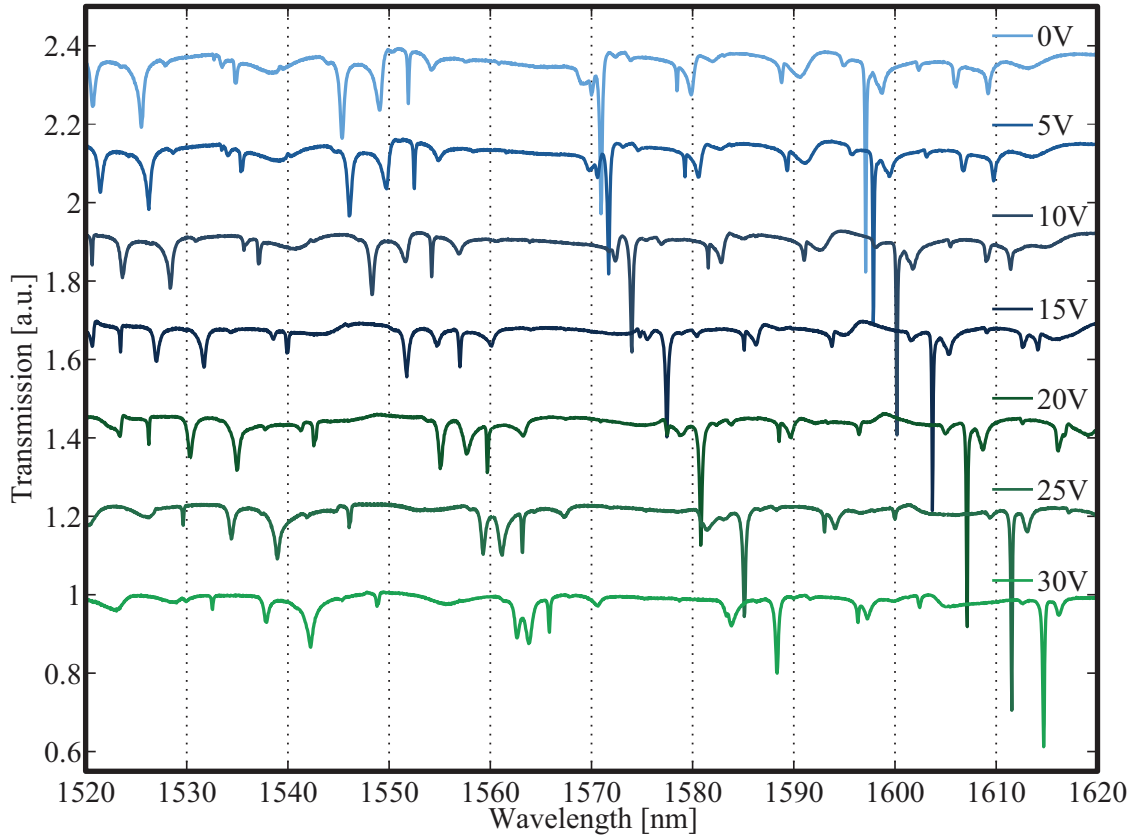


Figure 9.13: Tapered-fiber spectra of broad tuning in the same sample studied in Figs. 9.9-9.12. Here we show spectra taken at applied voltages from 0V-30V in 5V steps. The powers are 0W, $120\mu\text{W}$, $550\mu\text{W}$, $120\mu\text{W}$, 1.1mW, 1.7mW, 2.4mW, and 3.2mW respectively. This disk is slightly less energy efficient than the sample studied in Fig. 9.6, most likely due to a slightly broader pedestal.

9.4 Damage to microdisk mode spectrum due to sidewall contacts

We conclude this chapter with a discussion of the biggest weakness of this structure which will serve as a segue into the our discussion on ways to improve the device and prospects for future work.

In Fig. 6.5 we showed a tapered fiber spectrum from a silicon microdisk with $10\mu\text{m}$ diameter. This was an unperturbed unwired silicon microdisk, and in Fig. 6.6 we were able to identify four TE mode families and two TM mode families. This is what one would expect from a pristine silicon microdisk of this diameter. In Figs. 9.15-9.15 we present a similar analysis of a tapered fiber spectrum from a wired Si microdisk of the same diameter.

By analyzing the spectrum in Fig. 9.15 with the same technique utilized to identify the mode families in Fig. 6.6, we were only able to identify two TE and two TM mode families. In particular, the TE_1 and TE_2 mode families were not clearly observable. Inspection of Figs. 5.5-5.9 reveals that the TE_1 modes have the strongest field intensity just outside the perimeter of the disk. It is therefore logical that this mode family will be most highly impacted by the presence of a nanoscale contacts in the microdisk sidewall. The same argument can be made for TE_2 modes.

It is important to point out that the analysis of the data in Fig. 9.15 does not allow us to clearly identify the TE_1 or TE_2 mode families based upon well-defined FSRs that are in agreement with theoretical calculations. Still, this does not mean TE_1 or TE_2 modes are not present in the wired microdisks, but rather indicates that the presence of the nano wire contacts perturbs these modes in such a way that their wavelengths are shifted and do not occur exactly as would be predicted in an unperturbed Si microdisk. In Fig. 9.15(e) we have highlighted in blue six modes with small coupling as would be expected between TE_1 and TE_2 modes and a tapered optical fiber, as discussed in Chapter 6. Although these modes are not spaced by a well defined FSR, they are likely still due to modes with field profiles highly resembling those of a TE_1 or TE_2 mode, as shown in Fig. 5.5 and 5.6.

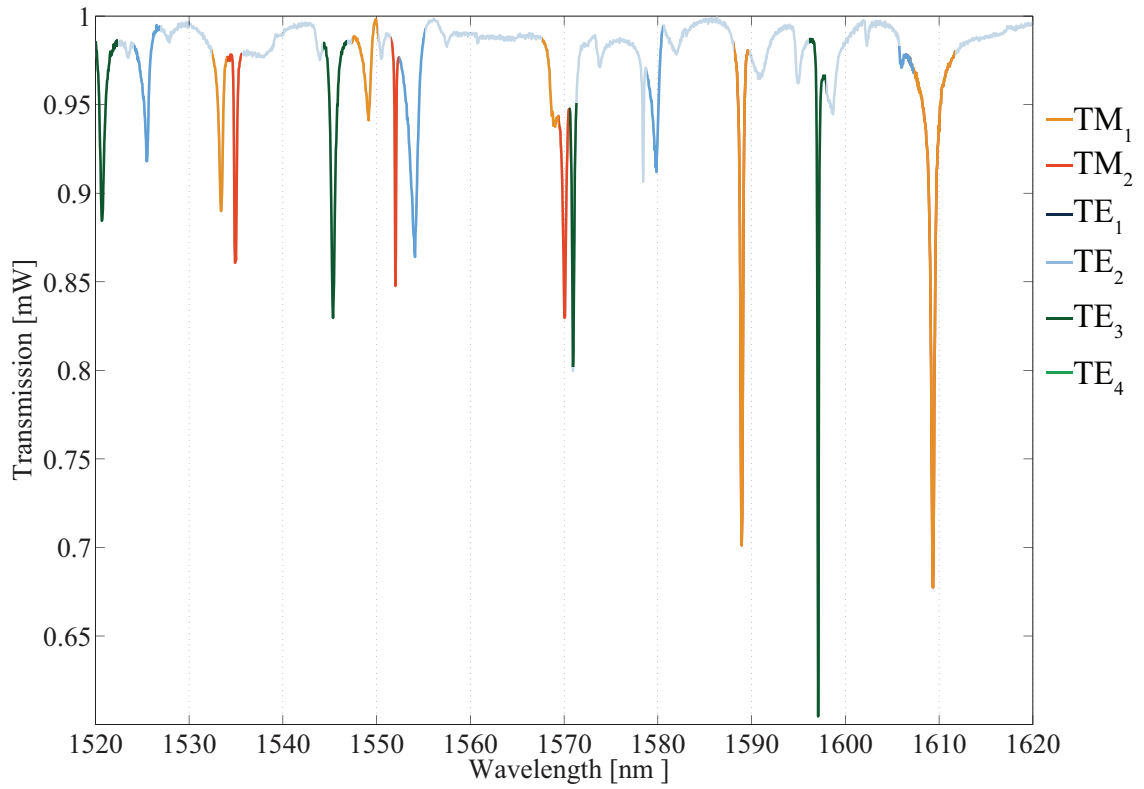


Figure 9.14: Color-coded mode family identification of the same tapered-fiber spectrum as shown in Fig. 9.9. The TE_1 and TE_2 mode families are not identified with the same techniques as described in Section 6.2.

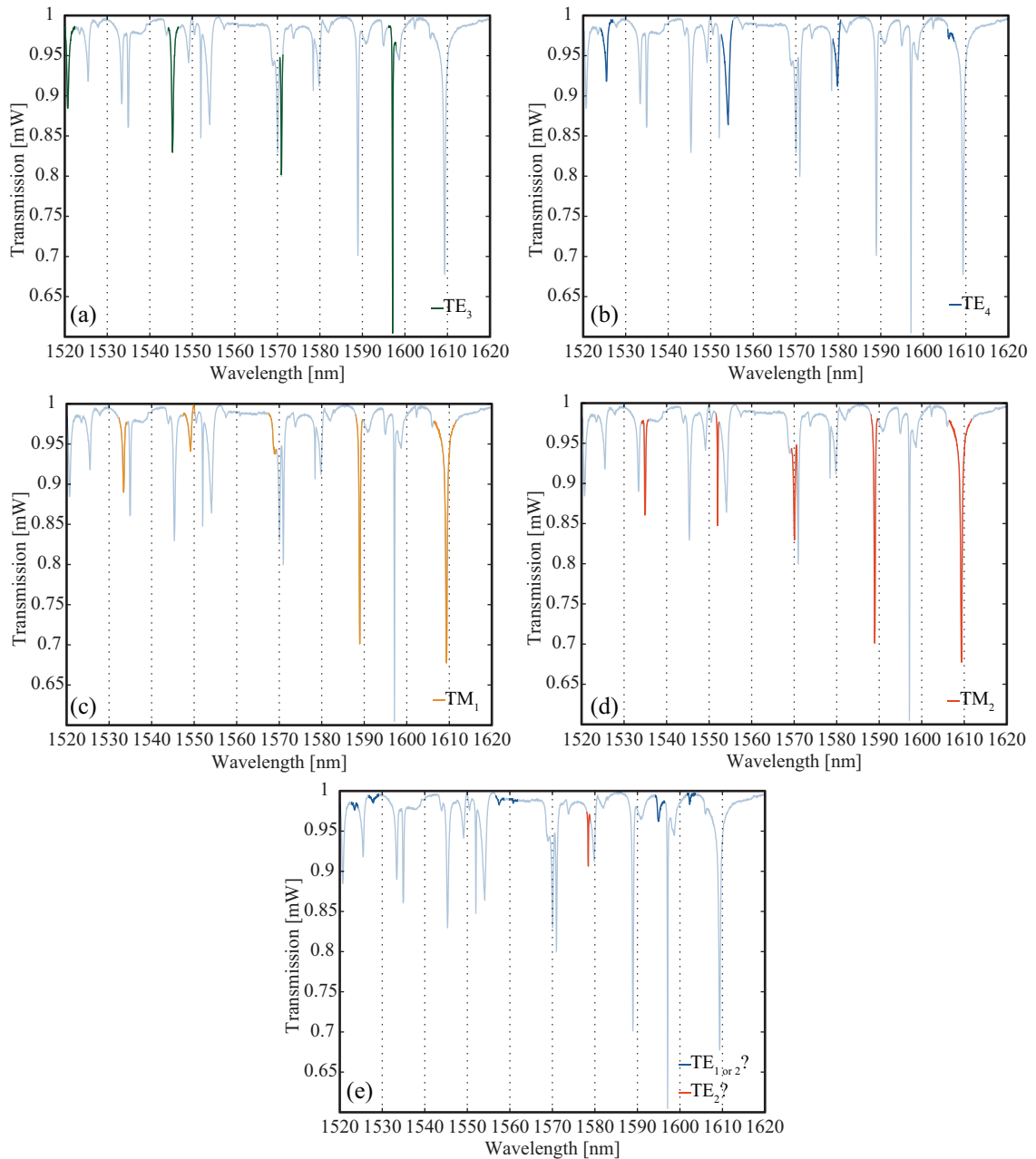


Figure 9.15: The same spectrum as shown in Figs. 9.9 and 9.14, but with individual modes families highlighted. The techniques described in Section 6.2 to identify mode families lead us to identify the TE_3 (a), TE_4 (b), TM_1 (c), and TM_2 (d) mode families, but the TE_1 and TE_2 mode families elude our identification. In (e) we have highlighted in blue six small peaks which are likely the scattered remnants of TE_1 and TE_2 modes which have suffered due to the perturbation of the nanowire contacts. In red we have highlighted the peak characterized in Fig. 9.10

In addition to these six small peaks shown in blue in Fig. 9.15(e), we have also highlighted one peak in red. This feature shown in red is the resonance investigated in Fig. 9.10. This is clearly a well-defined resonance, however it does not seem to fit into any mode family. Based on the magnitude of this mode's shift with temperature, we can identify it as a TE mode. Based on the depth of coupling, this mode would appear to be a TE₂ mode. Since we cannot identify a well-defined FSR relating this mode to a family, we hypothesize that the presence of the nanowire contacts perturbs some modes in a mode family more than others depending on the spatial overlap of the different modes with the scattering contacts. The different modes in a mode family will have differing overlap with the contacts due to the variance in angular dependence of the field profile.

It is important to summarize the weaknesses of this device. The presence of the nanowire contacts has deleterious effects on the first and second radial order TE modes. This is a fairly significant problem because in general the lower radial order TE modes are those most suitable for coupling to a waveguide. Although we believe some TE₂ modes are relatively unaffected by the contacts the general structure of the mode family is damaged. For some purposes such as on-chip information processing components, this renders the device unsuitable. However, for applications such as sensing the most important consideration is that you have a single high- Q resonance whose shifts can be monitored to signal detection events. For this purpose the device is already highly-functional in its current form. An additional weakness of this wired microdisk design is that the contacts degrade the Q factors. For ultrahigh- Q applications this will be a limitation, but as discussed above I believe these Q factors can be improved by at least a factor of four with better fabrication techniques and reduced doping, so unless one needs Q factors exceeding 10^5 (in which case Si microdisks are not suitable anyway), I don't see this as an insurmountable problem.

Having spelled out the major weaknesses with this device, let me reiterate what I see as the greatest strength of this device. In this tunable microdisk design we are utilizing thermal tuning which allows for extremely broad, stable tuning of microdisk resonances. What is really new in our device is that we are heating the discs with current passed directly

through the optical cavity. This allows for extremely-broad, highly-energy-efficient tuning. Our device design is also extremely easy to fabricate. In the closing chapter of this thesis we will discuss a device design that is somewhat more difficult to fabricate, leverages the strength of joule heating with current right through the optical cavity, and overcomes the problem of damaging the TE_1 and TE_2 mode families.

9.5 Summary of wired microdisk work

In conclusion, we have presented a study of a tunable silicon microdisk structure. The tuning range was demonstrated to be as much as 14nm for TE modes and 10nm for TM modes. A Q factor exceeding 23,000 was observed for a mode that was tuned 14.07nm by the application of 1.6mW of power. The structures are made from standard SOI wafers in a single lithographic step. These tunable resonators have many potential applications in a wide range of on-chip photonic devices and have the potential to enable new systems with coupled electronic and photonic degrees of freedom. Further, the fact that these tunable silicon resonators do not depend on the presence of a cladding layer for operation enables them to be used in a range of sensing applications.

Chapter 10

Future Directions

10.1 Tunable Interactions

In Chapter 9 we discussed our device design which enabled broad, energy-efficient tuning of the resonant modes of Si microdisks. In this chapter we will discuss new physical systems and technologies enabled by the tunable microcavities. All of the ideas presented in this chapter are things I would like to study more if I had infinite time and resources. Hopefully I will be blessed in my next position to be able to continue work on related systems.

Perhaps the most exciting aspect of the system we have developed is that it enables tunable interactions between adjacent microcavities, microcavities and quantum emitters, or microcavities and waveguides or photonic circuits. It is really this aspect of tunable interactions that we would like to explore in future research with the system. Tunable interactions are important phenomenon in physics and have recently garnered much attention in the field of cold atomic physics. Tuning the interactions between colliding atoms inside the atomic gases by sweeping across a Feshbach resonance has been a very powerful tool for exploring Bose-Einstein condensation and the BEC-BCS crossover.

In Fig. 9.1 we showed a photonic molecule comprised of three silicon microdisks and mentioned the challenge of actually getting coupling between the microdisks due to minute resonance shifts which result from subtle fabrication imperfections. Our tunable microdisk

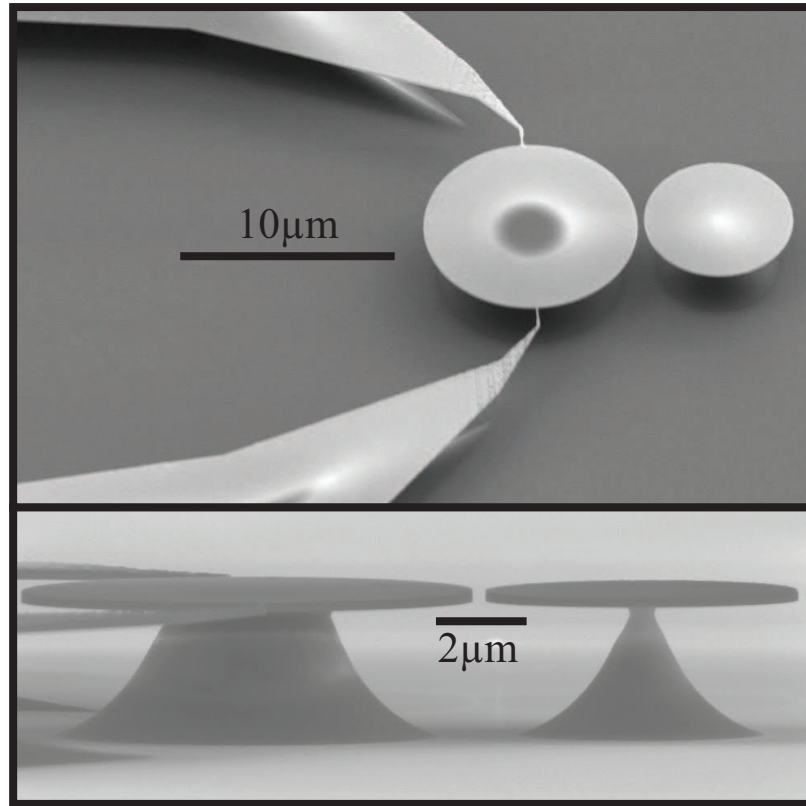


Figure 10.1: Dimer photonic molecule with one wired microdisk capable of being tuned into resonance with the adjacent disk. Here, one of the disks has been made smaller than the other so the pedestal is smaller and more flexible for possible optomechanical experiments.

structure offers a method to overcome these resonance mismatches post-fabrication. We would like to explore a number of systems enabled by the controllable tuning of adjacent resonators and therefore the controllable interaction between the resonators. In Fig. 10.1 we show an SEM image of one such system. The structure in Fig. 10.1 can be conceived of as a simple diatomic photonic molecule, and the optical properties of this alone are worthy of investigation [129]. However, in Fig. 10.1 we are proposing utilizing this system for an even more sophisticated physical interaction, namely the optomechanical coupling of two adjacent Si microdisks [146–149]. As is shown in the bottom panel of the figure, one of the two microdisks has been made smaller than the other so that when the HF undercut is performed the pedestal supporting the smaller disk has a narrow waist of $\sim 100\text{nm}$. Such

a narrow glass pedestal will be flexible under small forces. The idea with this device is that one can tune the modes of the larger disk into and out of resonance with modes of the smaller disk, and on resonance an optical force will be present that will either attract or repulse the two cavities. This system offers a unique setting to explore fundamental aspects of optomechanical coupling [146] in a structure with tunable interactions.

Another way that we could utilize this dynamic cavity design to explore systems with tunable interactions is to utilize the cavities as resonators to study cavity QED. As was discussed in Chapter 2.2, there are many point defects in silicon that emit into narrow, zero-phonon lines. The quantum optics and cavity QED of these emitters is a subject that would be quite fascinating to study. One of the most important parameters in quantum optics is the Purcell enhancement which quantifies the enhancement of the spontaneous emission rate in a cavity versus the rate in free space. The Purcell enhancement is given by

$$F_P = \frac{3Q(\lambda/n)^3}{4\pi^2\nu_{\text{eff}}}, \quad (10.1)$$

where Q is the cavity quality factor, λ is the resonant wavelength, n is the index of refraction of the cavity, and ν_{eff} is the effective mode volume given by Eq. 8.4. To maximize the Purcell enhancement, and therefore maximize the effect a cavity mode has on an emitting species, one must maximize the ratio of Q/ν_{eff} . As was discussed in Chapter 8, the Q factor of a cavity decays exponentially with the diameter of the cavity while ν_{eff} decays linearly with the diameter of the cavity. However, this exponential rise in Q as the size of the cavity increases stops—in the case of silicon microdisks—in disks of diameter near $2.5 - 3\mu\text{m}$, above which Rayleigh scattering is the factor limiting Q . Therefore, to maximize the Purcell enhancement one should use a cavity with approximately this diameter to maximize Q and minimize ν_{eff} . The challenge for coupling narrow-line emitters to such small cavities is that the small cavities have a very large FSR of $> 100\text{nm}$. Therefore, it is difficult to fabricate a cavity with a resonance at precisely the wavelength where the quantum emitter will emit. One technique to overcome this limitation is to tune the resonance of the cavity to the emission wavelength, as shown in Fig. 10.2. Several techniques have been developed to achieve this, and we believe our tunable microdisk design is amongst the most suitable.

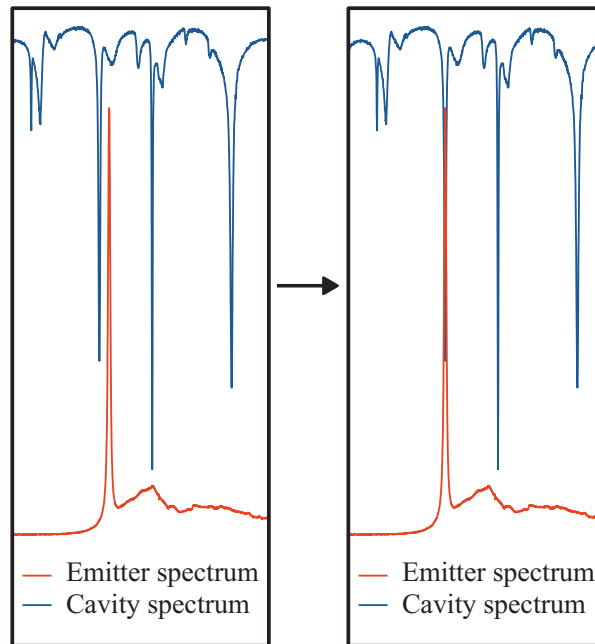


Figure 10.2: In cavity-QED it is critical that the emission wavelength be on resonance with a cavity mode. In small cavities (with desirable small mode volumes) the large FSR and sensitivity to fabrication imperfections makes it quite difficult to achieve coupling of narrow-line emitters to high- Q modes. Our device may offer a solution to this problem by enabling the cavity mode to be tuned to the emission wavelength.

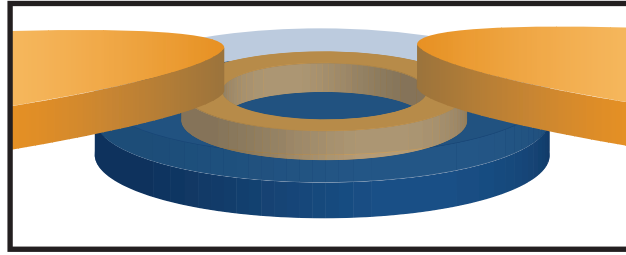


Figure 10.3: An alternative thermal tuning design. A metal ring is deposited at the center of the Si microdisk. Contacts made to this ring are isolated from the Si disk by a cladding layer. This structure requires several additional mask alignment steps (best performed with deep-UV lithography) and does not allow the disk to be used as a sensor, but the heating element is kept away from the whispering-gallery mode volume. Several features of this design were independently proposed in Ref. [10].

10.2 New tunable cavity designs

As was discussed in Section 9.4, the presence of the nanoscale contacts in the sidewall of the Si microdisks causes some damage to the optical modes. While this damage may be tolerable for many applications, it is worth discussing two potential device designs which could overcome this negative aspect of the design.

The first alternative thermal microdisk tuning design was actually conceived before the wired microdisk design presented in Chapter 9, but the fabrication is difficult enough that we sought a simpler design. Figure 10.3 shows a schematic of the device under consideration. In this device fabrication begins with patterning the microdisk. In the next step a cladding layer is deposited, presumably with PECVD. Another mask is aligned to the microdisk pattern, and RIE is performed to etch a thin ring through the cladding layer at the center of the microdisks. metal is then deposited in the etched trench. Another mask is that aligned to the pattern to deposit contacts on opposing sides of the metallic ring so that thermal tuning can be achieved with joule heating in the metal ring. This pattern would necessitate aligning at least three masks with micron-scale (or smaller) features. This is quite

difficult to achieve with electron beam lithography, and would best be performed with deep UV photolithography. However, this technology was not available to us at the CNS clean room. One advantage of this design is that the reduced resistance of the metallic heater would allow operation at much smaller voltages. It is likely, however, that more power would be required to achieve the same heating because it would be necessary to first heat the metal ring and then the microdisk through thermal conduction. Because metals are such excellent thermal conductors, much of the heat generated in the metal ring would efficiently be removed through the metal contacts. This would limit the efficiency of the device. Also, the device design requires a cladding layer, and this eliminates the possibility of using the device as a sensor. The greatest strength of this device is that the heating mechanism is located completely out of the way of the optical mode. First-radial-order TE modes would not be affected by this device.

Another potential thermally-tuned microcavity design is shown in Fig. 10.4. This device design is something of a hybrid between the device that we have studied in Chapter 9 and the device mentioned above where contact is made to the center of the disk. In this device we would construct a ring resonator and make contact to the center of it, still utilizing current passed directly through the optical medium to heat the disk. The fabrication of this device begins with the patterning of the micro-ring. A cladding layer is then deposited. Another mask is aligned to etch the holes and deposit the metal vias. A third mask is aligned for the deposition of the contacts. As in the above example, this fabrication is much more involved than our one mask process presented in Chapter 9. Fabrication of such a device is achievable in a standard CMOS foundry or any facility with deep UV lithography with $\sim 150\text{nm}$ feature capability and the ability to fabricate devices with sometimes 20 or more mask alignments. However, such involved fabrication was beyond our capability during this study. This device has several attributes which I believe make it the strongest candidate for future broad-tuning on-chip optical resonators. First, the ring resonator design eliminates all higher-order radial modes. This is advantageous for devices that seek single-mode operation with minimum noise and crosstalk. Also the presence of the contacts on

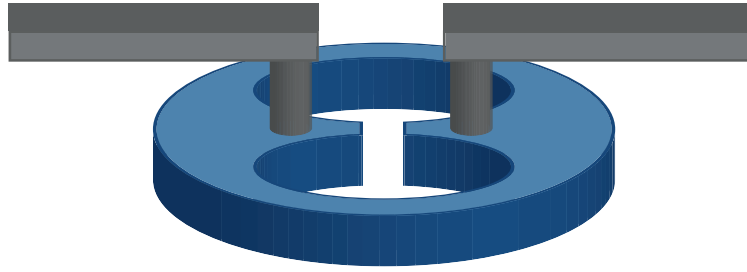


Figure 10.4: Another alternative thermal tuning design. Here, metallic vias are placed at the center of a microring. Current is passed through the ring. This design will be especially energy efficient due to the small thermal mass and the fact that the current is passing only directly through the optical mode volume. This structure will also require several mask alignments and is best fabricated with deep-UV photolithography. This device will likely be covered in a cladding layer, and so will also not be able to be used as a sensor. This design has been largely championed by Dr. Michael Watts [11, 12].

the inner wall of the micro-ring minimizes perturbation and scattering due to the contacts. By tapering the ring around its perimeter so that the ring is broader where the contacts enter and narrower away from the contacts one can select only first-radial-order modes which will occupy only the narrower portion of the ring and not be affected by the tapering near the contacts. A similar device design has been utilized by Watts et al. [11, 12] as the platform for a vertical $p - n$ junction microring modulator. This thermal tuning design will be quite efficient due to the very small volume of silicon that must be heated and the fact that all current will be passed directly through the optical mode volume rather than through the center of the microdisk as is the case in the device presented in Chapter 9. One drawback of this design is that the cladding layer, as above, eliminates the potential for the use of this device as a sensor.

It seems quite likely that thermal tuning of Si resonators will be of critical importance in many future optical information processing architectures. Although thermal tuning is not a fast switching mechanism, even devices that seek to use carrier injection or extraction as a means of rapidly modulating resonances must be tuned to the operating wavelength

of the photonic circuit [12]. For this purpose thermal tuning is the most energy-efficient and suitable candidate. Even without rapid modulation there are a number of exciting photonic circuit architectures that can be achieved with the capability of tuning resonators with microsecond switching times characteristic of thermal tuning. Several of these devices are presented in the next section.

10.3 Ultimate goals

There are several enormous goals of Si photonics. The first relates to large scale integration of optical components into CMOS devices [150, 151]. This is largely motivated by the need to overcome the bandwidth bottleneck of copper interconnects in high data rate and long distance data transmission. Progress is being made here by a number of groups, and most notably Intel who demonstrated the first 50Gb/s optical interconnect. They use a hybrid laser approach to generate the light. Another major push on this front is to use optical networks to connect multi-core processors to DRAM modules [152]. This is an active pursuit and will probably see success in the next five years. Thermally-tuned resonators will almost certainly be critical components in these architectures.

In addition to looking at dynamic photonic circuits as a means to enhance existing CMOS devices, there are many other fundamental optical experiments and novel devices which can be conceived. Slow light structures are being actively investigated [153, 154], and nonlinear propagation in resonator-modified waveguides has received a recent attention [130, 155, 156]. Many interesting and diverse devices such as delay lines [157] and rotation sensors [158] are possible with a similar photonic platform.

In the long term, perhaps the most exciting application of Si photonics and tunable resonators will be for optical computing. Tunable cavities will likely play a central role in chip-based optical computing, and mechanical degrees of freedom will likely enable even more sophisticated architectures for optical systems that process data and learn from stimulus [147]. To me, the most exciting prospect for Si photonics and for photonics in

general is the potential to create optical neural networks. An honorable ultimate goal of this line of research is to create structures which can learn from input stimulus to generate different output stimulus, make decisions, and perhaps even think. A sensible first step along this line of investigation is to design an optical neural network based on a building block with the “integrate-and-fire” functionality of an actual neuron. A chip-based version of such a building block based on Si waveguides and resonators should let no light down a waveguide until the intensity of incident light crosses a certain threshold, at which time an optical signal should be transmitted down the length of the waveguide. Following this integrate-and-fire element, the waveguide can route the signal to various locations with different weights. The determination of these weights as a function of time is integral to the ability of the circuit to learn. An example of one simple optical neuron design with integrate-and-fire functionality and variable output to two different channels is shown in Fig.10.5. In this device the first resonator performs the integrate-and-fire function while the second controls the subsequent routing. The second resonator controls the weight function between this element of the circuit and the two “downstream” elements to which this element is connected. All light through the circuit is at a given wavelength, and the first resonator is initially tuned to this wavelength. Optical input from any number of sources (similar circuit elements “upstream”) are stored in the first resonator. Once the intensity of light in the first resonator becomes sufficiently large, the nonlinear effect of two-photon absorption will heat the disk and cause its resonant frequency to shift relative to the incident light. While the first resonator is in this hot state, all incident light will pass the first resonator and arrive at the second resonator. The second resonator is tuned to split this signal down two paths with anywhere from 0-100% traversing either path.

While this crude optical model of a neuron may be naive, it illustrates the potential for an optical neural network comprised of integrate-and-fire components with variable coupling weights. Such a system could prove to be a powerful physical system to experiment with learning algorithms and to incorporate the speed and bandwidth of light into an neural network architecture.

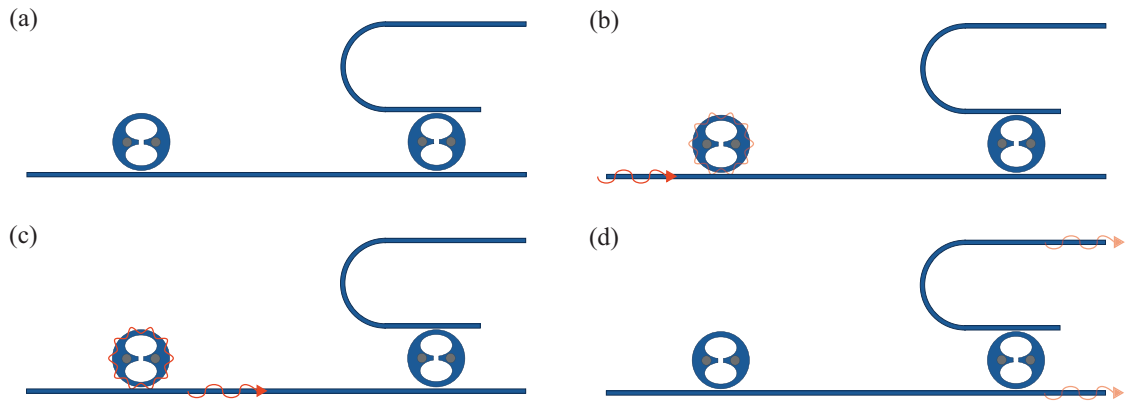


Figure 10.5: An optical device with integrate-and-fire behavior and variable output routing. The design utilizes two tunable resonators. (a) The device with no optical input. The first resonator is tuned to a given wavelength. For this design, all light in the circuit is at this wavelength. The tuning of the second resonator will be discussed shortly. (b) The optical input (possibly arriving from many independent channels) begins to build up in the first resonator. (c) The integrated optical field has built up to the point where it has heated the first resonator and detuned its resonant frequency. The incident optical signal now passes the first resonator. (d) The optical signal which passed the first resonator arrives at the second resonator and is split into two paths. The second resonator is tuned to determine the fraction of the light that travels down each path.

Appendix A

Erbium doping, porous silicon, silicon nanocrystals, and Raman generation

A number of techniques have been utilized in recent years to try to overcome the problem of poor silicon emission due to the indirect band gap [32, 33].

A.1 Er doping

Erbium (Er) doping of Si has been intensively studied for over twenty years, and early demonstrations of electroluminescence were very hopeful [159]. Er has an intra-4*f* shell transition with emission at $1.54\mu\text{m}$. This wavelength happens to fall at a minimum of silica absorption, a feature that has led to its wide use for telecommunications applications in silica optical fiber amplifiers. The nature of the optical transition of interest is defined by the electronic structure of Er^{3+} , and is perturbed little by the presence of the Si lattice. This differs from the nature of point defects (such as the *G* center to be discussed shortly) in that it is not meaningful to speak of the electronic structure of a point defect in the absence of the lattice; a point defect only exists within the atomic and electronic framework of the surrounding lattice. Still, Er-doped Si does not quite fall into the category of a system wherein Si is simply an inert host medium for the optical species. In Er-doped Si, Er (which, due to its rare-earth nature, ionizes to Er^{3+}) maintains key properties of its

electronic structure, but is also intimately connected to the electronic band structure of the surrounding Si.

Despite the many appeals of Er doping of Si, Er luminescence is quenched with temperature. An Auger process with either an electron or a hole are responsible for the quenching between 15K and 120K. Above 120K an energy back transfer process makes luminescence improbable. The fact that both mechanisms are so fundamental to the physical processes inherent in the system makes them very hard to control or improve upon. Another obstacle is the quenching of emission due to the tendency of Er atoms to cluster together. This limits the concentration of Er incorporation in Si [160].

One method that has proven useful for extracting light from Er in a Si-based platform is to couple the Er ions to Si nanocrystals or nanoclusters [161–163]. Optical gain[162] and electroluminescence[163] have recently been demonstrated in such devices. The cross section for excitation of Er ions by direct photon absorption is very small (10^{-15}cm^2), but the absorption cross section of Si nanocrystals is much larger [164], and it has been shown in SiO_2 films containing Si nanocrystals and Er^{3+} that the excitation of the Er is greatly enhanced by the presence of the nanocrystals[161]. It is believed the nanocrystals absorb the energy from the incident pump source and transfer it to the Er ions. In addition, deexcitation processes which occur in bulk Si are not a problem here, as the Er^{3+} ions are not embedded in a Si lattice. This, however, is not a complete solution to the problem because the presence of Si nanocrystals in the medium leads to increased absorption [165] and to date has not allowed for a Si-nanocrystal/Er-doped Si system with laser action.

One more scenario in recent work wherein Er has played the role of the emitter is in the demonstration of an Er-doped microdisk laser on a Si chip[166]. In this work high- Q silica microdisk cavities were fabricated on a Si chip and were doped with Er^{3+} . Threshold behavior was clearly demonstrated. While this work is not in the field of active Si photonics per se, it still represents a potential path forward for integrated optoelectronic circuit components.

A.2 Porous silicon

Anodization of Si in a hydrogen fluoride solution results in porous silicon (PS) which was found to give visible light emission at room temperature[167]. PS is a material wherein bulk Si has been etched into a mesh of nanoscale components. A sponge-like material results from the anodization of *p*-type Si, and a columnar structure with doping-dependent feature sizes results from the anodization of *n*-type Si. The emission from PS can be tuned by varying the etch recipe and is most commonly in the visible. Emission from PS is generally quite broad with a full width at half maximum of approximately 130nm. The above-gap emission from PS suggests confinement of the electron and hole wave functions in the material is sufficient to increase the band gap. Further, the spatial confinement leads to broadening of electron amplitudes in momentum space, effectively allowing for phononless radiative transitions from the conduction to the valence band. This quantum confinement of electron and hole wavefunctions as well as of phonons is the mechanism which leads to increased radiative efficiency in Si nanocrystals and nanowires which will be discussed shortly. The narrow zero-phonon lines of point defects result essentially from transitions represented by a single matrix element of a pair of well defined states, but the broad luminescence from quantum-confined Si results from non-vanishing transition amplitudes between states distributed in the Brillouin zone.

Interpretation of PL spectra of PS has long been a subject of some contention. By analogy to other porous materials known to luminesce at above-bandgap wavelengths, it seems possible that the luminescence from PS could be due to an introduction of optically-active surface states. Attempts to model the luminescence as resulting from an array of nanowires of varying diameters has met with much success, but skeptics argue that any theory with as many parameters could fit such a curve. A recent letter[168] has proposed a parameter-free model in which consideration of the electron-hole interaction leads to prediction of excitonic gaps and optical absorption functions which are in good agreement with experimental data. This many-body treatment accurately predicts the optical properties of Si nanowires and

porous Si and therefore may finally settle the nature of the luminescence from PS.

Although the discovery of efficient luminescence from PS was exciting, luminescence from PS is not without pitfalls. In particular distributing a limited amount of luminescence from PS over a broad band is not as desirable as narrow-band luminescence such as that resulting from transitions at point defects. Perhaps even more disconcerting is the manner in which the ability of a particular sample of PS to luminesce has a tendency to change in time.

Although improvements to PS technology have been made which deal with some of the main drawbacks, PS as a platform for Si light emitting technologies has yet to be proven to be particularly valuable. Due to the harsh nature of the anodization process PS is in general a material with high electronic and optical losses. Thus, as we found in the case of creation of point defects via irradiation damage, we find again that what we do to induce light emission in Si often damages the integrity of the material to the point where high performance operation of devices such as lasers has remained an elusive goal.

A.3 Quantum confined structures

Quantum confined structures such as superlattices [169], nanowires [168, 170], and nanocrystals [171–175] are structures with carrier confinement in one, two, and three spacial dimensions respectively wherein spacial confinement is the dominant mechanism for luminescence. Of these three geometries, nanocrystals have met with the most success as a Si-based light-emission platform. Si nanocrystals (Si-ncs) are commonly produced by thermal precipitation of Si atoms implanted in an SiO₂ matrix [173, 176], although chemical vapor deposition methods are also utilized [177]. A comprehensive account of the optical properties of Si-ncs is given in ref. [172]

Having evolved from the concepts explored in the context of PS, Si-ncs have proven to be a source of light emission [173, 178] across most of the visible spectrum [179], and the wavelength of emission can be tuned by controlling the size of the formed Si-ncs

[171]. In Si-based quantum confined structures confinement of carriers below the Si free-exciton Bohr radius of 5nm is required to achieve carrier confinement effects. Enhanced luminescence from Si-ncs smaller than 5nm is due to an increased overlap of electron and hole wave functions and a reduction in the rate of non-radiative events. Also, confinement of phonons [180] in configuration space leads to uncertainty in momentum space. This phonon k uncertainty leads to relaxation of the phonon k -selection rules [181] which govern radiative transition from the six symmetric Δ conduction band valleys to the Γ point of the valence band. This selection rule breaking also contributes to enhanced efficiency of luminescence in nanocrystals.

Exciting progress has been made in understanding the physics of Si-nc light emission and in the development of technologies based on Si-ncs. But more creative thinking is need for an electrically-pumped Si-nc-based laser to be realized. It may be discovered that hybrid approaches with III-V or II-VI nanocrystals in Si cavities hold more promise for devices [182].

{311} defects

Extended defects produce strain fields which can trap excitons and therefore lead to higher-temperature luminescence. Extended defects with interesting optical properties are known, but few devices leverage these defects because, in general, Si with extended defects is a very high-loss material. Still, it is worth discussing briefly a particular extended defect known as the {311} defect. {311} defects have been studied in much detail [22, 183–186]. They are rod-shaped accumulations of Si_is in {311} planes of the Si lattice. These defects are optically active with narrow sub-bandgap emission at 903meV at cryogenic temperatures. While emission from {311} defects is narrow at low temperatures, it is still broader than the ZPLs of point defects. What makes {311} defects worth mentioning is that their luminescence persists to higher temperatures; in particular, the luminescence from {311} defects was shown to decrease by only a factor of 30 from 4.2 to 240K. The persistence of the luminescence to higher temperature is due to exciton confinement in the

strain field induced by the presence of the cluster of interstitials [22].

Most experimental studies of the optical properties of $\{311\}$ defects have produced them by high doses of ions ($10^{12} - 10^{15} \text{ Si}^+ \text{ cm}^{-2}$) at MeV energies followed by annealing in the temperature range 680°C to 800°C . Such a treatment is very damaging to the lattice, and it is unlikely that a high performance device could be achieved with this fabrication. However, if a more controlled introduction of $\{311\}$ defects could be conceived, $\{311\}$ defects may be a valuable source of luminescence from Si.

A.4 Raman conversion and other non-linear methods

Non-linear optical properties of pristine bulk Si allowed for the creation by Jalali and coworkers of a Raman conversion laser [187], the first demonstration of coherent light generation in Si. This was followed by work done at Intel which led to a continuous-wave laser [188]. These achievements generated great excitement in the field, and progress with Raman Si lasers continues. Recently a low-threshold continuous-wave Raman Si laser was demonstrated [189]. However, this remains something of an incomplete solution to the problem of light generation in silicon because such a Raman laser still requires an optical pump.

Appendix B

Numerical aspects of the plasmonic crystal calculation

All common methods for calculating band structures become more cumbersome when dispersion is introduced. The non-linearity in the eigenproblem resulting from the introduction of the eigenvalue, ω , into the derivation necessitates diagonalization of a $3N \times 3N$ matrix within the formalism utilized in this study. This decreases the computational efficiency of the plane wave method for calculating band structures of dispersive systems.

For all cases of E -polarization considered in this study, satisfactory convergence was achieved. Up to 1681 plane waves were used, and the difference in the real parts of the eigenvalues calculated using 441 and 1681 plane waves was approximately 0.005% for the lowest bands and 0.05% for bands near ω_p . Convergence of the imaginary parts was equally satisfactory.

Although the tripling of the matrix slows the calculations, several aspects of the problem can speed the calculation. The calculation time is linear in k ; because the diagonalization for a given k is independent of diagonalization for all other k' , the calculation is easily parallelizable. Also, for the case of circular cylinders with infinite extent in one spatial dimension arranged in a square lattice, the $N \times N$ sub-matrices comprising the larger $3N \times 3N$ matrix are highly symmetric. This can be seen from an analysis of the reciprocal lattice vectors which serve as indices to the matrix elements $\mathbf{G} = m\mathbf{b}_1 + n\mathbf{b}_2$ where \mathbf{b}_i is

a primitive vector of the reciprocal lattice. If m and n each take \tilde{N} different values, then $N = \tilde{N}^2$. The $N \times N$ sub-matrices (Eqns. 3.8-3.12) are indexed by \mathbf{G} and \mathbf{G}' . For the square lattice, the reciprocal lattice is simply a Cartesian mesh. The $N \times N$ sub-matrices are each themselves comprised of $\tilde{N} \times \tilde{N}$ sub-matrices, each of which is a Toeplitz matrix. These sub-sub-matrices are themselves arranged in a Toeplitz matrix to fill the sub-matrix. Thus, calculation of each sub-matrix only requires calculation of the first row of the matrix and utilization of the Toeplitz symmetry. Since the matrix elements require calculation of Bessel functions, it is a great advantage to calculate only N matrix elements rather than N^2 . Incorporating this symmetry into the calculation speeds it up significantly so that virtually all of the time required to carry out the calculation is during diagonalization. Calculating the matrix elements and filling the matrices is nearly instantaneous.

In Figs. B.1, B.2 and B.3 we plot several eigenvalue spectra at the X point of the Brillouin zone in the complex plane. Figure B.1 shows all $3N$ eigenvalues of Eq. 3.9 for the case of a metallic core of filling factor 0.1 covered by a dielectric shell of filling factor 0.1 and $\epsilon_i = 12$. The first N of these states have negative real part and negative imaginary part approaching zero as the real part becomes more negative. The second N have very small real part and negative imaginary part. The third N have the same imaginary parts as the first N but positive real parts. It is the third N which have been plotted as the physical spectrum throughout this paper. The spectrum appears to have symmetry with respect to change of sign of the real part of the eigenvalues. In fact, in the absence of a dielectric shell or core the second N eigenvalues are noise at the level of 10^{-15} and if treated as zero the spectrum does have symmetry with respect to change of sign of the real part. When a dielectric component is accounted for in the eigenproblem the second N eigenvalues develop a band structure at the 10^{-9} level, and this very low frequency band structure is convergent with increasing basis size.

Figure B.2 shows a spectrum for the same configuration as Fig. B.1, but with a dielectric core of $\epsilon_1 = 12 - 0.1i$. Here we see a breaking of symmetry between positive and negative values of real part—in fact the first and third N eigenvalues of the spectrum develop an

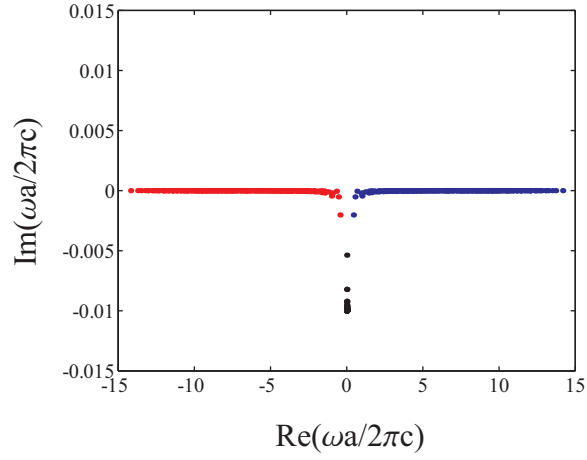


Figure B.1: The eigenvalue spectrum for E -polarization plotted in the complex plane for a metallic core surrounded by a dielectric shell with $\epsilon_i = 12$. The filling factor of each component is 0.1. The first N eigenvalues are plotted in red and have $\text{Re}(\omega) < 0$. The second N are in black and have $\text{Re}(\omega) \approx 0$. The third N are in blue with $\text{Re}(\omega) > 0$.

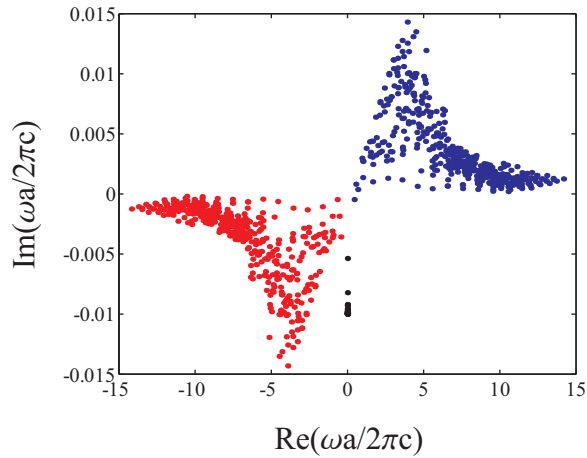


Figure B.2: The eigenvalue spectrum for E -polarization plotted in the complex plane for a metallic core surrounded by a dielectric shell with $\epsilon_i = 12 - .1i$. The filling factor of each component is 0.1. The first N eigenvalues are plotted in red and have $\text{Re}(\omega) < 0$. The second N are in black and have $\text{Re}(\omega) \approx 0$. The third N are in blue with $\text{Re}(\omega) > 0$.

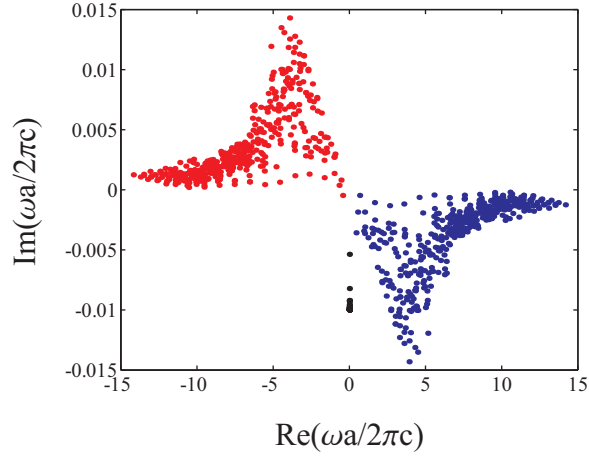


Figure B.3: The eigenvalue spectrum for E -polarization plotted in the complex plane for a metallic core surrounded by a dielectric shell with $\epsilon_i = 12 + 0.1i$. The filling factor of each component is 0.1. The first N eigenvalues are plotted in red and have $\text{Re}(\omega) < 0$. The second N are in black and have $\text{Re}(\omega) \approx 0$. The third N are in blue with $\text{Re}(\omega) > 0$.

antisymmetry. The third N states develop significant positive values of imaginary part of eigenfrequency while the third N acquire significant negative imaginary parts. Figure B.3 displays the spectrum for the same case as the previous two figures but with $\epsilon_i = 12 + 0.1i$. The spectrum is antisymmetric, as in Fig. B.2, but with the first N now having positive imaginary parts. In all three figures the tendency for large values of $\text{Re}(\omega)$ to be associated with small values of $\text{Im}(\omega)$ is demonstrated. This results from the decreased damping of the metal with increasing $\text{Re}(\omega)$. The imaginary part of the permittivity of the metallic component is given by

$$\text{Im}[\epsilon(\omega)] = \frac{\gamma\omega_p^2}{\omega^3 + \gamma^2\omega}, \quad (\text{B.1})$$

and so metallic damping decays as ω^{-3} .

Appendix C

Numerical methods for calculation of microdisk modes and quality factors.

In addition to the analytical model of optical modes in Si microdisks presented in Chapter 5, we utilized two numerical techniques to gain further insight into the resonant frequencies, mode volumes, and Q factors of our microdisks. The first method makes use of the finite-element software Comsol in a manner presented by Dr. Mark Oxborrow. This technique is very useful for obtaining resonant frequencies and mode volumes. The second technique was developed by Dr. Rashid Zia as an extension of the work by Lusse et al. [109]. This finite difference approach results in an eigenvalue equation with the complex azimuthal mode order as the eigenvalue. The Q factor can be obtained from this eigenvalue. Both numerical methods are fully vectorial, and the two methods agree in calculated values of resonant frequencies.

C.1 Resonant frequencies and mode volumes obtained with Comsol weak form approach

In Ref. [145], Dr. Oxborrow details the derivation of weak form expressions from Maxwell's equations for the case of axisymmetric resonators. In Ref. [190] he shows in de-

tail how to configure Comsol to make use of the weak form expressions. Such generosity with a code is rare in research these days. Due to Dr. Oxborrow's thorough and complete description of his calculations and utilization of Comsol, there is little to be added to his explanations. His explanation of the calculation of mode volume is sufficient. It may be helpful to point out that his presented method for calculation of radiation loss and therefore radiation-limited Q is somewhat cumbersome in that it requires one to input the expected resonant frequency in a boundary term. A value for the calculated Q and resonant frequency is then returned. This new resonant frequency is then re-inserted into the mode solver, and some iteration is required. The inconvenience and difficulty of convergence of this approach led us to seek a different means of calculating the Q factors of the resonators. Fortunately, Dr. Zia had written a code some years before to calculate the eigenmodes of ring resonators, and after some consideration we realized it could be used to obtain the Q factors as well. That method is briefly described below.

C.2 Finite-difference frequency-domain approach to calculation of microdisk Q factors

In Ref. [109], Lusse and coworkers explain in great detail their finite difference method for calculating the modes of waveguides with continuous translational symmetry. Like the azimuthal problem, the geometry is essentially two-dimensional. For the waveguide problem, one seeks the propagation constant, β . The derivation proceeds by simplifying the Helmholtz equations by applying boundary conditions between adjacent mesh nodes. The PDEs are then approximated as coupled difference equations which are formulated as an eigenvalue problem with β as the eigenvalue. For the cylindrical case, the approach is similar. Helmholtz equations for the various field components are written in cylindrical coordinates. Boundary conditions between adjacent mesh nodes simplify the equations, and the equations are approximated as difference equations. $e^{im\phi}$ angular dependence is assumed, and m becomes the eigenvalue to be solved for by matrix inversion. With this

approach, λ is given as an input parameter, and a complex m results from diagonalization of the eigenvalue problem. But for a given λ , $\text{Re}(m)$ will not, in general, be an integer. Practical implementation of the code requires setting a target integer $\text{Re}(m)$ to which we would like to converge. The matrix is diagonalized for values of λ until the target m is achieved. The λ which corresponds to the integer $\text{Re}(m)$ is then considered the resonant wavelength of the disk for that value of m . Resonant wavelengths calculated in this way are in excellent agreement with those calculated using weak forms in Comsol as described in Section C.1. It should be noted that resonances of various radial orders, vertical orders, and both polarizations can be calculated with this method, and one must determine which mode has been calculated by inspecting the field profiles. To converge to the desired radial order and polarization, one must make a good guess for the initial wavelength to begin the search. The Comsol code can be helpful for this.

From the complex azimuthal mode order one obtains the Q factor from

$$Q = \frac{\text{Re}(m)}{2\text{Im}(m)}. \quad (\text{C.1})$$

Equation C.1 is analogous to the expression

$$Q = \frac{\text{Re}(\omega)}{2\text{Im}(\omega)} \quad (\text{C.2})$$

except that Eq. C.1 relates to the fact that radiation occurs spatially as the mode circulates around the disk while Eq. C.2 relates to the fact that radiation occurs in time. Equation C.1 is derived as follows. The electric field has the form

$$\begin{aligned} \mathbf{E}(\mathbf{r}, t) &= \mathbf{E}(\rho, z) e^{im\phi} e^{-\omega_0(i + \frac{1}{2Q})t} \\ &= \mathbf{E}(\rho, z) e^{i\tilde{m}\phi} e^{-i\omega_0 t}, \end{aligned} \quad (\text{C.3})$$

where $\tilde{m} = m_r + im_i$ is the complex azimuthal mode order. From Eq. C.3 we can relate

$$im\phi - i\omega_0 t - \frac{\omega_0 t}{2Q} = im_r\phi - m_i\phi - i\omega_0 t, \quad (\text{C.4})$$

which gives

$$m_i\phi = \frac{\omega_0 t}{2Q}. \quad (\text{C.5})$$

The angular spatio-temporal dependence is governed by $e^{i(m_r\phi - \omega_0 t)}$ so that if at $t = 0$ a wave front is at $\phi = 0$, then the wave front will make a round trip to $\phi = 2\pi$ in time $\tau = \frac{2\pi m_r}{\omega_0}$. Equation C.5 becomes $2\pi m_i = \frac{2\pi m_r \omega_0}{2Q\omega_0}$, which reduces to Eq. C.1.

Appendix D

Simple model for thermal switching time in wired microdisks

We consider a simple model for the temperature as a function of time in a Si microdisk [191] under the influence of joule heating. The rate of change of temperature with respect to time is given by

$$\frac{dT}{dt} = \left(\frac{P}{c_{\text{Si}}m} - \gamma \right) T, \quad (\text{D.1})$$

where P is the power dissipated in the disk to joule heating, c_{Si} is the specific heat capacity of Si, m is the mass of the disk, and γ is rate of power dissipation out of the disk. The dominant cooling mechanism will be thermal conduction through the SiO_2 pedestal. For this study we consider only this cooling mechanism, and γ is given by [191]

$$\gamma = \frac{k}{c_{\text{Si}}m}, \quad (\text{D.2})$$

where k is the coefficient of thermal conduction through the SiO_2 pedestal;

$$k = \frac{\kappa_{\text{SiO}_2} \pi r_{\text{SiO}_2}^2}{h}, \quad (\text{D.3})$$

where κ_{SiO_2} is the thermal conductivity of SiO_2 , and r_{SiO_2} and h are the radius and height of the pedestal, respectively. Solving Eq. D.1 we get

$$T(t) = T_0 e^{t/\tau} \quad (\text{D.4})$$

with

$$\tau = \left(\frac{P}{c_{\text{Si}}m} - \gamma \right)^{-1}. \quad (\text{D.5})$$

We are interested in the time it takes to heat and cool the disk. This time is given by

$$t_f = \tau \ln\left(\frac{T_f}{T_0}\right) \quad (\text{D.6})$$

where, for cooling, $\tau = -\gamma^{-1}$.

We can plug numbers into Eq. D.6 to obtain estimates for the heating and cooling times. We assume a disk of $5\mu\text{m}$ radius and 250nm thickness, and a pedestal of $2\mu\text{m}$ radius and $3\mu\text{m}$ height. We use $2.33 \times 10^3\text{kg/m}^3$ as the density of Si, $7.12 \times 10^2\text{J/kg}\cdot\text{K}$ as the specific heat capacity of Si, and 1.38 as the thermal conductivity of SiO_2 . For high-speed application, we assume we only need to shift the resonance by a linewidth, and this can be done with a 1K temperature change for a mode with a Q of $15,000$. With 1mW heating power, this model predicts 0.1ns required to heat the device 1K and 15ns required to cool it back down 1K .

Since the cooling is slower than heating, we can reduce the cooling time by increasing the area of the pedestal through which heat can flow while simultaneously reducing the thickness of the pedestal. If we use $5\mu\text{m}$ as the radius of the pedestal (corresponding to a non-undercut disk) and use $1\mu\text{m}$ as the thickness of the oxide layer, the model predicts 0.12ns required to heat the disk 1K and 1ns required to cool it back down. These nanosecond switching times violate most people's intuition for the speed of thermal switching, and so experimental validation is necessary to confirm or refute this simple model. Unfortunately, experiments measuring the switching time of our wired microdisks were not available to us at the time of this work.

Bibliography

- [1] G. Davies, “The optical properties of luminescence centres in silicon,” *Physics Reports*, vol. 176, pp. 83–188, 1989.
- [2] S. Cloutier, P. Kossyrev, and J. Xu, “Optical gain and stimulated emission in periodic nanopatterned crystalline silicon,” *Nature Mater.*, vol. 4, p. 887, 2005.
- [3] E. Lightowers, L. Canham, G. Davies, M. Thewalt, and S. Watkins, “Lithium and lithium-carbon isoelectronic complexes in silicon: luminescence-decay-time, absorption, isotope splitting, and zeeman measurements,” *Phys. Rev. B*, vol. 29, p. 4517, 1984.
- [4] K. Thonke, A. Hangleiter, J. Wagner, and R. Sauer, “0.79 eV (C line) defect in irradiated oxygen-rich silicon: excited state structure, internal strain and luminescence decay time,” *J. Phys. C*, vol. 18, p. L795, 1985.
- [5] J. Liang, H. Chik, A. Yin, and J. Xu, “Two-dimensional lateral superlattices of nanostructures: Nonlithographic formation by anodic membrane template,” *J. Appl. Phys.*, vol. 91, p. 2544, 2002.
- [6] M. Eichenfield, R. Camacho, J. Chan, K. J. Vahala, and O. Painter, “A picogram- and nanometre-scale photonic-crystal optomechanical cavity,” *Nature*, vol. 459, pp. 550–555, 2009.
- [7] Q. Xu and M. Lipson, “Carrier-induced optical bistability in silicon ring resonators,” *Opt. Lett.*, vol. 31, pp. 341–343, 2006.

- [8] E. Kuramochi, M. Notomi, S. Mitsugi, A. Shinya, T. Tanabe, and T. Watanabe, “Ultra-high- Q photonic crystal nanocavities realized by the local width modulation of a line defect,” *Opt. Lett.*, vol. 88, p. 041112, 2006.
- [9] S. Spillane, “Fiber-coupled ultra-high- Q microresonators for nonlinear and quantum optics,” Ph.D. dissertation, California Institute of Technology, 2004.
- [10] A. Atabaki, A. Eftekhar, S. Yegnanarayanan, and A. Adibi, “Novel micro-heater structure for low-power and fast photonic reconfiguration.” Conference on Lasers and Electrooptics (CLEO), 2010, p. CWP6.
- [11] M. Watts, W. Zortman, D. Trotter, G. Nielson, D. Luck, and R. Young, “Adiabatic resonant microrings (ARMs) with directly integrated thermal microphotronics.” Conference on Lasers and Electrooptics (CLEO), 2009, p. CPDB10.
- [12] C. DeRose, M. Watts, D. Trotter, D. Luck, G. Nielson, and R. Young, “Silicon microring modulator with integrated heater and temperature sensor for thermal control.” Conference on Lasers and Electrooptics (CLEO), 2010, p. CThJ3.
- [13] Wikipedia, “Silicon — Wikipedia, the free encyclopedia,” 2010, [Online; accessed 15-August-2010]. [Online]. Available: <http://en.wikipedia.org/w/index.php?title=Silicon&oldid=377616196>
- [14] R. Soref and J. Lorenzo, “All-silicon active and passive guided-wave components for $\lambda=1.3$ and $1.6\mu\text{m}$,” *IEEE J. Quant. Electron.*, vol. QE-22, pp. 873–879, 1986.
- [15] R. Soref, J. Schmidtchen, and K. Petermann, “Large single-mode rib waveguides in GeSi and Si-on-SiO₂,” *IEEE J. Quant. Electron.*, vol. 27, pp. 1971–1974, 1991.
- [16] M. Lannoo and J. Friedel, *Point defects in semiconductors: Vol. 1: Theoretical aspects*, 1st ed., ser. Springer series in solid-state sciences. New York, New York: Springer, 1981.

- [17] ———, *Point defects in semiconductors: Vol. 2: Experimental aspects*, 1st ed., ser. Springer series in solid-state sciences. New York, New York: Springer, 1981.
- [18] R. J. Spry and W. D. Compton, “Recombination luminescence in irradiated silicon,” *Phys. Rev.*, vol. 175, p. 1010, 1968.
- [19] A. Bean, R. Newman, and R. Smith, “Electron irradiation damage in silicon containing carbon and oxygen,” *J. Phys. Chem. Solids*, vol. 31, p. 739, 1970.
- [20] C. E. Jones, E. S. Johnson, W. D. Compton, J. R. Noonan, and B. G. Streetman, “Temperature, stress, and annealing effects on the luminescence from electron-irradiated silicon,” *J. Appl. Phys.*, vol. 44, pp. 5402–5410, 1973.
- [21] O. Awadelkarim, A. Henry, B. Monemar, J. Lindstrom, Y. Zhang, and J. Corbett, “Photoluminescence study of radiative channels in ion-implanted silicon,” *Phys. Rev. B*, vol. 42, p. 5635, 1990.
- [22] D. Schmidt, B. Svensson, M. Seibt, C. Jagadish, and G. Davies, “Photoluminescence, deep level transient spectroscopy and transmission electron microscopy measurements on MeV self-ion implanted and annealed n-type silicon,” *J. Appl. Phys.*, vol. 88, p. 2309, 2000.
- [23] G. Davies, S. Hayama, L. Murin, R. Krause-Rehberg, V. Bondarenko, A. Sengupta, C. Davia, and A. Karpenko, “Radiation damage in silicon exposed to high-energy protons,” *Phys. Rev. B*, vol. 73, p. 165202, 2006.
- [24] A. Yuhnevich, “Towards a silicon laser based on emissive structural defects,” *Solid-state electronics*, vol. 51, p. 489, 2007.
- [25] G. Davies, H. Brian, E. Lightowers, K. Barraclough, and M. Thomaz, “The temperature dependence of the 969 meV ‘G’ optical transition in silicon,” *Semicond. Sci. Technol.*, vol. 4, pp. 200–206, 1989.

- [26] L. Song, X. Zhan, B. Benson, and G. Watkins, “Bistable interstitial–carbon–substitutional–carbon pair in silicon,” *Phys. Rev. B*, vol. 42, p. 5765, 1990.
- [27] A. Dolgolenko, M. Varentsov, and G. Gaidar, “Energy–level position of bistable CiCs defect in the B configuration in the forbidden band of n-Si,” *Physica Status Solidi B*, vol. 241, pp. 2914–2922, 2004.
- [28] A. V. Yukhnevich, “The structure of the spectrum of the radiative capture of holes by a centers in silicon,” *Sov. Phys. Sol. State*, vol. 7, p. 259, 1965.
- [29] G. Davies, K. Kun, and T. Reade, “Annealing kinetics of the dicarbon radiation-damage center in crystalline silicon,” *Phys. Rev. B*, vol. 44, p. 12146, 1991.
- [30] L. Canham, K. Barraclough, and D. Robbins, “1.3 μm light-emitting diode from silicon electron irradiated at its damage threshold,” *Applied physics letters*, vol. 51, pp. 1509–1511, 1987.
- [31] E. Rotem, J. M. Shainline, and J. M. Xu, “Enhanced photoluminescence from nanopatterned carbon-rich silicon grown by solid-phase epitaxy,” *Appl. Phys. Lett.*, vol. 91, p. 051127, 2007.
- [32] J. Shainline and J. Xu, “Silicon as an emissive optical medium,” *Laser & Photon. Rev.*, vol. 1, pp. 334–348, 2007.
- [33] ———, “Directly pumped silicon lasers,” *Opt. and Photon. News*, vol. 19, pp. 34–39, 2008.
- [34] G. W. Watkins, “Defects in irradiated silicon: EPR and electron–nuclear double resonance of interstitial boron,” *Phys. Rev. B*, vol. 12, pp. 5824–5839, 1975.
- [35] P. N. K. Deenapanray, N. E. Perret, D. J. Brink, F. D. Auret, and J. B. Malherbe, “Characterization of optically active defects created by noble gas ion bombardment of silicon,” *J. Appl. Phys.*, vol. 83, pp. 4075–4080, 1998.

- [36] S. Campisano, G. Foti, P. Baeri, M. G. Grimaldi, and E. Rimini, “Solute trapping by moving interface in ion–implanted silicon,” *Appl. Phys. Lett.*, vol. 37, pp. 719–722, 1980.
- [37] J. W. Strane, S. R. Lee, H. J. Stein, S. T. Picraux, J. K. Watanabe, and J. W. Mayer, “Carbon incorporation into Si at high concentrations by ion implantation and solid phase epitaxy,” *J. Appl. Phys.*, vol. 79, pp. 637–645, 1996.
- [38] G. Davies, E. Lightowers, and M. do Carmo, “Carbon-related vibronic bands in electron-irradiated silicon,” *J. Phys. C*, vol. 16, pp. 5503–5515, 1983.
- [39] K. Thonke, H. Klemisch, J. Weber, and R. Sauer, “New model of the irradiation-induced 0.97-eV (G) line in silicon: A Cs-Si* complex,” *Phys. Rev. B*, vol. 24, pp. 5874–5886, 1981.
- [40] S. Cloutier, C. Hsu, P. Kossyrev, and J. Xu, “Enhancement of radiative recombination in silicon via phonon localization and selection-rule breaking,” *Advanced Materials*, vol. 18, pp. 841–844, 2006.
- [41] R. Markiewicz, J. Wolfe, and C. Jeffries, “Strain-confined electron-hole liquid in germanium,” *Phys. Rev. B*, vol. 15, pp. 1988–2016, 1977.
- [42] A. J. Yin, J. Li, W. Jian, A. J. Bennett, , and J. M. Xu, “Fabrication of highly ordered metallic nanowire arrays by electrodeposition,” *Appl. Phys. Lett.*, vol. 79, pp. 1039–1041, 2001.
- [43] E. Yablonovitch, “Inhibited spontaneous emission in solid-state physics and electronics,” *Phys. Rev. Lett.*, vol. 58, pp. 2059–2062, 1987.
- [44] S. John and R. Rangarajan, “Optimal structures for classical wave localization: an alternative to the Ioffe-Regel criterion,” *Phys. Rev. B*, vol. 38, pp. 10 101–10 104, 1988.

- [45] R. Sprik, B. V. Tiggelen, and A. Lagendijk, “Optical emission in periodic dielectrics,” *Europhys. Lett.*, vol. 35, pp. 265–270, 1996.
- [46] T. Trifonov, L. F. Marsal, A. Rodriguez, J. Pallares, and R. Alcuilla, “Analysis of photonic band gaps in two-dimensional photonic crystals with rods covered by a thin interfacial layer,” *Phys. Rev. B*, vol. 70, p. 195108, 2004.
- [47] P. R. Evans, G. A. Wurtz, R. Atkinson, W. Hendren, D. O’Connor, W. Dickson, R. J. Pollard, and A. V. Zayats, “Plasmonic core/shell nanorod arrays: subattoliter controlled geometry and tunable optical properties,” *J. Phys. Chem. C*, vol. 111, pp. 12 522–12 527, 2007.
- [48] J. B. Pendry and A. MacKinnon, “Calculation of photon dispersion relations,” *Phys. Rev. Lett.*, vol. 69, pp. 2772–2775, 1992.
- [49] K. Sakoda, N. Kawai, T. Ito, A. Chutinan, S. Noda, T. Mitsuyu, and K. Hirao, “Photonic bands of metallic systems. I. Principle of calculation and accuracy,” *Phys. Rev. B*, vol. 64, p. 045116, 2001.
- [50] T. Ito and K. Sakoda, “Photonic bands of metallic systems. II. Features of surface plasmon polaritons,” *Phys. Rev. B*, vol. 64, p. 045117, 2001.
- [51] A. Christ, T. Zentgrafand, J. Kuhl, S. G. Tikhodeev, N. A. Gippius, and H. Giessen, “Optical properties of planar metallic photonic crystal structures: Experiment and theory,” *Phys. Rev. B*, vol. 70, p. 125113, 2004.
- [52] J. B. Pendry, “Photonic band structures,” *J. Mod. Opt.*, vol. 41, pp. 209–229, 1994.
- [53] M. Plihal and A. A. Maradudin, “Photonic band structure of two-dimensional systems: The triangular lattice,” *Phys. Rev. B*, vol. 44, pp. 8565–8571, 1991.
- [54] A. Glushko and L. Karachevtseva, “PBG properties of three-component 2D photonic crystals,” *Photonics and nanostructures-fundamentals and applications*, vol. 4, pp. 141–145, 2006.

- [55] V. Kuzmiak and A. Maradudin, “Photonic band structures of one- and two-dimensional periodic systems with metallic components in the presence of dissipation,” *Phys. Rev. B*, vol. 55, pp. 7427–7444, 1997.
- [56] ———, “Distribution of electromagnetic field and group velocities in two-dimensional periodic systems with dissipative metallic components,” *Phys. Rev. B*, vol. 58, pp. 7230–7251, 1998.
- [57] M. Kretschmann and A. A. Maradudin, “Band structures of two-dimensional surface-plasmon polaritonic crystals,” *Phys. Rev. B*, vol. 66, p. 245408, 2002.
- [58] O. Sakai, T. Sakaguchi, and K. Tachibana, “Photonic bands in two-dimensional microplasma arrays. i. theoretical derivation of band structures of electromagnetic waves,” *J. Appl. Phys.*, vol. 101, p. 073304, 2007.
- [59] T. Sakaguchi, O. Sakai, and K. Tachibana, “Photonic bands and two-dimensional microplasma arrays. ii. band gaps observed in millimeter and subeterahertz ranges,” *J. Appl. Phys.*, vol. 101, p. 073305, 2007.
- [60] C. Hafner, C. Xudong, and R. Vahldieck, “Metallic photonic crystals at optical frequencies,” *Journal of computational and theoretical nanoscience*, vol. 2, pp. 240–250, 2005.
- [61] R.-L. Chern, C. C. Chang, and C. C. Chang, “Analysis of surface plasmon modes and band structures for plasmonic crystals in one and two dimensions,” *Phys. Rev. E*, vol. 73, p. 036605, 2004.
- [62] C. C. H. Tang, “Backscattering from dielectric-coated infinite cylindrical obstacles,” *J. Appl. Phys.*, vol. 28, pp. 628–633, 1957.
- [63] P. Nordlander and F. Le, “Plasmonic structure and electromagnetic field enhancements in the metallic nanoparticle-film system,” *Appl. Phys. B*, vol. 84, pp. 35–41, 2006.

- [64] M. T. Hill, Y.-S. Oei, B. Smalbrugge, Y. Zhu, T. D. Vries, P. V. Veldhoven, F. V. Otten, T. J. Eijkemans, J. Turkiewicz, H. D. Waardt, E. Geluk, S.-H. Kwon, Y.-H. Lee, R. Notzel, and M. Smit, “Lasing in metallic-coated nanocavities,” *Nature Photon.*, vol. 1, pp. 589–593, 2007.
- [65] C. Manolatou and F. Rana, “Subwavelength nanopatch cavities for semiconductor plasmon lasers,” *IEEE J. Quant. Elec.*, vol. 44, pp. 435–447, 2008.
- [66] B. Min, E. Ostby, V. Sorger, E. Ulin-Avila, L. Yang, X. Zhang, and K. Vahala, “High-Q surface-plasmon-polariton whispering-gallery microcavity,” *Nature*, vol. 457, pp. 455–458, 2009.
- [67] R. Richtmyer, “Dielectric resonators,” *J. Appl. Phys.*, vol. 10, pp. 391–398, 1939.
- [68] S. McCall, A. Levi, R. Slusher, S. Pearton, and R. Logan, “Whispering-gallery mode microdisk lasers,” *Appl. Phys. Lett.*, vol. 60, pp. 289–291, 1992.
- [69] A. Levi, R. Slusher, S. McCall, T. Tanbun-Ek, D. Coblenz, and S. Pearton, “Room temperature operation of microdisc lasers with submilliamp threshold current,” *Electron. Lett.*, vol. 28, pp. 1010–1012, 1992.
- [70] A. Levi, S. McCall, S. Pearton, and R. Logan, “Room temperature operation of submicrometre radius disk laser,” *Electron. Lett.*, vol. 29, pp. 1666–1667, 1993.
- [71] M. Borselli, T. Johnson, and O. Painter, “Measuring the role of surface chemistry in silicon microphotronics,” *Appl. Phys. Lett.*, vol. 88, p. 131114, 2006.
- [72] M. Borselli, K. Srinivasan, P. Parclay, and O. Painter, “Rayleigh scattering, mode coupling and optical loss in silicon microdisks,” *Appl. Phys. Lett.*, vol. 85, pp. 3693–3695, 2004.
- [73] S. Gaponenko and V. Khilmanovich, “Nanophotonics: a transfer of concepts and ideas from quantum physics to electromagnetism,” *Physics, chemistry and application of nanostructures*, vol. Unk, pp. 101–104, 2007.

- [74] K. Zhang and D. Li, *Electromagnetic Theory for Microwaves and Optoelectronics*. Springer, 1998.
- [75] R. Wang and M.-M. Dumitrescu, “Theory of optical modes in semiconductor microdisk lasers,” *J. Appl. Phys.*, vol. 81, pp. 3391–3397, 1997.
- [76] J. Jackson, *Classical Electrodynamics*, 3rd ed. New York, New York: John Wiley and Sons, 1999.
- [77] J. Nöckel, “Resonances in nonintegrable open systems,” Ph.D. dissertation, Yale University, 1997.
- [78] H. Benisty, J.-M. Gerard, R. Houdre, J. Rarity, and E. C. Weisbuch, *Confined Photon Systems*, ser. Lecture Notes in Physics. New York, New York: Springer, 1999.
- [79] R. Boyd, *Nonlinear Optics*. Burlington, Massachusetts: Academic Press, 2008.
- [80] J. Knight, G. Cheung, F. Jacques, and T. Birks, “Phase-matched excitation of whispering-gallery-mode resonances by a fiber taper,” *Opt. Lett.*, vol. 22, pp. 1129–1131, 1997.
- [81] M. Cai, O. Painter, and K. J. Vahala, “Observation of critical coupling in a fiber taper to a silica-microsphere whispering-gallery mode system,” *Phys. Rev. Lett.*, vol. 85, pp. 74–77, 2000.
- [82] S. M. Spillane, T. J. Kippenberg, O. Painter, and K. J. Vahala, “Ideality in a fiber-taper-coupled microresonator system for application to cavity quantum electrodynamics,” *Phys. Rev. Lett.*, vol. 91, p. 043902, 2003.
- [83] N. Kapany, “High-resolution fibre optics using sub-micron multiple fibres,” *Nature*, vol. 184, pp. 881–883, 1959.
- [84] J. Love, W. Henry, W. Stewart, R. Black, S. Lacroix, and F. Gonthier, “Tapered single-mode fibres and devices Part 1: Adiabaticity criteria,” *IEE Proceedings-J*, vol. 138, pp. 343–354, 1991.

- [85] R. Black, S. Lacroix, F. Gonthier, and J. Love, “Tapered single-mode fibres and devices Part 2: Experimental and theoretical quantification,” *IEE Proceedings-J*, vol. 138, pp. 355–364, 1991.
- [86] T. Birks and Y. Li, “The shape of fiber tapers,” *J. Lightwave Technol.*, vol. 10, pp. 432–438, 1992.
- [87] L. Tong, R. Gattass, J. Ashcom, S. He, J. Lou, M. Shen, I. Maxwell, and E. Mazur, “Subwavelength-diameter silica wires for low-loss optical wave guiding,” *Nature*, vol. 426, pp. 816–819, 2003.
- [88] M. Sumetsky, Y. Dulashko, and A. Hale, “Fabrication and study of bent coiled free silica nanowires: self-coupling microloop optical interferometer,” *Opt. Express*, vol. 12, pp. 3521–3531, 2004.
- [89] M. Sumetsky, “How thin can a microfiber be and still guide light?” *Opt. Lett.*, vol. 31, pp. 870–872, 2006.
- [90] —, “Optics of tunneling from adiabatic nanotapers,” *Opt. Lett.*, vol. 31, pp. 3420–3422, 2006.
- [91] V. Balykin, K. Hakuta, F. Kien, J. Liang, and M. Morinaga, “Atom trapping and guiding with a subwavelength-diameter optical fiber,” *Phys. Rev. A*, vol. 70, p. 011401(R), 2004.
- [92] F. Kien, V. Balykin, and K. Hakuta, “Light-induced force and torque on an atom outside a nanofiber,” *Phys. Rev. A*, vol. 74, p. 033412, 2006.
- [93] F. L. Kien, V. Balykin, and K. Hakuta, “Angular momentum of light in an optical nanofiber,” *Phys. Rev. A*, vol. 73, p. 053823, 2006.
- [94] K. Nayak, P. Melentiev, M. Morinaga, F. Kien, V. Balykin, and K. Hakuta, “Optical nanofiber as an efficient tool for manipulating and probing atomic fluorescence,” *Opt. Express*, vol. 15, pp. 5431–5438, 2007.

- [95] M. Borselli, T. Johnson, and O. Painter, “Beyond the rayleigh scattering limit in high-q silicon microdisks: theory and experiment,” *Opt. Express*, vol. 13, pp. 1515–1530, 2005.
- [96] K. Srinivasan, M. Borselli, O. Painter, A. Stintz, and S. Krishna, “Cavity Q, mode volume, and lasing threshold in small diameter AlGaAs microdisks with embedded quantum dots,” *Opt. Express*, vol. 14, pp. 1094–1105, 2006.
- [97] M. Borselli, “High- Q microresonators as lasing elements for silicon photonics,” Ph.D. dissertation, California Institute of Technology, 2006.
- [98] K. Srinivasan, “Semiconductor optical microcavities for chip-based cavity QED,” Ph.D. dissertation, California Institute of Technology, 2006.
- [99] T. J. Kippenberg, S. M. Spillane, and K. J. Vahala, “Modal coupling in traveling-wave resonators,” *Opt. Lett.*, vol. 27, pp. 1669–1671, 2002.
- [100] L. Deych and J. Rubin, “Rayleigh scattering of whispering gallery modes of microspheres due to a single dipole scatterer,” *Phys. Rev. A*, vol. 80, p. 061805(R), 2009.
- [101] A. Hoole, M. Welland, and A. Broers, “Negative PMMA as a high-resolution resist—the limits and possibilities,” *Semicond. Sci. Technol.*, vol. 12, pp. 1166–1170, 1997.
- [102] Q. Song, H. Cao, S. T. Ho, and G. S. Solomon, “Near-ir subwavelength microdisk lasers,” *Appl. Phys. Lett.*, vol. 94, p. 061109, 2009.
- [103] Q. Xu, D. Fattal, and R. G. Beausoleil, “Silicon microring resonators with $1.5\mu\text{m}$ radius,” *Opt. Express*, vol. 16, pp. 4309–4315, 2008.
- [104] K. Srinivasan, P. E. Barclay, M. Borselli, and O. Painter, “Optical-fiber-based measurement of an ultrasmall volume high- q photonic crystal microcavity,” *Phys. Rev. B*, vol. 70, p. 081306, 2004.

- [105] J. Heebner, T. Bond, and J. Kallman, “Generalized formulation for performance degradations due to bending and edge scattering loss in microdisk resonators,” *Opt. Express*, vol. 15, pp. 4452–4473, 2007.
- [106] A. Yariv, *Quantum Electronics, Chap. 22*. New York, New York: John Wiley and Sons, 1989.
- [107] R. Wang and M.-M. Dumitrescu, “Optical modes in semiconductor microdisk lasers,” *IEEE J. Quant. Elec.*, vol. 34, pp. 1933–1937, 1998.
- [108] N. Frateschi and A. Levi, “The spectrum of microdisk lasers,” *J. Appl. Phys.*, vol. 80, p. 644, 1996.
- [109] P. Lüsse, P. Stuwe, J. Schüle, and H.-G. Unger, “Analysis of vectorial mode fields in optical waveguides by a new finite difference method,” *J. Lightwave Technol.*, vol. 12, pp. 487–494, 1994.
- [110] R. Zia, M. Selker, and M. Brongersma, “Leaky and bound modes of surface plasmon waveguides,” *Phys. Rev. B*, vol. 71, p. 165431, 2005.
- [111] K. Vahala, “Optical microcavities,” *Nature*, vol. 424, pp. 839–846, 2003.
- [112] Y. Chassagneux, J. Palomo, R. Colombelli, S. Dhillon, C. Sirtori, H. Beere, J. Alton, and D. Ritchie, “Terahertz microcavity lasers with subwavelength mode volumes and thresholds in the milliamperere range,” *Appl. Phys. Lett.*, vol. 90, p. 091113, 2007.
- [113] M. A. Noginov, G. Zhu, A. M. Belgrave, R. Bakker, V. M. Shalaev, E. E. Narimanov, S. Stout, E. Herz, T. Suteewong, and U. Wiesner, “Demonstration of a spaser-based nanolaser,” *Nature*, vol. 460, pp. 1110–1112, 2009.
- [114] K. Yu, A. Lakhani, and M. C. Wu, “Subwavelength metal-optic semiconductor nanopatch lasers,” *Opt. Express*, vol. 18, pp. 8790–8799, 2010.

- [115] M. P. Nezhad, A. Simic, O. Bondarenko, B. Slutsky, A. Mizrahi, L. Feng, V. Lomakin, and Y. Fainman, “Room-temperature subwavelength metallo-dielectric lasers,” *Nature Photon.*, 2010.
- [116] Z. Zhang, L. Yang, V. Liu, T. Hong, and A. S. K. Vahala, “Visible submicron microdisk lasers,” *Appl. Phys. Lett.*, vol. 90, p. 111119, 2007.
- [117] R. Perahia, T. P. M. Alegre, A. H. Safavi-Naeini, and O. Painter, “Surface-plasmon mode hybridization in subwavelength microdisk lasers,” *Appl. Phys. Lett.*, vol. 95, p. 201114, 2009.
- [118] J. Chen, O. Malis, A. M. Sergent, D. L. Sivco, N. Weimann, and A. Y. Cho, “In_{0.68}Ga_{0.32}As/Al_{0.64}In_{0.36}As/InP 4.5 μ m quantum cascade lasers grown by solid phosphorus molecular beam epitaxy,” *J. Vac. Sci. Technol. B*, vol. 25, pp. 913–915, 2007.
- [119] J. Faist, C. Gmachl, M. Striccoli, C. Sirtori, F. Capasso, D. L. Sivco, and A. Y. Cho, “Quantum cascade disk lasers,” *Appl. Phys. Lett.*, vol. 69, pp. 2456–2458, 1996.
- [120] C. Gmachl, J. Faist, F. Capasso, C. Sirtori, D. L. Sivco, and A. Y. Cho, “Long-wavelength (9.5–11.5 μ m) microdisk quantum-cascade lasers,” *IEEE J. Quant. Electron.*, vol. 33, pp. 1567–1573, 1997.
- [121] O. Madelung, *Semiconductors: data handbook*, 3rd ed. New York, New York: Springer, 2004.
- [122] M. Bayer, T. Gutbrod, J. Reithmaier, A. Forchel, T. Reinecke, P. Knipp, A. Dremin, and V. Kulakovskii, “Optical modes in photonic molecules,” *Phys. Rev. Lett.*, vol. 81, pp. 2582–2585, 1998.
- [123] T. Mukaiyama, K. Takeda, H. Miyazaki, Y. Jimba, and M. Kuwata-Gonokami, “Tight-binding photonic molecule modes of resonant bispheres,” *Phys. Rev. Lett.*, vol. 82, pp. 4623–4626, 1999.

- [124] M. Barnes, S. Mahurin, A. Mehta, B. Sumpter, and D. Noid, “Three-dimensional photonic molecules from sequentially attached polymer-blend microparticles,” *Phys. Rev. Lett.*, vol. 88, p. 015508, 2002.
- [125] Y. Hara, T. Mukaiyama, K. Takeda, and M. Kuwata-Gonokami, “Photonic molecule lasing,” *Opt. Lett.*, vol. 28, pp. 2437–2439, 2003.
- [126] Y. Rakovich, J. Donegan, M. Gerlach, A. Bradley, T. Connolly, J. Boland, N. Gaponik, and A. Rogach, “Fine structure of coupled optical modes in photonic molecules,” *Phys. Rev. A*, vol. 70, p. 051801, 2004.
- [127] A. Nakagawa, S. Ishii, and T. Baba, “Photonic molecule laser composed of GaInAsP microdisks,” *Appl. Phys. Lett.*, vol. 86, p. 041112, 2005.
- [128] S. Boriskina, “Theoretical prediction of a dramatic Q -factor enhancement and degeneracy removal of whispering gallery modes in symmetrical photonic molecules,” *Opt. Lett.*, vol. 31, pp. 338–340, 2006.
- [129] M. Benyoucef, S. Kiravittaya, Y. F. Mei, A. Rastelli, and O. G. Schmidt, “Strongly coupled semiconductor microcavities: A route to couple artificial atoms over micrometric distances,” *Phys. Rev. B*, vol. 77, p. 035108, 2008.
- [130] J. Heebner, R. Boyd, and Q.-H. Park, “SCISSOR solitons and other novel propagation effects in microresonator-modified waveguides,” *J. Opt. Soc. Am. B*, vol. 19, pp. 722–731, 2002.
- [131] Q. Xu, S. Manipatruni, B. Schmidt, J. Shakya, and M. Lipson, “12.5 Gbit/s carrier-injection-based silicon microring silicon modulators,” *Opt. Express*, vol. 15, pp. 430–436, 2007.
- [132] S. Manipatruni, Q. Xu, B. Schmidt, J. Shakya, and M. Lipson, “High speed carrier injection 18 Gb/s silicon micro-ring electro-optic modulator.” The 20th Annual Meeting of the IEEE Lasers and Electro-Optics Society, 2007, pp. 537–538.

- [133] S. Manipatruni, R. Dokania, B. Schmidt, N. Sherwood-Droz, C. Poitras, A. Apsel, and M. Lipson, "Wide temperature range operation of micrometer-scale silicon electro-optic modulators," *Opt. Lett.*, vol. 33, pp. 2185–2187, 2008.
- [134] M. R. Watts, D. C. Trotter, R. W. Young, and A. L. Lentine, "Ultralow power silicon microdisk modulators and switches." Sorrento, Italy: Proc. IEEE 2008 Int. Meeting Group IV Photon., 2008, pp. 4–6.
- [135] I. Fushman, E. Waks, D. Englund, N. Stoltz, P. Petroff, and J. Vuckovic, "Ultrafast nonlinear optical tuning of photonic crystal cavities," *Appl. Phys. Lett.*, vol. 90, p. 091118, 2007.
- [136] K. Srinivasan and O. Painter, "Optical fiber taper coupling and high-resolution wavelength tuning of microdisk resonators at cryogenic temperatures," *Appl. Phys. Lett.*, vol. 90, p. 031114, 2007.
- [137] M. Humar, M. Ravnik, S. Pajk, and I. Muevi, "Electrically tunable liquid crystal optical microresonators," *Nature Photon.*, vol. 3, pp. 595–600, 2009.
- [138] I. Frank, P. Deotare, M. McCutcheon, and M. Lončar, "Programmable photonic crystal nanobeam cavities," *Opt. Express*, vol. 18, pp. 8705–8712, 2010.
- [139] P. T. Rakich, M. A. Popović, M. R. Watts, T. Barwicz, H. I. Smith, and E. P. Ippen, "Ultrawide tuning of photonic microcavities via evanescent field perturbation," *Opt. Lett.*, vol. 31, pp. 1241–1243, 2006.
- [140] D. Arani, B. Min, A. Martin, and K. J. Vahala, "Electrical thermo-optic tuning of ultrahigh-Q microtoroid resonators," *Appl. Phys. Lett.*, vol. 85, pp. 5439–5441, 2004.
- [141] N. Sherwood-Droz, H. Wang, L. Chen, B. G. Lee, A. Biberman, K. Bergman, and M. Lipson, "Optical 4x4 hitless silicon router for optical networks-on-chip (NoC)," *Opt. Express*, vol. 16, pp. 15915–15922, 2008.

- [142] Y. Varshni, "Temperature dependence of the energy gap in semiconductors," *Physica*, vol. 34, pp. 149–154, 1967.
- [143] F. D. Corte, M. E. Montefusco, L. Moretti, I. Rendina, and G. Cocorullo, "Temperature dependence analysis of the thermo-optic effect in single and double oscillator models," *J. Appl. Phys.*, vol. 88, pp. 7115–7119, 2000.
- [144] J. Shainline, S. Elston, Z. Liu, G. Fernandes, R. Zia, and J. Xu, "Subwavelength silicon microcavities," *Opt. Express*, vol. 17, pp. 23 323–23 331, 2009.
- [145] M. Oxborrow, "Traceable 2-D finite element simulation of the whispering gallery modes of axisymmetric electromagnetic resonators," *IEEE Trans. Microw. Theory Tech.*, vol. 55, pp. 1209–1218, 2007.
- [146] T. Kippenberg and K. Vahala, "Cavity opto-mechanics," *Opt. Express*, vol. 15, pp. 17 172–17 205, 2007.
- [147] P. Rakich, M. Popović, M. Soljačić, and E. Ippen, "Trapping, corralling and spectral bonding of optical resonances through optically induced potentials," *Nature Photon.*, vol. 1, pp. 658–665, 2007.
- [148] P. Rakich, M. Popović, and Z. Wang, "General treatment of optical forces and potentials in mechanically variable photonic systems," *Opt. Express*, vol. 17, pp. 18 116–18 135, 2009.
- [149] E. Xifré-Pérez, F. G. de Abajao, R. Fenollosa, and F. Meseguer, "Photonic binding in silicon-colloid microcavities," *Phys. Rev. Lett.*, vol. 103, p. 103902, 2009.
- [150] B. Little and S. Chu, "Toward very large-scale integrated photonics," *Opt. and Photon. News*, vol. 11, pp. 24–29, 2000.
- [151] M. Izhaky, M. Morse, S. Koehl, O. Cohen, D. Rubin, A. Barkai, G. Sarid, R. Cohen, and M. Paniccia, "Development of CMOS-compatible integrated silicon photonics devices," *IEEE J. Select. Topics Quantum Electron.*, vol. 12, pp. 1688–1698, 2006.

- [152] C. Batten, A. Joshi, J. Orcutt, A. Khilo, B. Moss, C. Holzwarth, M. Popović, H. Li, H. Smith, J. Hoyt, F. Kärtner, R. Ram, V. Stojanović, and K. Asanović, “Building many-core processor-to-DRAM networks with monolithic CMOS silicon photonics,” *IEEE Micro*, vol. PP, pp. 8–21, 2009.
- [153] V. Govindan and S. Blair, “Analysis of optical ring architectures in the slow-light regime,” *J. Opt. Soc. Am. B*, vol. 25, pp. C116–C126, 2008.
- [154] —, “Nonlinear pulse interaction in microresonator slow-light waveguides,” *J. Opt. Soc. Am. B*, vol. 25, pp. C23–C30, 2008.
- [155] J. Heebner, P. Chak, S. Pereira, J. Sipe, and R. Boyd, “Distributed and localized feedback in microresonator sequences for linear and nonlinear optics,” *J. Opt. Soc. Am. B*, vol. 21, pp. 1818–1832, 2004.
- [156] J. Heebner, V. Wong, A. Schweinsberg, R. Boyd, and D. Jackson, “Optical transmission characteristics of fiber ring resonators,” *J. Quant. Electron.*, vol. 40, p. 726, 2004.
- [157] J. Khurgin and P. Morton, “Tunable wideband optical delay line based on balanced coupled resonator structures,” *Opt. Lett.*, vol. 34, pp. 2655–657, 2009.
- [158] L. Yan, Z. Xiao, X. Guo, and A. Huang, “Circle-coupled resonator waveguide with enhanced Sagnac phase-sensitivity for rotation sensing,” *Appl. Phys. Lett.*, vol. 95, p. 141104, 2009.
- [159] H. Ennen, G. Pomrenke, A. Axmann, K. Eisele, W. Haydl, and J. Schneider, “1.54 μ m electroluminescence of erbium-doped silicon grown by molecular beam epitaxy,” *Appl. Phys. Lett.*, vol. 46, p. 381, 1985.
- [160] A. Polman, G. van den Hoven, J. Custer, J. Shin, R. Serna, and P. Alkemade, “Erbium in crystal silicon: optical activation, excitation, and concentration limits,” *J. Appl. Phys.*, vol. 77, p. 1256, 1995.

- [161] M. Fujii, M. Yoshida, Y. Kanzawa, S. Hayashi, and K. Yamamoto, “1.54 μm photoluminescence of Er^{3+} doped into SiO_2 films containing Si nanocrystals: evidence for energy transfer from Si nanocrystals to Er^{3+} ,” *Appl. Phys. Lett.*, vol. 71, p. 1198, 1997.
- [162] H.-S. Han, S. young Seo, and J. H. Shin, “Optical gain at 1.54 μm in erbium-doped silicon nanocluster sensitized waveguide,” *Appl. Phys. Lett.*, vol. 79, p. 4568, 2001.
- [163] F. Iacona, D. Pacifici, A. Irrera, M. Mirirtello, G. Franzo, F. Priolo, D. Sanfilippo, G. D. Stefano, and P. Fallica, “Electroluminescence at 1.54 μm in Er-doped Si nanocluster-based devices,” *Appl. Phys. Lett.*, vol. 81, p. 3242, 2002.
- [164] D. Kovalev, J. Diener, H. Heckler, G. Polisski, N. Kunzner, and F. Koch, “Optical absorption cross sections of Si nanocrystals,” *Phys. Rev. B*, vol. 61, p. 4485, 2000.
- [165] R. D. Kekatpure and M. L. Brongersma, “Quantification of free-carrier absorption in silicon nanocrystals with an optical microcavity,” *Nano Lett.*, vol. 8, pp. 3787–3793, 2008.
- [166] T. J. Kippenberg, J. Kalkman, A. Polman, and K. J. Vahala, “Demonstration of an Erbium-doped microdisk laser on a silicon chip,” *Phys. Rev. A*, vol. 74, p. 051802(R), 2006.
- [167] L. Canham, “Silicon quantum wire array fabrication by electrochemical and chemical dissolution of wafers,” *Appl. Phys. Lett.*, vol. 57, p. 1046, 1990.
- [168] M. Bruno, M. Palummo, A. Marini, R. D. Sol, and S. Ossicini, “Si nanowires to porous silicon: the role of excitonic effects,” *Phys. Rev. Lett.*, vol. 98, p. 036807, 2007.
- [169] D. J. Lockwood, Z. H. Lu, and J. M. Baribeau, “Quantum confined luminescence in Si- SiO_2 superlattices,” *Phys. Rev. Lett.*, vol. 76, p. 539, 1996.

- [170] S. Piscanec, M. Cantoro, A. Ferrari, J. Zapien, Y. Lifshitz, S. Lee, S. Hofmann, and J. Robertson, “Raman spectroscopy of silicon nanowires,” *Phys. Rev. B*, vol. 68, p. 241312(R), 2003.
- [171] T. Takagahara and K. Takeda, “Theory of the quantum confinement effect on excitons in quantum dots of indirect-gap materials,” *Phys. Rev. B*, vol. 46, p. 15578, 1992.
- [172] D. Kovalev, H. Heckler, G. Polisski, and F. Koch, “Optical properties of silicon nanocrystals,” *Phys. Stat. Sol. B*, vol. 215, p. 871, 1999.
- [173] L. Pavesi, L. D. Negro, C. Mazzoleni, G. Franzo, and F. Priolo, “Optical gain in silicon nanocrystals,” *Nature*, vol. 408, p. 440, 2000.
- [174] D. Jurbergs, E. Rogojina, L. Mangolini, and U. Kortshagen, “Silicon nanocrystals with ensemble quantum yields exceeding 60 percent,” *Appl. Phys. Lett.*, vol. 88, p. 233116, 2006.
- [175] F. Trani, D. Ninno, and G. Iadonisi, “Role of local fields in the optical properties of silicon nanocrystals using the tight binding approach,” *Phys. Rev. B*, vol. 75, p. 033312, 2007.
- [176] R. J. Walters, G. I. Bourianoff, and H. A. Atwater, “Field-effect electroluminescence in silicon nanocrystals,” *Nature Mater.*, vol. 4, pp. 143–146, 2005.
- [177] M. Cavarroc, M. Mikikian, G. Perrier, and L. Boufendi, “Single-crystal silicon nanoparticles: An instability check to their synthesis,” *Appl. Phys. Lett.*, vol. 89, p. 013107, 2006.
- [178] H. Morisaki, F. Ping, H. Ono, and K. Yazawa, “Above-band-gap photoluminescence from Si fine particles with oxide shell,” *J. Appl. Phys.*, vol. 70, p. 1869, 1991.
- [179] H. Takagi, H. Ogawa, Y. Yamaxaki, A. Ishizaki, and T. Nakagiri, “Quantum size

- effects on photoluminescence in ultrafine Si particles,” *Appl. Phys. Lett.*, vol. 56, p. 2379, 1990.
- [180] J. Zi, H. Buscher, C. Falter, W. Ludwig, K. Zhang, and X. Xie, “Raman shifts in Si nanocrystals,” *Appl. Phys. Lett.*, vol. 69, p. 200, 1996.
- [181] D. Kovalev, H. Heckler, M. Ben-Chorin, G. Polisski, M. Schwartzkopff, and F. Koch, “Breakdown of the k -conservation rule in Si nanocrystals,” *Phys. Rev. Lett.*, vol. 81, p. 2803, 1998.
- [182] Z. Wu, Z. Mi, P. Bhattacharya, T. Zhu, and J. Xu, “Enhanced spontaneous emission at $1.55\mu\text{m}$ from colloidal PbSe quantum dots in a Si photonic crystal microcavity,” *Appl. Phys. Lett.*, vol. 90, p. 171105, 2007.
- [183] J. Kim, F. Kirchoff, J. Wilkins, and F. Khan, “Stability of Si-interstitial defects: from point to extended defects,” *Phys. Rev. Lett.*, vol. 84, p. 503, 2000.
- [184] J. Kim, J. W. Wilkins, F. S. Khan, and A. Canning, “Extended Si $\{311\}$ defects,” *Phys. Rev. B*, vol. 55, p. 16186, 1997.
- [185] C. J. Ortiz, P. Pichler, T. Fuhner, F. Cristiano, B. Colombeau, N. E. Cowern, and A. Claverie, “A physically based model for the spatial and temporal evolution of self-interstitial agglomerates in ion-implanted silicon,” *J. Appl. Phys.*, vol. 96, p. 4866, 2004.
- [186] S. Libertino, S. Coffa, and J. Benton, “Formation, evolution, and annihilation of interstitial clusters in ion-implanted Si,” *Phys. Rev. B*, vol. 63, p. 195206, 2001.
- [187] O. Boyraz and B. Jalali, “Demonstration of a silicon Raman laser,” *Opt. Express*, vol. 13, pp. 796–800, 2004.
- [188] H. Rong, R. Jones, A. Liu, O. Cohen, D. Hak, A. Fang, and M. Pannicia, “A continuous-wave Raman silicon laser,” *Nature*, vol. 433, pp. 725–728, 2005.

- [189] H. Rong, S. Xu, Y.-H. Kuo, V. Sih, O. Cohen, O. Raday, and M. Paniccia, “Low-threshold continuous-wave Raman silicon laser,” *Nature Photon.*, vol. 1, p. 232, 2007.
- [190] M. Oxborrow, “*Ex-house* 2D finite-element simulation of the whispering-gallery modes of axisymmetric electromagnetic resonators,” *arXiv:quant-ph/0607156v2*.
- [191] T. Johnson, M. Borselli, and O. Painter, “Self-induced optical modulation of the transmission through a high- Q silicon microdisk resonator,” *Opt. Express*, vol. 14, pp. 817–831, 2006.